

MATERIALS PHYSICS AND MECHANICS

Vol. 51, No. 6, 2023

125[©]

MATERIALS PHYSICS AND MECHANICS

Principal Editors:

Alexander Belvaev

Andrei Rudskoi

Institute for Problems in Mechanical Engineering of the Russian Academy of Science (RAS), Russia

Peter the Great St. Petersburg Polytechnic University, Russia

Founder and Honorary Editor: Ilya Ovid'ko (1961-2017)

Institute for Problems in Mechanical Engineering of the Russian Academy of Sciences (RAS), Russia

Associate Editor:

Anna Kolesnikova

Artem Semenov

Institute for Problems in Mechanical Engineering of the Russian Academy of Sciences (RAS), Russia

Peter the Great St. Petersburg Polytechnic University, Russia

Editorial Board:

E.C. Aifantis

Aristotle University of Thessaloniki, Greece

K.E. Aifantis

University of Florida, USA

U. Balachandran

Argonne National Laboratory, USA

A. Bellosi

Research Institute for Ceramics Technology, Italy

S.V. Bobylev

Institute for Problems in Mechanical Engineering (RAS), Russia

A.I. Borovkov

Peter the Great St.Petersburg Polytechnic University, Russia

G.-M. Chow

National University of Singapore, Singapore

Yu. Estrin

Monash University, Australia

A.B. Freidin

Institute for Problems in Mechanical Engineering (RAS), Russia

Y. Gogotsi

Drexel University, USA

I.G. Goryacheva

Institute of Problems of Mechanics (RAS), Russia

D. Hui

University of New Orleans, USA

G. Kiriakidis

IESL/FORTH, Greece

D.M. Klimov

Institute of Problems of Mechanics (RAS), Russia

G.E. Kodzhaspirov

Peter the Great St. Petersburg Polytechnic University, Russia

S.A. Kukushkin

Institute for Problems in Mechanical Engineering (RAS), Russia

T.G. Langdon

University of Southampton, U.K.

V.P. Matveenko

Institute of Continuous Media Mechanics (RAS), Russia

A.I. Melker

Peter the Great St. Petersburg Polytechnic University, Russia

Yu.I. Meshcheryakov

Institute for Problems in Mechanical Engineering (RAS), Russia

N.F. Morozov

St.Petersburg State University, Russia

R.R. Mulyukov

Institute for Metals Superplasticity Problems (RAS), Russia

Yu.V. Petrov

St.Petersburg State University, Russia

N.M. Pugno

Politecnico di Torino, Italy

B.B. Rath

Naval Research Laboratory, USA

A.E. Romanov

Ioffe Institute (RAS), Russia

A.M. Sastry

University of Michigan, Ann Arbor, USA

B.A. Schrefler

University of Padua, Italy

N.V. Skiba

Institute for Problems in Mechanical Engineering (RAS), Russia

A.G. Sheinerman

Institute for Problems in Mechanical Engineering (RAS), Russia

R.Z. Valiev

Ufa State Aviation Technical University, Russia

K. Zhou

Nanyang Technological University, Singapore

"Materials Physics and Mechanics" Editorial Office:

Phone: +7(812)552 77 78, ext. 224 E-mail: mpmjournal@spbstu.ru Web-site: http://www.mpm.spbstu.ru

International scientific journal "Materials Physics and Mechanics" is published by Peter the Great St. Petersburg Polytechnic University in collaboration with Institute for Problems in Mechanical Engineering of the Russian Academy of Sciences in both hard copy and electronic versions.

The journal provides an international medium for the publication of reviews and original research papers written in English and focused on the following topics:

- Mechanics of composite and nanostructured materials.
- Physics of strength and plasticity of composite and nanostructured materials.
- Mechanics of deformation and fracture processes in conventional materials (solids).
- Physics of strength and plasticity of conventional materials (solids).
- Physics and mechanics of defects in composite, nanostructured, and conventional materials.
- Mechanics and physics of materials in coupled fields.

Owner organizations: Peter the Great St. Petersburg Polytechnic University; Institute of Problems of Mechanical Engineering RAS.

Materials Physics and Mechanics is indexed in Chemical Abstracts, Cambridge Scientific Abstracts, Web of Science Emerging Sources Citation Index (ESCI) and Elsevier Bibliographic Databases (in particular, SCOPUS).

© 2023, Peter the Great St. Petersburg Polytechnic University © 2023, Institute for Problems in Mechanical Engineering RAS



МЕХАНИКА И ФИЗИКА МАТЕРИАЛОВ

Materials Physics and Mechanics

Том 51, номер 6, 2023 год

Учредители:

Редакционная коллегия журнала Главные редакторы:

д.ф.-м.н., чл.-корр. РАН А.К. Беляев Институт проблем машиноведения Российской академии наук (РАН)

д.т.н., академик РАН А.И. Рудской Санкт-Петербургский политехнический университет Петра Великого

Основатель и почетный редактор: д.ф.-м.н. И.А. Овидько (1961-2017)

Институт проблем машиноведения Российской академии наук (РАН)

Ответственный редактор

д.ф.-м.н. А.Л. Колесникова

Институт проблем машиноведения Российской академии наук (РАН)

д.ф.-м.н. А.С. Семенов Санкт-Петербургский политехнический университет Петра Великого

Международная редакционная коллегия:

д.ф.-м.н. С.В. Бобылев

Институт проблем машиноведения РАН, Россия

к.т.н., проф. А.И. Боровков

Санкт-Петербургский политехнический ун-т Петра Великого, Россия д.ф.-м.н., проф. Р.З. Валиев

Уфимский государственный технический университет, Россия д.ф.-м.н., академик РАН И.Г. Горячева

Институт проблем механики РАЙ, Россия

д.ф.-м.н., академик РАН Д.М. Климов

Институт проблем механики РАН, Россия

д.т.н., проф. Г.Е. Коджаспиров

Санкт-Петербургский политехнический ун-т Петра Великого, Россия

д.ф.-м.н., проф. С.А. Кукушкин

Институт проблем машиноведения РАН, Россия

д.ф.-м.н., академик РАН В.П. Матвеенко Институт механики сплошных сред РАН, Россия

д.ф.-м.н., проф. А.И. Мелькер

Санкт-Петербургский политехнический ун-т Петра Великого, Россия

д.ф.-м.н., проф. Ю.И. Мещеряков

Институт проблем машиноведения РАН, Россия

д.ф.-м.н., академик РАН Н.Ф. Морозов

Санкт-Петербургский государственный университет, Россия

д.ф.-м.н., чл.-корр. РАН Р.Р. Мулюков

Институт проблем сверхпластичности металлов РАН, Россия

д.ф.-м.н., чл.-корр. РАН Ю.В. Петров

Санкт-Петербургский государственный университет, Россия д.ф.-м.н., проф. А.Е. Романов

Физико-технический институт им. А.Ф. Иоффе РАН, Россия

д.ф-м.н., Н.В. Скиба

Институт проблем машиноведения РАН, Россия

д.ф.-м.н., проф. А.Б. Фрейдин

Институт проблем машиноведения РАН, Россия

д.ф-м.н., А.Г. Шейнерман

Институт проблем машиноведения РАН, Россия

Prof., Dr. E.C. Aifantis

Aristotle University of Thessaloniki, Greece

Dr. K.E. Aifantis

University of Florida, USA

Dr. U. Balachandran

Argonne National Laboratory, USA

Dr. A. Bellosi

Research Institute for Ceramics Technology, Italy

Prof., Dr. G.-M. Chow

National University of Singapore, Singapore

Prof., Dr. Yu. Estrin

Monash University, Australia

Prof., Dr. Y. Gogotsi

Drexel University, USA

Prof., Dr. D. Hui

University of New Orleans, USA

Prof., Dr. G. Kiriakidis

IESL/FORTH, Greece

Prof., Dr. T.G. Langdon

University of Southampton, UK

Prof., Dr. N.M. Pugno

Politecnico di Torino, Italy

Dr. B.B. Rath

Naval Research Laboratory, USA

Prof., Dr. A.M. Sastry

University of Michigan, Ann Arbor, USA

Prof., Dr. B.A. Schrefler

University of Padua, Italy Prof. Dr. K. Zhou

Nanyang Technological University, Singapore

Тел.: +7(812)552 77 78, доб. 224 E-mail: mpmjournal@spbstu.ru Web-site: http://www.mpm.spbstu.ru

Тематика журнала

Международный научный журнал "Materials Physics and Mechanics" издается Санкт-Петербургским политехническим университетом Петра Великого в сотрудничестве с Институтом проблем машиноведения Российской академии наук в печатном виде и электронной форме. Журнал публикует обзорные и оригинальные научные статьи на английском языке по следующим тематикам:

- Механика композиционных и наноструктурированных материалов.
- Физика прочности и пластичности композиционных и наноструктурированных материалов.
- Механика процессов деформации и разрушения в традиционных материалах (твердых телах).
- Физика прочности и пластичности традиционных материалов (твердых тел).
- Физика и механика дефектов в композиционных, наноструктурированных и традиционных материалах.
- Механика и физика материалов в связанных полях.

Редколлегия принимает статьи, которые нигде ранее не опубликованы и не направлены для опубликования в другие научные издания. Все представляемые в редакцию журнала "Механика и физика материалов" статьи рецензируются. Статьи могут отправляться авторам на доработку. Не принятые к опубликованию статьи авторам не возвращаются.

Журнал "Механика и физика материалов" ("Materials Physics and Mechanics") включен в систему цитирования Web of Science Emerging Sources Citation Index (ESCI), SCOPUS и РИНЦ.

> © 2023, Санкт-Петербургский политехнический университет Петра Великого © 2023, Институт проблем машиноведения Российской академии наук

Contents

A review on the mechanical behaviour of aluminium matrix composites under high strain rate loading S. Agarwal, S. Angra, S. Singh	1-13
Qualitative and quantitative interdependence of physical and mechanical properties of stir-casted hybrid aluminum composites D. Kumar, S. Singh, S. Angra	14-23
Study on nanosized Al ₂ O ₃ and Al ₂ O ₃ -SiC on mechanical, wear and fracture surface of Al7075 composites for soil anchoring applications M. Ravikumar, R. Naik, B.R. Vinod, K.Y. Chethana, Y.S. Rammohan	24-41
On the precipitation behavior of Al-based automotive alloy with low Si content M.S. Kaiser, A.K. Hossain	42-53
Effect of industrial hot rolling mode on microstructure and properties of low carbon bainitic steel A.A. Zisman, S.N. Petrov, N.Yu. Zolotorevsky, E.A. Yakovleva	54-64
Electronic, magnetic properties and pressure-induced phase transition of new D019 Fe ₂ MnSn Heusler alloy I. Bouhamou, H. Abbassa, C. Abbes, A. Boukortt, E.H. Abbes, A. Benbedra	65-75
Disclination models in the analysis of stored energy in icosahedral small particles A.L. Kolesnikova, M.V. Dorogov, S.A. Krasnitckii, A.M. Smirnov, A.E. Romanov	76-83
Determination of the formation energy of edge, screw and twinning dislocations in fcc metals using the molecular dynamics G.M. Poletaev, R.Y. Rakitin	84-91
Nanomaterials coating for bio-implant applications: a re-analysis N. Kumar, A. Bharti, A. Kumar, R.K. Kushwaha, K.K. Patel	92-106
Effect of curing temperature on surface and subsurface properties of polyurethane elastomer I.A. Morozov, A.Yu. Beliaev, M.G. Scherban	107-118
Study of the influence of dispersed fillers on properties of rubber for gaskets of rail fastening E.N. Egorov, S.I. Sandalov, N.I. Kol'tsov	119-126
Electromagnetic radiation reflection, transmission and absorption characteristics of microwave absorbers based on dilatant liquids and powdered activated wood charce O.V. Boiprav, V.A. Bogush, L.M. Lynkou	
Tribological characteristics of bulk ($\overline{2}01$) β-Ga ₂ O ₃ substrate crystals grown by EFG P.N. Butenko, M.E. Boiko, A.V. Chikiryaka, L.I. Guzilova, A.O. Pozdnyakov, M.D. Sharkov, A.V. Almaev, V.I. Nikolaev	135-144
Hydrogen diffusion in rotating cylindrical elastic bodies A.K. Belyaev, A.R. Galyautdinova, S.A. Smirnov	145-151
Modeling the skin effect, associated with hydrogen charging of samples, within the framework of the HEDE mechanism of cracking Yu.S. Sedova, V.A. Polyanskiy, A.K. Belyaev, Yu.A. Yakovlev	152-159

A review on the mechanical behaviour of aluminium matrix composites under high strain rate loading

Submitted: November 6, 2022

Approved: March 14, 2023

Accepted: July 5, 2023

S. Agarwal [□] S. Angra, S. Singh [□]

Abstract. AMCs (aluminium matrix composites) are commonly utilized in various structural applications as they possess high strength, low weight, and improved wear resistance properties in comparison to monolithic aluminium alloys. The properties of AMCs generally improve by adding reinforcements. These reinforcements can be ceramics like Alumina, Silicon carbide, or inorganic materials like fly ash. It was noticed that AMCs behave differently with a change in strain rate. Additionally, failure mechanisms under dynamic loading settings are discovered to be distinct from those under quasistatic or low strain rate loading conditions. The wide applications of AMCs rely both on their low strain rate behaviour and high strain rate characteristics. The emphasis of this study is to review the dynamic behaviour of AMCs where the strain rate varies from 100-10,000 s⁻¹. AMCs were discovered to be strain rate sensitive at increasing strain rates, where their strength and failure strain increases with the strain rate. **Keywords:** aluminium matrix composites; metal matrix composites; high strain rate; dynamic behaviour; mechanical properties

Citation: Agarwal S, Angra S, Singh S. A review on the mechanical behaviour of aluminium matrix composites under high strain rate loading. *Materials Physics and Mechanics*. 2023;51(6): 1-13. DOI: 10.18149/MPM.5162023_1.

Introduction

Composite is a combination of any two of the material types (polymer, metal, or ceramic) that differ in chemical composition and phases [1,2]. A composite has two phases, the matrix phase, and the reinforcement phase. Reinforcement carries the load whereas the matrix phase helps in transferring and distributing the load to the reinforcement. The matrix phase is generally ductile in nature and it binds the fibres together whereas the reinforcement phase is hard and brittle [3]. The classification of composites can be seen in Fig. 1. In the metal matrix composites (MMCs), the matrix phase is necessarily a metal and the reinforcement can be a polymer, ceramic, or even metal [4]. Aluminium, copper, magnesium, and titanium are the most commonly used matrix material in MMC. In this review paper, the focus is on the aluminium matrix composites (AMCs) where different aluminium alloys are used as matrix materials such as Al6061, Al5083, Al7075, A356, A359, etc. The reinforcement material in AMCs can either be in the form of particles (nano or micron size) or fibres (continuous or discontinuous type) [5,6]. The ceramic type reinforcements are mostly used [7,8] like silicon carbide (SiC), tungsten carbide (WC), alumina (Al₂O₃), titanium diboride (TiB₂), zirconia (ZrO₂), etc. Amongst various ceramic reinforcements, Al₂O₃ and SiC are largely used reinforcement materials types due to their easy availability and cheapness. Organic materials like fly ash, rice husk, etc. [9,10] can also be used as reinforcement materials. The first development of MMCs with ceramic reinforcements was in the early 1960s with Aluminium metal as matrix and graphite particles as reinforcement material [11]. Nowadays, the focus is more on hybrid composites [12,13], where two or more materials are used as reinforcements. The MMCs can be fabricated using

© S. Agarwal, S. Angra, S. Singh, 2023.

Publisher: Peter the Great St. Petersburg Polytechnic University

either liquid state, solid-state, or in-situ fabrication techniques (refer to Fig. 2). The universally used techniques for synthesizing of MMCs in the liquid state are stir casting and squeeze casting whereas powder metallurgy is preferred among various solid-state techniques [14].

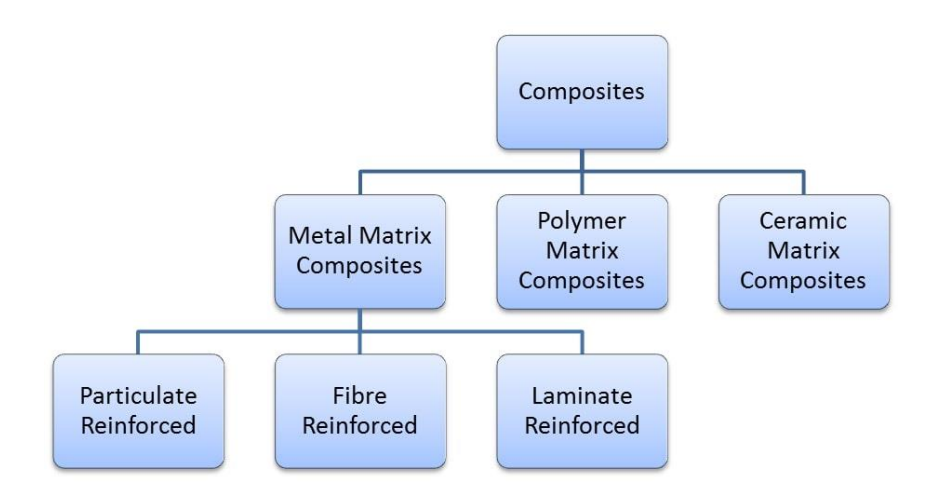


Fig. 1. Classification of composites

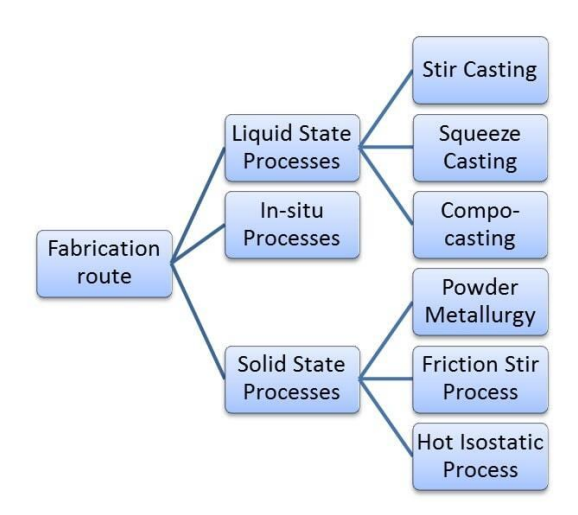


Fig. 2. Different types of fabrication routes for MMCs

AMCs are typically used in marine, aerospace, and automotive industries owing to their low weight, good load-bearing capacity, better wear resistance, and corrosion resistance as compared to monolithic metals [15–17]. Due to lower thermal strain, the wires of conductor cables in power transmission towers are made of MMCs instead of monolithic metals like steel, aluminium, and copper [18–20].

The AMCs used in engineering and structural designs such as aerospace, automotive and marine vehicles are susceptible to dynamic loads such as sudden impact due to foreign objects (animals, birds, marine life-forms, etc.) or high-speed collision due to human error while navigating such vehicles [21]. Even armour shields used for the protection of vehicles or any human are made of AMCs. Such shields must possess good anti-penetrative properties as they are prone to ballistic incidents. Such dynamic loading may lead to localized deformation of AMCs.

This review study concentrates on the mechanical behaviour of the AMCs under the dynamic loading.

Effects of reinforcement material on the properties of AMCs

With the introduction of reinforcements, there will be few changes in the mechanical, physical, and tribological properties of the AMCs compared to that of monolithic metals or their alloys. Some changes are beneficial and some are unwanted. The mechanical properties can be divided into two parts based on the strain rate -(a) low strain rate (LSR) properties due to static loading, and (b) high strain rate (HSR) properties due to dynamic loading.

LSR mechanical properties and tribological behaviour of AMCs. In static loading conditions, the strain rates for the mechanical tests are usually less than 10⁻³ s⁻¹ [22]. Mechanical properties like tensile strength, compressive strength, and hardness usually improve with the addition of reinforcement particles into the base matrix as these particles act as barriers to the dislocation movement (Orowan strengthening) which increases the value of stress required for the same amount of plastic deformation [23–26]. Whereas properties like ductility and percentage elongation are negatively affected as the wt. % of reinforcement is increased which may be due to the grain refinement of particles [27–29]. The wear resistance of AMCs was also observed to increase with reinforcement content because the addition of strong ceramic particles minimizes material loss during wear tests [30]. The fracture toughness and creep properties may also improve with the addition of reinforcement [31,32].

HSR mechanical properties of AMCs. Under dynamic loading circumstances, strain rates typically range from 10² to 10⁴ s⁻¹ or even above [33]. For HSR tests, the split Hopkinson pressure bar (SHPB) test (also referred to as the kolsky bar test) is employed [34]. In the SHPB test, the test sample is pressed between an incidence bar and a transmission bar (Fig. 3).

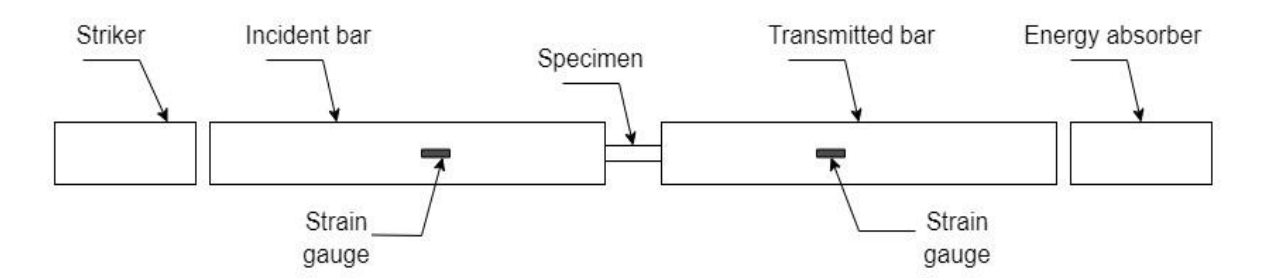


Fig. 3. Schematic of SHPB test apparatus. Redrawn from [35]

An elastic wave is generated when the striker bar collided with the incident bar with some velocity. This elastic wave passes through the interface between the incidence bar and the sample, where a portion of it is transferred to the transmission bar and the remainder is reflected back to the incident bar [36]. The reflected and transmitted wave values can be monitored using strain gauges installed at the incidence and transmission bars [37]. Stress (σ) , strain rate (ε) , and strain (ε) can be calculated from reflected and transmitted waves [38] using the given Eqs. (1) - (3):

$$\sigma_{S}(t) = \frac{A_{O}E_{O}}{A_{S}} \varepsilon_{T}(t), \tag{1}$$

$$\sigma_{S}(t) = \frac{A_{O}E_{O}}{A_{S}} \varepsilon_{T}(t), \tag{1}$$

$$\dot{\varepsilon}_{S}(t) = \frac{2C_{O}}{L_{S}} \varepsilon_{R}(t), \tag{2}$$

$$\varepsilon(t) = \int_{0}^{\tau} \dot{\varepsilon}_{S}(t) dt, \tag{3}$$

$$\varepsilon(t) = \int_0^\tau \dot{\varepsilon}_S(t) \, dt,\tag{3}$$

where A, E, and L are cross-sectional area, elastic modulus, and length respectively, s and o represent specimen and bar, ε_T is the transmitted wave signal and ε_R is the reflected wave signal, and C_0 is wave speed in the incident bar which is given by Eq. (4):

$$C_O = \sqrt{\frac{E}{\rho}}. (4)$$

There are mainly three types of HSR mechanical tests upon which the previous researchers had worked, namely HSR compressive, HSR tensile, and HSR torsional test or HSR shear test. In this study, the behaviour of AMCs under these dynamic tests and their failure mechanism is summarized by reviewing past research.

Behaviour of AMCs under HSR tensile test. Perng et al. [39] observed the HSR tensile behaviour of Al₂O₃ reinforced AMC. The HSR tensile specimens were prepared in accordance with the ASTM E8 standard. It was found that composites were highly sensitive to strain rate (about 10⁻³, 1, 140, and 400 s⁻¹) when compared to the base metal. UTS (ultimate tensile strength) of both composite and base metal were increased with the increase in the strain rate. When tested at room temperature, UTS of Al/15 %Al₂O₃ was increased from 366.53 to 468.06 MPa; and UTS for base metal Al6061-T6 was increased from 322.68 to 397.15 MPa. It was hypothesized that the decrease in dislocation velocity increased the strain rate sensitivity (SRS). The reinforcement particles acted as a barrier to dislocation motion thereby reducing dislocation velocity.

Chichili and Ramesh [40] studied the dynamic behaviour of Al/Al₂O₃ composite and also monolithic alloy under HSR tensile test by varying the strain rates over a range of 185 to 750 s⁻¹. The failure strain was observed to be increased with an increase in strain rate which suggested high values of dynamic fracture toughness compared to that of quasistatic one. There was no significant strain hardening under the dynamic tensile test. The composite test samples showed brittle fracture when viewed macroscopically but the occurrence of dimples on the broken surface of specimens indicated ductile fracture of the matrix at the microscopic level. The failure mechanism for the monolithic alloy was found to be ductile fracture with necking.

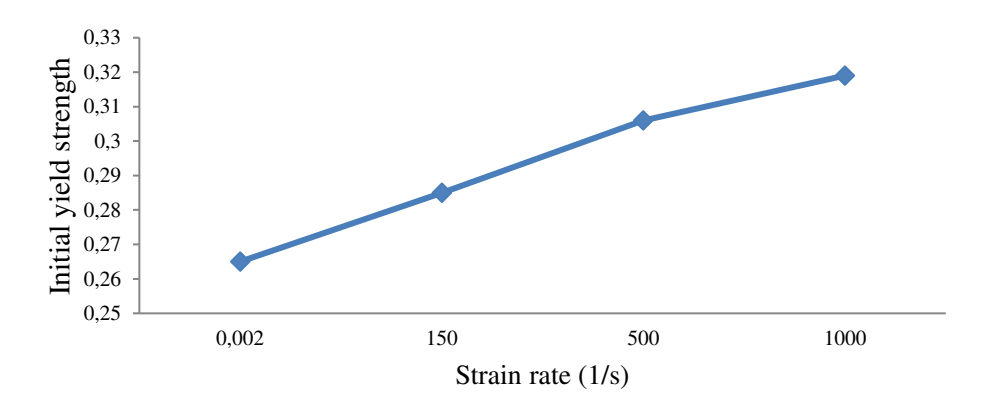


Fig. 4. Relationship between Initial yield strength and strain rate under HSR tensile test. Based on [41]

Wang et al. [41] investigated the tensile dynamic behaviour of AMC with 10 % SiC particles as reinforcement with varying strain rates (0.002, 150, 500, and 1000 s⁻¹). The composite was revealed to be rate responsive as specimen yield stress increased with strain rate (refer to Fig. 4). Li et al. [42] monitored the deformation of A359/SiC composites under a dynamic tensile test using Laser Occlusive Radius Detector for measuring the local strain of specimens. For this investigation, the strain rates were 10⁻³ and 250 s⁻¹. The rate dependency of the composite was observed with a change in yield stress by varying strain rates. The dynamic failure strain was found to be less than the quasistatic strain. This was due to the fact the strain measured was local strain whereas the previous studies measured overall strain for the specimens. The failure of the composite was mainly due to matrix failure. Reddy [43] discovered that the yield stress of Al6061/SiC composites dropped with increasing temperature but increased with increasing strain rate.

Wang et al. [44] performed HSR tensile tests on Al/CNT composites with a strain rate of about 2000 s⁻¹. The composites were manufactured with CNT particles having two different aspect ratios (AR25 and AR55). The stress-strain diagram revealed that the flow stresses were higher for AMCs with a lower aspect ratio (AR25) under both quasistatic and dynamic test conditions (refer to Fig. 5). Large values of failure strain suggest increased strain rate sensitivities within AMCs. The SEM micrographs of fractured surfaces revealed finer and shallower dimples for AMCs tested at

2000 s⁻¹ compared to quasi-statically tested AMCs. Table 1 summarizes the variations in tensile characteristics of various AMCs with strain rate.

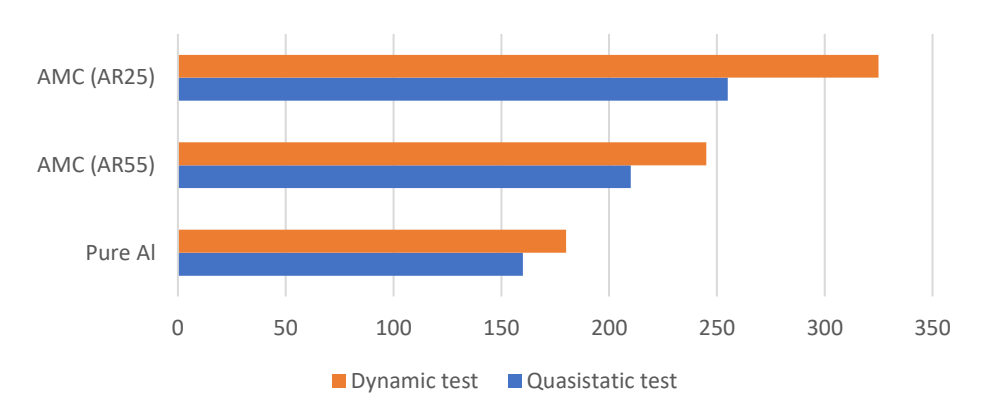


Fig. 5. Flow stress under Quasistatic and HSR Tensile test conditions. Based on [44]

Table 1. Tensile properties of various AMCs at varying strain rates

AMCs	Strain rate, s ⁻¹	Tensile strength, MPa	Strain, %
A16061 T6/15 0/ A1 O [20]	10-3	366.53	5.1
Al6061-T6/15 % Al ₂ O ₃ [39]	416.93	468.06	5.59
A16061 T6/20 0/ A1 O [40]	10-3	380	2.4
Al6061-T6/20 % Al ₂ O ₃ [40]	750	390	6.75
A1/9:C [41]	0.002	265	5
Al/SiC [41]	1000	319	7.5
A 250/20 0/ S:C [42]	10-3	160	1.2
A359/20 % SiC [42]	250	180	1.08

Behaviour of AMCs under HSR torsion test. There are very few past studies on the dynamic behaviour of AMCs under the HSR torsion or shear test. Those investigations are summarized in this section. Shear property is vital for composites with fibrous reinforcements [45]. Marchand et al. [46] used the HSR torsional test to investigate the dynamic behaviour of AMCs reinforced with SiC whiskers. The specimens were made in the shape of a thin-walled tube with flanges (refer to Fig. 6). The strain rates of 10⁻⁴, 900, 1300, 1600, and 3500 s⁻¹ were considered for the observation. Fracture toughness was found to be improved when loaded dynamically. The shear ductility of AMCs was also found to be increased from 29 % at a 10⁻⁴ s⁻¹ strain rate to 40 % at a strain rate of 3500 s⁻¹, but there were no significant changes in UTS of composites with a change in strain rate.

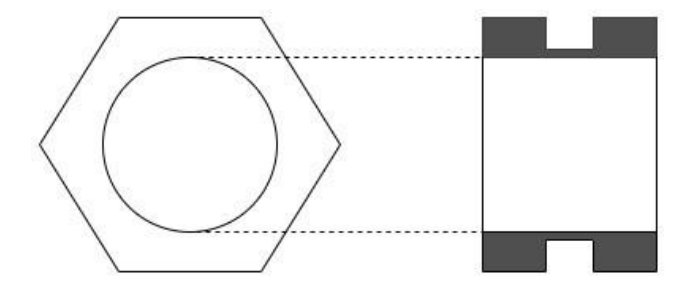


Fig. 6. Schematic of Torsional test specimen. Redrawn from [47]

Yadav et al. [48] observed that Al/Al₂O₃ composites were more sensitive to high strain rate (above 1000 s⁻¹) compared to the monolithic metal when samples were tested using HSR compression and HSR torsional tests. This change in SRS of composites was attributed to 1)

hindrance to the dislocation motion, at a high strain rate, due to adding of reinforcement and 2) increase in the dislocation density as a result of the creation of dislocations due to varied strains. The increase in the values of flow stresses at HSR was credited to the restrained plastic flow due to reinforcements. Li et al. [49] investigated the dynamic torsional behaviour of newly developed specimens, made out of A359/SiC MMC and base alloy, which helped in reducing the cost of machining and also resulted in simpler machining of the specimen. The failure strain and yield stress in shear of the base alloy were increased with an increase in the shear strain rate from 260 to 1420 s⁻¹ (refer to Fig. 7). The increase in shear yield stress and failure shear strain was also observed for the composite sample. It was found that the base alloy and composite were more ductile in shear than in tension.

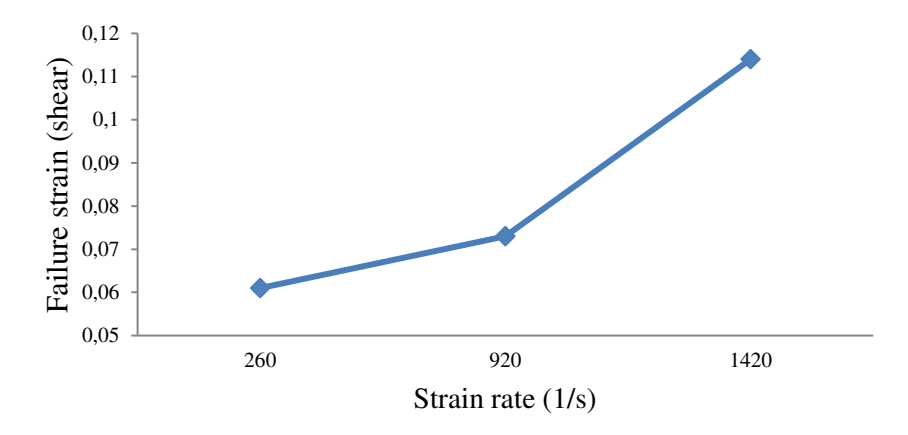


Fig. 7. Failure stress (shear) vs strain rate. Based on [49]

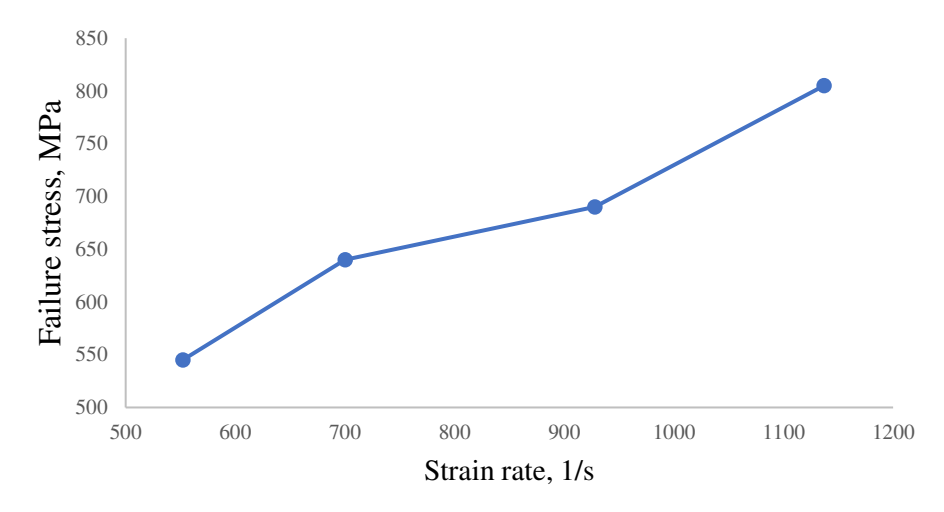


Fig. 8. Failure stress values of AMC composite with 10 wt. % Al₂O₃ under HSR torsional test. Based on [50]

Table 2. Torsional characteristics of AMCs over different strain rates

AMCs	Strain rate, s ⁻¹	Strain rate, s ⁻¹ Shear strength, MPa		
A12124 T6/SiC whishows [46]	10-4	390	29	
Al2124-T6/SiC whiskers [46]	3500	375	40	
Al6061-T6/20%Al ₂ O ₃ [48]	6.2×10 ⁴	385		
A10001-10/20%A1 ₂ O ₃ [48]	1.7×10 ⁵	465		
A359/20%SiC [49]	260	165	6.1	
A559/20%SIC [49]	1420	175	11.4	
A16061 T6/200/ A1 O [50]	687	680	19	
Al6061-T6/20%Al ₂ O ₃ [50]	1008	820	28	

Odeshi et al. [50] studied the dynamic shear and compression behaviour of Al6061/Al₂O₃ composite with strain rates varying up to about 1200 s⁻¹. The strain rate caused a rise in shear failure stress and failure strain (refer to Fig. 8). It was also observed that the AMCs were more susceptible to shear failure than failure due to compressive loading. Nucleation of micro voids and particle fracture were the reason for shear failure as observed from the SEM micrograph of fractured surfaces. Table 2 highlights the variations in torsional characteristics among different AMCs with strain rates.

Behaviour of AMCs under HSR compression test. Li and Ramesh [21] analyzed the dynamic compression behaviour of AMC with help of numerical modelling. The effect of shape, aspect ratio, and volume fraction of reinforcement particles on AMC under dynamic loading was investigated. With the increase in volume fraction of reinforcement, the strength increased even at high strain rates. Yield stresses of AMC at high strain rates were higher for cylindrical-shaped reinforcement particles as compared to spherical-shaped particles. Thus, SRS is higher for AMC at high volume fractions and also for cylindrical-shaped particles. Lee et al. [51] examined the HSR compressive properties of AMCs reinforced with 10 vol. % carbon fibres (C_f). The strain rates of 1300, 2300 and 3300 s⁻¹ were used for HSR tests. The composites were manufactured with both longitudinal and transverse fibre orientations. The HSR compressive strengths of composites with both fibre orientations at different strain rates and temperatures are mentioned in Table 3. The compressive strength increased with strain rate; however, it decreased as the temperature increased from 25 to 300 °C.

Table 3. HSR compressive strengths of Al7075-T6 based AMCs reinforced with C_f at different temperatures [51]

Test Sample	Strain rate, s ⁻¹	Temperature, °C	Compressive strength, MPa
	1200	25	654.3
AMC with longitudinal	1300	300	288.3
fibre orientation		25	692.8
		300	277.1
	1200	25	832.8
AMC with transverse	1300	300	332.0
fibre orientation	2200	25	899.4
	3300	300	367.2

Guden and Hall [52] performed HSR compression tests for three different AMCs – (a) Al-1.25 % Cu alloy reinforced with 20 % Al₂O₃ short fibres, (b) Al2124-T6 reinforced with 25 % SiC whiskers (SiCw), and (c) Al2024 reinforced with 15% SiC particles (SiC_P). The strain rate was varied from 10^{-3} to 3000 s⁻¹. Composites showed higher SRS which resulted in an increase in yield or flow stress at higher strain rates. Whisker reinforced AMCs were least sensitive to strain rate compared to fibre and particle reinforced AMCs. Lee et al. [53] explored the HSR compressive behaviour of the Al7075-T6 AMCs reinforced with varying grain sizes of SiC particles (10 and 20 μ m). A strain rate of 2800 s⁻¹ was used for compressive HSR tests of composites. The increase in yield stress was observed when AMCs were loaded under dynamic conditions. The compressive strength of AMCs with SiC particles of grain size 10 μ m was higher than AMCs with particle size 20 μ m. The strain percentage also increased with the increase in strain rate. A similar improvement in strain percentage with strain was observed by Li et al. [54] when Al2124/SiC composites were tested under dynamic compressive loading (refer to Fig. 9).

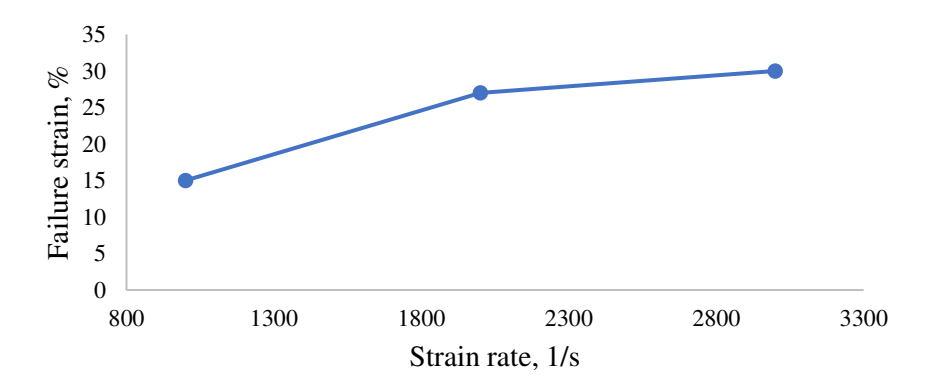


Fig. 9. Relation between strain and strain rate for AMC under HSR compression test. Based [54]

Tan et al. [55] tested the SRS of Al2024 composite reinforced with 50 % SiC particles. The quasistatic (0.001 s⁻¹) and dynamic compression tests (1250 to 2500 s⁻¹) were performed at 3 and 5 % strain for the study. There was an increase in flow stress when the strain rate was increased up to 2000 s⁻¹. The flow stress was increased by increasing the strain% from 3 to 5 % indicating strain hardening but the increase in flow stress by changing the strain rate was larger in magnitude. Thus, the hardening due to the change in strain rate is more significant than hardening due to the change in strain percentage. When the strain rate was increased from 2000 to 2500 s⁻¹, the value of flow stress dropped which was due to softening of the sample as a result of adiabatic heating during HSR compression. Zhu et al. [56] performed quasistatic (or LSR) and HSR compression tests on Al2024/60 %TiB₂ composite with strain rates of 0.0007, 1100, 1400, and 1850 s⁻¹. The flow stress values were increased by increasing the strain rate up to 1400 s⁻¹. At the strain rate of 1850 s⁻¹, there was a reduction in flow stress and an increase in elongation due to the thermal softening of the specimen during compression. For strain rates up to 1400 s⁻¹, there was brittle fracture of samples; but the failure mode for samples examined at a strain rate of 1850 s⁻¹ was ductile fracture due to softening of the composite because of heating during HSR compression.

Similar findings were observed by Ye et al. [35] by testing SiC reinforced AMCs with SiC having average particle size (APS) of 10 and 50 μ m under quasistatic compression test and dynamic compression test with strain rates spanning between 2200 and 5200 s⁻¹. Figures 10 and 11 demonstrate the increase in the value of flow or yield stress and fracture strain under compression with strain rate.

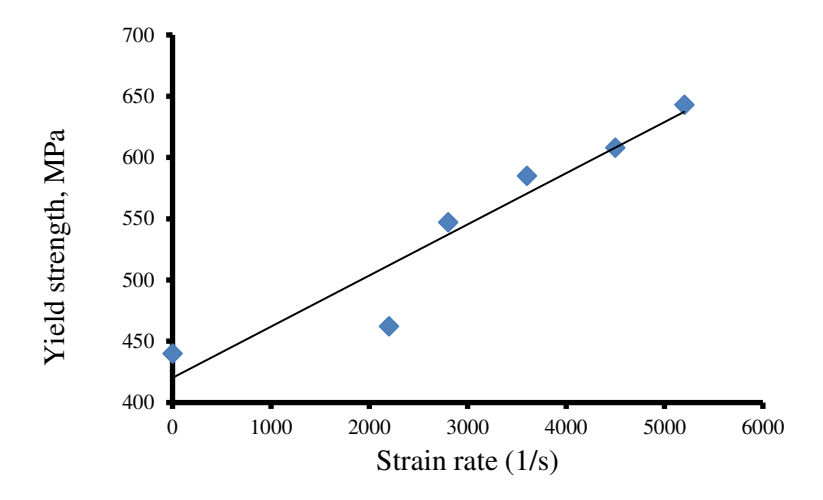


Fig. 10. Variation of Yield stress (compression) with strain rate for AMC reinforced with 10 μm SiC particles. Based on [35]

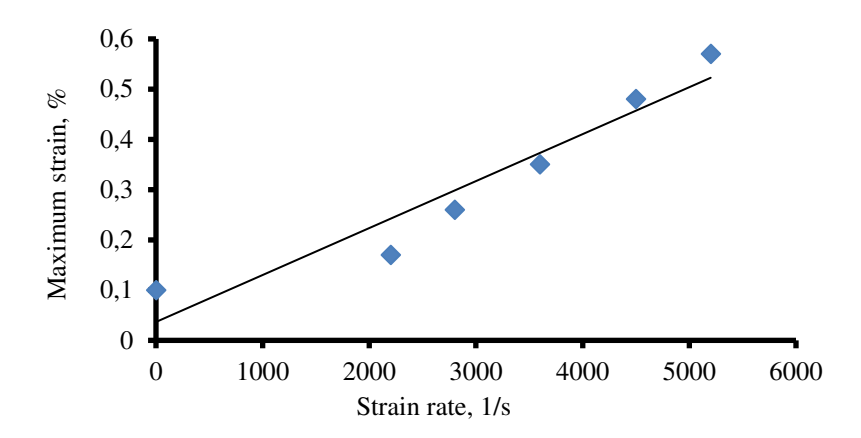


Fig. 11. Variation of fracture strain (compression) with strain rate for AMC reinforced with 10 µm SiC particles. Based on [35]

Changes in compressive strength and strain percent of numerous AMCs with the strain rate at room temperature are mentioned in Table 4.

Table 4. Compressive properties of AMCs at varying strain rates

AMCs	Strain rate, s ⁻¹	Compressive strength, MPa	Total strain, %
Al2024/15 % SiC	4.2×10 ⁻⁴	380	16
[52]	2200	420	28
Al7075-T6/SiC (10 μm)	0.001	886±68	6.4±0.8
[53]	2800	1309±108	8.4±0.8
A12124/SiC	1000	543	15
[54]	3000	569	30
A12024/50 % SiC	0.001	580	7.2
[55]	2000	775	13
Al/Al_2O_3 (4.5 µm)	10-4	340	18
[57]	1600	480	11.5
Al6092/30 % SiC	1600	535	19
[58]	4300	605	54

Table 5. Summary of HSR compression tests performed on AMCs

MMC composition	Strain rate	Findings
Al7075 AMC reinforced	0.1 to 3300 s ⁻¹	1. Flow stress increased with strain rate but decreases with
with laminated	at 25, 200	temperature.
carbon fibre [34]	and 300 °C	2. High-temperature results in an increase in ductility.
A356/Al ₂ O ₃ composite [36]	100	1. AMC was sensitive to reinforcement % and strain rate.
A330/Ai ₂ O ₃ composite [30]	to 1200 s ⁻¹	2. Strength of samples was increased at strain rates.
AMC reinforced with nano-particles of Al ₂ O ₃ (2.5 to 12.5 wt. %) [38]	700, 1400, and 3000 s ⁻¹	 Threshold Stress and fracture strain increases with strain rate. Energy absorption also increases at HSR with the maximum at 5 wt. % SiC. SSR increases with strain rate and deformation strain.
Al6092/B ₄ C composite [59]	varied up to 10^4 s ⁻¹	 Strength of composites increased with strain rate above 1000 s⁻¹. Strain hardening of AMCs reduced at high strain rates with an increase in reinforcement content.
Al/SiC with APS of 12 and 45 µm [60]	800 to 5200 s ⁻¹	 AMCs were sensitive to HSR. Dynamic Strength increases with a decrease in APS. SRS decreased with a decrease in APS. Strain softening region was observed above 3400 s⁻¹ due to thermal softening.
A356/SiC [61]	about 1200- 1500 s ⁻¹	Increased strength of composite at dynamic loading.

The strength and fracture strain of the composites under dynamic loading (HSR) were found to be more than the strength of composites when tested under static conditions (LSR). The composite with a smaller particle size had higher values of yield strength and energy absorption compared to a composite with a larger particle size.

A summary of the composition of AMCs, strain rates used in the HSR compression test, and the findings of a few other previous investigations can be found in Table 5.

Conclusions

The review paper has discussed the dynamic behaviour of AMCs under different HSR tests. The following conclusions are made from a review of the earlier investigations done on various AMCs under dynamic loading conditions:

- 1. The quasistatic mechanical properties like tensile strength, compressive strength, hardness, and fracture toughness are generally improved with the addition of reinforcement into the matrix of AMCs.
- 2. AMCs were discovered to be extremely sensitive to variations in strain rate.
- 3. At higher strain rate (HSR) values, flow stress or yield stress, energy absorption, and deformation strain are more sensitive and their values are increased at HSR.
- 4. The impact of strain rate hardening is greater than the impact of strain hardening in the increase of flow or yield stress of AMCs.
- 5. At very high strain rate values, some thermal softening phenomena were observed which caused a decrease in flow stress and an increase in elongation.
- 6. With the increase in temperature at HSR the values of flow stress decrease.
- 7. The particle size of reinforcement also affects HSR mechanical properties.

References

- 1. Poria S, Sahoo P, Sutradhar G. Tribological Characterization of Stir-cast Aluminium-TiB2 Metal Matrix Composites. *Silicon*. 2016;8(4): 591–599.
- 2. Suresh S, Moorthi NSV. Process development in stir casting and investigation on microstructures and wear behavior of TiB2 on A16061 MMC. *Procedia Engineering*. 2013;64: 1183–1190.
- 3. Khalili V, Heidarzadeh A, Moslemi S, Fathyunes L. Production of Al6061 matrix composites with ZrO2 ceramic reinforcement using a low-cost stir casting technique: Microstructure, mechanical properties, and electrochemical behavior. *Journal of Materials Research and Technology*. 2020;9(6): 15072–15086.
- 4. Karthikeyan G, Jinu GR. Experimental investigation on mechanical and wear behaviour of aluminium LM6 / ZrO2 Composites Fabricated by Stir Casting Method. *Journal of the Balkan Tribological Association*. 2015;21(3): 539–556.
- 5. Nair SV, Tien JK, Bates RC. SiC-reinforced aluminium metal matrix composites. *International Materials Reviews*. 1985;30(1): 275–290.
- 6. Singh S, Angra S. Flexural and impact properties of stainless steel based glass fibre reinforced fibre metal laminate under hygrothermal conditioning. *International Journal of Engineering, Transactions A: Basics.* 2018;31(1): 164–172.
- 7. Surappa MK. Aluminium Matrix Composites: Challenges and Opportunities. *Sadhana*. 2003;28(1–2): 319–334.
- 8. Sulardjaka S, Nugroho S, Iskandar N. Mechanical properties of AlSiMg/SiC and AlSiMgTiB/SiC produced by semi-solid stir casting and high pressure die casting. *Materials Physics and Mechanics*. 2021;47(1): 31–39.
- 9. David Raja Selvam J, Robinson Smart DS, Dinaharan I. Microstructure and some mechanical properties of fly ash particulate reinforced AA6061 aluminum alloy composites prepared by compocasting. *Materials and Design*. 2013;49: 28–34.

- 10. Rajesh S, Rajakarunakaran S, Pandian RS. Modeling and optimization of sliding specific wear and coefficient of friction of aluminum based red mud metal matrix composite using taguchi method and response surface methodology. *Materials Physics and Mechanics*. 2012;15(2): 150–166.
- 11. Rohatgi P, Schultz B, Gupta N, Daoud A. Solidification During Casting of Metal-Matrix Composites. *Casting*. 2018;15: 390–397.
- 12. Baradeswaran A, Elaya Perumal A. Study on mechanical and wear properties of Al 7075/Al2O3/graphite hybrid composites. *Composites Part B: Engineering*. 2014;56: 464–471.
- 13. Kashyap S, Tripathi H, Kumar N. Mechanical properties of marble dust reinforced aluminum matrix structural composites fabricated by stir casting process. *Materials Physics and Mechanics*. 2022;48(2): 282–288.
- 14. Chak V, Chattopadhyay H, Dora TL. A review on fabrication methods, reinforcements and mechanical properties of aluminum matrix composites. *Journal of Manufacturing Processes*. 2020;56: 1059–1074.
- 15. Sreenivasan A, Paul Vizhian S, Shivakumar ND, Muniraju M, Raguraman M. A study of microstructure and wear behaviour of TiB2/Al metal matrix composites. *Latin American Journal of Solids and Structures*. 2011;8(1): 1–8.
- 16. Purohit R, Qureshi MMU, Jain A. Forming behaviour of aluminium matrix nano Al2O3 composites for automotive applications. *Advances in Materials and Processing Technologies*. 2020;6(2): 324–335.
- 17. Saleem M, Ashok Raj J, Sam Kumar GS, Akhila R. Design and analysis of aluminium matrix composite spur gear. *Advances in Materials and Processing Technologies*. 2020;8(1): 408-416.
- 18. Suthar J, Patel KM. Processing issues, machining, and applications of aluminum metal matrix composites. *Materials and Manufacturing Processes*. 2018;33(5): 499–527.
- 19. Miracle DB. Metal matrix composites From science to technological significance. *Composites Science and Technology*. 2005;65(15-16): 2526–2540.
- 20. Kaczmar JW, Pietrzak K, Włosiński W. The production and application of metal matrix composite materials. *Journal of Materials Processing Technology*. 2000;106(1–3): 58–67.
- 21. Li Y, Ramesh KT. Influence of particle volume fraction, shape, and aspect ratio on the behavior of particle-reinforced metal-matrix composites at high rates of strain. *Acta Materialia*. 1998;46(16): 5633–5646.
- 22. Behm N, Yang H, Shen J, Ma K, Kecskes LJ, Lavernia EJ, Schoenung JM, Wei Q. Quasistatic and high-rate mechanical behavior of aluminum-based MMC reinforced with boron carbide of various length scales. *Materials Science and Engineering A*. 2016;650: 305–316.
- 23. Casati R, Vedani M. Metal matrix composites reinforced by Nano-Particles—A review. *Metals*. 2014;4(1): 65–83.
- 24. Kumar D, Angra S, Singh S. Mechanical Properties and Wear Behaviour of Stir Cast Aluminum Metal Matrix Composite: A Review. *International Journal of Engineering, Transactions A: Basics.* 2022;35(04): 794–801.
- 25. Kuldeep B, Ravikumar KP, Pradeep S. Effect of hexagonal boron nitrate on microstructure and mechanical behavior of Al7075 metal matrix composite producing by stir casting technique. *International Journal of Engineering, Transactions A: Basics.* 2019;32(7): 1017–1022.
- 26. Golestanipour M, Ayask HK, Sasani N, Sadeghian MH. A Novel, Simple and Cost Effective Al A356/Al2O3 Nano-composite Manufacturing Route with Uniform Distribution of Nanoparticles. *International Journal of Engineering Transactions C: Aspects*. 2015;28(9): 1320–1327.
- 27. Aigbodion VS, Hassan SB. Effects of silicon carbide reinforcement on microstructure and properties of cast Al-Si-Fe/SiC particulate composites. *Materials Science and Engineering A*. 2007;447(1–2): 355–360.
- 28. Kala H, Mer KKS, Kumar S. A Review on Mechanical and Tribological Behaviors of Stir Cast Aluminum Matrix Composites. *Procedia Materials Science*. 2014;6: 1951–1960.
- 29. Singh G, Goyal S. Microstructure and mechanical behavior of AA6082-T6/SiC/B4C-based aluminum hybrid composites. *Particulate Science and Technology*. 2018;36(2): 154–161.
- 30. Harti JI, Prasad TB, Nagaral M, Jadhav P, Auradi V. Microstructure and Dry Sliding Wear Behaviour of Al2219-TiC Composites. *Materials Today: Proceedings*. 2017;4(10): 11004–11009.

- 31. Aswad MA, Awad SH, Kaayem AH. Study on Iraqi Bauxite ceramic reinforced aluminum metal matrix composite synthesized by stir casting. *International Journal of Engineering, Transactions A: Basics.* 2020;33(7): 1331–1339.
- 32. Azadi M, Aroo H. Temperature effect on creep and fracture behaviors of nano-SiO2-composite and AlSi12Cu3Ni2MgFe aluminum alloy. *International Journal of Engineering, Transactions B: Applications.* 2020;33(8): 1579–1589.
- 33. Liu J, Huang X, Zhao K, Zhu Z, Zhu X, An L. Effect of reinforcement particle size on quasistatic and dynamic mechanical properties of Al-Al2O3 composites. *Journal of Alloys and Compounds*. 2019;797: 1367–1371.
- 34. Lee WS, Sue WC, Lin CF. The effects of temperature and strain rate on the properties of carbon-fiber-reinforced 7075 aluminum alloy metal-matrix composite. *Composites Science and Technology*. 2000;60(10): 1975–1983.
- 35. Ye T, Xu Y, Ren J. Effects of SiC particle size on mechanical properties of SiC particle reinforced aluminum metal matrix composite. *Materials Science & Engineering A*. 2019;753: 146–155.
- 36. Nawale SP, Vyavahare RT, Aradhye AS. High Strain Rate Response of A356/Al2O3 Aluminum Alloy MMCs Using Ls-Dyna. *Procedia Engineering*. 2017;173: 1967–1974.
- 37. Sudheera, Rammohan YS, Pradeep MS. Split Hopkinson Pressure Bar Apparatus for Compression Testing: A Review. *Materials Today: Proceedings*. 2018;5(1): 2824–2829.
- 38. Zaiemyekeh Z, Liaghat GH, Ahmadi H, Khan MK, Razmkhah O. Effect of strain rate on deformation behavior of aluminum matrix composites with Al2O3 nanoparticles. *Materials Science and Engineering A*. 2019;753: 276–284.
- 39. Perng CC, Hwang JR, Doong JL. High strain rate tensile properties of an (Al2O3 particles)-(Al alloy 6061-T6) metal matrix composite. *Materials Science and Engineering A*. 1993;171(1–2): 213–221.
- 40. Chichili DR, Ramesh KT. Dynamic failure mechanisms in a 6061-T6 Al/Al2O3 metal-matrix composite. *International Journal of Solids and Structures*. 1995;32(17–18): 2609–2626.
- 41. Wang Y, Zhou Y, Xia Y. Tensile behavior of SiCp/Al composites subjected to quasi-static and high strain-rate loading. *Journal of Materials Science*. 2004;39(9): 3191–3193.
- 42. Li Y, Ramesh KT, Chin ESC. Plastic deformation and failure in A359 aluminum and an A359-SiC p MMC under quasistatic and high-strain-rate tension. *Journal of Composite Materials*. 2007;41(1): 27–40.
- 43. Reddy AC. Influence of strain rate and temperature on superplastic behavior of sinter forged Al6061/SiC metal matrix composites. *International Journal of Engineering Research and Technology*. 2011;4(2): 189–198.
- 44. Wang M, Li Y, Chen B, Shi D, Umeda J, Kondoh K, Shen J. The rate-dependent mechanical behavior of CNT-reinforced aluminum matrix composites under tensile loading. *Materials Science & Engineering A*. 2021;808: 140893.
- 45. Dai LH, Bai YL, Lee SWR. Experimental Investigation of the Shear Strength of a Unidirectional Carbon/Aluminum Composite under Dynamic Torsional Loading. *Composites Science and Technology*. 1998;58(10): 1667–1673.
- 46. Marchand A, Duffy J, Christman TA, Suresh S. An experimental study of the dynamic mechanical properties of an AlSiCw composite. *Engineering Fracture Mechanics*. 1988;30(3): 295–315.
- 47. Ramesh KT. On the localization of shearing deformations in tungsten heavy alloys. *Mechanics of Materials*. 1994;17(2–3): 165–173.
- 48. Yadav S, Chichili DR, Ramesh KT. The mechanical response of a 6061-T6 A1/A12O3 metal matrix composite at high rates of deformation. *Acta Metallurgica Et Materialia*. 1995;43(12): 4453–4464.
- 49. Li Y, Ramesh KT, Chin ESC. The mechanical response of an A359/SiCp MMC and the A359 aluminum matrix to dynamic shearing deformations. *Materials Science and Engineering A*. 2004;382(1–2): 162–170.

- 50. Odeshi AG, Owolabi GM, Singh MNK, Bassim MN. Deformation and Fracture Behavior of Alumina Particle-Reinforced Al 6061-T6 Composite during Dynamic Mechanical Loading. *Metallurgical and Materials Transactions A*. 2007;38: 2674–2680.
- 51. Lee WS, Sue WC, Chiou ST. Effect of Reinforcement Orientation on the Impact Fracture of Carbon Fiber Reinforced 7075-T6 Aluminium Matrix Composite. *Materials Transactions*, *JIM*. 2000;41(8): 1055–1063.
- 52. Guden M, Hall IW. Dynamic properties of metal matrix composites: a comparative study. *Materials Science and Engineering A*. 1998;242: 141–152.
- 53. Lee H, Choi JH, Jo MC, Lee D, Shin S, Jo I, Lee SK, Lee S. Effects of SiC particulate size on dynamic compressive properties in 7075-T6 Al-SiCp composites. *Materials Science and Engineering: A.* 2018;738: 412–419.
- 54. Li X, Kim J, Roy A, Ayvar-Soberanis S. High temperature and strain-rate response of AA2124-SiC metal matrix composites. *Materials Science and Engineering: A.* 2022;856: 144014.
- 55. Tan ZH, Pang BJ, Gai BZ, Wu GH, Jia B. The dynamic mechanical response of SiC particulate reinforced 2024 aluminum matrix composites. *Materials Letters*. 2007;61(23–24): 4606–4609.
- 56. Zhu D, Wu G, Chen G, Zhang Q. Dynamic deformation behavior of a high reinforcement content TiB2/Al composite at high strain rates. *Materials Science and Engineering A*. 2008;487(1–2): 536–540.
- 57. San Marchi C, Cao F, Kouzeli M, Mortensen A. Quasistatic and dynamic compression of aluminum-oxide particle reinforced pure aluminum. *Materials Science and Engineering: A*. 2002;337(1-2): 202–211.
- 58. Suo Y, Li J, Deng Z, Wang B, Wang Q, Ni D, Jia P, Suo T. High-temperature compressive response of SiCp/6092Al composites under a wide range of strain rates. *Materials*. 2021;14(21): 6244.
- 59. Zhang H, Ramesh KT, Chin ESC. High strain rate response of aluminum 6092/B4C composites. *Materials Science and Engineering A*. 2004;384(1–2): 26–34.
- 60. Zhang J, Shi H, Cai M, Liu L, Zhai P. The dynamic properties of SiCp/Al composites fabricated by spark plasma sintering with powders prepared by mechanical alloying process. *Materials Science and Engineering A*. 2009;527(1–2): 218–224.
- 61. Lee H, Sohn SS, Jeon C, Jo I, Lee SK, Lee S. Dynamic compressive deformation behavior of SiC-particulate-reinforced A356 Al alloy matrix composites fabricated by liquid pressing process. *Materials Science and Engineering A*. 2017;680: 368–377.

THE AUTHORS

Agarwal S. 🗓

e-mail: saumy_61900049@nitkkr.ac.in

Singh S. 📵

e-mail: satnamsingh@nitkkr.ac.in

Angra S.

e-mail: angrasurjit@yahoo.com

Qualitative and quantitative interdependence of physical and mechanical properties of stir-casted hybrid aluminum composites

Submitted: March 9, 2023

Accepted: August 10, 2023

Approved: July 21, 2023

D. Kumar [™], S. Singh [™], S. Angra

Abstract. Aluminum alloys are lightweight, castable, machinable, and have good mechanical and physical properties. Aluminum alloys are used in aerospace, automotive, defense, and structural sectors because of their promising qualities. This work examined how stirring speed, preheating temperature, and particle size affect the mechanical characteristics of stir-cast hybrid aluminum nanocomposites supplemented with GNPs and CeO₂ at 0–3 wt. %. The microstructural investigation was done using SEM. EDAX confirmed components in nanocomposite samples. Increased reinforcing percentage improved physical and mechanical properties. The (3 % GNPs and 3 % CeO₂) hybrid nanocomposites have 1.06 % porosity. The highest hardness, tensile strength, and yield strength were 104.3, 347.01, and 215.13 MPa. SEM micrographs indicated that hybrid composite samples had a more uniform distribution of reinforcements and defects-free morphology.

Keywords: Al-6061; nanocomposite; porosity; density; mechanical properties; microstructure

Citation: Kumar D, Singh S, Angra S. Qualitative and quantitative interdependence of physical and mechanical properties of stir-casted hybrid aluminum composites. *Materials Physics and Mechanics*. 2023;51(6): 14-23. DOI: 10.18149/MPM.5162023_2.

Introduction

The aerospace and automotive sectors, in particular, have expanded their need for sophisticated materials in recent years. In this case, you need a specially formulated combination of materials exhibiting novel and advanced characteristics. [1]. Advanced composite materials can satisfy these requirements. Currently, hybrid composites are being replaced by traditional composites. Hybrid composites have considerable potential in engineering applications owing to their enhanced reliability and performance [2]. The combination of two or more different constituents has distinct physical and chemical characteristics at the microscopic level and possesses better characteristics than the base material, which is termed a hybrid composite material. The hybrid composite has excellent strength-to-weight ratio, stiffness, wear resistance, and corrosion resistance [3-5]. As we are very much aware of the fact that the accessibility of aluminum in Earth's crust is abundant, it is also the second prime metal in the core. Since 1990, aluminum and alloys have been traditionally employed in all engineering sectors, including aerospace, marine, automotive, and structural sectors. Metal matrix composites (MMC) are also made from aluminum by adding very small quantities of reinforcement [6]. Aluminum or aluminum alloys are combined with two or more reinforcing particulates in varying ratios to create hybrid aluminum metal matrix composites (HAMMC). If the reinforcements are nanoparticles, they are termed as nanocomposites. Stir-Cast Hybrid aluminum nanocomposites (HAIMNCs) are popular in various industries because of their enhanced customized mechanical and tribological properties. HAlMNCs also provide a

versatile, attractive, and technological platform for value-added applications such as lithiumion batteries, superconductors, lightweight structures, and photovoltaic cells [7]. William Hume-Rothery, a metallurgist scientist, described the solubility limits of elements in metals. The enhancement of the characteristics of hybrid nanocomposite materials is greatly dependent on the selection of reinforcements and their distribution throughout the matrix material [8]. A wide range of ceramic and non-ceramic nano-particulates is available for use as reinforcements. Carbon nanotubes, alumina, titanium boride, and silicon carbide have been used as reinforcements [9]. The next most significant factor is the selection of suitable fabrication techniques. The inherent process capability and process-oriented defects are the limitations of traditional casting methods. The overall quality of the fabricated material is also affected by these traditional casting processes. Shrinkage, blow-holes, and dendritic structures are casting defects that affect the mechanical properties of the casted components [10]. To avoid such defects and problems during casting, advanced casting techniques can be used, such as stir casting, friction-stir processing, spray decomposition, and powder metallurgy. The stir casting technique is highly effective in achieving uniform dispersion and strong bonding of reinforcement particles [11]. In this study, nano-powder of graphene and ceria were used as reinforcements owing to their high melting temperatures and low densities, respectively. nanoparticles were also found to enhance the characteristics of the hybrid nanocomposite material. Al-6061 is used as a matrix material because it is lightweight, low-density, has a low melting point, and is applicable in tripartite and quadruple engineering applications. In the course of this investigation, measurements were taken to determine density, porosity, hardness, and tensile strength. The microstructural behavior was also studied to validate the enhancement of the aforementioned properties.

Materials

Matrix material. The matrix used was Al-6061 alloy, and with purity of 98.0 %. A spectrophotometer was used in order to discover the precise chemical components of the Al-6061 alloy, and the alloy contained the following elements and percentages: Si (0.51 %), Fe (0.257 %), Cu (0.219 %), Mn (0.043 %), Zn (0.094 %), Mg (0.797 %), Ni (0.001 %), Cr (0.157 %), Ti (0.027 %), and Al (balance).

Reinforcement materials. GNPs (graphene nanoplatelets) and CeO_2 (cerium oxide/ceria). The purity of the CeO_2 powder was 99.5% and the mean particle size was 3-6 nm. The melting temperature of CeO_2 was 3670 °C, and its density was 7.2 g/cm³. The purity of GNPs was 99.9% and the mean particle size was 24-28 nm. The melting temperature of GNPs was 2400 °C, and their density was 2.3 g/cm³. The nano-reinforcement particulates were in the range 0–3 wt. % to prepare the test specimens.

Fabrication method

Stir-casting procedure. Hybrid aluminum composite specimens were fabricated using a stir-casting approach, as outlined in the flow diagram (Fig. 1). The electric furnace of the stir-casting machine was superheated at 800 °C and then AA-6061 was added to the electric furnace. Next, graphene and cerium oxide nanoparticles wrapped in aluminum foil were added to the electric furnace. The nano-reinforcements were already preheated at 300 °C for half an hour. This preheating operation was performed to limit the amount of moisture and absorbed gases in the reinforcements, as well as to minimize the temperature differential caused by the addition of particles to the molten metal after it had already been heated. It also reduces the temperature difference of the molten metal after the addition of particulates.

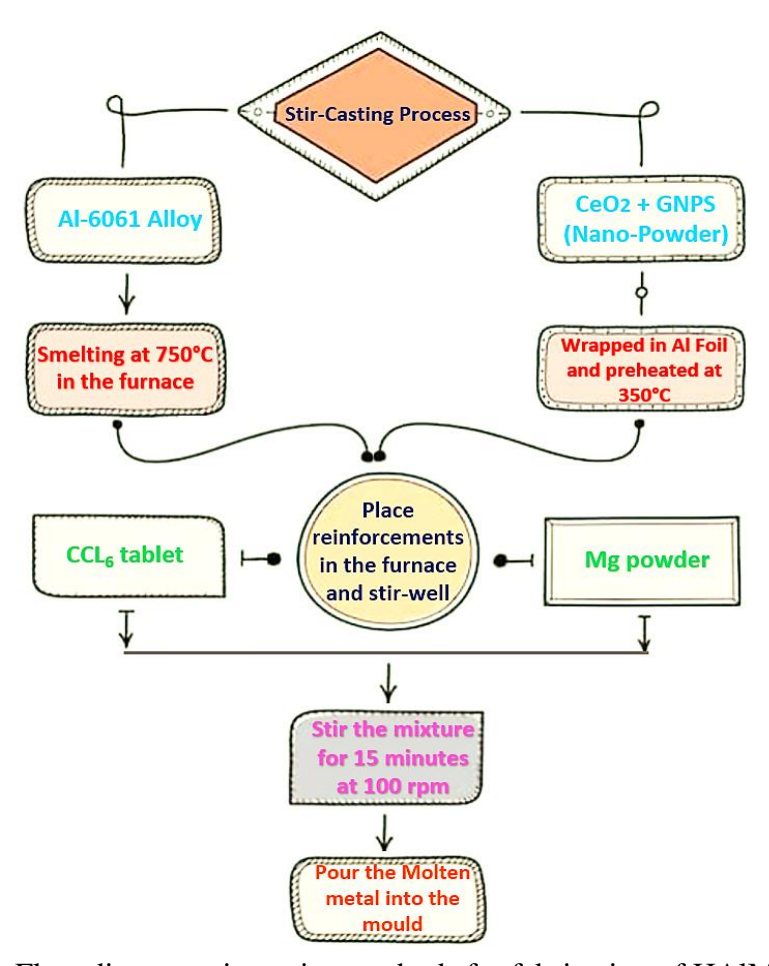


Fig. 1. Flow diagram stir casting methods for fabrication of HAIMNCs

Hexachloroethane (CCl₆) tablets were used to degases the molten metal. A temperature of $750\,^{\circ}\text{C}$ was maintained, with adequate viscosity. An appropriate vortex was created using a diamond-coated impeller by stirring at 350 rpm for 15 minutes. The high stirring speed created a powerful vortex in molten metal, which mixed the nano-reinforcement particles uniformly. This was performed to ensure that the nano-reinforcements were mixed evenly in the base material, which is essential for achieving the desired properties of the produced composites. The addition of 2 % of magnesium was performed to enhance the wettability of the reinforcement particulates. A stirring speed of 100 rpm was maintained for the next 15 min, followed by a decrease to 80 rpm for the next 5 min to ensure uniform mixing of the particulates. In the end, the liquid metal was poured into the mould, and then it was left to cool and harden at normal temperature. Four specimens with different compositions were prepared by the stircasting method, as listed in Table 1.

Table 1. Fabricated sample's nomenclature

Sample	Nomenclature	Composition
1	HAIMNC1	100 % Al-6061 + (0 % CeO ₂ + 0 % GNPs)
2	HAIMNC2	96 % Al-6061 + (3 % CeO ₂ + 1 % GNPs)
3	HAIMNC3	96 % Al-6061 + (1 % CeO ₂ + 3 % GNPs)
4	HAIMNC4	94 % Al-6061 + (3 % CeO ₂ + 3 % GNPs)

Characterization techniques

The developed HAIMNCs sub-surface was observed using field-emission scanning electron microscopy (FESEM). Examination of the fabricated HAIMNCs revealed the dispersion nature of the reinforcement in the matrix material. The mixture's experimental density was measured using Archimedes' rule and ASTM B 962-13. The mixing rule was utilized to compute theoretical density. The predicted and experimental densities were used to determine the mixture's porosity. The theoretical density of the hybrid composite can be derived as Eq. (1) [12]:

$$\rho_{HAlMNCs} = \rho_{Al-6061} W_{Al-6061} + \rho_{Graphene} W_{Graphene} + \rho_{Ceria} W_{Ceria}. \tag{1}$$

Relative densification (%) can be derived from Eq. (2) [13]:

Relative densification (%) =
$$\left(\frac{Experimental \ density}{Theoretical \ density} \times 100\right)$$
. (2)

The porosity (%) of the specimens was calculated using Eq. (3) [14]:

Porosity (%) =
$$\left(1 - \frac{Relative\ densification}{100}\right)$$
. (3)

Before putting the test specimens through the Vickers hardness tester, they were rigorously wiped and buffed. On each of the 10 places, a load of 200 g was applied for a period of 20 seconds during the dwell time, after which the average was taken and noted. The tensile and yield strengths were determined based on the Vickers hardness values in MPa by applying Cahoon's Eqs. 4 and 5, which were recommended and suggested by Cahoon et al. [15] and acknowledged by various researchers [16–18].

Tensile strength (MPa) =
$$\frac{VHN}{2.9} \times \left(\frac{m}{0.217}\right)^m$$
, (4)

Yield strength (MPa) =
$$\frac{VHN}{3} \times 0.1^m$$
, (5)

where VHN and m are the Vickers hardness (MPa) and the strain-hardening exponent, respectively. In this study, m was set to 0.02, which should be less than unity, as reported by Callister and Rethwisch [19].

Results and Discussions

Physical properties. Figure 2 shows a graphical representation of the theoretical and experimental densities of the HAlMNCs samples. The analysis showed the dense nature of the stir-cast HAlMNCs owing to their high theoretical densities compared to the experimental densities. To calculate the theoretical densities of different HAlMNCs samples, Equation (1) was used, and the values after calculations are as follows.

Table 2. Densities of HAIMNCs samples

Samples / Nomenclature	Theoretical densities, g/cm ³	Experimental density, g/cm ³
HAIMNC1	2.71	2.68
HAIMNC2	2.78	2.76
HAIMNC3	2.68	2.67
HAIMNC4	2.88	2.87

Table 3. Densification and porosities of HAlMNCs samples

Samples / Nomenclature	Relative densification, %	Porosity, %
HAIMNC1	98.89	1.11
HAIMNC2	99.05	0.95
HAIMNC3	99.32	0.68
HAIMNC4	99.42	0.58

A graphical representation of the physical properties, such as the experimental and theoretical densities in Table 2 and the densifications and porosities are presented in Table 3. The densities increased linearly with an increase in the nano-reinforcements, as shown in Fig. 2.

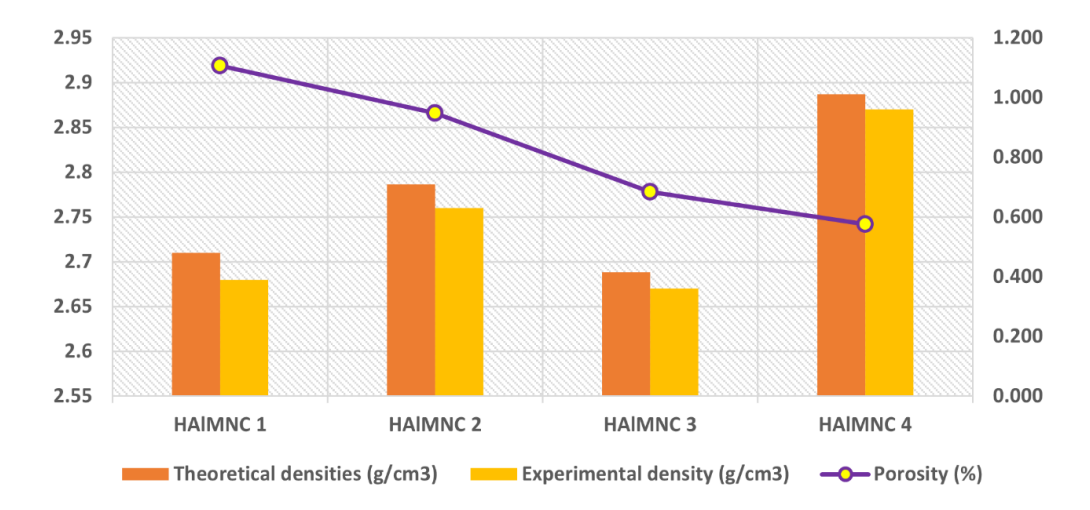


Fig. 2. Physical properties of stir-casted HAIMNCs samples

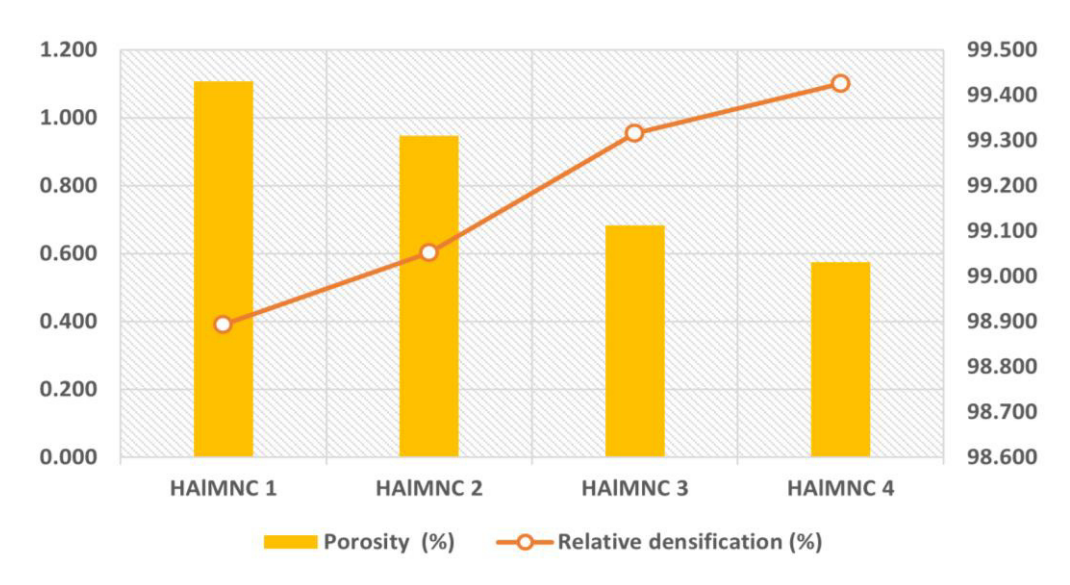


Fig. 3. Plot of relative densification vs density

Figure 3 illustrates relative densification (%) and porosity (%) of developed HAIMNCs samples. The theoretical data (Table 2) revealed certain decrement in porosity and increment in densification as nano-reinforcement wt. % increased. Both physical characteristics are inversely proportional in nature. The hybrid composite's relative densification increased when CeO₂ and GNP weight percentages increased. The uniform dispersion of both nanoreinforcements could be the reason for the decrease in the porosity. A decrease of 69.5 % in porosity was observed in HAIMNC4 sample compared to HAIMNC1. The effect on the porosity was observed with the addition of CeO₂ to Al6061-SiC-Al₂O₃ using a stir-casting route. Furthermore, the porosity decreases with increasing CeO₂ content (0.5, 1.5, and 2.5 wt. %) in the hybrid composites [20]. MMCs made of A356-15 % ZrO₂ were produced by Abdizadeh et al. using a stir casting process at 750 °C. Within the same composition of the MMCs, an increase of 10 % in density and a hardness increase of 52 % were also found [21]. Leo et. al. prepared Al-8090/2 % SiC/x % B₄C hybrid composites, where x = 2, 4, and 6 %, using the stir casting method. The results showed a decrease in density with the reinforcement percentage in the HMMCs. The 2.53 g/cm³ actual density was observed in as-casted Al-8090 alloy and lowest density 2.51 g/cm³ was found in Al-8090 /6 % B₄C/2 % SiC specimen [22]. Similarly, Tamuly et al. observed that an increase in the weight percentage increases the density of the fabricated

material owing to grain refinement after the fabrication of a cast aluminum composite [23]. Stir-cast AMCs strengthened with SiC and Mo were prepared by Kumar et al. The findings showed that the AMCs samples with a higher volume percentage of reinforcements had higher densities. [24]. The current study strictly followed the trends of previous studies, and the porosity values were within the acceptable range. The relative densification (ratio of theoretical to experimental density) increased with increasing reinforcement wt. %. This can be attributed to an enhancement in the wettability of the HAIMNCs as the reinforcement weight percentage increased in the matrix material, which was the result of proper dispersion of the reinforcement particles in the base alloy [25].

Mechanical properties. The microhardness, tensile strength, and yield strength of the test specimens are presented in Fig. 4. An increase of 53.85 % (from 53 to 80 VHN) was recorded when Al-6061 was reinforced with 3GNPs and 1CeO₂. Further, 86.35 and 100.58 % increment was observed as compared to base alloy with addition of (3CeO₂ + 1 GNPs) and (3GNPs + 3CeO₂) wt. % reinforcement to matrix material. An enrichment in hardness values was observed with reference to previous findings. Prakash et al. stirred a composite of Al-6061 alloy reinforced with multi-walled CNTs with various wt. %. The increment of 18.6, 11.93, and 66.6 % in hardness, tensile, and impact strength, respectively, in the MMCs by 1.5 wt. % addition of MWCNTs. The proper distribution of MWCNTs particles in the Al-6061 alloy matrix was also determined through microstructural investigation [26]. Vipin Kumar Sharma et al. [27] observed the effect of cerium oxide (CeO₂) on hybrid composites. The 2.5 wt. % of CeO₂ gives the optimum values for mechanical properties like; hardness increased by 17.02 %, tensile strength increased with 80 and 78 % increment gain in flexural strength of fabricated hybrid composite. The wear behavior was also observed to enhanced by 87.28 % with the same composition in fabricated hybrid composite [27]. Table 5 presents the theoretical mechanical properties of the fabricated HAIMNCs samples.

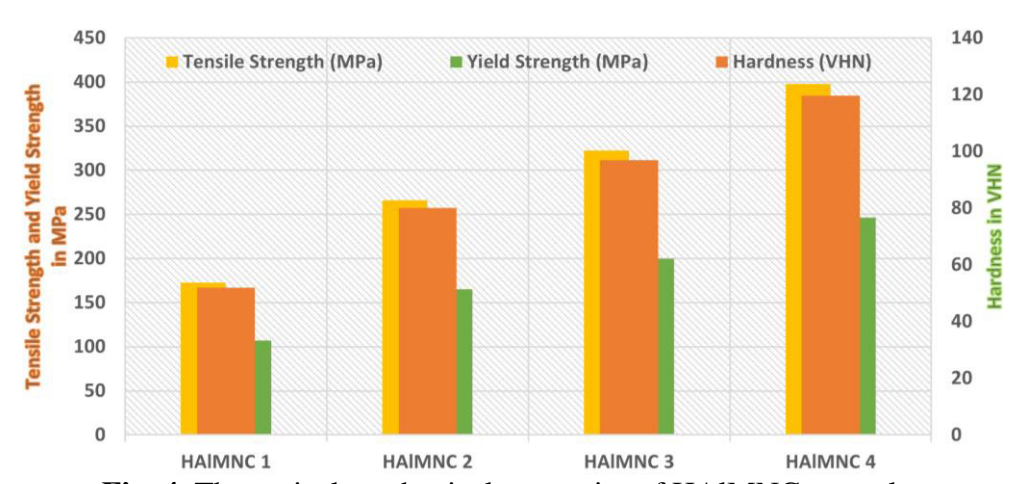


Fig. 4. Theoretical mechanical properties of HAIMNCs samples

Table 5. Mechanical properties of HAIMNCs samples

	1	I	
Sample Number	Hardness, VHN	Tensile Strength, MPa	Yield Strength, MPa
HAIMNC1	52.00	173.00	107.26
HAIMNC2	80.00	266.16	165.01
HAIMNC3	96.90	322.39	199.87
HAIMNC4	119.60	397.90	246.68

The highest tensile strength (347.01 MPa in the HAlMNC4 specimen. The HAlMNC1 specimen exhibited the lowest tensile strength (173 MPa). The contribution of various stir-casting parameters enhanced the tensile strength. Senthil Kumar et al. [28] cast A356 alloy/6 % TiB₂

The highest tensile strength (347.01 MPa in the HAIMNC4 specimen. The HAIMNC1 specimen exhibited the lowest tensile strength (173 MPa). The contribution of various stir-casting parameters enhanced the tensile strength. Senthil Kumar et al. [28] cast A356 alloy/6 % TiB₂ MMCs at various temperatures. Three levels of pouring temperature were chosen: 750, 780, and 810 °C. The effect on hardness was observed at these pouring temperatures. It has been noted that hardness increases linearly with increasing pouring temperature [28].

Shayan et al. [29] examined the effects of TiO₂ as a reinforcement particle in a molten matrix AA2024. According to the research conducted, ductility in terms of elongation increased by 163 % and hardness increased by 25 % compared to base alloys. A 28 % increase was observed in ultimate tensile strength, and 4 % growth was seen in modulus of elasticity when compared to matrix alloys [29]. Gireesh et al. [30] fabricated the stir-cast HAMMC reinforced with SiC and Al₂O₃ particulates at a constant weight fraction (5 %). The aim of this study was to improve the hardness and strength of the fabricated Al-6061/SiC/ Al₂O₃ HAMMCs. A 10 % increase was observed in hardness, 15 % improvement in terms of tensile strength, and 6 % growth was seen in yield strength of the produced HAMMCs [30]. Amouri et al. [31] also reported that the tensile and compressive strengths were enhanced in a composite material with 1.5 wt. % of nano SiC particles to the A356 aluminum alloy fabricated through stir casting method. The tensile strength of 232 MPa was achieved with stir-cast MMCs of A356-15 % ZrO₂ composites produced at 750 °C. An increment of 10 and 52 % in density and hardness was also observed for the same composition of the MMCs [21]. HAlMNC4 specimen exhibited a maximum yield strength of 215.13 MPa, which was 100.57 % that of Al-6061 alloy (107.26 MPa). The present study attributes uniform dispersion to the enhancement of mechanical characteristics.

Microstructure analysis. SEM and EDAX micrographs of the stir-cast HAlMNCs samples are shown in Fig. 5. Four regions were observed in the SEM images: Grey represented the Al-6061 alloy, white represented CeO₂, and black represented GNPs in the SEM images, respectively. Finally, the porosity of the HAlMNCs sample is represented by darker shades of grey.

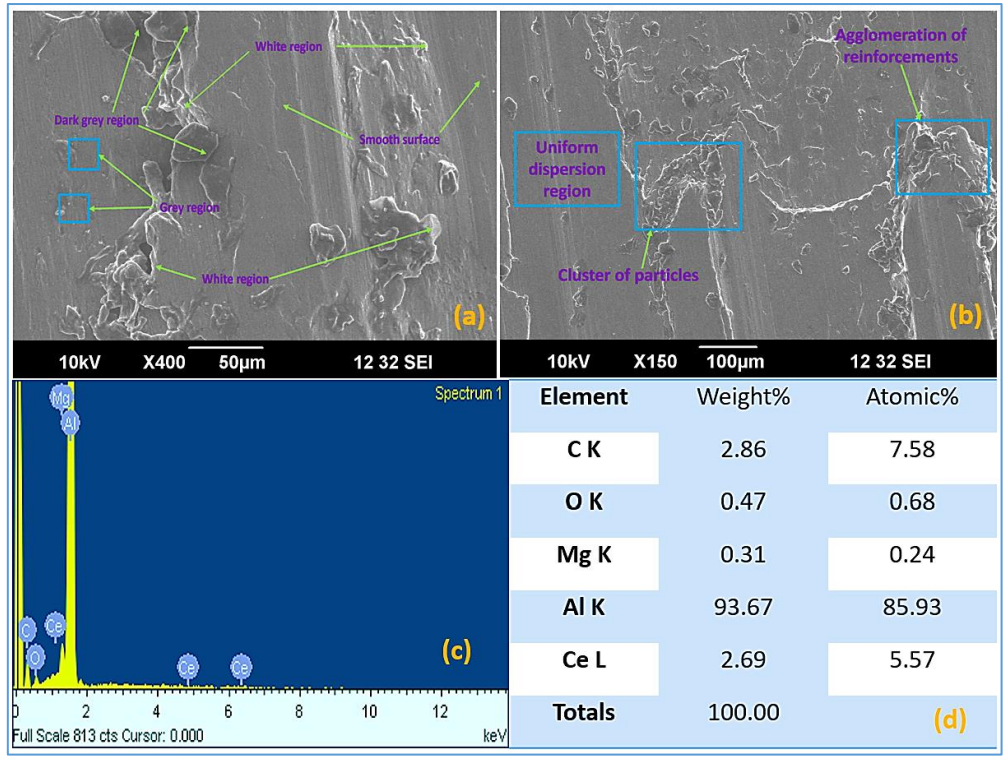


Fig. 5. Specimens SEM Images: (a) HAlMNC2; (b) HAlMNC4; (c) HAlMNC4 EDAX spectrum, and (d) HAlMNC4 EDAX with element wt. %

A change in the microstructural behavior was observed owing to the addition of the nanoreinforcements. A uniform dispersion and defect-free morphology can be observed in the HAIMNCs specimens compared with the base material. EDAX analysis verified the incorporation of nano reinforcement particles into the hybrid composite with the inclusion of Mg for enhanced wettability. Hexa-chloro-ethane tablets were also used to avoid the harmful reactions observed in the HAlMNCs specimens. Strong contact between the matrix material and reinforcements improves the mechanical characteristics of the manufactured composites, as was also observed in previous investigations. Anandaraj et al. [32] utilized a liquid metallurgical method to create AA5083-MoO₃ composites and investigated their characteristics. Molybdenum trioxide (MoO₃) has been investigated as a reinforcement to improve the performance of metal-matrix composites (MMCs). Composites were prepared by incorporating varying amounts of MoO₃ into an AA5083 matrix. In this study, we compare AA5083 to AA5083 with 4 wt. % MoO₃, AA5083 with 8 wt. % MoO₃, and AA5083 with 12 wt. % MoO₃. Composites with 12 wt. % MoO₃ had the highest tensile strength (207 MPa) [32]. Raja et al. [33] produced hybrid aluminum surface composites. Reinforcing particles consisting of boron carbide (B₄C), silicon carbide (SiC), and calcium carbonate (CaCO₃) were combined at a 1:1:1 ratio to create a hybrid mixture. The fabrication procedure involved three different hybrid reinforcement weight percentages: 5 (T1), 10 (T2), and 15 % (T3). Sample T3, with 15 % reinforcement content, outperformed samples T1 and T2 in Ultimate Tensile strength (UTS) by 62.63 and 15.17 percent, respectively. However, when comparing these samples, T3's Elongation (%) was lower by 38.46 (T1 sample) and 15.38 % (T1 sample), respectively. Sample T3 exhibited a more brittle reaction, as evidenced by its higher hardness in the stirred zone compared to the other two samples. The microstructural investigation verified the presence of reinforcements and their distribution in the stir zone [33]. In keeping with these developments, the current study demonstrates that including GNPs and CeO₂ in the melting process enhances the metal fluidity and, in turn, the mechanical properties of the resulting HAIMNCs. The porosity of the manufactured HAIMNCs samples was shown to increase inversely with their reinforcement content, as validated by scanning electron microscopy [34–36].

Conclusions

The physical, mechanical, and microstructural characteristics of the fabricated nanocomposite were examined, and the following conclusions were drawn.

- 1. An aluminum nanocomposite was successfully fabricated and reinforced by the addition of GNPs and CeO₂ nanoparticles using a stir-casting route.
- 2. A hybrid aluminum composite containing GNPs and CeO₂ nanoparticles (1–3 wt. %) possesses improved physical and mechanical properties compared to as-casted sample.
- 3. The experimental and theoretical densities increased with the addition of the reinforcement percentages, and the porosity decreased for identical percentages of GNPs and CeO₂. The density and porosity were inversely proportional to each other.
- 4. Vickers hardness, tensile strength, and yield strength were all maximised at 104.3, 352.01, and 207.98 MPa, respectively, when reinforcing nanoparticles proportions of 3% CeO₂ and 3% GNPs were added to Al-6061 alloy.
- 5. The microstructural study confirmed the uniform dispersion and defect-free morphology of the hybrid aluminum nanocomposite specimens. No cracks or pores are observed in the fabricated nanocomposites. This is because of the refined grain size and the bonding action of the reinforcements in the HAIMNCs sample with 3 % GNPs and 3 % CeO₂ proportions.

References

- 1. Kumar D, Angra S, Singh S. Mechanical Properties and Wear Behaviour of Stir Cast Aluminum Metal Matrix Composite: A Review. *Int. J. Eng. Trans. A Basics*. 2022;35: 794–801.
- 2. Yeshiye T, Gizaw M. A review on Effects of reinforcements on properties and wear behaviour of aluminium metal matrix material. *International Journal of Renewable Energy Technology*. 2021;6: 1–17.
- 3. Kumar D, Singh S, Angra S. Dry sliding wear and microstructural behavior of stir-cast Al6061-based composite reinforced with cerium oxide and graphene nanoplatelets. *Wear*. 2023;516–517: 204615.
- 4. Kumar D, Angra S, Singh S. High-temperature dry sliding wear behavior of hybrid aluminum composite reinforced with ceria and graphene nanoparticles. *Eng. Fail. Anal.* 2023;151: 107426.
- 5. Kumar D, Singh S, Angra S. Morphology and Corrosion Behavior of Stir-Cast Al6061- CeO 2 Nanocomposite Immersed in NaCl and H2So4 Solutions. Evergr. *Jt. J. Nov. Carbon. Resour. Sci. Green. Asia Strateg.* 2023;10: 94–104.
- 6. Aktaş S, Anll Diler E. Effect of ZrO2Nanoparticles and Mechanical Milling on Microstructure and Mechanical Properties of Al-ZrO2Nanocomposites. *J. Eng. Mater. Technol.* 2021;143: 041002.
- 7. Nojima A, Sano A, Kitamura H, Okada S. Electrochemical Characterization, Structural Evolution, and Thermal Stability of LiVOPO _ 4 over Multiple Lithium Intercalations Electrochemical Characterization, Structural Evolution, and Thermal Stability of LiVOPO 4 over Multiple Lithium. Evergr. Jt. J. Nov. Carbon Resour. Sci. Green Asia Strateg. 2019;6: 267–274.
- 8. Aydin F, Turan ME. The Effect of Boron Nitride on Tribological Behavior of Mg Matrix Composite at Room and Elevated Temperatures. *J. Tribol.* 2020;142: 011601.
- 9. Hugar N, Prashanth S, Lalji P, Hegde SG, Narayana BV, Kumar KM, Waddar S. Fabrication and characterization of high performance aluminium composites for automotive components. *AIP Conf. Proc.* 2022;2421: 040006.
- 10. Li T, Davies JMT, Zhu X. Effect of carrier gases on the entrainment defects within AZ91 alloy castings. *J. Magnes. Alloy.* 2022;10: 129–145.
- 11. Murugan S, Jegan S, Velmurugan V. Tribological Wear Behaviour and Hardness Measurement of SiC , Al 2 O 3 Reinforced Al. Matrix Hybrid Composite. *J. Inst. Eng. Ser. D.* 2017;98: 291–296.
- 12. Krishan K. Chawla. Composite Materials: Science and Engineering. 2019.
- 13. Rm SS, Ramanathan K. A study on tribological behaviour and analysis of ZnO reinforced AA6061 matrix composites fabricated by stir casting route. *Industrial Lubrication and Tribology*. 2021;4: 642–651.
- 14. Zhang WY, Du YH, Zhang P. Vortex-free stir casting of Al-1.5 wt% Si-SiC composite. *J. Alloys Compd.* 2019;787: 206–215.
- 15. Cahoon JR. The Determination of Yield Strength From Hardness Measurements. 1979.
- 16. Ujah C, Popoola P, Popoola O, Aigbodion V. Enhanced mechanical, electrical and corrosion characteristics of Al-CNTs-Nb composite processed via spark plasma sintering for conductor core. *Journal of Composite Materials*. 2019;53(26-27): 3775–3786.
- 17. Annaz AA, Irhayyim SS, Hamada ML, Hammood HS. Comparative study of mechanical performance between Al Graphite and Cu Graphite self-lubricating composites reinforced by nano-Ag particles. *AIMS Materials Science*. 2020;7(5): 534–551.
- 18. Irhayyim SS, Hammood HS, Abdulhadi HA. Effect of nano-TiO 2 particles on mechanical performance of Al CNT matrix composite. *AIMS Materials Science*. 2019;6(6): 1124–1134.
- 19. Callister WD, Rethwisch DG. *Materials Scienceand Engineering. An Introdaction*. John Wiley & Sons, Inc.; 2018.
- 20. Kumar V, Kumar V, Singh R. Parametric study of aluminium-rare earth based composites with improved hydrophobicity using response surface method. *Integr. Med. Res.* 2020;9: 4919–4932.

- 21. Abdizadeh H, Baghchesara MA. Investigation into the mechanical properties and fracture behavior of A356 aluminum alloy-based ZrO2-particle-reinforced metal-matrix composites. Mech. Compos. Mater. 2013;49: 571-576.
- 22. Leo Bright Singh R, Jinu GR, Manoj M, Elaya Perumal A. Tribological Behaviour of Al8090-SiC Metal Matrix Composites with Dissimilar B4C Addition. Silicon. 2022;14: 8895–8908.
- 23. Tamuly R, Behl A, Borkar H. Effect of Addition of Grain Refiner and Modifier on Microstructural and Mechanical Properties of Squeeze Cast A356 Alloy. Trans. Indian Inst. Met. 2022;75: 2395-2408.
- 24. Kumar J, Singh D, Kalsi NS, Sharma S, Mia M, Singh J, et al. Investigation on the mechanical, tribological, morphological and machinability behavior of stir-casted Al/SiC/Mo reinforced MMCs. J. Mater. Res. Technol. 2021;12: 930-946.
- 25. Kumar D, Singh PK. ScienceDirect Microstructural and Mechanical Characterization of Al-4032 based Metal Matrix Composites. Mater. Today Proc. 2019;18: 2563–2572.
- 26. Prakash B, Sivananthan S, Vijayan V. Materials Today: Proceedings Investigation on mechanical properties of Al6061 alloy – Multiwall carbon nanotubes reinforced composites by powder metallurgy route. Mater. Today Proc. 2020;37: 336–340.
- 27. Sharma VK, Kumar V, Joshi RS. Investigation of rare earth particulate on tribological and mechanical properties of Al-6061 alloy composites for aerospace application. *Integr. Med. Res.* 2019;8: 3504–3516.
- 28. Senthil Kumar P, Kavimani V, Soorya Prakash K, Murali Krishna V, Shanthos Kumar G. Effect of TiB2 on the Corrosion Resistance Behavior of In Situ Al Composites. Int. J. Met. 2020;14: 84–91.
- 29. Shayan M, Eghbali B, Niroumand B. Fabrication of AA2024-TiO2 nanocomposites through stir casting process. Trans Nonferrous Met Soc China. 2020;30: 2891–2903.
- 30. Gireesh CH. Experimental Investigation on Mechanical Properties of an Al6061 Hybrid Metal Matrix Composite. J. Compos. Sci. 2018;2(3): 49.
- 31. Amouri K, Kazemi S, Momeni A, Kazazi M. Microstructure and mechanical properties of Alnano/micro SiC composites produced by stir casting technique. Mater. Sci Eng. A. 2016;674: 569–578.
- 32. Anandaraj T, Sethusundaram PP, Meignanamoorthy M, Ravichandran M. Investigations on properties and tribological behavior of Investigations on properties and tribological behavior of method. Surf. Topogr.: Metrol. Prop. 2021;9(2): 025011.
- 33. Raja R, Shanmugam R, Jannet S, Kumar GBV, Venkateshwaran N, Naresh K, Ramoni M. Development of Al-Mg2Si Alloy Hybrid Surface Composites by Friction Stir Processing: Mechanical, Wear, and Microstructure Evaluation. *Materials*. 2023;16(11): 4131.
- 34. Hima Gireesh C, Durga Prasad K, Ramji K. Experimental Investigation on Mechanical Properties of an Al6061 Hybrid Metal Matrix Composite. J. Compos. Sci. 2018;2: 49.
- 35. Ponugoti GR, Alluru GK, Vundavilli PR. Response Surface Methodology Based Modelling of Friction-Wear Behaviour of Al6061/9%Gr/WC MMCs and Its Optimization Using Fuzzy GRA. Trans. Indian Inst. Met. 2018:71: 2465–2478.
- 36. Królczyk G, Feldshtein E, Dyachkova L, Michalski M, Baranowski T, Chudy R. On the microstructure, strength, fracture, and tribological properties of iron-based MMCs with addition of mixed carbide nanoparticulates. Materials. 2020;13(13): 2892.

THE AUTHORS

Kumar Dinesh 🗓

e-mail: dinesh_61900120@nitkkr.ac.in

Singh Satnam (1)

e-mail: satnamsingh@nitkkr.ac.in

Angra Surjit

e-mail: surjit.angra@yahoo.com

Study on nanosized Al₂O₃ and Al₂O₃-SiC on mechanical, wear and fracture surface of Al7075 composites for soil anchoring applications

Submitted: March 27, 2023

Approved: May 30, 2023

Accepted: June 20, 2023

M. Ravikumar ^{10 1 ∞}, R. Naik ^{10 1}, B.R. Vinod ², K.Y. Chethana ¹, Y.S. Rammohan ¹

¹ BMS College of Engineering, Karnataka, India

² BMS Institute of Technology and Management, Karnataka, India

⊠ ravikumar.muk@gmail.com

Abstract. Mechanical and tribological tests of aluminium 7075 alloy, mono-composite $(A17075 + 1 \% Al_2O_3)$, and hybrid composite $(A17075 + 1 \% Al_2O_3 + 1 \% SiC)$ have been performed in this study according to ASTM standards. Through the stir casting process, mono and hybrid composite materials were prepared. It was discovered that adding more hard ceramic particles improved hardness and strengthened tensile strength. In contrast to Al7075 alloy, hybrid MMCs enhanced tensile strength and superior hardness. The obtained results indicate that highest hardness of 78 VHN and tensile strength of 126 MPa were achieved for developed hybrid composites. A pin-on-disc wear test rig was used to conduct wear experiments. The Taguchi approach was used to optimise the wear parameters. The findings showed that the load had a greater impact on the wear behaviour of Al7075 alloys than did sliding distance and speed. The wear behaviour in mono composites and hybrid composites was improved by the addition of nano sized Al₂O₃ and SiC particulates to Al₇O₇5. Improved wear resistance for monolithic, mono and hybrid composites was achieved at 5 N of load, 100 rpm of speed and 250 m of sliding distance. Abrasion and adhesion-related damages were discovered by micrograph studies. Flows with the deep grooves were observed on the wornout surface of mono composite. It provided the evidence of the mono composites' abrasive mechanism. Comparing the hybrid MMCs to the monolithic and mono composite MMCs it was seen that, the hybrid composites (Al7075 + 1 % Al₂O₃ + 1 % SiC) exhibited better wear

Keywords: Al7075; Al₂O₃/Al₂O₃-SiC; mechanical behavior; wear behavior; fracture analysis; Taguchi technique

Acknowledgements. The authors are very thankful to Dr. R Suresh, Professor, Department of Mechanical and Manufacturing Engineering, M S Ramaiah University of Applied Sciences for continuous support in completion of this research work.

Citation: Ravikumar M, Naik R, Vinod BR, Chethana KY, Rammohan YS. Study on nanosized Al₂O₃ and Al₂O₃-SiC on mechanical, wear and fracture surface of Al7075 composites for soil anchoring applications. *Materials Physics and Mechanics*. 2023;51(6): 24-41. DOI: 10.18149/MPM.5162023_3.

Introduction

From the last few decades, due to their superior mechanical properties compared to the basic materials, light metal matrix composites (MMCs) materials with ceramic reinforcement particles have drawn a lot of focus in recent years [1]. The aluminium (Al) alloy composites are mainly used for several functional applications like agriculture mechanization, soil anchoring and building structures due to their high strength, lightweight design, high wear resistance, better thermal and electrical conductivity, excellent castability, and strengthening using precipitation hardening [2]. These alloys restrict the materials' ability to be used for

© M. Ravikumar, R. Naik, B.R. Vinod, 2023.

Publisher: Peter the Great St. Petersburg Polytechnic University

This is an open access article under the CC BY-NC 4.0 license (https://creativecommons.org/li-censes/by-nc/4.0/)

functional purposes because of their moderate hardness, low elastic modulus, and low temperature properties. By incorporating various ceramic strengthening particles into the matrix of the Al alloy, it is saturated. The Al metals used in soil anchoring applications is Al7075. Increased stiffness, strength, better wear resistance, and excellent thermal conductivity were all added by the hard particulate reinforcement. Al₂O₃, SiC, B₄C, TiB₂, TiO₂, ZrO₂, Si₃N₄, Gr, TiC, and MgB₂ are used as supports. Al₂O₃, ZrO₂, SiC, and Gr [3] are the most frequently used reinforcing materials. Composites made from silicon carbide and aluminium oxide could be used in a variety of engineering disciplines. Al₂O₃-SiC is now particularly well suited for ballistic protection equipment, rockets engine nozzle throats, space shuttle surface tiles, piston crowns and cylinders, nose cones of hypersonic re-entry vehicles, and the harp shaped structures of hypersonic rocket engines. Because SiC dispersoids prevent the Al₂O₃ matrix's grain development, the reinforcement of SiC particles in the Al matrix produces better mechanical, wear, physical and interfacial properties. The pre-processing, post-processing, and production techniques, in addition to the reinforcement, significantly improve the properties. In their study of the mechanical and tribological properties of Al-Al₂O₃ composites, Kumar et al. [4] found that while elongation decreases, alloy composites' tensile strength, toughness, and wear resistance increase. In their analysis of the wear characteristics of AA356/Al₂O₃ composites, Alhawari et al. [5] found that the wear rate reduces as the weight fraction of Al₂O₃ particulates rises. The physical and mechanical properties of AA356/Al₂O₃ composites with the inclusion of micro and nanosized Al₂O₃ particulates were investigated by Sajjadi et al. [6]. They noticed that porosity and hardness increased with weight percentage and decreased with Al₂O₃ particulate size. Al₂O₃ has a significant influence on the tensile strength and hardness of the welded joint, according to research by B.M. Nagesh et al. on the effects of weld parameters on AA 6082 reinforced with Al₂O₃ at three different weight percentages (5, 10, and 15 wt. %) [7]. Reddy et al. [8] analysis of the tensile properties of AA356/SiC nanocomposites revealed a notable rise in performance with increasing SiC nanoparticle content. The microstructural, mechanical, and tribological properties of Al/SiC alloys were investigated by Ghandvar et al. [9]. They discovered that adding 25 wt. % SiC particulates increased hardness, whereas adding 20 wt. % SiC particulates increased wear resistance in metal composites. The mechanical properties of the AA356 alloy reinforced with nano and micro SiC particulates were researched by Amouri et al. [10]. When nano-SiC particles up to 1.5 wt. % were added, they discovered improvements in the mechanical properties. Using pin-on-disc equipment, Shivmurthy et al. [11] investigated the tribological behaviour of AA356/SiC composites. They discovered that compared to other proportions, 10 vol. % SiC particles exhibit a lower rate of wear. The survey that was previously described shows the mechanical and tribological characteristics of composites with various ceramic particles. However, little attention has been paid to the wear and mechanical properties of composite reinforced with hard ceramic particles under the various process circumstances. In this investigation, the mechanical characteristics and wear patterns of mono and hybrid MMCs made of Al7075 alloy were examined. The findings of the present study demonstrate how two distinct reinforcements influence mechanical behaviour. In order to analyse the wear behaviour of MMCs, numerous parameters and factors, such as speed (rpm), load (N), and sliding distance (m), were taken into account. The results were then compared to the optimized values. In order to evaluate the worn surfaces of test materials, SEM analysis was used.

Materials and Method

As the base material, Al alloy 7075 was utilized. It has superior fracture toughness, wear, and corrosion resistance. It is widely employed in automobiles and aerospace field. Al7075's material compositions are shown in Table 1 as a weight percentage. Nano sized (50 nm) SiC

and Al₂O₃ with a pH value of 6.5 to 7.5 were used as reinforcing materials. In this study, two different MMC types such as mono composite (Al7075 + 1 % Al₂O₃) and hybrid composites (Al7075 + 1 % Al₂O₃ + 1 % SiC) were produced and compared to Al7075. Both types of composites, mono and hybrid MMCs, were produced utilising stir casting method in a coke furnace. To prevent particle aggregation, stirring was carried out using a 4-blade stirrer for a total of 5 minutes at an average speed of 250 rpm. A graphite crucible was used to melt the base alloy. The pre-heated nano sized Al₂O₃ and SiCp were mixed into the ready molten melt while stirring. Inert gases existing in the molten metal were removed using a degasifying tablet. The pre-heated mould box was filled with molten composite melt. Finally, a CNC lathe was used to machine the composite materials. Composite specimens with various cross sections were constructed for the microstructure analysis, and they were polished with diamond paste on emery paper with a 400 grit size. Finally, in accordance with the procedure for a metallographic examination, test specimens were then polished by using velvet cloth disk polishing apparatus to provide a satisfactory finish on the test sample surface.

Table 1. Composition of Al 7075 with wt. %

Content	Zn	Mg	Cu	Si	Fe	Ni	Mn	Sn	Cr	Al
Wt. %	5.42	2.30	1.48	0.06	0.25	0.05	0.05	0.01	0.28	Remaining

Result and the Discussions

Microstructural analysis. The microstructure of A17075, mono-composites $(A17075 + 1 \% Al_2O_3)$, and hybrid composites $(A17075 + 1 \% Al_2O_3 + 1 \% SiC)$ is depicted in Fig. 1. The monolithic micrograph image shown in Fig. 1(a) demonstrates the presence of intermetallic complexes. A mono composite with a uniform Al₂O₃ particle dispersal in the Al alloy matrix material is shown in Fig. 1(b). Typically, this is attributable to the precise stirring method used during production. The micrographs in Fig. 1(c) show homogeneous dispersion of Al₂O₃-SiC particles in hybrid composites. We can see that the alloy's reinforced particles are dispersed at random. However, at several locations the particulates are seen to be clumping together. Other researchers also got comparable outcomes [12-15]. Due to a rise in the weight percentage of hard particles in the hybrid MMCs, particle aggregation increased in several areas.

Hardness. According to ASTM-E92 standards, the microhardness of Al7075, mono MMCs (Al7075 + 1 % Al₂O₃), and hybrid MMCs (Al7075 + 1 % Al₂O₃ + 1 % SiC) were examined. Under a steady load of 2 kg, a diamond shaped 10 mm indenter was used. Three separate locations on the test samples were evaluated for their hardness. The average hardness value was then noted. Figure 2 shows the microhardness for each composition. When compared to monolithic, the hardness values of the mono composites and hybrid composites are higher, as can be shown in Fig. 2. The base matrix's base matrix is more tightly coupled and evenly distributed with the hard ceramic particles. Therefore, as the dislocations come into contact with these tough ceramic particles, additional tension is necessary for movement. Therefore, better dispersion strengthening through proper particles dislocation interaction may be responsible for the uniform distribution of hard ceramic particles [16–18]. Since Al₂O₃ and SiC are two separate hard ceramic particles, the MMCs reinforced with them have improved hardness.

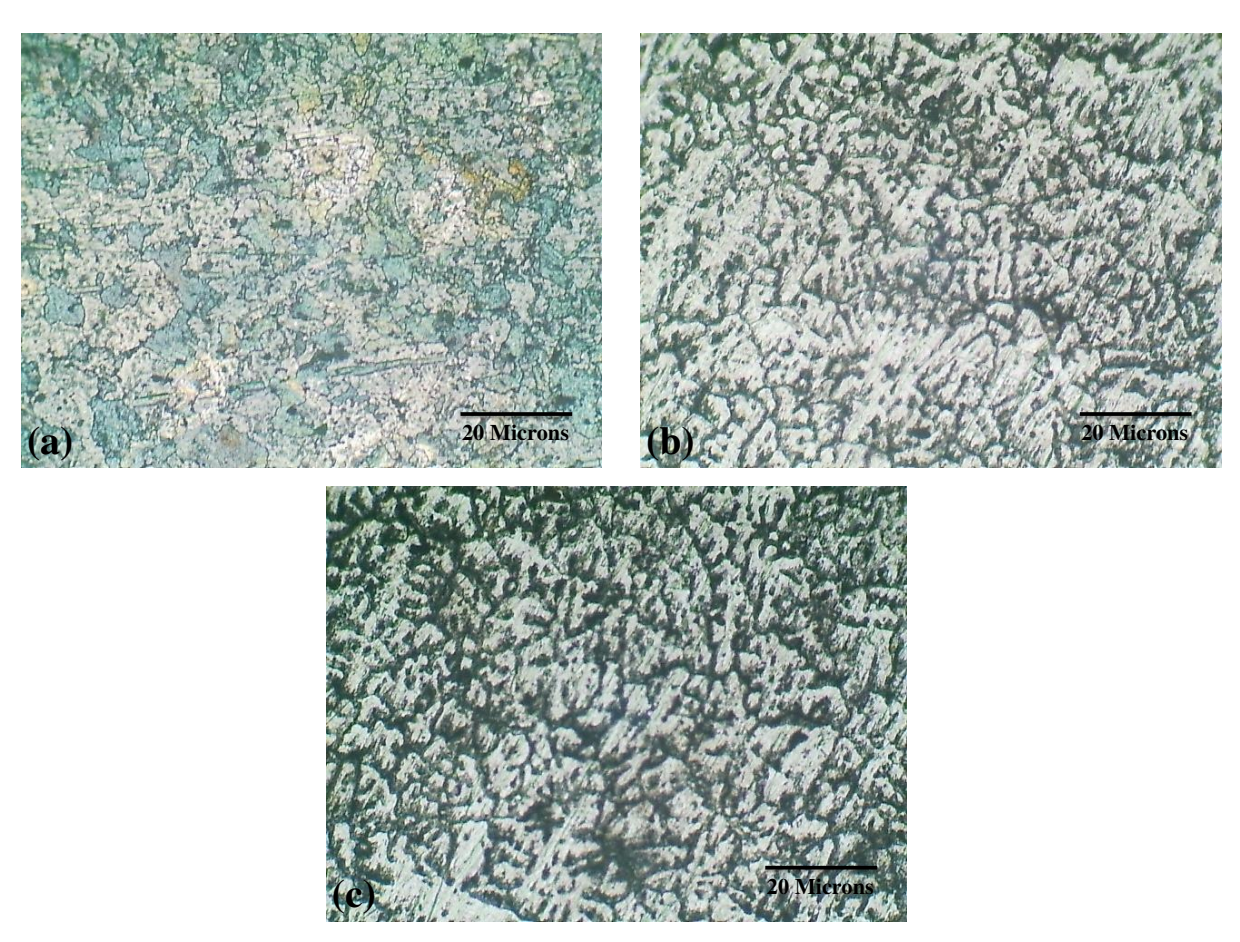


Fig. 1. Micro-structure of (a) monolithic, (b) mono MMCs (Al7075 + 1% Al₂O₃) and (c) hybrid MMCs (Al-7075 + 1% Al₂O₃ + 1% SiC)

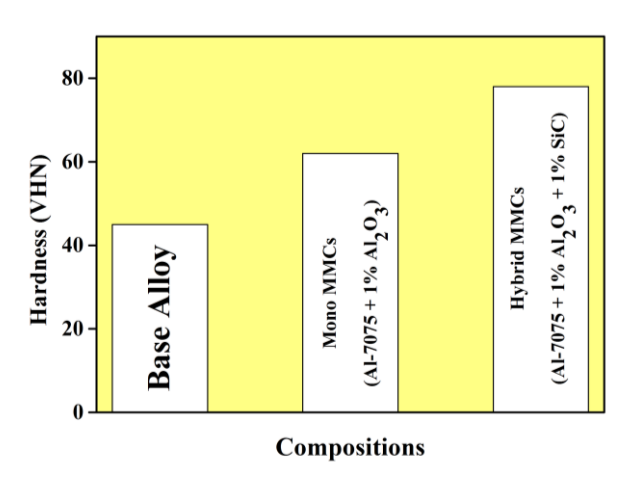


Fig. 2. Microhardness of base alloy, mono and the hybrid MMCs

Tensile behavior. Tensile tests trials were carried out utilising UTM at a maximum loading capacity of 450 KN in accordance with ASTM-E8 regulations. In the current study, three test samples with comparable compositions were examined to determine the average tensile strength. The values' fluctuation in this instance was under 5 %. Figure 3(a) displays the tensile strength findings for each mixture. When compared to monolithic and mono MMCs, the hybrid MMCs have higher tensile strengths. Results show that the tensile strength is enhanced by adding more hard ceramic particles. Enhancement in tensile strength is due to the addition of hard nano sized Al_2O_3 particles in mono composites and nano sized Al_2O_3 + SiC in hybrid MMCs, which enhanced the tensile strength. Enhancement in tensile

strength could also be attributed to the uniform particle dispersion and reduced porosity found in composite and hybrid MMCs. This finding is consistent with the outcomes of the majority of Al composites reinforced with hard ceramic particulates [16,17,19]. In Fig. 3(b), the stir casting method's composite samples' tensile stress-strain curves are displayed. For monolithic, mono-composites, and hybrid-composites, a stress-strain diagram is drawn. The primary characteristics of this graph are that the fracture strain decreases with increasing particle content, and the tensile strength rises in response. In comparison to mono-composite and hybrid-composites, the monolithic alloy is found to have the largest plastic strain and the least resistance to plastic deformation due to its relatively lower flow stress. It has been found that all MMCs offer increased strength above the basic alloy. The grain refining and particle strengthening are the main reasons for this development. Al₂O₃ and SiC, two hard ceramic nanoparticles, strengthen the composite to enable it to endure greater stresses. The graph of the stress-strain curve shown in Fig. 3(b) also shows that a hybrid composite containing 1 % nanoscale Al₂O₃ and 1 % nanoscale SiC particulates can bear the highest stress. The stress-strain curve shows that in addition to strong tensile strength, the toughness has improved. This matters a lot. Meanwhile, ductility is reduced by the majority of ways for increasing strength.

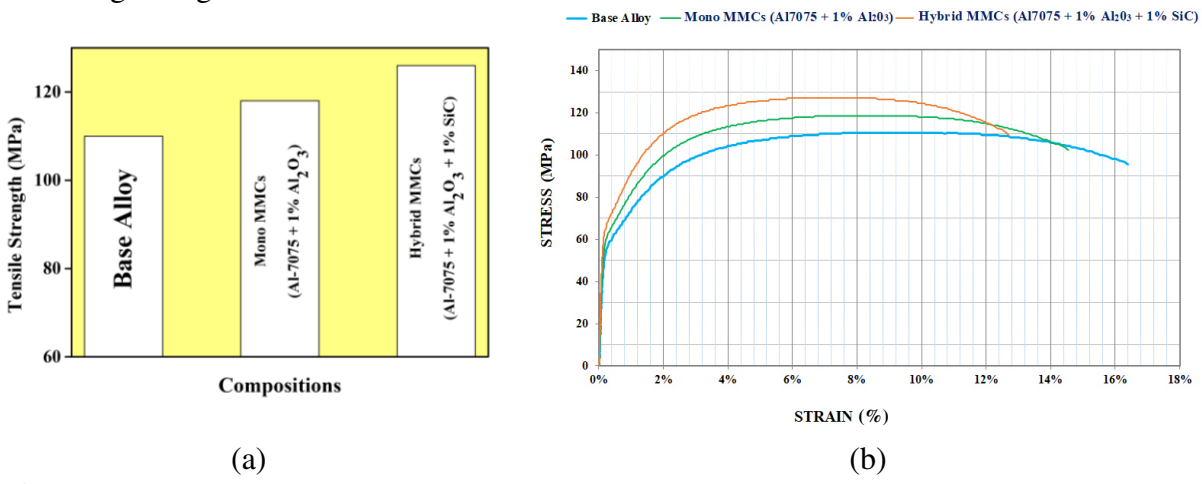


Fig. 3. Tensile strength (a) and stress-strain curves (b) of base alloy, mono and hybrid MMCs

A Scanning Electron Microscope (SEM) is used to examine the newly formed crack surface that was produced by the fracture test. After conducting the test, Fig. 4(a) depicts the shattered surface of the base material, Fig. 4(b) the fractured surface of mono composites, and Fig. 4(c) the fractured surface of hybrid composites. Surface analysis showed that the fracture occured in both transgranular and intergranular types of fracture, combining broken particles, pulled regions, and tiny plastic dimples to produce mixed mode fracture, which has high strength prior to fracture. Fracture surfaces for the composites and hybrid MMCs containing nano sized Al₂O₃ and SiC particles displayed various topographies. The majority of the dimples on the shattered surface, according to a close inspection, were connected to the matrix material. Large dimples and a significant degree of plastic deformation were found as a result of shattered surface analysis performed on fracture toughness specimens of FCC structured Aluminum alloy samples, indicating ductile fracture (ref Fig. 4(a)). The fractured surface shows that the matrix material is primarily represented by the fractured particles, which indicates ductile fracture. Due to the presence of too many nanoparticles, the fracture surface of mono composites (ref. Fig. 4(b)) reveals mixed mode fracture, while hybrid composites (ref. Fig. 4(c)) reveals cleavage type fracture. Also, it should be highlighted that clustered particles are vulnerable to early composite degradation, and large particles appear to be more likely to fracture, which resulted in a decrease in the fracture toughness value [20,21].

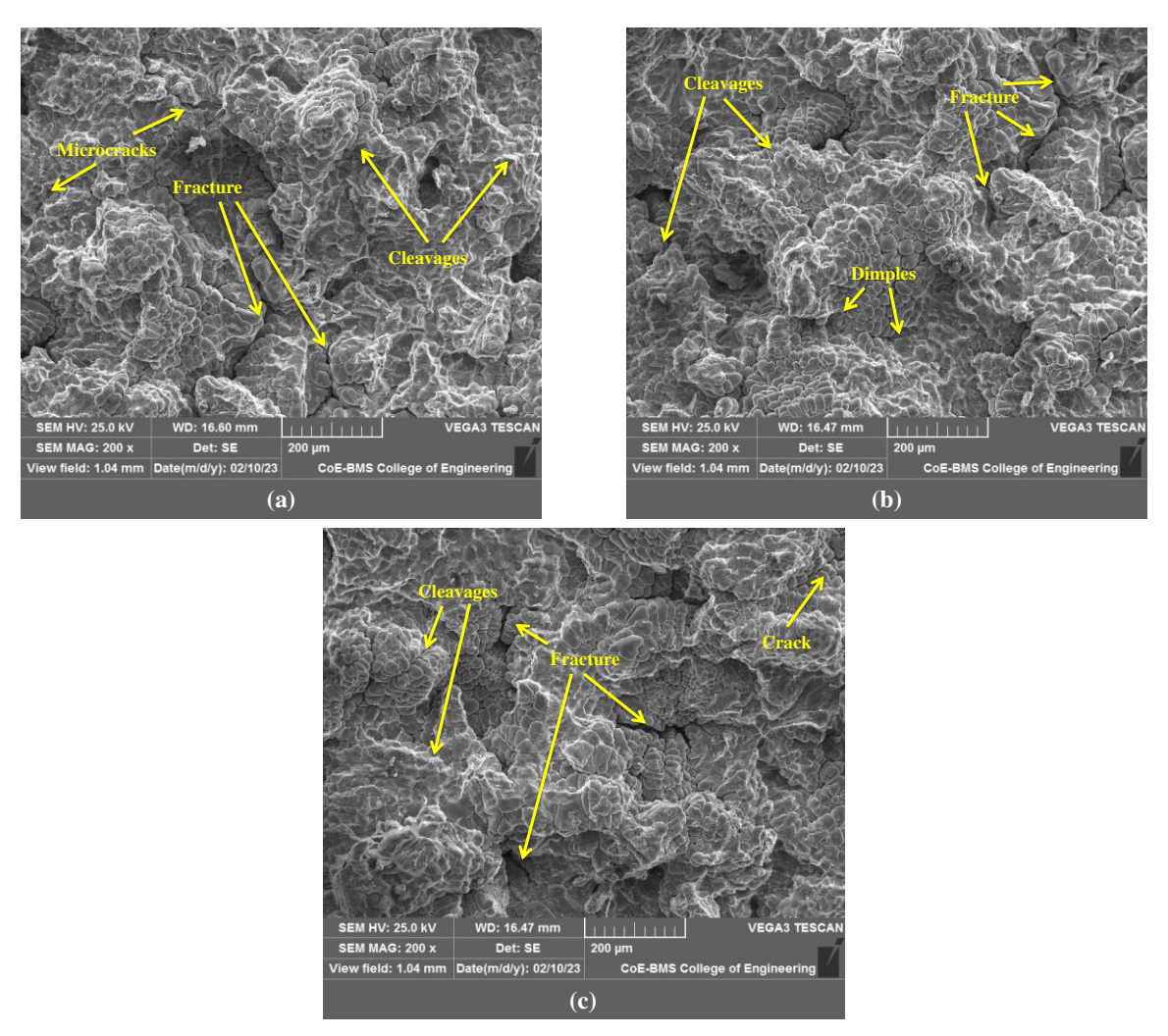


Fig. 4. Fracture surface of (a) monolithic, (b) mono and (c) hybrid MMCs

Based on the literature review and preliminary experimentation conducted by the authors, the research work is carried out on the effect of monolithic, mono and hybrid reinforcement on mechanical and wear properties in Al7075 were studied. The obtained results indicated that, the effect of nano sized 1 % $Al_2O_3 + 1$ % SiC reinforcements on mechanical and wear properties in Al7075 hybrid composites is more when compared to the monolithic and mono composites. So, the strengthening effect in hybrid composite is more compared to monolithic and mono composites because of synergistic properties were obtained more in hybrid composites.

Experimenting with wear behaviour using the Taguchi method. This method is a potent design concept that is frequently used in many different industries [22,23]. It is frequently developed to provide superior goods at a lesser price. It is typically used to analyse the effects of varrying the parameters. Testing was carried out on the test samples utilising Taguchi evaluation of the L27 orthogonal array at room temperature (27 °C) (OA). Wear test specimens were produced using the ASTMG99 size of 6 mm in diameter and 30 mm in length. During the wear tests, the test specimens were firmly pressed against the hard rotating steel disc. After every trial, the disc and test samples were carefully cleaned with an organic chemical (acetone) to ensure the correctness of the results. The current experiment evaluates the wear behaviour as a loss of weight (gm) of a test material. The specimens were frequently cleaned with acetone solution before being weighed on a digital scale to ensure an accuracy of 0.0001 gm throughout the studies. The test specimens were cleaned, and the final weight was accurately measured. Wear loss was evaluated by considering the difference between initial and final weight of the test samples. Test trials were conducted on the basis of factors that

were selected and respective levels, which are shown in Table 2. Using samples of Al7075, mono MMCs (Al7075 + 1 % Al $_2$ O $_3$), and hybrid MMCs (Al7075 + 1 % Al $_2$ O $_3$ + 1 % SiC), 27 orthogonal array (OA) tests were performed. The findings are given in Table 3.

Table 2. Process parameters and levels

Sl. No.	Parameters	Levels	Levels	Levels
1	Load, N	5	7.5	10
2	Sliding Speed, rpm	100	300	500
3	Sliding Distance, m	250	500	750

Table 3. Taguchi L27 Orthogonal Array and their outcomes

Table	aguelli	L2/ Ormogor	nai Array and ti	len outcomes			
				Wear loss, g			
Trial No.	Load, N	Sliding Speed, rpm	Sliding Distance, m	Monolithic	Mono MMCs (1 % Al ₂ O ₃)	Hybrid MMCs (1 % Al ₂ O ₃ + 1 % SiC)	
1	5.0	100	250	0.030	0.020	0.010	
2	5.0	100	500	0.040	0.025	0.015	
3	5.0	100	750	0.050	0.035	0.020	
4	5.0	300	250	0.040	0.020	0.010	
5	5.0	300	500	0.040	0.023	0.015	
6	5.0	300	750	0.060	0.035	0.025	
7	5.0	500	250	0.056	0.030	0.010	
8	5.0	500	500	0.065	0.037	0.020	
9	5.0	500	750	0.070	0.040	0.030	
10	7.5	100	250	0.050	0.025	0.012	
11	7.5	100	500	0.070	0.045	0.033	
12	7.5	100	750	0.075	0.055	0.040	
13	7.5	300	250	0.060	0.047	0.020	
14	7.5	300	500	0.070	0.055	0.037	
15	7.5	300	750	0.075	0.060	0.045	
16	7.5	500	250	0.055	0.035	0.021	
17	7.5	500	500	0.065	0.040	0.030	
18	7.5	500	750	0.065	0.050	0.032	
19	10.0	100	250	0.050	0.035	0.015	
20	10.0	100	500	0.050	0.035	0.025	
21	10.0	100	750	0.070	0.045	0.030	
22	10.0	300	250	0.070	0.050	0.040	
23	10.0	300	500	0.075	0.060	0.030	
24	10.0	300	750	0.079	0.065	0.055	
25	10.0	500	250	0.081	0.070	0.045	
26	10.0	500	500	0.085	0.075	0.060	
27	10.0	500	750	0.089	0.080	0.065	

Table 4. ANOVA outcomes of monolithic material

TWOID IN THE CONTROLLED OF MICHOLINIA MANUFACTOR								
Parameters	DoF	Seq. S S	Adj. S S	Adj. M S	F- Values	P-Values	Contri- bution, %	Observation
Load, N	1	0.0021780	0.0021780	0.0021780	34.8894	0.0000051	36.89	Significant
Sliding speed, rpm	1	0.0011842	0.0011842	0.0011842	18.9700	0.0002321	20.06	Significant
Sliding distance, m	1	0.0011045	0.0011045	0.0011045	14.6930	0.0003367	18.71	Significant
Error	23	0.0014358	0.0014358	0.0000624			24.32	
Total	26	0.0059025					100	

R-Sq = 75.67 %

Parameters	DoF	Seq. S S	Adj. S S	Adj. M S	F- Values	P-Values	Contri- bution, %	Observation
Load, N	1	0.0034722	0.0034722	0.0034722	46.7095	0.0000006	48.17	Significant
Sliding speed, rpm	1	0.0010427	0.0010427	0.0010427	14.0270	0.0010567	14.46	Significant
Sliding distance, m	1	0.0009827	0.0009827	0.0009827	13.2199	0.0013828	13.63	Significant
Error	23	0.0017097	0.0017097	0.0000743			23.72	
Total	26	0.0072074					100	

Table 5. ANOVA outcomes of mono MMCs

R-Sq = 76.28 %

Table 6. ANOVA outcomes of hybrid MMCs

Parameters	DoF	Seq. S S	Adj. S S	Adj. M S	F- Values	P-Values	Contri- bution, %	Observation
Load, N	1	0.0024500	0.0024500	0.0024500	37.2366	0.0000032	40.31	Significant
Sliding speed, rpm	1	0.0007094	0.0007094	0.0007094	10.7817	0.0032566	11.67	Significant
Sliding distance, m	1	0.0014045	0.0014045	0.0014045	21.3464	0.0001199	23.11	Significant
Error	23	0.0015133	0.0015133	0.0000658			24.90	
Total	26	0.0060772					100	

R-Sq = 75.10 %

The ANOVA method, main effect plots, surface plots, linear regression, and normal probability graphs were used to examine the effects of process parameter changes. The "smaller is better" criteria was used for the study of wear loss in developed composites. Tables 4-6 show the results of the ANOVA for wear loss. P-values with a confidence level lower than 0.05 were deemed to have a substantial impact on performance [24, 25]. The main effects graph shown in Fig. 5 were used to verify the parameters' relevance. Table 4 displays the results of an ANOVA analysis of the wear parameters of the alloy Al 7075.

According to an ANOVA finding, the load (36.89 %) has a greater impact on wear loss than sliding speed (20.06) or distance (18.71). In contrast, the wear loss shown in Table 5 for Al7075 + 1 % Al₂O₃ is significantly influenced by load (N) (48.17 %), sliding speed (rpm) (14.46 %), and sliding distance (m) (13.63 %). However, the wear loss shown in Table 6 for developed hybrid Composite (Al7075/1 % Al₂O₃/ 1 % SiC) is significantly influenced by load (48.17 %), sliding distance (23.11) and sliding speed (14.46). The results show that the load is the most important relevant parameter for wear loss for all the developed composites, followed by the other two parameters. According to the outcomes, hard particles enable hybrid composites to have a lower wear rate than Al alloy and mono composite. Similar findings have been reported by several investigators [26]. The hard ceramic particulates protruding from the surface of the composites generate sharp asperities and produce uneven interaction between the counter-face and samples, which leads to increase wear rate. With the presence of secondary hard ceramic reinforcement, the distances between the particles in MMCs are close, resulting in the existence of more reinforcement phase. Hard reinforcing particles have been demonstrated to boost toughness in previous studies. It has been demonstrated that wear behaviour, material hardness, and wear loss are related [27]. When the increases in wear factor led to an increase in the wear loss, as can be observed in Fig. 5(a-c). Usually, the primary factor behind the outcomes is the formation of an oxide film on the matrix surface, which leads to increased wear. Hence, both a rise in temperature and a weakening of the composite surface lead to excessive wear. On the other hand, adding tough

particles makes mono MMCs more resistant to wear. As can be seen, the rapid sliding speed frequently increased wear loss and led to the delamination. Developed hybrid composites have better wear resistance than mono composite and monolithic materials [28, 29].

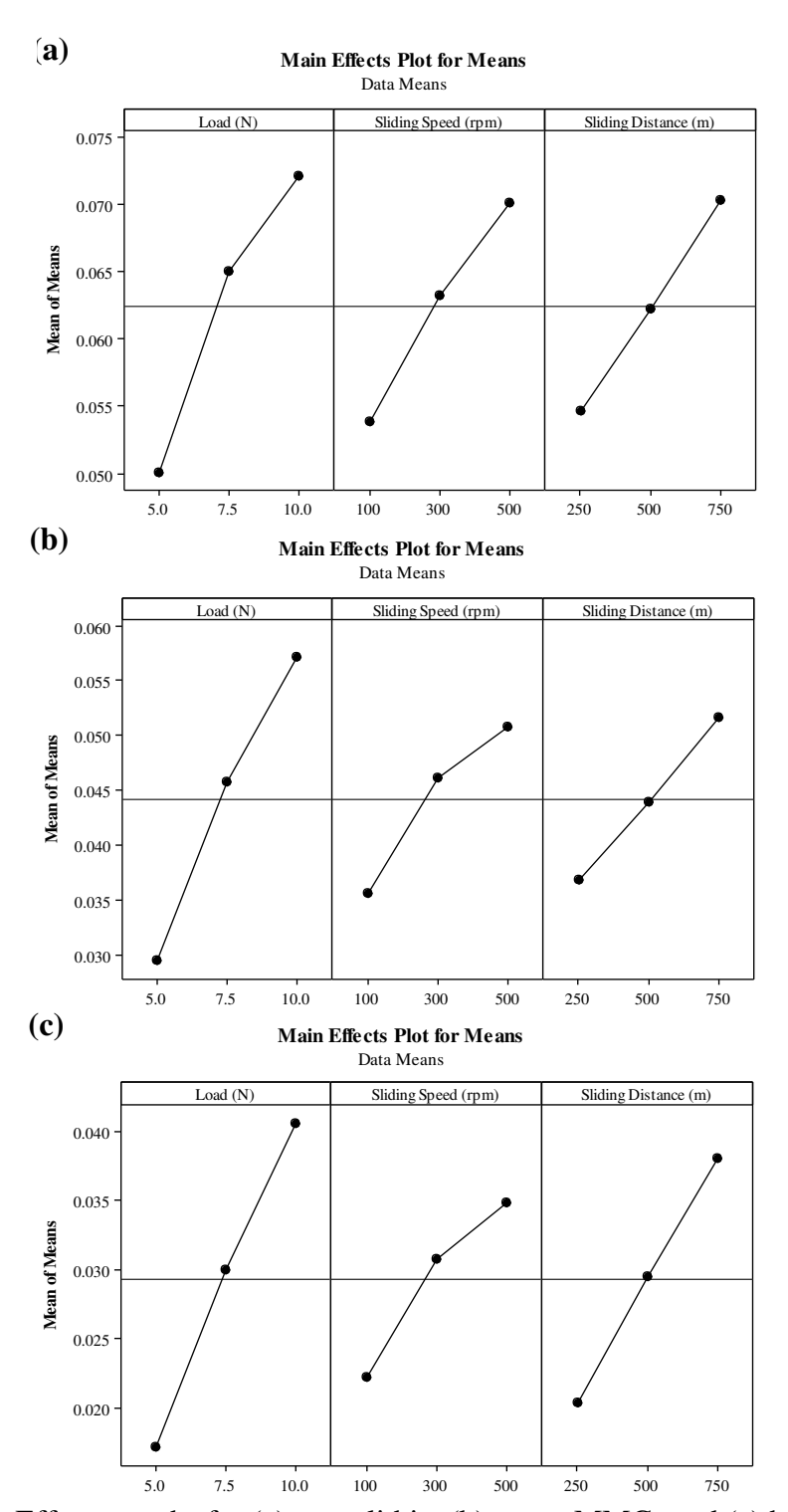


Fig. 5. Main Effects graphs for (a) monolithic, (b) mono MMCs and (c) hybrid MMCs

Based on rank given obtained to the mean points as depicted in Tables 7-9, the mean answer has been assessed. The variables are significant, and it is also clear that the load (N) which the delta of mean value placed as rank 1 and was followed by speed (rpm) and the sliding distance (m) for the aluminium alloy and developed composites is a significant factor.

Table 7. The response data for monolithic material

Levels	Load	Sliding speed	Sliding distance
1	0.05011	0.05389	0.05467
2	0.06500	0.06322	0.06222
3	0.07211	0.07011	0.07033
Delta	0.02200	0.01622	0.01567
Rank	1	2	3

Table 8. The response data for mono composites

Levels	Load	Sliding speed	Sliding distance
1	0.02944	0.03556	0.03689
2	0.04578	0.04611	0.04389
3	0.05722	0.05078	0.05167
Delta	0.02778	0.01522	0.01478
Rank	1	2	3

Table 9. The response data for hybrid composites

Levels	Load	Sliding speed	Sliding distance
1	0.01722	0.02222	0.02033
2	0.03000	0.03078	0.02944
3	0.04056	0.03478	0.03800
Delta	0.02333	0.01256	0.01767
Rank	1	3	2

Regression analysis uses a linear regression equation to illustrate the correlation between two or more predictor variables. The relationship between the wear factors and their interactions is established via a regression equation. Eqs. (1), (2), and (3), respectively, represent the regression analysis equations for matrix, mono, and the hybrid MMCs materials.

Wear rate of monolithic alloy =
$$0.00157407 + 0.0044 Load + 4.05556e^{-005} Sliding speed + 3.13333e^{-005} Sliding distance,$$
 (1)

Wear rate of mono
$$MMCs = -0.023713 + 0.00555556 Load +$$

$$+ 3.80556e^{-005}$$
 Sliding speed $+ 2.95556e^{-005}$ Sliding distance, (2)

Wear rate of hybrid MMCs =
$$-0.0328241 + 0.00466667 Load + 3.13889e^{-0.05} Sliding speed + 3.53333e^{-0.05} Sliding distance.$$
 (3)

The regression analysis has typically been employed to investigate the responses between the parameters. Test trials have been run to ensure that anticipated values are accurate, and graphical representations are used to compare experimentation results with predictions. In Fig. 6, the wear behaviour of base material, mono MMCs, and hybrid composites is depicted in response to expected and experimental values.

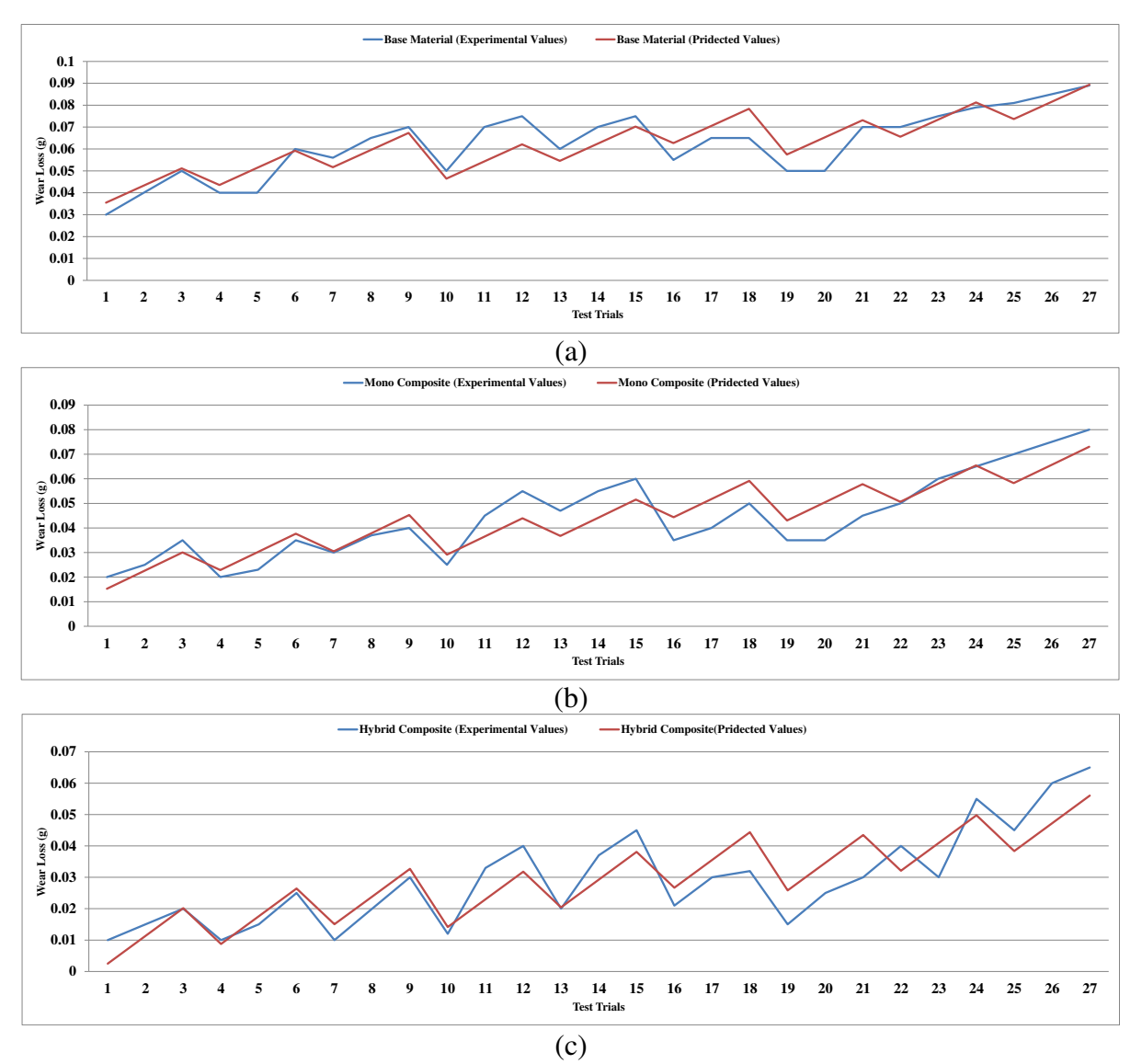


Fig. 6. Experimental vs. predicted values of wear loss for (a) monolithic alloy, (b) mono MMCs and (c) hybrid MMCs

The regression model's contour plots, are drawn and utilised to display the combined impact of the parameters used in the current inquiry. These graphs are typically used to show how the two parameters interact with one another. The optimal values of each parameter could be anticipated by analysing these plots [30]. Figures 7-9 display the contour graphs for the wear loss based on the independent factors for all the developed materials.

The results of wear behaviour in variations of wear factors with different material composition are shown in Fig. 7-9. It has been found that when load, speed and sliding distance are increased, wear loss also increases. Higher loads and faster speeds revealed considerable friction. As a result, a higher temperature was developed on the test sample surface. Brittleness has caused materials' hardness to decrease as a result, and the wear loss was increased. When there is increase in temperature, the link between the reinforcement and matrix gradually weakened, and the material softened [31]. The primary goal of the confirmatory trials was to determine the ideal ranges for the various process parameters that were chosen. Based on the Main Effects Plot (MEP) optimal values, confirmation tests were carried out (Fig. 5). Table 10 shows the parameters at the chosen levels. The results of the confirmatory experimental trials are reported in Table 11 and compared to experimental data

from OA. The outcome shows that for all composite materials, the computed errors are fewer than 10%. This falls inside allowable bounds.

Table 10. Confirmatory test parameters with optimized values

Factors	Load, N	Sliding speed, rpm	Sliding distance, m
Optimized values for all the developed materials	5	100	250

Table 11. Confirmation test outcomes for all developed materials

Configuration	Parameters	Confirmatory test results	OA experimental results	Error, %
Base alloy (Al-7075)	Load (N): 5	0.030	0.029	3.33
Mono composite (10 % Al ₂ O ₃)	Sliding speed (rpm): 100 Sliding distance (m): 250	0.020	0.019	5.00
Hybrid composite (10 % Al ₂ O ₃ + 5 % SiC)		0.010	0.011	9.09

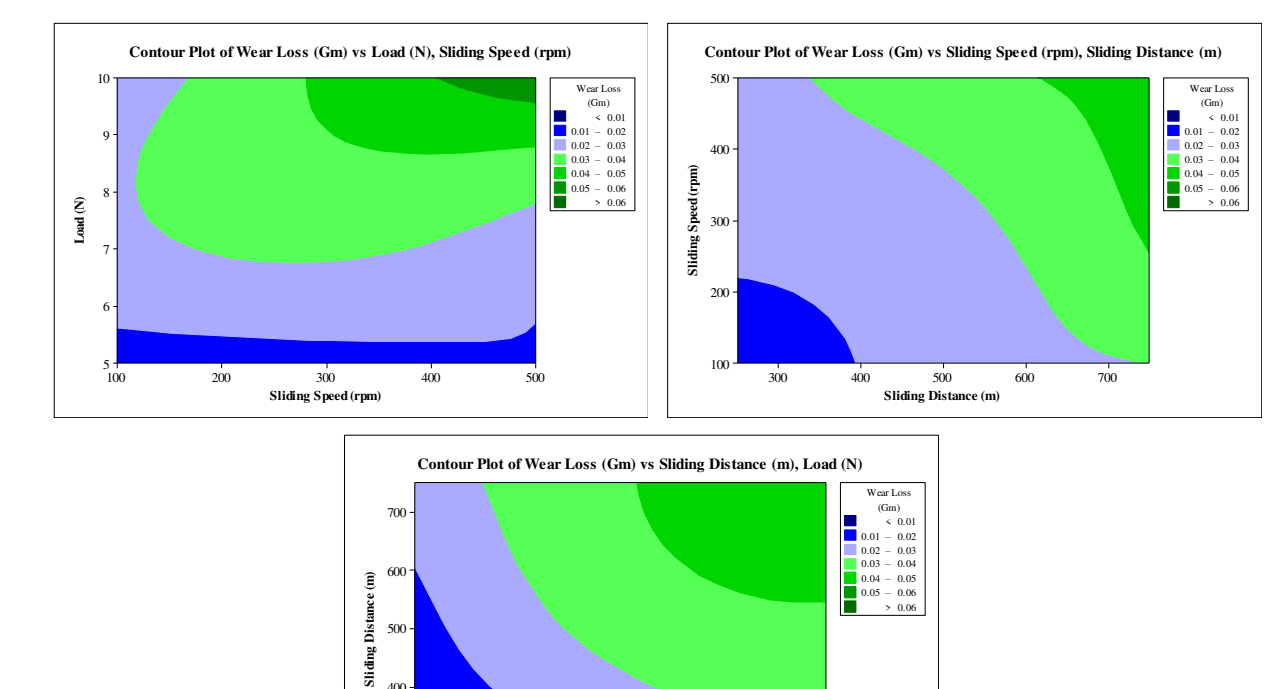


Fig. 7. Contour Plot of monolithic alloy

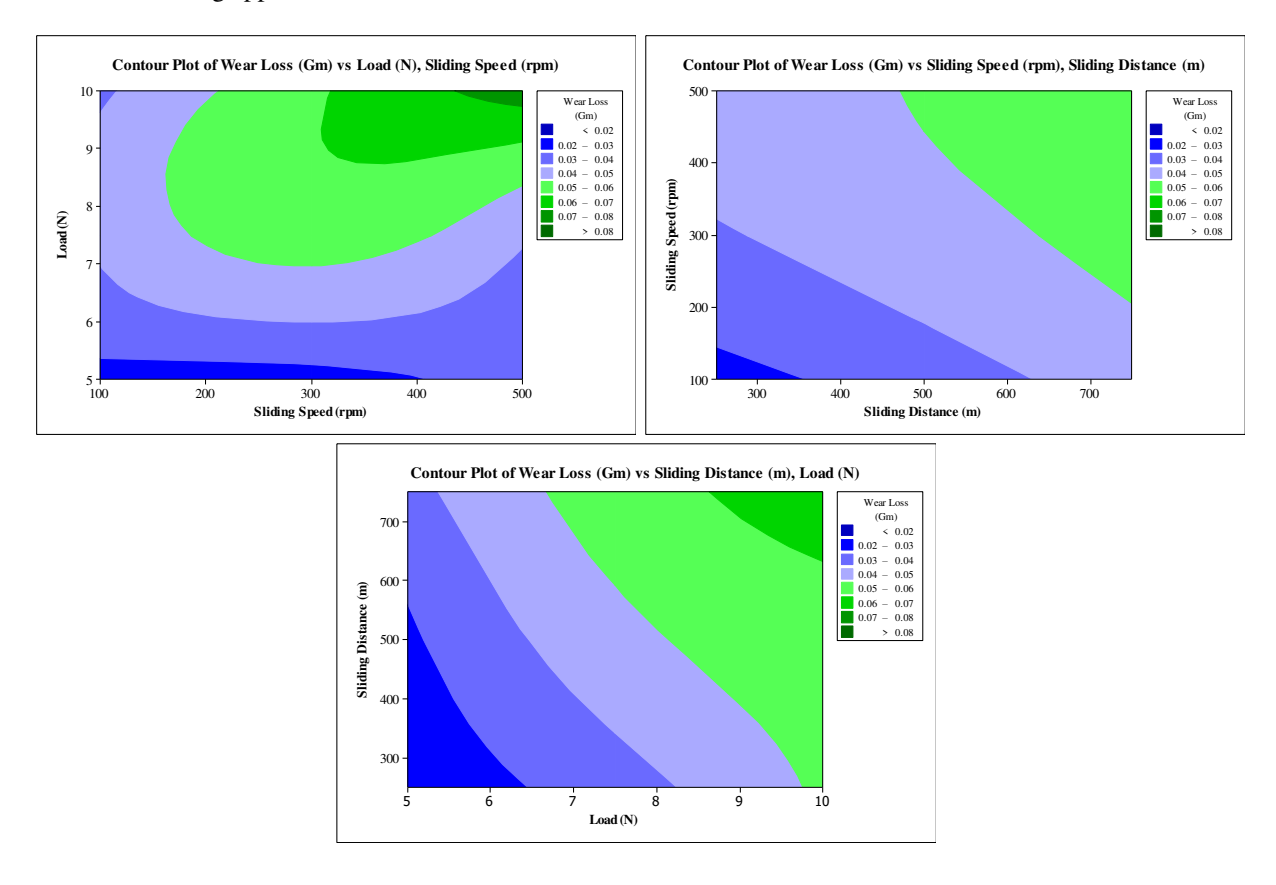


Fig. 8. Contour Plot of mono MMCs

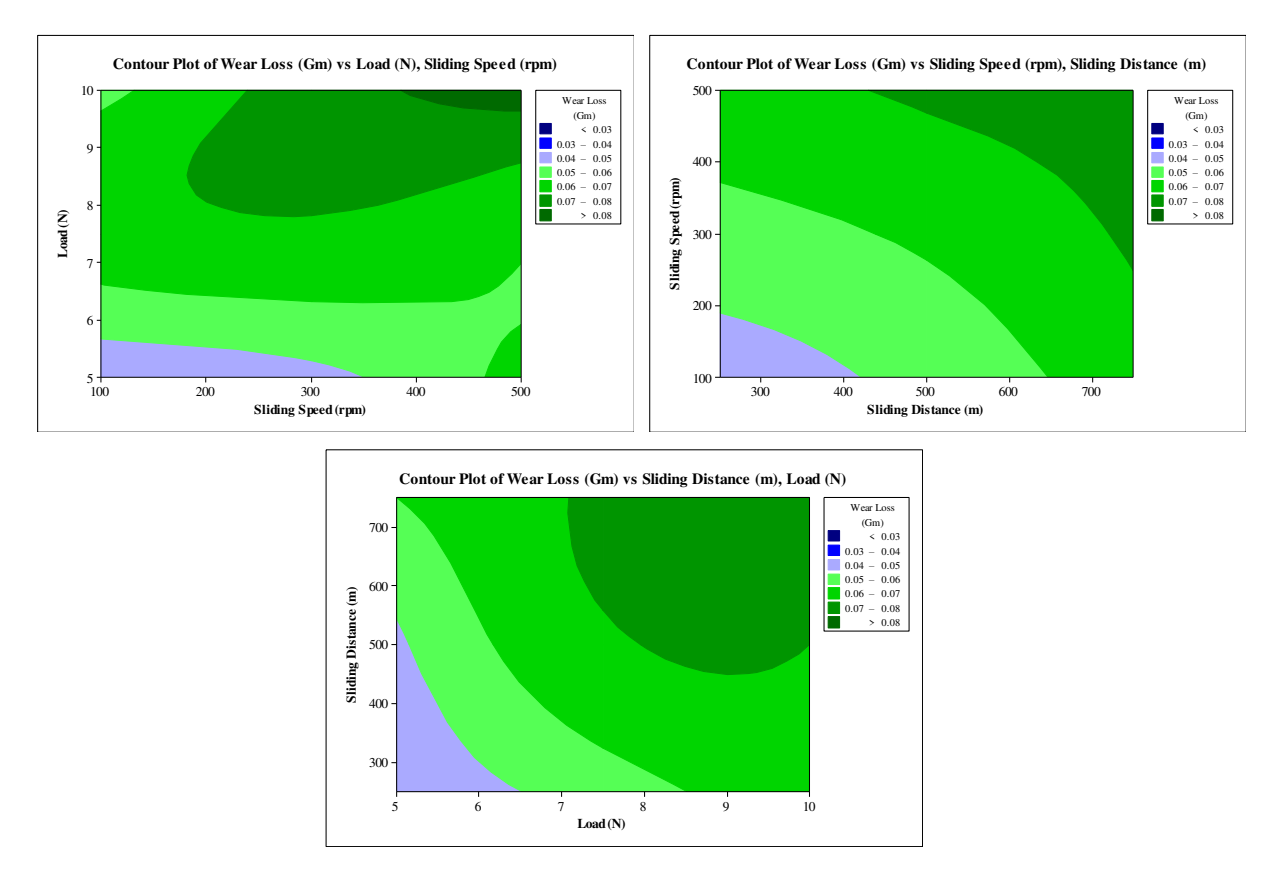
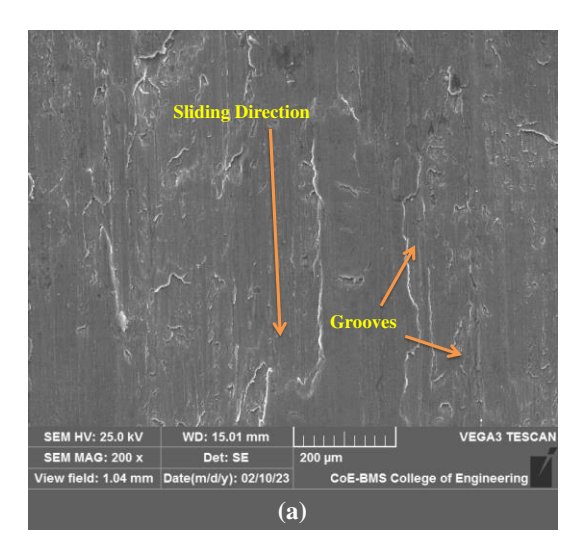
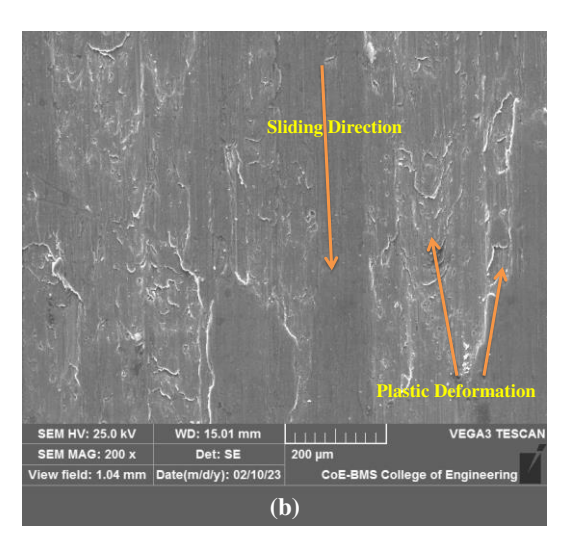


Fig. 9. Contour Plot of hybrid MMCs





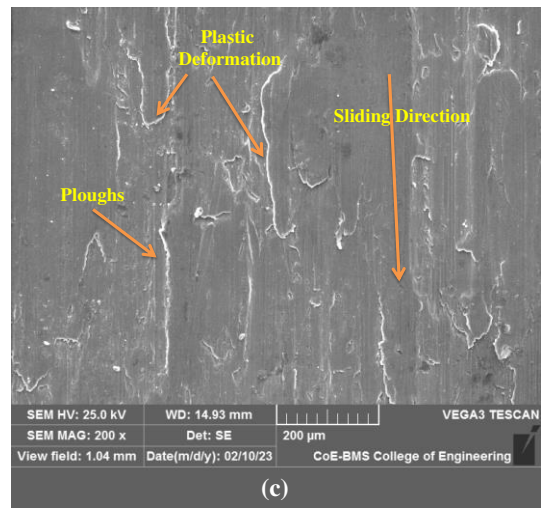


Fig. 10. Worn-out surface of (a) monolithic alloy, (b) mono MMCs and (c) hybrid MMCs

SEM analysis of the worn-out composites samples was done to analyse the wear characteristics of the MMCs. Typically, the MMCs' worn-out surface's properties will have an impact on the wear behaviour. Figure 10 shows a SEM image of a worn-out surface from matrix, mono, and hybrid composites that were evaluated under conditions of 10 N load, 500 rpm speed, and 1000 m sliding distance. The wear track that forms on the surface of the Al 7075, mono, and hybrid MMCs is clearly visible in the SEM pictures. Figure 10(a) depicts the basic alloy Al7075's worn-down surface. The image shows plastic deformation caused by the monolithic becoming less rigid at the interface temperature. Al7075 exhibited an adhesive wear mechanism at greater levels of stress, speed, and sliding distance. Without reinforcement, the image demonstrates with clarity how intense the wear is. It is concluded that the absence of reinforcements typically results in extensive plastic deformation of the matrix. Thus, the worn surface exhibits more material losses. Figure 10(b) shows a SEM image of an Al7075 composite with 1 % Al₂O₃ and more shallow grooves. Generally speaking, the wear resistance will be very high due to the existence of hard reinforcement. Moreover, the worn-out surface is rough due to ceramic particles that were exposed while the composite was being worn down during sliding on the steel disc. The abrasion on the composite surface caused by the hard particles being pulled out resulted in plastic deformation of the particles. It demonstrates that when Al₂O₃ particles were added, wear loss in the monolithic composite was reduced to a minimum. The SEM picture of the composite made of Al7075 with 1 % Al₂O₃ and 1 % SiC is shown in Fig. 10(c). Al₂O₃ and SiC particles in this area boost wear resistance. When it is compared to the mono composite and base material, the image demonstrates that hybrid MMCs has a significantly rougher surface. The wear surfaces of the composite show many, deep grooves and voids. High reinforcement weight percentages result in high wear resistance. The addition of hard ceramic particles has been researched for its impact on the wear process, which provides a number of explanations for the exceptional wear resistance of hybrid MMCs. Due to the hard SiCp reinforcement undergoing chemical interactions during sliding, typically acts as a lubricant. This is especially true at high sliding speeds. MML's protection is seen to improve as the reinforcement content is increased. Several researchers [32–35] noted comparable results.

Figure 11 displays the results of an EDS analysis of base material, mono-composite, and hybrid composites. An EDS analysis of the mono composite surface depicted in Fig. 11(a) indicated the existence of oxygen ("O" peak) as a result of an oxidised layer, suggesting that the composite contains Al₂O₃ (aluminium oxide). Together with the mono reinforcing, the presence of a "Si" peak was noted in the developed hybrid composite (Fig. 11(b)). This demonstrates that SiC particles are present in the hybrid composite. The carbide particles have a significant impact on the wear behaviour of composite materials because, in contrast to mono composite and base materials, wear loss is decreased due to the existence of hard ceramic particulates. Several researchers [36–39] have reported similar results.

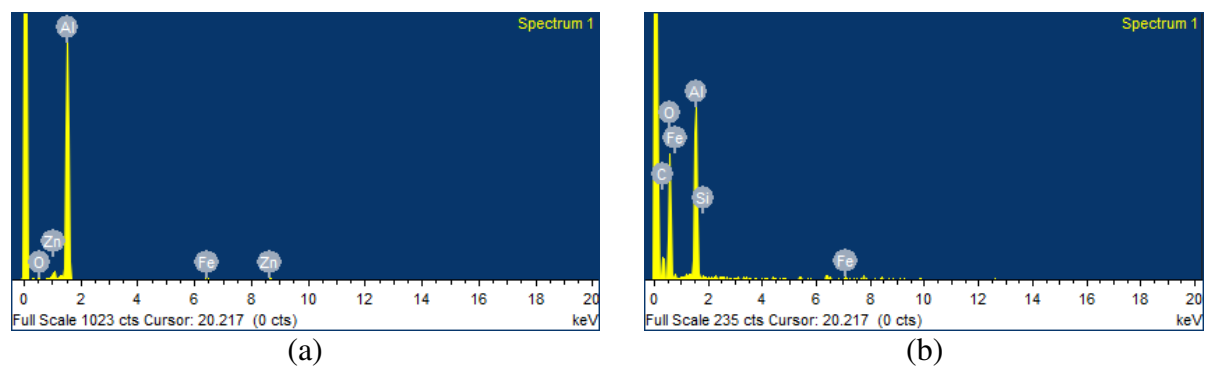


Fig. 11. EDS analysis of (a) mono composites (Al7075 + 1% Al₂O₃) and (b) hybrid composites (Al7075 + 1% Al₂O₃ + 1% SiC)

Conclusions

The evaluation of Al-7075, mono composites (Al7075 + 1 % Al₂O₃), and hybrid MMCs (Al7075 + 1 % Al₂O₃ + 1 % SiC) revealed several significant aspects.

Using the stir casting technology, the monolithic alloy, mono, and hybrid composites were effectively produced in the current experiment. It was observed that adding more tough ceramic particles increased the material's hardness and tensile strength. In contrast to mono composites and aluminium alloy, hybrid MMCs exhibited improved tensile and hardness strength. It has been revealed that the inclusion of SiCp reinforcement produces hybrid MMCs materials that have excellent wear resistance when it is compared to base materials and mono MMCs. ANOVA study revealed that the applied load had a stronger influence on wear rate than sliding speed and the sliding distance. The correlation between the parameters and wear properties has been studied using Regression Analysis. R-Sq (R2), the coefficient of determination, was calculated and found to be within acceptable limits. According to the results of the confirmation test, the error associated with base material, mono, and hybrid MMCs is less than 10 %. In comparison to mono-composite and monolithic surfaces, wornout hybrid composite surfaces exhibit high levels of abrasion wear, as shown by a SEM image. It's because the developed mono composites and hybrid composites contain strong ceramic reinforcement like nano sized Al₂O₃ and SiC content. According to EDS data, mono composite materials include nano sized Al₂O₃, while hybrid composite materials contain nano

sized Al_2O_3 -SiC. According to the results of the confirmatory experiment test, the maximum error for hybrid MMCs was 9.09 %, but it was significantly lower for the other two compositions. This falls inside allowable limits.

References

- 1. Ganesh K, Hemachandra Reddy K, Sudhakar Babu S, Ravikumar M. Study on microstructure, tensile, wear, and fracture behavior of A357 by modifying strontium (Sr) and calcium (Ca) content. *Materials Physics and Mechanics*. 2023; 51(2): 128-139.
- 2. KumarV, Angra S, Singh S. Influence of rare earth elements on aluminium metal matrix composites: A review. *Materials Physics and Mechanics*. 2023; 51(2): 1-20.
- 3. Arunprasath K, Amuthakkannan P, Vijayakumar M, Sundarakannan R, Selwin M, Kavitha S, Lavish Kumar Singh. Effect of Mechanical Properties of AL7075/Mica Powder Hybrid Metal Matrix Composite. *Materials Physics and Mechanics*. 2023; 51(1): 142-150.
- 4. Kumar MSA, Kumar KCM, Prasad SLA. Experimental investigations on mechanical and Tribological properties of extruded Aluminium A356 Al₂O₃ stir cast MMC. *Mater Today Proc.* 2018;5(1): 3044–3051.
- 5. Alhawari KS, Omar MZ, Ghazali MJ, Salleh MS, Mohammed MN. Wear properties of A356/Al₂O₃ metal matrix composites produced by semisolid processing. *Procedia Eng.* 2013;68: 186–192.
- 6. Sajjadi SA, Torabi Parizi M, Ezatpour HR, Sedghi A. Fabrication of A356 composite reinforced with micro and nano Al₂O₃ particles by a developed compocasting method and study of its properties. *J. Alloys Compd.* 2012;511: 226–231.
- 7. Ahmed KE, Nagesh BM, Raju BS, Drakshayani DN, Holla ASC. Studies on the effect of welding parameters for friction stir welded AA6082 reinforced with Aluminium oxide. *Mater Today Proc.* 2020;20: 108–119.
- 8. Prasad Reddy A, Vamsi Krishna P, Narasimha Rao R, Murthy NV. Silicon carbide reinforced Aluminium metal matrix Nano composites-a review. *Mater Today Proc.* 2017;4(2): 3959–3971.
- 9. Ghandvar H, Idris MH, Ahmad N Moslemi N. Microstructure development, mechanical and tribological properties of a semisolid A356/xSiCp composite. *J. Appl. Res Technol*. 2017;15(6): 533–544.
- 10. Amouri K, Kazemi S, Momeni A, Kazazi M. Microstructure and mechanical properties of Al-nano/micro SiC composites produced by stir casting technique. *Mater Sci. Eng. A.* 2016;674: 569–578.
- 11. Shivamurthy RC, Surappa MK. Tribological characteristics of A356 Al alloy SiCp composite discs. *Wear*. 2011;271(9-10): 1946–1950.
- 12. Iyengar SRS, Sethuramu D, Ravikumar M. Mechanical, Wear, and Fracture Behavior of Titanium Diboride (TiB₂) Cerium Oxide (CeO₂) Reinforced Al-6061 Hot-rolled Hybrid Composites. *Frattura ed Integrità Strutturale*. 2023;63: 289-300.
- 13. Ghosh S, Sahoo P, Sutradhar G. Tribological Performance Optimization of Al-7.5 % SiCp Composites Using the Taguchi Method and Grey Relational Analysis. *J. Comp.* 2013;2013: 274527.
- 14. Ekka KK, Chauhan SR, Varun. Study on the sliding wear behaviour of hybrid aluminium matrix composites using Taguchi design and neural network. *J. Materials: Design and Applications*. 2016;230(2): 537–549.
- 15. Panwar RS, Pandey OP. Study of Wear Behavior of Zircon Sand-Reinforced LM13 Alloy Composites at Elevated Temperatures. *J. of Materi Eng and Perform.* 2013;22: 1765–1775.
- 16. Sharma P, Sharma S, Khanduja D. Production and some properties of Si3N4reinforced aluminium alloy composites. *Journal of Asian Ceramic Societies*. 2015;3(3); 352–359.
- 17. Suresh S, Gowd GH, Deva Kumar MLS. Experimental investigation on mechanical properties of Al 7075/Al₂O₃/Mg NMMC's by stir casting method. *Sadhana*. 2019;44(51): 1–10.

- 18. Bhaskar S, Kumar M, Patnaik A. Effect of Si3N4 Ceramic Particulates on Mechanical, Thermal, Thermo-Mechanical and Sliding Wear Performance of AA2024 Alloy Composites. *Silicon*. 2022;14: 239–262.
- 19. Sekar K. Mechanical and tribological properties of Al7475-SiCp composites by stir casting method and wear rate modeling using RSM. *Sadhana*. 2019;44: 129.
- 20. Ravikumar M, Suresh R. Study on mechanical and machinability characteristics of n-Al₂O₃/SiC-reinforced Al7075 composite by design of experiment technique. *Multiscale and Multidisciplinary Modeling, Experiments and Design*. 2018; https://doi.org/10.1007/s41939-023-00179-4.
- 21. Balakumar G. Fracture Behavior of Aluminum alloy Reinforced with Nano-ZrO2Metal Matrix Composite (NMMCs) by DMD Technique. *International Journal of NanoScience and Nanotechnology*, 2013; 4(2): 153–161.
- 22. Kavimani V, Gopal PM, Sumesh KR, Kumar NV. Multi Response Optimization on Machinability of SiC Waste Fillers Reinforced Polymer Matrix Composite Using Taguchi's Coupled Grey Relational Analysis. *Silicon*. 2020;14: 65–73.
- 23. Murali Mohan R, KempaiahUN, Manjunatha B, Madeva Nagaral, Auradi V. Processing and wear behavior optimization of B₄C and rice husk ash dual particles reinforced ADC12 alloy composites using Taguchi method. *Materials Physics and Mechanics*. 2022; 50(2): 304-318.
- 24. Dhanalakshmi S, Mohanasundararaju N, Venkatakrishnan PG, Karthik V. Optimization of friction and wear behaviour of Al7075-Al₂O₃-B₄C metal matrix composites using Taguchi method. *IOP Conf. Series: Materials Science and Engineering*. 2018;314: 012025.
- 25. Narasimha GB, Krishna MV, Sindhu R. Prediction of Wear Behaviour of Almg1sicu Hybrid MMC Using Taguchi with Grey Rational Analysis. *Procedia Engineering*. 2014;97: 555–562.
- 26. Radhika N. Fabrication of LM25/SiO₂ Metal Matrix Composite and Optimization of Wear Process Parameters Using Design of Experiment. *Tribology in Industry*. 2017; 39(1): 1–8.
- 27. Jafari F, Sharifi H, Saeri MR, Tayebi M. Effect of Reinforcement Volume Fraction on the Wear Behavior of Al-SiCp Composites Prepared by Spark Plasma Sintering. *Silicon*. 2018;10: 2473–2481.
- 28. Wakjira MW, Altenbach H, Perumalla JR. Analysis of CSN 12050 Carbon Steel in Dry Turning Process for Product Sustainability Optimization Using Taguchi Technique. *Journal of Engineering*. 2019;2019: 7150157.
- 29. Satyanarayana T, Rao PS, Krishna MG. Influence of wear parameters on friction performance of A356 aluminum graphite/granite particles reinforced metal matrix hybrid composites. *Heliyon*. 2019;5(6): e01770.
- 30. Ashengroph M, Nahvi I, Amini J. Application of Taguchi Design and Response Surface Methodology for Improving Conversion of Isoeugenol into Vanillin by Resting Cells of Psychrobacter sp. CSW4. *Iranian Journal of Pharmaceutical Research*. 2013;12(3): 411–421.
- 31. Marigoudar RN, Sadashivappa K. Effect of reinforcement percentage on wear behavior of SiCp reinforced ZA43 alloy metal matrix composites. *Sci. Eng. Compos. Mater.* 2013;20(4): 311–317.
- 32. Gajakosh A, Keshavamurthy R, Vasanth Kumar R. Friction and Wear Characteristics of Hot-Rolled Al7075-TiO2-Graphite Hybrid Composites. *J. Inst. Eng. India Ser. D.* 2022.
- 33. Kumar D, Singh S, Angra S. Effect of reinforcements on mechanical and tribological behavior of magnesium-based composites: a review. *Materials Physics and Mechanics*. 2022;50(3): 439-458.
- 34. Chen W, Wenhui H, Zhao Z, He N, Xiuqing L. Mechanical properties and tribological characteristics of B4C-SiC ceramic composite in artificial seawater. *Journal of Asian Ceramic Societies*. 2021;9(4): 1495–1505.
- 35. Ünlü BS. Investigation of tribological and mechanical properties Al₂O₃-SiC reinforced Al composites manufactured by casting or P/M method. *Materials and Design*. 2008;29(10): 2002–2008. 36. Riquelme A, Rodrigo P, Escalera-Rodríguez MD, Rams J. Corrosion Resistance of Al/SiC Laser Cladding Coatings on AA6082. *Coatings*. 2020;10(673): 1–12.

- 37. Arif S, Alam T, Ansari AH, Shaikh MBN. Morphological characterization, statistical modelling and tribological behaviour of aluminum hybrid nanocomposites reinforced with micronano-silicon carbide. *Journal of Asian Ceramic Societies*. 2019;7(4): 434–448.
- 38. Matus K, Matula G, Pawlyta M, Krzysteczko-Witek J, Tomiczek B. TEM Study of the Microstructure of an Alumina/Al Composite Prepared by Gas-Pressure Infiltration. *Materials*. 2022;15(17): 6112.
- 39. Muraliraja R, Arunachalam R, Al-Fori I, Al-Maharbi M, Piya S. Development of alumina reinforced aluminum metal matrix composite with enhanced compressive strength through squeeze casting process. *J. Materials: Design and Applications*. 2019;233(3): 307–314.

THE AUTHORS

Ravikumar M. 🗓

e-mail: ravikumar.muk@gmail.com

Vinod B.R.

e-mail: vinod.vbr@gmail.com

Rammohan Y.S.

e-mail: ysrmohan.mech@bmsce.ac.in

Naik R.

e-mail: rudranaik.mech@bmsce.ac.in

Chethana K.Y.

e-mail: chethanaky.aer@bmsce.ac.in

On the precipitation behavior of Al-based automotive alloy with low Si content

Submitted: May 26, 2023

Approved: July 18, 2023

Accepted: August 3, 2023

M.S. Kaiser ^{1 ™}, A.K. Hossain ^{1 ™}

¹ International University of Business Agriculture and Technology, Dhaka, Bangladesh

² Bangladesh University of Engineering and Technology, Dhaka, Bangladesh

⊠ dkaiser.res@iubat.edu

Abstract. It investigates the function of Si content at lower level on the precipitation behaviour in terms of hardness, resistivity, impedance, X-ray diffraction analysis, differential scanning calorimetry along with structural transformation of Al-based automotive alloys. Conventional metal cast alloys are subsequently allowed to T6 thermal treatment at progression of homogenizing, solutionizing, quenching and ageing. Solution treated samples are aged naturally and artificially, including isochronal and isothermal for different time and temperature. The results suggest that the formation of clusters and GP zones together with metastable phases leads to considerable hardening in aged alloys. As a result, electrical resistivity also increases but decreases at higher ageing temperature for stress relieving followed by metastable phase dissolution and coarsening of fine precipitation. DSC and XRD study confirms the formation of such phases, showing the different peaks. The Si addition entirely changes the precipitation peak of the base alloy for its increasing properties of heterogeneous nucleation and diffusion kinetics in concert with the Si-rich intermetallic. Microstructural observations confirm that solution treatment improves grains distribution and Si additions creates the eutectic phases and coarsens the alloy grain boundaries. Both alloys as well attained more or less entirely re-crystallized after ageing at 350 °C for 60 minutes.

Keywords: Al-alloys; T6 heat treatment; intermetallic; resistivity; activation energy; microstructure

Acknowledgments. The corresponding author would like to express his gratitude towards Prof. Selina Nargis, the Treasurer & Director Administration at IUBAT, for her valuable support and encouragement in promoting research activities at the university. Her efforts in fostering collaborations with other institutions have also been commendable.

Citation: Kaiser MS, Hossain AK. On the precipitation behavior of Al-based automotive alloy with low Si content. *Materials Physics and Mechanics*. 2023;51(6): 42-53. DOI: 10.18149/MPM.5162023_4.

Introduction

The 4xxx series aluminum-silicon alloys have a wide selection of properties used in the manufacture of automobiles, aircraft and electronic components [1,2]. Outstanding castability property, it is suitable for manufacturing of these complex and heavy parts. Binary Al-Si alloys have no special mechanical properties other than castability. To improve the different properties Cu, Ni, Zn, Mg, etc. as minor elements, Ti, Zr, Sc, B, etc. grain refiner and Fe, Pb, Sn impurity elements are also considered into this alloy [3–6]. Common alloying elements Cu and Mg are most of the cases added in this alloy to enhance the higher strength. These two

alloying elements not only improve the strength but also responsive to precipitation hardening of the alloys. To get the superior properties of this Al-Si automotive alloy, Cu well-thought-out 1.0 to 4.0 wt. % and Mg vary from 0.3 to 1.0 wt. % [7,8]. As silicon the major alloying element, so the high strength to weight ratio is the most attractive feature of this alloy. In this Al-Si system, 5 to 23 wt. % Si is used in most of the cases, but the eutectic level is attained at 12.6 wt. % Si [9]. It is well established that Si doping in aluminium alloys increases the fluidity and castabilty, better corrosion resistance, mechanical properties, and machinability. It also forms intermetallics with Mg and other trace elements. As the alloy content different elements, the quantity of the elements presents into the alloys play an important role on every process along with the properties. So, application of heat treatment can change the character and distribution of metallurgical elements in these alloys. The properties of alloys under agehardening depend entirely on the applied temperature and the duration of the aging process. In the course of ageing process various kinds of coherent aggregates such as solute-rich clusters, GP zones and precipitates can be formed. The presence of these fine intragranular dispersion particles all through the grains promotes high levels of strength of these alloys [10,11].

The investigated work is portion of a general study on precipitation behaviour of Al-Cu-Mg automotive alloy system doped by lower level of Si. Specifically, this investigation involves changes in hardness that occurs during natural and artificial ageing and supplemented by resistivity, impedance, X-ray diffraction (XRD), differential scanning calorimetry (DSC) as well as microstructural study. From the experiment, obtained results will be helpful in future alloy and process development and modelling work of this type of Al-based automotive alloy.

Materials and Methods

Al-based automotive alloys with low level of Si was the most important concern of this study, other than without Si also tried to consider for comparison the property. Commercial purity aluminum, copper and magnesium along with Al-50 wt. %Si master alloy ingot were used to prepare the two experimental alloys. The alloys were cast using a pit furnace of natural gasfired. Degasser like borax also used for the period of melting in the clay-graphite crucible. The furnace temperature was monitored with the help of Laser Temperature Gun and always maintained the temperature of 750 ± 10 °C. The melt was stirring at 700 °C for homogenizing and then poured into 250 °C preheated mild steel mould of $20 \times 200 \times 300$ in millimeter. The chemical compositions of both alloys, obtained by Shimadzu PDA 700 optical emission spectrometer, are as follows in Table 1.

Table 1. By wt% average chemical composition from OES analysis

	Si	Cu	Mg	Fe	Ni	Pb	Zn	Mn	Ti	Al
Alloy 1	0.244	2.158	0.767	0.211	0.199	0.163	0.076	0.065	0.005	Bal
Alloy 2	3.539	2.309	0.784	0.273	0.217	0.166	0.083	0.067	0.010	Bal

First, the oxide layer of the cast alloy surfaces was removed by machining and then allowed to hold in a muffle furnace at 450 °C for 12 h for homogenization. To obtain a supersaturated single-phase region of the alloys, the samples were then solutionized at 535 °C for 2 h followed by rapid quenching in salt water. For the ageing study, the thermally treated alloys were pieced of $18 \times 18 \times 5$ in mm. The samples were subjected to natural ageing for more than two months. Artificial ageing conducted as isochronal for 60 minutes up to 350 °C and isothermal at 200 °C for 30–360 minutes. Following this, the finished surface of the samples was produced by polishing for this measurement. Automatic Turret Micro Vickers Hardness Tester, model: HV-1000DT was used for measuring the microhardness of the different processes aged samples and this time 1 Kg load for 10 seconds was applied with the Knoop indenter. Fifteen indentations were taken from different positions on every finish

sample and the average value was considered. The electrical resistivity of the alloys was determined using a Type 979, electrical conductivity meter, calculated from that electrical conductivity data.

The experiment of differential scanning calorimetry was done under inert N_2 gas atmosphere using DSC131 EVO Analyser. The samples weight was a lump of 34 mg. The test was conducted with scan rate of 10 °C/min from room temperature to 600 °C. The activation energy was calculated through the DSC heating run of the alloys using Nagasaki–Maesono analysis [12]. The X-ray diffraction analysis of the aged samples was done using a PHILIPS PW1830 diffractometer with Cu-K α (0.154 nm) radiation. The operating voltage for all the diffraction analysis was 45KV and the tube current was 35 MA respectively. The diffraction angle scan rate was 10/mm and step used 0.02 in the range of 25 to 90 °C. At room temperature, LCR meter and Impedance Analyzer were used for the AC electrical measurements where the considered range of 100 Hz \leq f \leq 100 MHz. A 10 × 8 × 3 mm finish surface was prepared for this study. For the metallographic studies, the heat-treated samples were polished with alumina, etched with Keller's reagent and observed under a Versamet-II Microscope. SEM of the aged samples was carried out by a Jeol Scanning Electron Microscope type of JSM-5200 with X-ray analyzer to verify the different elements present in the experimental alloys.

Results and Discussion

Age-hardening behavior. Natural ageing. Figure 1 shows the change in average microhardness of the solution treated base Alloy 1 and 3.5 %Si added Alloy 2 during natural ageing condition. It is clear that both alloys gain some degree of hardness within 65 days of natural aging. It is postulated that during natural ageing, the solute atoms form clusters or coclusters of Mg, Si and Cu. Such clusters are supposed to hinder the free movement of dislocations as a result of an increase in hardness. However, the Si added alloy initially shows higher hardness because of different alloying elements with Si are re-dissolved for producing a solute-rich homogeneous solid solution. Higher formation of Si clusters accelerates the ageing response of 3.5 %Si added alloy. Except it Si also refines the grain structure, so the hardness improved as stated by the Hall-Petch equation [13,14]. A decrease in hardness is observed for both alloys after a few days, which can be attributed to the relieving of internal stresses due to casting and solution treatment. It is slightly higher for Si added alloys, as higher foreign particles cause higher internal stress.

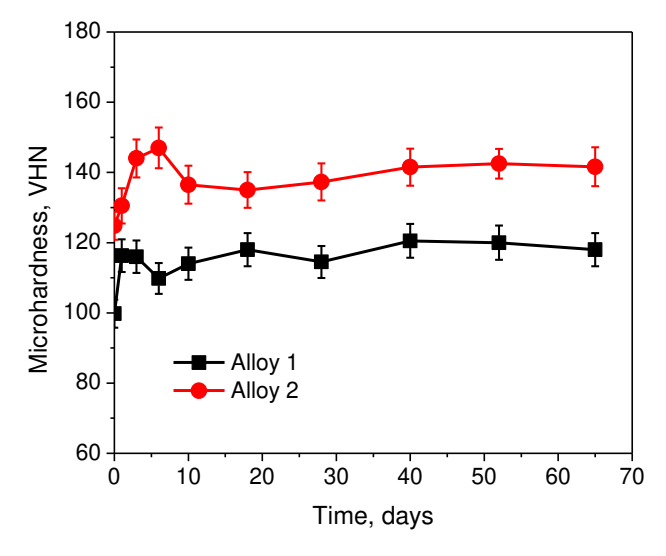


Fig. 1. Natural ageing behavior of two experimental alloys for 65 days

M.S. Kaiser, A.K. Hossain

Artificial ageing. Isochronal ageing. The effect of isochronal ageing for one hour on the micro-hardness of the alloys is plotted in Fig. 2. The curves associated with hardness exhibit the twice ageing peaks during the entire aging period. But Si added Alloy 2 shifts the hardness peaks in terms of intensity and temperature than that of base Alloy 1. The first precipitates, formed during the aging process, are usually linked with atomic clusters, and GP zones form rapidly in the Al matrix. These precipitates are very fine and coherent with the matrix of Al, and thus cause a strong strengthening effect by inhibiting dislocation movement. A further metastable phase is formed following the aging process which is semi-coherence with the matrix and can efficiently oppose the movement of dislocations, so creating some reinforcing effect. The age-hardening effect between the two peaks is less for both alloys. During this aging period, the GP zones dissolve to form metastable phases. Hence, the level of GP zones for dissolution is considerably reduced, and metastable precipitates are not formed since then. So it is effectively damaged to prevent dislocation movement. Such alloys exhibit double aging peaks, as reported in earlier investigations [10,15]. Additionally, during aging solution treated Alloy 1 follow the precipitation sequence formation of atomic clusters, GP zones, homogeneous intermediate phase θ'' -Al₂Cu, heterogeneous intermetallic phase θ' -Al₂Cu and equilibrium phase θ-Al₂Cu. Alloy 2 doped with Si produces supplementary intermediate β"-Mg₂Si phase, heterogeneous precipitation of β'-Mg₂Si and rod or plate-shaped equilibrium β-Mg₂Si phase. The utmost strength of the alloy is attained immediately prior to the precipitation of incoherent θ and, β -platelets. The S-CuAlMg₂ phases may be formed in case of Alloy 1 and Silink precipitates as Q-Al₅Cu₂Mg₈Si₆, π-Al₉FeMg₃Si₅ and β-Al₅FeSi etc. for Alloy 2, but this has a minor contribution in strength than the θ' and β' phases [16].

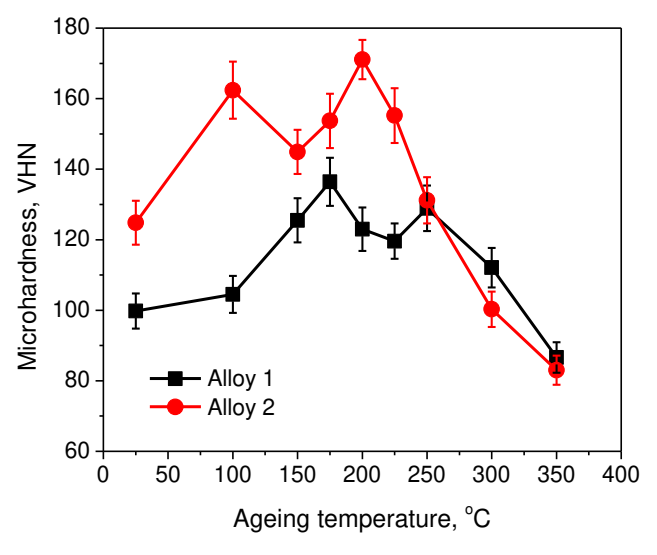


Fig. 2. Microhardness changes of two experimental alloys under isochronal ageing treatment

However, significant evidence shows that Si addition not only extends the age hardening intensity but also provide an earlier aging response. These experiences can be attributed to the Si-phase having a great control over the diffusion behavior of Cu in the Almatrix. The nucleation as well as the growth process of θ' (Al₂Cu) take place earlier because of the heterogeneously nucleation, this contributes to amplify the aging kinetics and superior strength via the early aging. In addition, it is associated with higher diffusion rates of Si and Mg elements compared to Cu [17,18]. Si doped alloy leads to the formation of Si-rich precipitates as responsible for the high strength. At the final aging stage, a sharp decline in the hardness of alloys is observed. This is obvious, the over ageing effect on the alloys. Metastable strengthening precipitates become coarser and grain growth occurs faster, resulting in transformation of even stable incoherent precipitates, which are inefficient in

limiting dislocation motion. Another point to note is that the alloy with Si addition at higher aging temperature shows lower hardness since higher diffusion rate of Si.

The changes of the average values of electrical resistivity with the aging temperature of the experimental alloys is put on show in Fig. 3. The early fall in resistivity during ageing is related to stress relieving of the alloys. The transition materials attach the vacancies into the alloy strongly. Therefore, the concentration of scattering centers decreases, hence the resistivity drop off. The following increase in resistivity is due to formation of fine intermetallic precipitates. The sharp fall in electrical resistivity of the alloys is associated with recovery of strain and dissolution of metastable phases already present in the alloy matrix. The initial resistivity of solution treated Alloy 2 containing 3.5 Si shows higher values than base Alloy 1 due to higher Si-rich intermetallic in the alloy. During ageing higher amount of Si forms different intermetallic with different elements, dissolution also occurs as a result some variations are there. Dissolution of β precipitate and hence strain recovery is the factor responsible for the above drop in resistivity [15,19]. These resistivity values depend on two things, as the GP zone and various precipitation formations increase the resistivity and stress relieving and recovery decrease the resistivity of the alloys. So the sum of these results is displayed in the graph. The Si added alloy demonstrates the higher rate of decreasing because of higher stress reliving behaviour as it contents the higher fraction of intermetallic in solid solution. Alloys with Si addition at intermediate stages also show signs of early precipitation peaks.

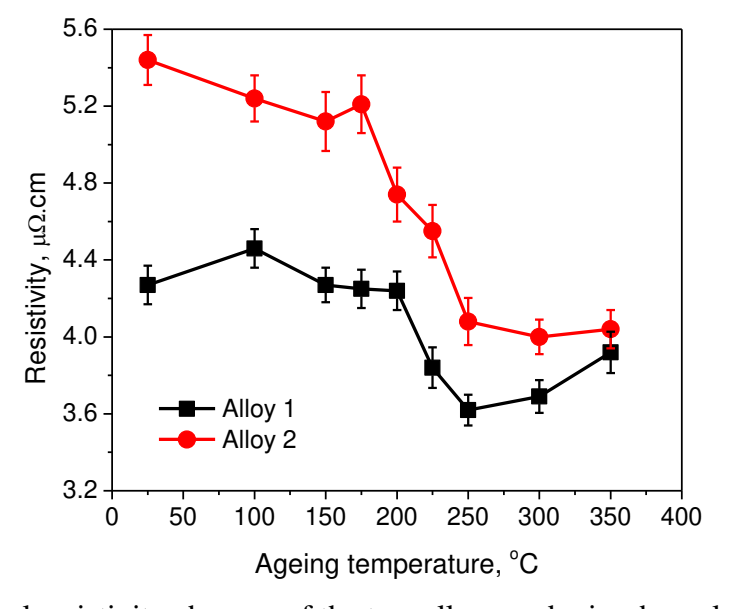


Fig. 3. Electrical resistivity changes of the two alloys under isochronal ageing treatment

Isothermal ageing. Figures 4 and 5 show the values of average hardness and the resistivity of the alloys when aged isothermally at 200°C for varying timelines. For both, the alloys first increases with ageing time due to fine high density GP zones formation which have the capacity to strengthen, and then the hardness decreased due to dissolution of GP zone (Fig. 4). As the GP zone dissolves, the precipitates then grow to a stable phase, which has a relatively weak strengthening effect. Following this, a subsequent strengthening effects are observed as associated with nanoscale metastable precipitates [20]. Ageing for a long time, the hardness decreases due to continuously precipitates coarsening and even start

transforming to stable θ precipitate. In case of Si doped alloy, early aging reaction is visible due to increase in nucleation characteristics [18].

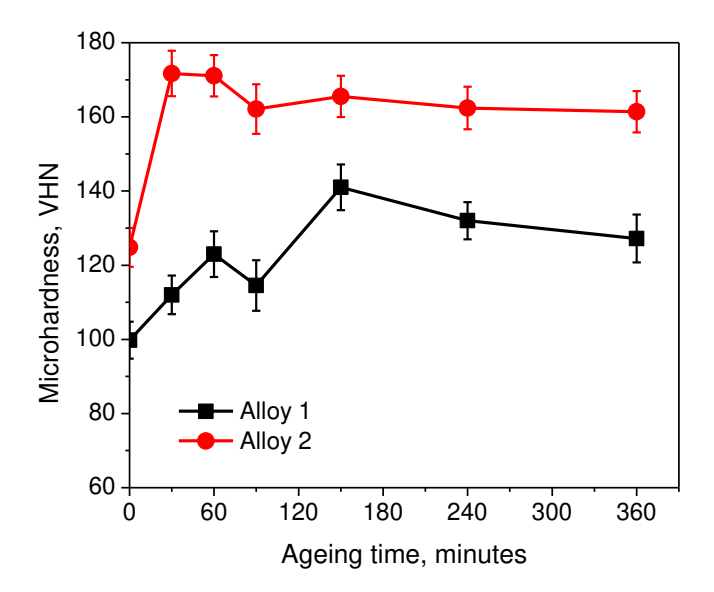


Fig. 4. Microhardness changes of the two alloys under isothermal ageing treatment

Both alloys exhibit a general trend of decreasing of resistivity with aging time (Fig. 5). However, Si added Alloy 2 at early stage of aging offers a higher reduction in resistivity compared to base Alloy 1. It is already point out that GP zone and different precipitation formation increase the resistivity of the alloys, and stress reliving and recovery decrease the resistivity of the alloys. So the summation of these results is displayed in the graph. At extend ageing time, the decrease of resistivity fully related with precipitation and grain coarsening of the alloys. Fine precipitates make the alloy defects which obstruct the electron movement and coarsen precipitates losses the efficiency, hence the higher and lower resistivity [15].

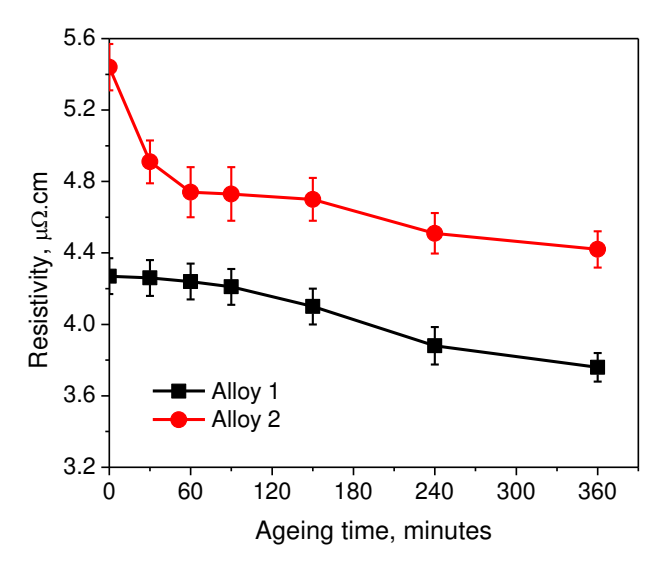


Fig. 5. Resistivity changes of two alloys under isothermal ageing treatment

Impedance behavior. At room temperature, the frequency dependence impedance behaviour of Al-based automotive alloys are plotted in Fig. 6. It is observed that both solutions treated alloys exhibited higher impedance at low frequencies and decreases with the higher frequency. According to Drude Lorentz model, capacitive effects are higher at low frequencies because there are scattering effects of electrons colliding with the lattice as well

as electric polarization of bound electrons not in the conduction band. A number of interfacial polarization may be occurred. At lower frequencies it leads to high impedance because grouping of both effects capacitive and purely resistive [21]. The graph also demonstrated that 3.5Si added Alloy 2 attain the higher impedance followed the base Alloy 1. The impedance properties of any material depend on different factors. These are microstructural defects like porosity, microcracks, dislocations, vacancies, along with impurities, dopant atoms etc. Normally, addition of impurities significantly increases the impedance characteristics of the metal.

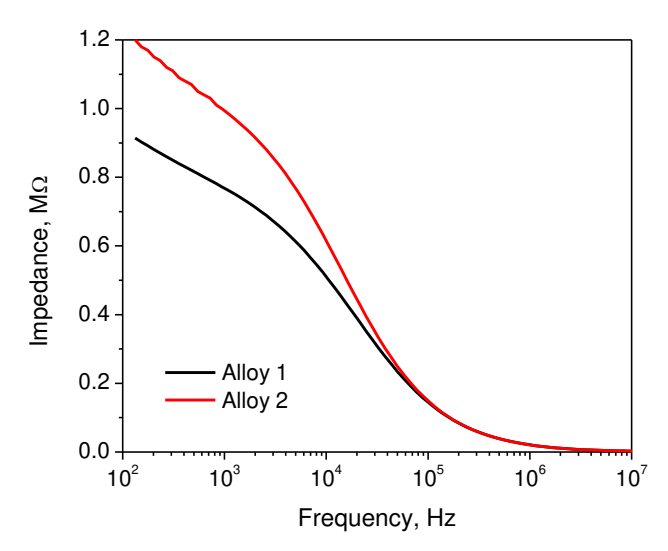


Fig. 6. Comparison of impedance behaviour of both alloys with applied frequency

Thermal analysis. Figure 7 represents the DSC heating curve of both alloys at solution treated condition. Two alloys each consists of the similar number of four exothermic and one endothermic peak, but the happening temperatures are different. Four consecutive exothermic peaks indicative formation of GP zones, β'' phase, β' phase and β phase followed the endothermic peak corresponds to the dissolution of β phase. It may be supposed that dissolution of previous phases occurs only to form a later phase [22,23].

From Fig. 7 along with Table 2, it is put on show for Alloy 1 that GP zones form at 130 °C with an activation energy 64 kJ/mol of the process. But corresponding to Alloy 2, it occurs earlier as at 115 °C and 60 kJ/mol respectively. It is inferred that Si added alloy forms Mg₂Si phases which perform as heterogeneous nucleation site for formation of Al₂Cu and Si phase subsequently devoid of any particular crystal orientation. As a result, the peak occurs earlier along with lower process activation energy. Similarly, for Alloy 1, the activation energy of the heterogeneous precipitation β' and stable equilibrium phase β phase are calculated as 283 and 203 kJ/mol, corresponding temperature at 285 and 435 °C respectively whereas Alloy 2 demonstrate at 265 and 185 kJ/mol at 273 and 335 °C. Intermediate β" phase for Alloy 1 forms at 205 °C with an activation energy of 115 kJ/mol, other than Alloy 2 form this phase at 247 °C with 126 kJ/mol activation energy [24]. Intermediate phase occurs homogeneous as a result no symptom of early on. Again, the lastly endothermic peak in course of heating associated with dissolution of stable β phase, form at 534 °C with an activation energy of 240 kJ/mol for Alloy 1 and a sharper exothermic peak at 510 °C with an activation energy of 222 kJ/mol for Alloy 2. Similar nature is observed earlier regarding the occurrence of the peak. In case of dissolution of β phase, there is a tendency to occupy the Cu atoms by blocky Al₂Cu and not dissolved in Al matrix easily, so the higher both values. The diffusion rates of Si and Mg elements are higher compare to Cu as a result earlier formation of dissolution peak with lower activation energy of the Si doped alloy [18].

Table 2. Results of DSC study

	Table 2. Results of Doe study								
Alloy	Transformation	Peak temperature (°C)	Activation energy (kJ/mol)						
	GP zone	130	64						
	β" phase	205	115						
Alloy 1	β' phase	285	283						
	β phase	435	203						
	Dissolution of β phase	534	240						
	GP zone	115	60						
	β" phase	247	126						
Alloy 2	β' phase	273	265						
	β phase	335	185						
	Dissolution of β phase	510	222						

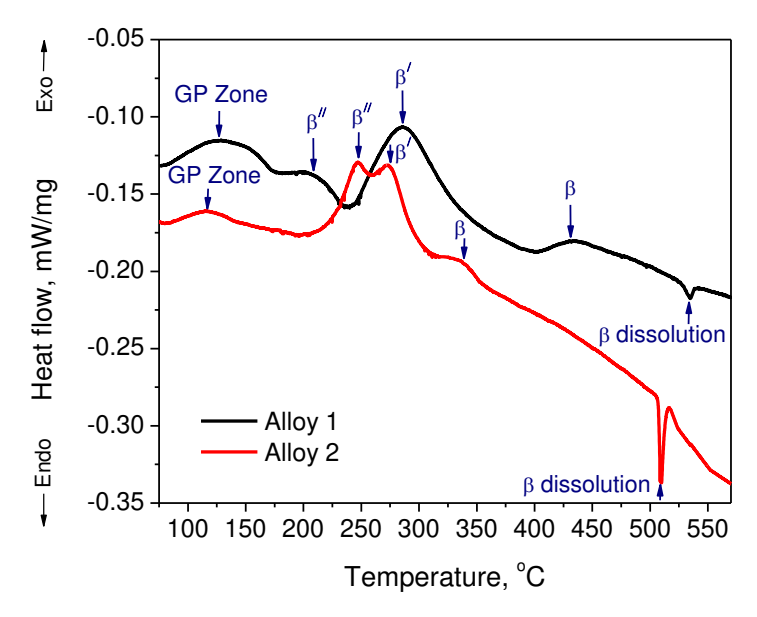


Fig. 7. DSC heating curve of the solution treated two alloys

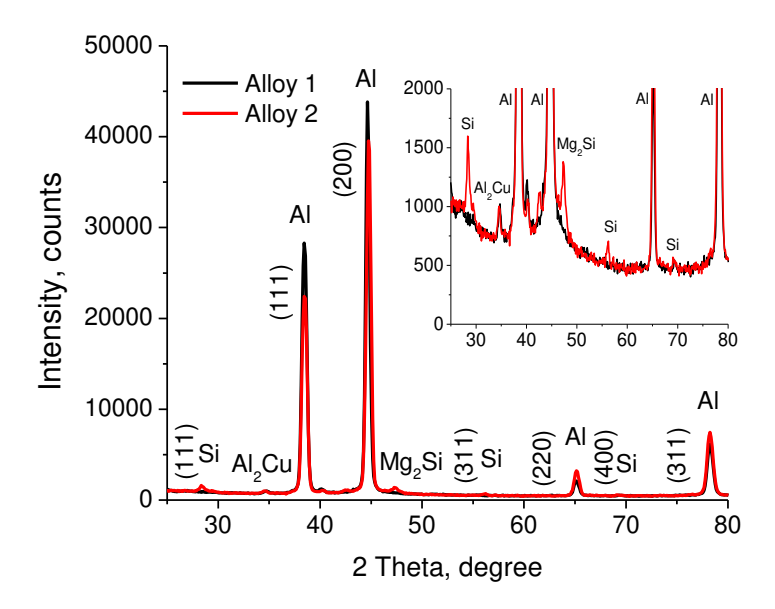


Fig. 8. XRD patterns of two alloys ageing treated at 200 °C for 150 minutes

The XRD data analysis of both alloys at T6 heat-treated state is presented in Fig. 8. The base Alloy 1 shows the peak Al phase along with the Al₂Cu. As the silicon is doped, additionally Alloy 2 creates the peak of the silicon phase Mg₂Si. It is also noted that Alloy 2 produces the Si peaks and reduces the level of Al, resulting in a decrease in the peak position of Al compared to Alloy 1. These two intermetallics play the important role on the strengthening of the alloys as stated earlier. At the T6 heat treatment condition other peaks are not clearly observed, as the associated intermetallics are in an extremely narrow range, which is untraceable by X-ray analysis [25].

Optical microscopy. After solution heat treatment at 535 °C for 2 h, the microstructure of the tested alloys are shown in Fig. 9 to illustrate the effect of Si. The microstructure of base Alloy 1 consists mainly of primary Al dendrites with minor elements like Cu, Mg, Fe in solid solution (Fig. 9(a)). These are consistently spread into Al-matrix since the solidification under fast cooling [26]. Silicon added by 3.5 wt. % Alloy 2, to some extent, refines the microstructure and coarsens the grain boundaries (Fig. 9(b)). The microstructure also displays eutectic silicon clearly fragmented with more spherical.

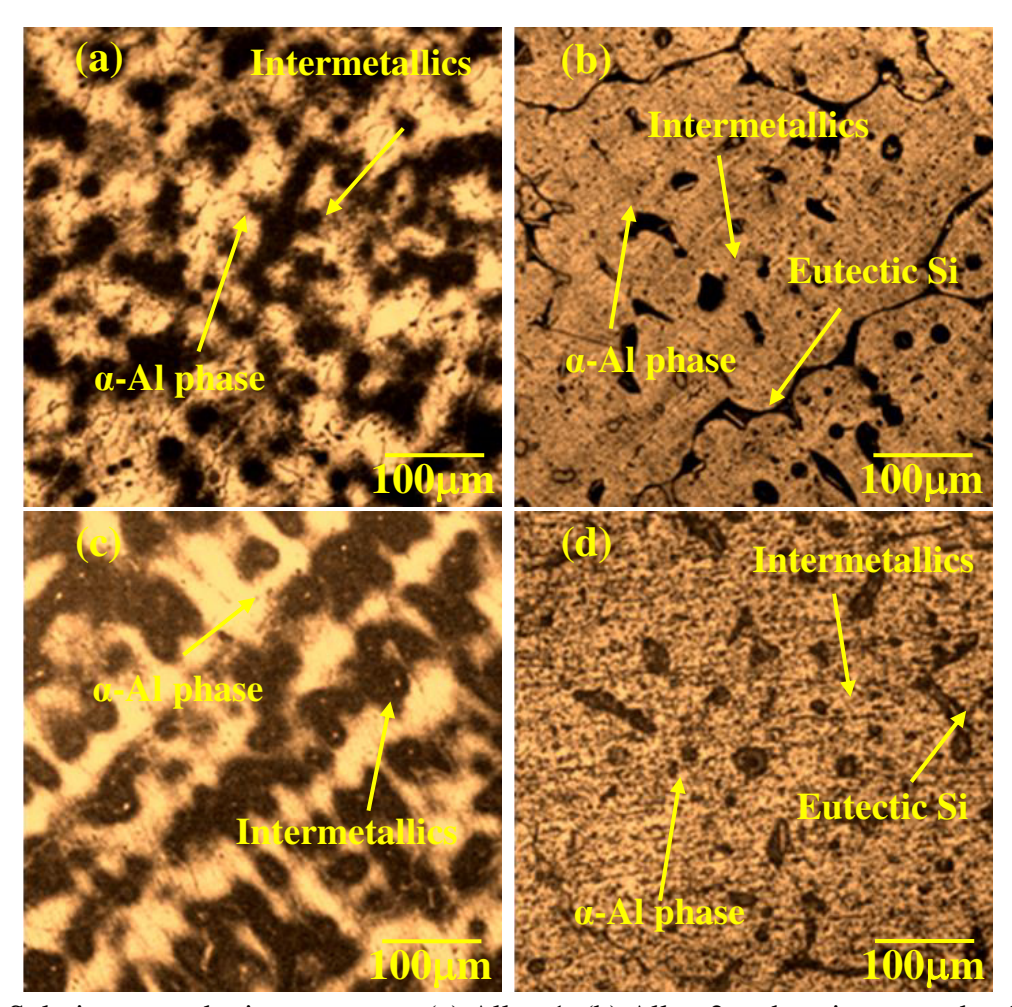


Fig. 9. Solution treated microstructures (a) Alloy 1, (b) Alloy 2 and ageing treated at 350 °C for 60 minutes (c) Alloy 1, (d) Alloy 2

After an ageing treatment at 350 °C for a timeline of one hour, both alloy microstructures are found to be more or less entirely recrystallized (Fig. 9(c,d)). Dendrites appear to be dissolved as well as precipitates coarsening occurred that are uniformly distributed in the matrix [27]. Consequently, the microstructure consists of equiaxed grains. Whereas the microstructure background is not very clear as the prior solution treated alloys.

This is due to the presence of intermetallic aggregates in growth α -Al phase of the base alloys. Moreover, for alloy containing Si, the elongated Si particles are well seen in the microstructure diffused from the aluminium matrix as it does not dissolve in this ageing condition.

Scanning electron microscopy. SEM micrographs along with EDS spectra of the two alloys in Fig. 10 are performed to complement the optical microstructural studies. The typical micrographs are in T6 heat-treated condition as solutionizing, rapid cooling and then aged at 200 °C for 150 minutes. No symptom of crystallization in the microstructure of the two alloys is observed at these ageing conditions. As usual in base Alloy 1 exists various intermetallic particles uniformly distributed in the α -Al phase and at grain boundaries also (Fig. 10(a)). When Si is doped by 3.5 wt. % Alloy 2, a number of rough as well as elongated eutectic phases turn to visible, which separate the alloy α -Al matrix (Fig. 10(b)). These plate-like eutectic Si distributes at the grain boundaries, causing coarsening of the grain boundaries [15,28]. The corresponding EDX of the SEM indicate the following elements by wt. % in Alloy 1, 97.28 %Al, 0.03 %Si, 1.94 %Cu, 0.64 %Mg, 0.05 %Fe and 0.06 %Ni similarly Alloy 2 are 92.08 %Al, 4.81 %Si, 2.26 %Cu, 0.57 %Mg, 0.15 %Fe and 0.13 %Zn. The results obtained from the analysis satisfy the elements composition of the experimental alloys, as presented in Table 1.

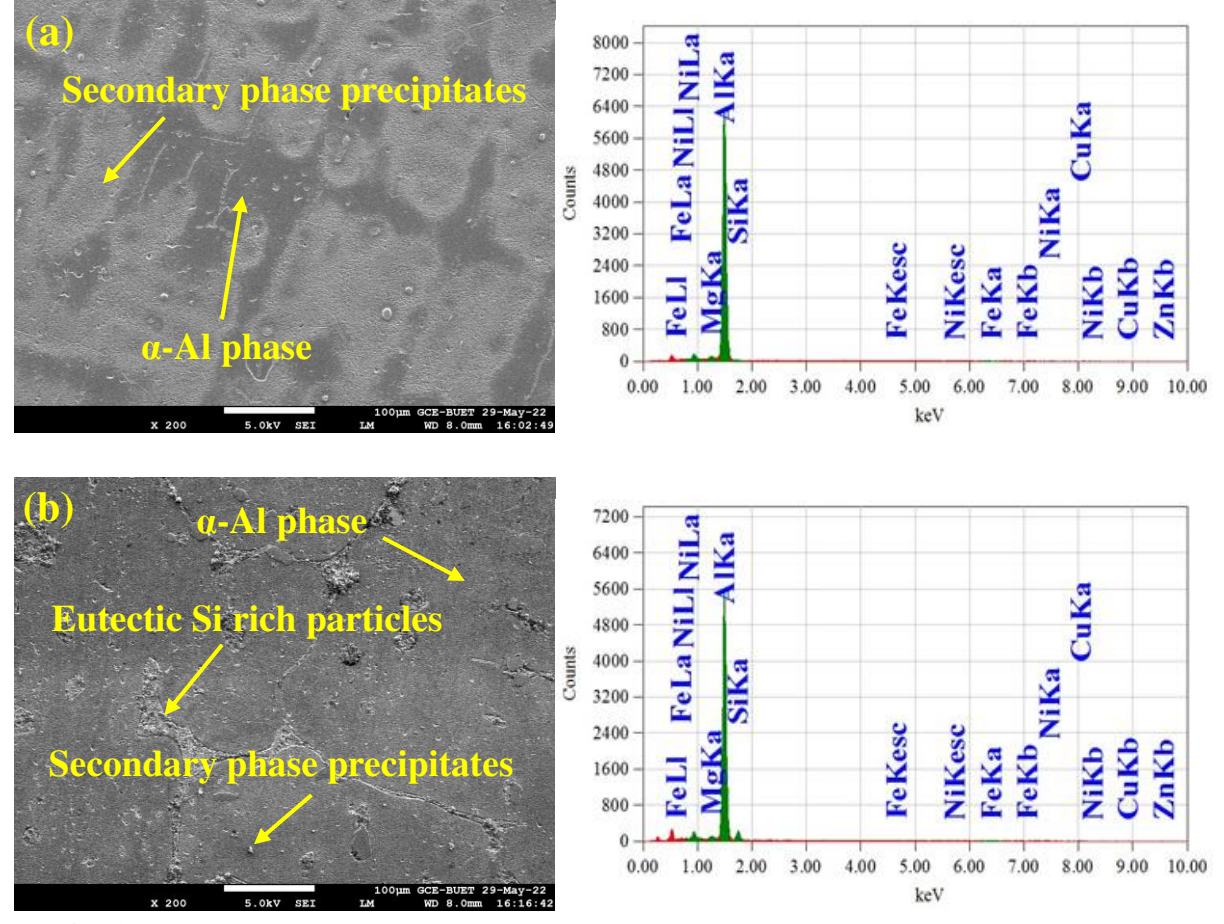


Fig. 10. SEM images of (a) automotive base Alloy 1 and (b) 3.5Si added Alloy 2 ageing treated at 200°C for 150 minutes

Conclusions

The precipitation behavior of low Si doped Al-based automotive alloys is addressed and conclusions can be drawn based on the above investigations:

1. Two consecutive hardening peaks are generated in both the aged alloys. Ageing sequence consists of different phases, but GP zones and the metastable phases are associated to these peaks. The main strengthening phases are θ -Al₂Cu, Q-Al₅Cu₂Mg₈Si₆. The Si rich intermetallics make the difference of strengthening properties when Si is alloyed to this alloy. Adding up of Si showed earlier ageing peaks with higher intensities by its increasing properties of heterogeneous nucleation and diffusion kinetics. The optimum hardness of the alloys can be achieved after aging around at 200 °C for 150 minutes. 2. Electrical resistivity of the alloy increases with Si addition to form the higher Si-rich intermetallics along with others that hinder the movement of electrons and phonons. But it increases throughout ageing for precipitates formation and decrease due to internal stress relieving, metastable phase dissolution and the precipitates coarsening in to the alloys.

The addition of silicon led to more degree of eutectic silicon in the alloy microstructure and makes the grain boundary coarsen. Ageing at 350 °C for 60 minutes, the alloys attain the fully re-crystallized state and consist of equiaxed grains.

References

- 1. Polmear J. Light Alloys-Metallurgy of the Light Metals. 3rd. ed. Arnold; UK; 1995.
- 2. Zhou P, Wang D, Nagaumi H, Wang R, Zhang X, Li X, Zhang H, Zhang B. Microstructural Evolution and Mechanical Properties of Al-Si-Mg-Cu Cast Alloys with Different Cu Contents. *Metals*. 2023;13(1): 1–13.
- 3. Khalikova GR, Zakirova GR, Farkhutdinov AI, Korznikova EA, Trifonov VG. Surface hardening of an Al-Si-Cu-Ni-Mg aluminum alloy by friction stir processing and T6 heat treatment. *Letters on Materials*. 2022;12(3): 255–260.
- 4. Gutkin MY, Skiba NV, Orlova TS. Grain-boundary nanoprecipitates-mediated mechanism of strengthening in Al-Cu-Zr alloy structured by high-pressure torsion. *Materials Physics and Mechanics*. 2022;50(3): 431–438.
- 5. Park SI, Han SZ, Choi SK, Lee HM. Phase equilibria of Al3(Ti, V, Zr) intermetallic system. *Scripta Mater*. 1996;34(11): 1697–1704.
- 6. Kaiser MS, Basher MR, Kurny ASW. Effect of scandium on microstructure and mechanical properties of cast Al-Si-Mg alloy. *J. Mater. Eng. Perform.* 2012;21(7): 1504–1508.
- 7. Davis JR. ASM Specially Handbook, Aluminum and Aluminum alloys. OH, USA: ASM International; 1993.
- 8. Chen F, Liu C, Zuo L, Wu Z, He Y, Dong K, Li G, He W. Effect of thermal exposure on mechanical properties of Al-Si-Cu-Ni-Mg aluminum alloy. *Crystals*. 2023;13(236): 1–12.
- 9. Biswas P, Patra S, Roy H, Tiwary CS, Paliwal M, Mondal MK. Effect of Mn addition on the mechanical properties of Al-12.6Si alloy: Role of Al15(MnFe)3Si2 intermetallic and microstructure modification. *Met. Mater. Int.* 2021;27: 1713–1727.
- 10. Toschi S. Optimization of A354 Al-Si-Cu-Mg alloy heat treatment: effect on microstructure, hardness, and tensile properties of peak aged and overaged alloy. *Metals*. 2018;8(11): 1–16.
- 11. Kaiser MS. Solution treatment effect on tensile, impact and fracture behaviour of trace Zr added Al-12Si-1Mg-1Cu piston alloy. *Journal of the Institution of Engineers (India): Series D.* 2018;99(1): 109–114.
- 12. Nagasaki S, Maesono A. High Temp. High Press. Metals Physics. 1965;11: 182.
- 13. Ding L, Jia Z, Zhang Z, Sanders RE, Liu Q, Yang G. The natural aging and precipitation hardening behaviour of Al-Mg-Si-Cu alloys with different Mg/Si ratios and Cu additions. *Mater. Sci. Eng. A.* 2015;627: 119–126.

- 14. Ghassemali E, Riestra M, Bogdanoff T, Kumar BS, Seifeddine S. Hall-Petch equation in a hypoeutectic Al-Si cast alloy: grain size vs. secondary dendrite arm spacing. *Procedia Eng.* 2017;207: 19–24.
- 15. Kaiser MS. Effect of solution treatment on the age-hardening behavior of Al-12Si-1Mg-1Cu piston alloy with trace-Zr addition. *J. Cast. Mater. Eng.* 2018;2(2): 30-37.
- 16. Mao H, Bai X, Song F, Song Y, Jia Z, Xu H, Wang Y. Effect of Cd on Mechanical Properties of Al-Si-Cu-Mg Alloys under Different Multi-Stage Solution Heat Treatment, *Materials*. 2022;15(15): 1–14.
- 17. Vo NQ, Dunand DC, Seidman DN. Role of silicon in the precipitation kinetics of dilute Al-Sc-Er-Zr alloys. *Mater. Sci. Eng. A.* 2016;677: 485–495.
- 18. Mohamed AMA, Samuel FH. A review on the heat treatment of Al-Si-Cu/Mg casting alloys. London, UK: IntechOpen; 2012.
- 19. Junho OP, Noronha MML, Mello SRS, Oliveira CD. Relationship between Electrical Conductivity and the Stage of the Heat Treatments of Aging and Overaging of the Aluminum Alloy AA2024. *Mater. Sci. Forum.* 2018;930: 400–404.
- 20. Abdelaziz MH, Elgallad EM, Doty HW, Samuel FH. Strengthening precipitates and mechanical performance of Al-Si-Cu-Mg cast alloys containing transition elements. *Mater. Sci. Eng. A.* 2021:820: 1–8.
- 21. Kaiser MS. Effect of trace impurities on the thermoelectric properties of commercially pure aluminum. *Materials Physics and Mechanics*. 2021;47(1): 582–591.
- 22. Hamdi I, Boumerzoug Z, Chabane F. Study of precipitation kinetics of an Al-Mg-Si alloy using differential scanning calorimetry. *Acta Metall. Slovaca*. 2017;23(2): 155-160.
- 23. Chen Z, Liu K, Elgallad E, Breton F, Chen XG. Differential scanning calorimetry fingerprints of various heat-treatment tempers of different aluminum alloys. *Metals*. 2020;10(6): 763.
- 24. Liu M, Wu Z, Yang R, Wei J, Yu Y, Skaret PC, Roven HJ. DSC analyses of static and dynamic precipitation of an Al-Mg-Si-Cu aluminum alloy. *Prog. Nat. Sci.: Mater. Int.* 2015;25(2): 153–158.
- 25. Ahn SS, Pathan S, Koo JM, Baeg CH, Jeong CU, Son HT, Kim YH, Lee KH, Hong SJ. Enhancement of the mechanical properties in Al-Si-Cu-Fe-Mg alloys with various processing parameters. *Materials*. 2018;11(11): 2150.
- 26. Liu K, Cao X, Chen XG. Effect of Mn, Si, and cooling rate on the formation of iron-rich intermetallics in 206 Al-Cu cast alloys. *Metall. Mater. Trans. B.* 2012;43(5): 1231–1240.
- 27. Liu M, Wada T, Suzuki A, Takata N, Kobashi M, Kato M. Effect of annealing on anisotropic tensile properties of Al-12%Si alloy fabricated by laser powder bed fusion. *Crystals*. 2020;10(11): 1007.
- 28. Li L, Zheng Y, Chen Y, Feng J, Li C, Chen L, Zuo L, Zhang Y. Study on microstructure distribution of Al-Cu-Mg alloy in squeeze casting process. *J. Phys. Conf. Ser.* 2022;2338: 012038.

THE AUTHORS

Mohammad Salim Kaiser e-mail: dkaiser.res@iubat.edu

Al-Kabir Hossain 🗓

e-mail: 1610161@me.buet.ac.bd

Effect of industrial hot rolling mode on microstructure and properties of low carbon bainitic steel

Submitted: May 17, 2023

Approved: July 14, 2023

Accepted: August 10, 2023

A.A. Zisman ^{[D] 1,2}, S.N. Petrov ^{[D] 1,2}, N.Yu. Zolotorevsky ^{[D] 2 ⊠}, E.A. Yakovleva ¹

¹ National research center "Kurchatov institute" - Central research institute of structural materials "Prometey",

St. Petersburg, Russia

² Peter the Great St. Petersburg Polytechnic University, St. Petersburg, Russia ⊠ zolotorevsky@phmf.spbstu.ru

Abstract. Slabs of low carbon bainitic steel have been subjected to various modes of fractional hot rolling at fixed conditions of the next direct quenching and tempering. To assess influence of such treatments, microstructures and textures of bainite are determined by EBSD on representative areas and then analyzed with allowance for the resulting mechanical properties. The obtained data reveal a specific effect of hot deformation as far as the tempering does not significantly change crystallographic constitution of the quenched steel. According to the bainite textures, all considered modes lead to deformed states of parent austenite; at the same time, dissimilar types of the transformation product have been detected. Specifically, the softer (granular) bainite appears at higher strains and lower temperatures of the finish rolling stage because the work hardening of austenite increases the transformation temperature. Conversely, the lath bainite providing the maximum steel strength corresponds to properly limited strains of austenite at high enough temperatures.

Keywords: bainitic steels; hot rolling; phase transformation; microstructure; strengthening

Acknowledgements. The authors acknowledge a financial support of this work by the Russian Science Foundation, project No 22-19-00627. Microstructures were studied on the equipment of the Core shared research facilities "Composition, structure and properties of structural and functional materials" of the NRC "Kurchatov Institute" - CRISM "Prometey".

Citation: Zisman AA, Petrov SN, Zolotorevsky NY, Yakovleva EA. Effect of industrial hot rolling mode on microstructure and properties of low carbon bainitic steel. *Materials Physics and Mechanics*. 2023;51(6): 54-64. DOI: 10.18149/MPM.5162023_5.

Introduction

Low carbon bainitic steels are widely used owing to their high strength and fracture toughness, combined with good weldability. At the same time, it is rather hard to control the properties of bainite because volume fractions of its various types depend on the plastic strain of parent austenite and the cooling rate in quenching. Moreover, the problem aggravates since such steels normally undergo the tempering that changes their properties relative to the quenched state. These issues complicate development of industrial technologies in general and become crucial in case of thick semi-products where both the strain and cooling rate are particularly non-uniform. To analyze effects of them, various combinations of hot deformation and quenching have been applied on thermo-mechanical simulators [1–3] and rolling mills [4–6]. The present paper aims to isolate specific influence of the hot rolling modes at fixed conditions of the direct quenching

and subsequent tempering. The last two operations and varied rolling parameters are relevant to industrial treatments of the considered steel.

Higher strain degrees and lower rolling temperatures, which retard both the recovery and recrystallization of austenite, generally result in increase of the transformation temperature and hence in softer bainite of granular morphology [1,2,7–9]. Conversely, the stronger lath bainite appears at lower temperatures if the parent phase undergoes weaker hardening due to less strains or/and higher rolling temperature [8,9]. However, to make use of this regularity, the quenching should be sufficiently rapid [1] as is the case in the present work. As to the tempering that diminishes the dislocation density and results in some redistribution of carbon, corresponding effects on the crystallographic constitution of bainite [10] are usually insignificant so that EBSD can reveal microstructures of the *quenched* state.

Based on EBSD orientation data, several mutually complimentary methods are employed to characterize the material state. Thus, along with the microstructure, the texture of steel can be determined. Unlike the XRD method that derives the orientation distribution function (ODF) from a number of *incomplete* pole figures, EBSD immediately expresses this function in terms of measurement results at periodically arranged discrete points. Respective complete pole figures comply with those obtained by XRD technique [11] and are often more distinct since the underlying ODF is derived from a greater set (up to 10⁶) of orientations. At the same time, the opinion is spread that *representativeness* of EBSD data is inferior to that of XRD. To get proper results while avoiding a formal analysis of this issue, we employ a rather large EBSD area covering several hundreds of prior grains and the scanning step providing in each of them thousands of measurement points.

In case of bainitic or martensitic steels, which have pronounced orientation relationships (OR) between the parent and product phases, the transformation texture enables assessment of the parent austenite state because its rolling and recrystallization textures significantly differ. A simple way to recognize them [12,13] is to make use of approximate similarity between $(111)_{\gamma}$ and $(110)_{\alpha}$ pole figures. Whether reference [14–16] or measured OR are used, parallelism of these crystal planes is kept with accuracy of about one degree. At the same time, to properly distinguish between various bainite types by means of coupling statistics for admitted OR variants [17–19], a specific inter-phase relationship of any steel is needed. Following [20], each OR used in the present work is fitted to the interfacial misorientations in the final structure. Such an approach avoids errors caused by non-uniformity of deformation in prior grains and highly facilitates computations.

Apart from EBSD orientation maps, steel microstructures can be specified by respective distributions of crystal curvature (orientation gradient) that depends on the dislocation density and hence local phase constituents [10,21–23]. Among popular curvature measures [24], the grain average misorientation (GAM) is most convenient in analyzing the transformation products as far as it treats *whole* structural elements separated by closed interfaces. To properly draw the latter, their tolerance angle θ_t should correspond to the least inter-variant misorientation of the employed OR. It is worth noting that such a non-local estimate is relevant to the average density of lattice dislocations [25] rather than their "geometrically necessary" agglomerations with a net Burgers vector forming low-angle boundaries. This simplification is wittingly used in the present paper because the main contribution to strength of lath bainite or martensite is provided by the bulk dislocation density [26,27].

Materials and Methods

Chemical composition of the considered steel (wt. %: 0.08C, 0.21Si, 0.34Mn, 2.5(Ni+Cu), 0.59(Cr+Mo), 0.034V, 0.004Nb) ensures its mostly bainitic structures by quenching in a wide range of cooling rates. Three slabs of 300 mm thickness were reheated to 1200 °C and hot rolled on a reversing mill. Plates subjected to various rolling modes were directly quenched in a

sprinkler installation at the same final thickness of 18 mm and then tempered for 8.5 hours at 645 °C.

Analyzed sections normal to the transversal direction (TD) were prepared by the usual metallographic procedures and then subjected to electrolytic polishing in perchloric acidethanol solution at 0 °C. EBSD over areas of 2.25 mm² with a scanning step of 1 μ m was implemented on SEM Lyra 3-XMH at an accelerating voltage of 20 kV. Crystal orientations were determined by Channel 5 software. Based on the obtained data, bainite textures have been determined by means of MTEX software and then used following [28] to reconstruct textures of parent austenite. To image morphology of bainite by the band contrast (BC), smaller areas are rescanned with a step of 0.1 μ m. The related orientation data are employed to assess crystal curvature in individual laths and derive OR from inter-lath misorientations [20]. The coupling statistics for admitted variants of each specific OR is assessed on the section plane according to length fractions of respective interfaces revealed with angular accuracy of one degree.

Table 1. Hot rolling modes and respective mechanical properties of quenched and tempered steel

		Conditions of the last five passes					
Rolling mode	Number of passes	Average temperature, °C	Average thickness reduction, %	Accumulated thickness reduction, %	YS, MPa	UTS, MPa	Reduction in area, %
A	16	913	16	58	610	690	82
В	18	977	14	53	630	710	80
С	22	953	11	44	670	720	80

Table 1 lists whole numbers of rolling passes for the three applied modes and characteristics of finish rolling stages as well as resulting mechanical properties of steel (yield stress, ultimate tensile strength and reduction in area prior to fracture) determined by standard tests. First, relative thickness reductions at the last five passes are expressed by

$$\delta_i = (H_{i-1} - H_i)/H_{i-1} \tag{1}$$

at i=N-4, N-3, ..., N where N is the whole number of passes. The table represents average values of these δ_i and of related temperatures as well as the relative thickness reduction accumulated during the last passes:

$$\Delta = (H_{N-5} - H_N)/H_{N-5}. \tag{2}$$

It is meaningful that arrangement of steel properties follows strain degrees rather than respective temperatures. As expected, less deformed austenite results in stronger bainite.

Note that the specific allowance for the finish rolling stage is motivated by two reasons. First, owing to higher temperatures of the previous passes gradually diminishing from 1200°C, the softening of austenite by its recovery or/and recrystallization in inter-pass pauses weakens influence of related deformations on the final steel properties. That is why the hot rolling mode is often specified by the least FRT (finish rolling temperature) [5,6]. In this regard, our consideration of the last five passes refines the analysis. Second, the whole complex mode is problematic to quantify by few parameters as far as averaging over too wide ranges of temperature and strain would be hardly relevant physically.

Results

Bainite microstructures and textures by EBSD. Orientation distributions at the considered rolling modes are conventionally represented in Fig. 1 by colors corresponding to TD with respect to a standard triangle of the inverse pole figure (IPF). Each of these maps demonstrates performance of EBSD on a large (2.25 mm²) area that covers about a thousand of prior grains and presumably provides the representative texture. However, such images cannot properly

display bainite microstructures because the employed scanning step exceeds their fine scale to reasonably limit time of the data acquisition. To refine analysis as shown in inserted fragments, smaller domains have been rescanned with a step of $0.1 \, \mu m$.

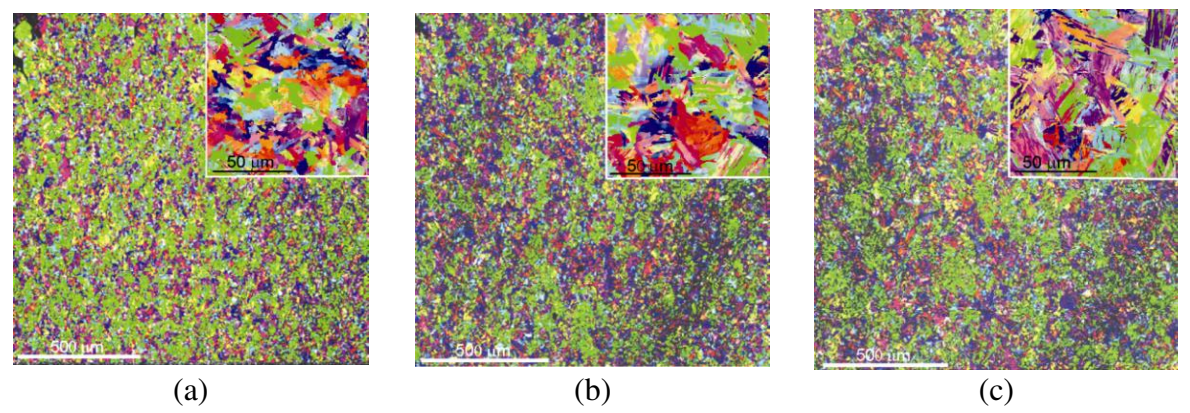


Fig. 1. Orientation (IPF) maps of large areas of bainite corresponding to hot rolling modes A (a), B (b) and C (c). Inserts show microstructures revealed on small areas with a finer scanning step

Figure 2 provides higher magnification of bainite microstructures by means of BC maps also derived with the refined scanning step. It is worth noting that such maps are sensitive to crystal imperfections and hence perfectly substitute metallographic images usually obtained by the chemical etching. As expected, the most pronounced lath morphology of the transformation product corresponds to the least deformed austenite (mode C) whereas the strongest work hardening of the parent phase (mode A) leads to predominance of granular bainite peculiar to higher transformation temperatures.

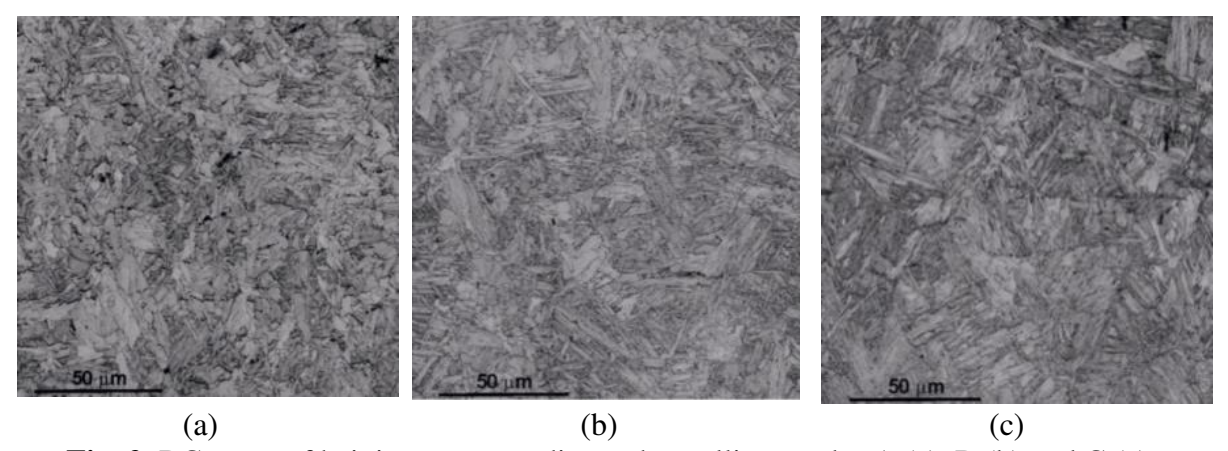


Fig. 2. BC maps of bainite corresponding to hot rolling modes A (a), B (b) and C (c)

Pole figures $(110)_{\alpha}$ of bainite close to $(111)_{\gamma}$ ones observed in the parent phase deformed by rolling [12] are shown in Fig. 3 where RD and TD conventionally indicate the rolling and transverse directions. Owing to the least temperatures and maximum thickness reductions, mode A results in strong components of the rolling texture which become notably weaker at modes B and C. At the same time, with respect to B, the latter texture somewhat sharpens. This effect wants explanations since it takes place at the minimum thickness reductions of austenite (Table 1) which expectedly lead to the high strength and lath morphology of the product phase. As will be discussed in the next section, the texture and hardening of austenite may not ideally correlate as far as they differently depend on deformation conditions.

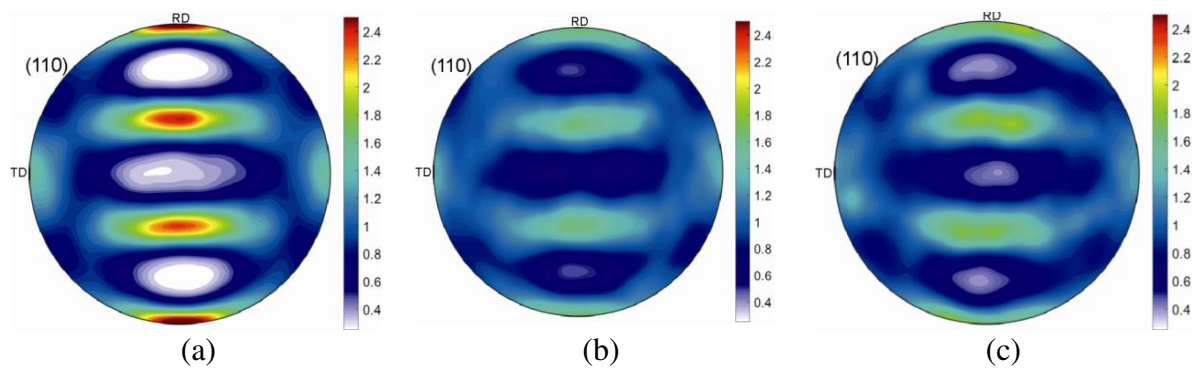


Fig. 3. Pole figures $(110)_{\alpha}$ for bainite textures corresponding to hot rolling modes A (a), B (b) and C (c)

To refine analysis, characteristic ODF sections (ϕ_2 =45°) are represented in Fig. 4. In all, they comply with the above-considered arrangement of rolling modes in strength of related textures except for a red spot at mode B. As considered in the next subsection, such maximums of probability density, as well those at the upper right corner can appear from either parent cube component due to recrystallization of austenite or the brass component of its rolling texture. To exclude this uncertainty, the parent textures reconstructed from those of bainite will be further analyzed. With the inter-phase OR kept in mind [13], Fig. 4 evidence for predominance of the "transformed brass component" [13], though signs of the "transformed copper component" are also displayed at modes A and, somewhat weaker, at C. It should be remarked as well that at mode C several features of the transformed brass in the bainite texture differ from those of mode B.

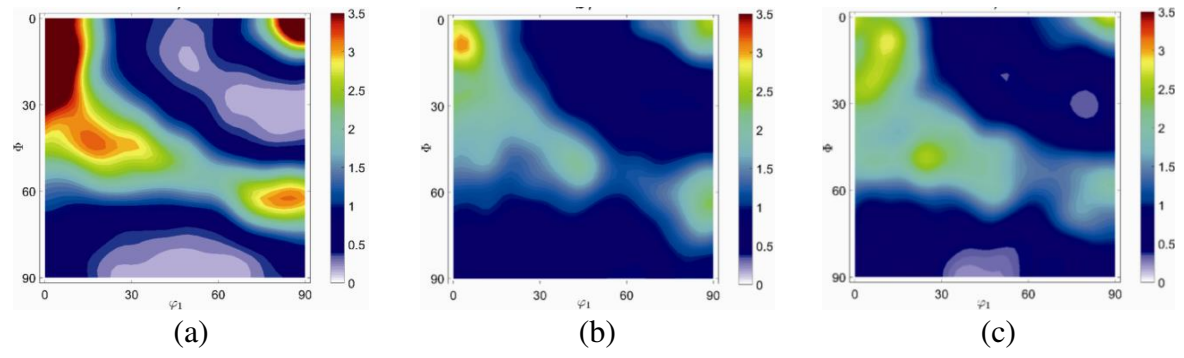


Fig. 4. Bainite ODF sections (ϕ_2 =45°) corresponding to hot rolling modes A (a), B (b) and C (c)

To reveal the coupling statistics for admitted variants of whatever OR, the latter should be properly determined first. Specifically derived following [20] at the considered rolling modes, resulting OR are represented in Fig. 5(a) by the inter-phase angles between close packed planes $(111)_{\gamma}$ & $(110)_{\alpha}$ and directions $[110]_{\gamma}$ & $[111]_{\alpha}$ further called CPP and CPD, respectively. According to the last quoted work, the OR very close to that by Greninger & Troyano [15] at mode C corresponds to lath bainite whereas other two are relevant to the granular morphology of this phase.

The least inter-variant angle corresponding to each of the considered OR is about five degrees; therefore, we will carefully employ $\theta_t = 4^{\circ}$ to allow for real accuracy of measured orientations while ignoring smaller inter-lath angles within any single block (variant) of bainite. The same θ_t will be used to draw closed interfaces in determination of GAM. Coupling spectra for admitted variants of OR are shown in Fig. 5(b-d) with respect to an arbitrarily selected variant V_1 where the dashed lines indicate the average probability of considered pairs. With the

reference data [17] kept in mind, these bar charts confirm the above-mentioned microstructure types. Indeed, predominance of couples V_4/V_1 and V_8/V_1 at modes A and B evidences for granular morphology of bainite, that is, its formation at higher temperatures, whereas the strongest V_2/V_1 at mode C is characteristic of low-temperature lath bainite.

To sum up the above-considered results, the growth of steel strength with the weakened hardening of parent austenite complies with the transition from the granular to lath morphology of bainite.

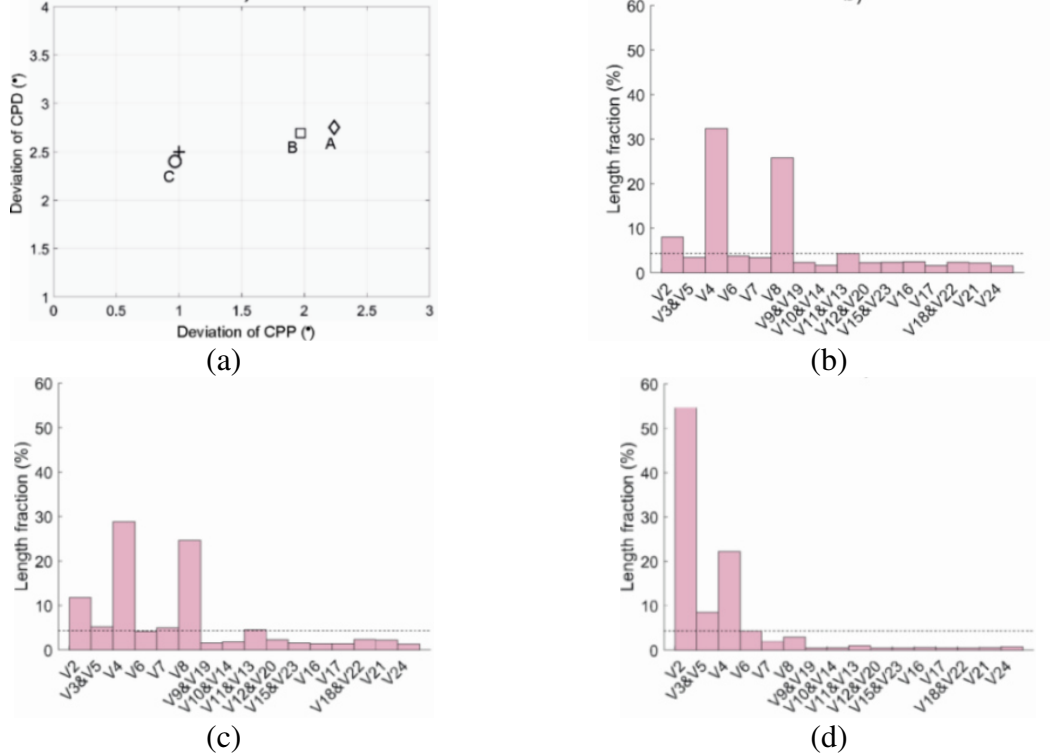


Fig. 5. (a) Inter-phase deviations of CPP and CPD for various OR corresponding to hot rolling modes A, B and C; a cross indicates the Greninger-Troyano relationship. Respective spectra in (b-d) show statistics of variant coupling with allowance for specific OR

The revealed regularity is additionally illustrated in Fig. 6 by appearance of OR variant coupling where high-angle V_2/V_1 boundaries expectedly predominate at mode C according to Fig. 5 and previous BC maps (Fig. 2).

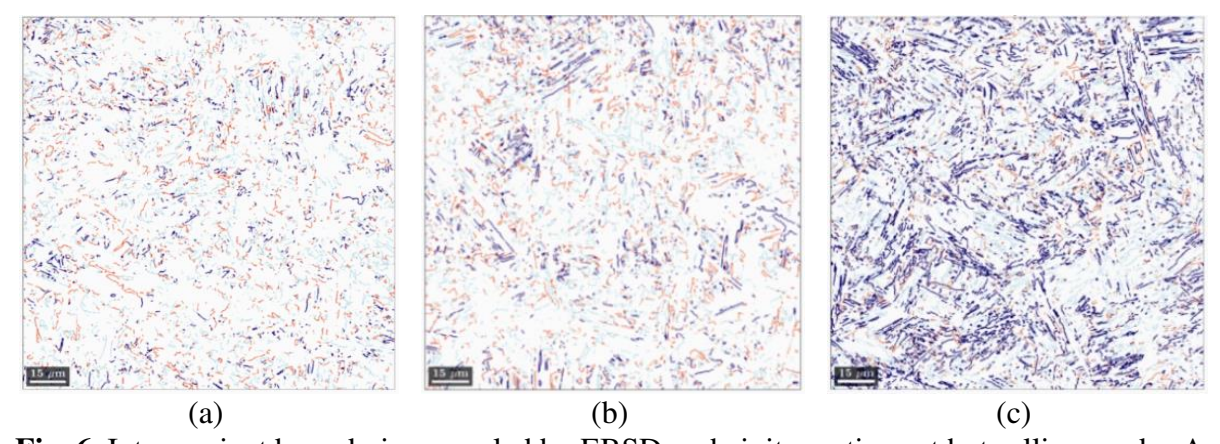
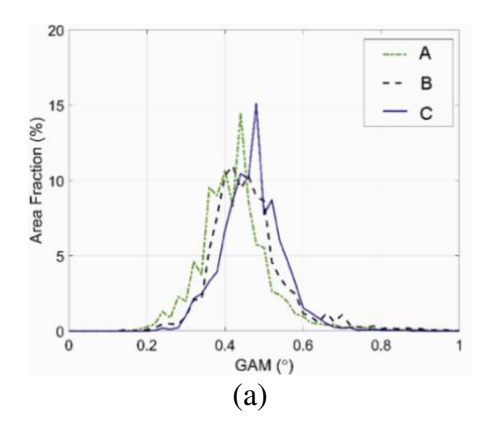


Fig. 6. Inter-variant boundaries revealed by EBSD on bainite sections at hot rolling modes A (a), B (b) and C (c). Blue, cyan and red correspond to couples V_2/V_1 , V_4/V_1 and, V_8/V_1

GAM spectra of bainite corresponding to applied hot rolling modes are shown in Fig. 7(a), and the bar chart in Fig. 7(b) represents respective yield stresses and average GAM values. The two characteristics naturally prove to change in the same order. However, the former most strongly increases at mode C whereas the latter notably grows at mode B and then only slightly changes. In more detail, this difference related to the combined influence of dislocation density and morphology of bainite will be discussed after.



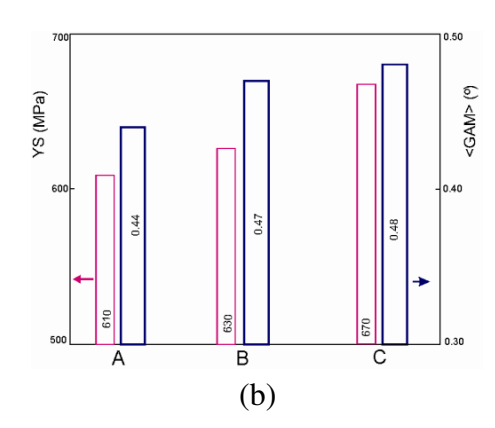


Fig. 7. (a) Spectra of GAM in bainite at the three hot rolling modes; (b) bar chart for respective yield stresses and average values of GAM

Reconstructed textures of parent austenite. Figure 8 represents pole figures $(111)_{\gamma}$ corresponding to the reconstructed ODF of parent austenite which satisfactorily comply with their $(110)_{\alpha}$ counterparts in bainite (Fig. 3) determined by EBSD. Thus, the rolling texture at mode A is very strong as compared to those of B and C, the latter of the two being somewhat sharper with respect to B.

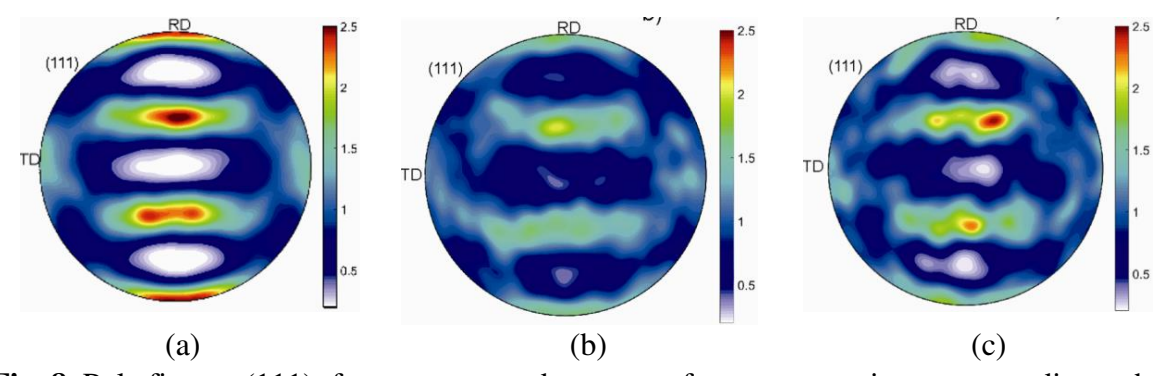


Fig. 8. Pole figures $(111)_{\gamma}$ for reconstructed textures of parent austenite corresponding to hot rolling modes A (a), B (b) and C (c)

The ODF sections for bainite (Fig. 4) are supported by respective sections for the parent phase shown in Fig. 9. They display the brass components of rolling texture (middle parts of $\Phi = 90^\circ$ sides) at all considered modes as well as the copper components ($\phi_1 \approx 90^\circ$, $\Phi \approx 30^\circ$) at modes A and, to less degree, C. Besides, positions of the ODF maximums at ($\Phi \approx 0$, $\phi_1 \approx 45^\circ$) in Fig. 9(a,b) reveal the cube component indicative of austenite recrystallization [13], which could *partly* transform in the maximums at upper corners of Fig. 4(a,b). However, in case of mode A this component is rather weak with respect to the pronounced brass that apparently was the main origin of such maximums. As to mode B, the *integrated* cube probability and hence the related volume fraction are still relatively small so that even in this case the two discussed features of bainite are mostly transformed from the rolling (brass) component of parent texture.

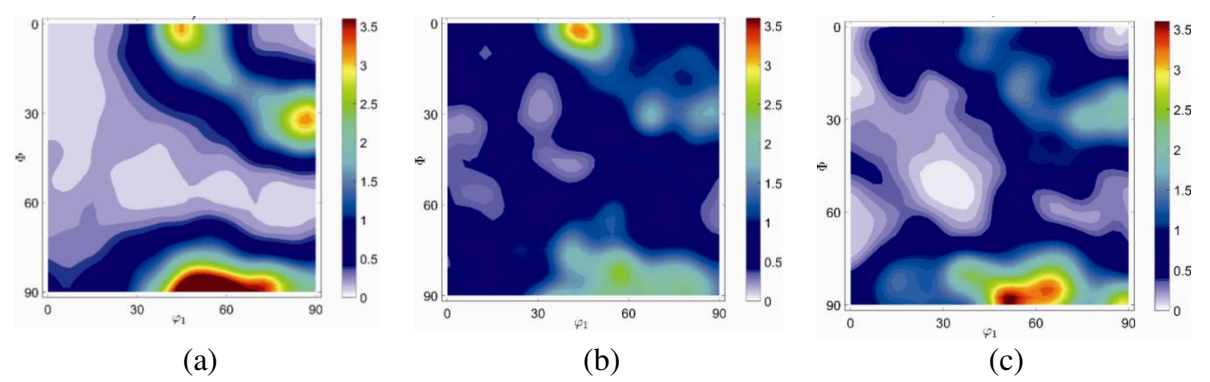


Fig. 9. Reconstructed ODF sections (ϕ_2 =45°) of parent austenite corresponding to hot rolling modes A (a), B (b) and C (c)

Discussion

The present results indicate that strength of low carbon bainitic steel at various finish modes of hot rolling mostly depends on thickness reductions rather than respective temperatures. Variations of the latter *in the considered range* do not affect this regularity although somewhat influence recrystallization of parent austenite and hence its texture. In particular, with respect to mode B, the texture of bainite observed at mode C proves to be sharper and seemingly suggests stronger hardening of austenite and, as a result, softer bainite. However, the lath morphology and higher strength of the transformation product contradict to this assumption. To discuss such a paradox, we will recollect results of the previous experiments [29] on a thermomechanical simulator where the kinetics of *static* recrystallization in the parent phase of similar steel has been recorded at various pre-strains and temperatures. Besides, as shown in the same work, the usual conditions of fractional hot rolling exclude *dynamic* recrystallization which requires an unrealistically high thickness reduction per pass.

According to [29], at an inter-pass time lapse up to 15 s the considered stages of modes A and B admit only *incomplete* recrystallization involving a minor austenite fraction, whereas mode C completely excludes this phenomenon because of insufficient partial strains. Although Table 1 describes five rolling passes rather than a single thickness reduction employed in the above-mentioned experiments, the same regularity is supported by the reconstructed ODF sections of parent austenite. Indeed, the cube component ($\Phi \approx 0$, $\phi_1 \approx 45^{\circ}$) appears in Fig. 9 only at modes A and B, being stronger at the latter owing to higher temperature. However, since the most part of material avoids recrystallization, the average hardening degrees in both cases should exceed that of mode C with minimum strains per pass.

Although final mechanical properties expectedly depend on strains accumulated during finish rolling stages, a question appears of why the textures corresponding to modes B and C so drastically weaken with respect to mode A (Figs. 3 and 8). This behavior may be ascribed to whether lower thickness reductions or higher temperatures as well as to their combined influence. However, to quantify the texture development in hot deformation of the *parent* phase is a very hard problem that wants special efforts beyond the scope of this work.

The reconstruction method [28] deserves a special remark as follows. Though it is mostly used to restore parent austenite structures, the corresponding textures can be also determined as demonstrated in the present work. Moreover, in the authors' opinion, this approach is generally more reliable when assessing states of the parent phase in cases, when the latter is not recrystallized. Indeed, both non-uniform deformations of prior grains and some inaccuracy of measured orientations significantly complicate the *local* structure reconstruction, whereas related random errors should be averaged out by an *overall* texture extracted from a representative EBSD scan.

Another interesting issue is the correlated growth (Fig. 7b) of average GAM and yield stress (YS) presumably dependent on dislocation density ρ according to Taylor ($\sigma \sim \rho^{\frac{1}{2}}$, [30]). This finding should be analyzed because the most distinct increases of the two characteristics take place at dissimilar rolling modes. One can suggest that the growth of bainite $\langle GAM \rangle$ at mode B results from the softening of parent austenite at higher temperatures, whereas the increasing YS at mode C is related to the significant lath refinement, that is, the Hall-Petch mechanism of hardening. As shown in [26], when the lath thickness diminishes to less than 1 μ m, the size effect weakens and the yield stress variations can be attributed to those of dislocation density as well as solid solutions, disperse carbides and carbon atmospheres at dislocations. However, at very small fractions of carbon, as is the case for our steel, the latter three factors prove to be less significant whereas Taylor's equation becomes relevant to the main component of bainite strength. That is why it would be desirable to facilitate assessment of dislocation density in refined lath structures by making use of EBSD data as follows.

The elastic rotation field of a single dislocation is inversely proportional to distance [31] so that randomly distributed (mutually screened) dislocations with characteristic spacing L will result in the average level of crystal curvature almost linearly dependent on $\rho^{\frac{1}{2}} \approx 1/L$. Therefore, <GAM> should be roughly proportional to $\rho^{\frac{1}{2}}$, that is, the dislocation component of yield stress predominating at thin laths peculiar to lower transformation temperatures. Let alone convenience of panoramic EBSD method, it will be superior to TEM in representativeness of thus evaluated ρ and, unlike XRD, can apply to various structural scales. Of course, the corresponding estimates of dislocation density should be verified by conventional techniques [32]. Note that EBSD data are often used to quantify geometrically necessary dislocations which form low-angle boundaries and other agglomerations of Burgers vector. This is not the case in the proposed method aimed at the bulk dislocation density of any lath *as a whole*. A low tolerance angle ($\theta_t < 4^\circ$) for boundaries and small thickness of the laths seem to be proper reasons to ignore their inhomogeneity in the first approximation.

Conclusion

Textures and microstructures of low carbon bainitic steel have been analyzed by EBSD for various finish modes of industrial hot rolling at the same conditions of direct quenching and subsequent tempering. Although all these modes strongly decelerate or exclude recrystallization of parent austenite, the mechanical properties of steel mostly dependent on accumulated strains significantly vary. The considered data lead to the following findings:

- 1. To get the lath bainite providing the maximum steel strength, the thickness reduction accumulated during the finish rolling stage should be properly limited. Thus, for example, such a reduction by the last five passes of mode C did not exceed 45 %.
- 2. The overall texture of bainite determined on an appropriately large EBSD scan enables accurate reconstruction of the parent texture and hence assessment of austenite state prior to the steel quenching.
- 3. Observed at the applied hot rolling modes of low carbon steel, a correlation between its yield stresses and *average* levels of crystal curvature apparently suggests a simple way to assess the bulk dislocation density of lath bainite in terms of EBSD data.

References

- 1. Zhao H, Palmiere EJ. Influence of cooling rate on the grain-refining effect of austenite deformation in a HSLA steel. *Materials Characterization*. 2019;158: 109990.
- 2. Panpurin SN, Zolotorevsky NY, Titovets YF, Zisman AA, Khlusova EI. Crystallographic features of low-carbon bainite formed under non-isothermal conditions. *Materials Science Forum*. 2013;762: 110-115.

- 3. Kumar S, Manda S, Giri SK, Kundu S, Karagadde S, Balamuralikrishnan R, Murty SVSN, Anoop CR, Samajdar I. Relating martensite variant selection with prior austenite microstructure: A coupled study of experiments and pixel-by-pixel reconstruction. *Materials Characterization*. 2023;199: 112822.
- 4. Kaijalainen A, Javaheri V, Lindell D, Porter DA. Development of crystallographic texture under plane and shear strain in ultrahigh-strength strip steels. *Materials Science and Engineering A.* 2018;375: 012026.
- 5. Bernier N, Bracke L, Malet L, Godet S. Crystallographic reconstruction study of the effects of finish rolling temperature on the variant selection during bainite transformation in C-Mn high-strength steels. *Metallurgic and Materials Transactions A*. 2014;45: 5937–5955.
- 6. Wang H, Chen Y. The effect of finish rolling temperature on the microstructure and properties of non-quenched and tempered bainite steel. *Procedia Engineering*. 2017;207: 1839–1843.
- 7. Cizek P, Wynne BP, Davies CHJ, Muddle BC, Hodgson PD. Effect of composition and austenite deformation on the transformation characteristics of low-carbon and ultralow-carbon microalloyed steels. *Metallurgic and Materials Transactions A*. 2002;33: 1331–1349.
- 8. Lan L, Yu M, Qiu C. On the local mechanical properties of isothermally transformed bainite in low carbon steel. *Materials Science and Engineering A*. 2019;742: 442–450.
- 9. De-Castro D, Eres-Castellanos A, Vivas J, Caballero FG, San-Martín D, Capdevila C. Morphological and crystallographic features of granular and lath-like bainite in a low carbon microalloyed steel. *Materials Characterization*. 2022;184: 111703.
- 10. Zisman AA, Zolotorevsky NYu, Petrov SN, Khlusova EI, Yashina EA. Panoramic crystallographic analysis of structure evolution in low-carbon martensitic steel under tempering. *Metal Science and Heat Treatment*. 2018;60: 142–149.
- 11. Eres-Castellanos A, Morales-Rivas L, Jimenez JA, Caballero FG, Garsia-Mateo C. Effect of ausforming on the macro- and micro-texture of bainitic microstructures. *Metallurgic and Materials Transactions A*. 2021;52: 4033.
- 12. Brown EL, Deardo AJ. On the origin of equiaxed austenite grains that result from the hot rolling of steel. *Metallurgic and Materials Transactions A*. 1981;12: 39–47.
- 13. Jonas JJ. Transformation textures associated with steel processing. In: Haldar A, Suwas S, Bhattacharjee D. (eds.) *Microstructure and Texture in Steels*. New York: Springer; 2009; p.3–17.
- 14. Kurdjumov G, Sachs Z. Uber den machanismus der stahlhartung. *Zeitschrift für Physic*. 1930; 64: 325–343.
- 15. Greninger AB, Troyano AR. The mechanism of martensite formation. *Metals Transactions*. 1949; 185: 590–598.
- 16. Nishiyama Z. Lattice distortion and atomic displacements during the fcc/bcc martensitic transformation. *Scientific Reports of the Tohoku Imperial University*. 1932;3: 637–644.
- 17. Miyamoto G, Iwata N, Takayama N, Furuhara T. Quantitative analysis of variant selection in ausformed lath martensite. *Acta Materialia*. 2012;60(3): 1139–1148.
- 18. Takayama N, Miyamoto G, Furuhara T. Effects of transformation temperature on variant pairing of bainitic ferrite in low carbon steel. *Acta Materialia*. 2012;60(5): 2387–2396.
- 19. Stormvinter A, Miyamoto G, Furuhara T, Hedström P, Borgenstam A. Effect of carbon content on variant pairing of martensite in Fe–C alloys. *Acta Materialia*. 2012;60(20): 7265–7274.
- 20. Zolotorevsky NY, Panpurin SN, Zisman AA, Petrov S.N. Effect of ausforming and cooling condition on the orientation relationship in martensite and bainite of low carbon steels. *Materials Characterization*. 2015;107: 278–282.
- 21. Adams BL, Wright SI, Kunze K. Orientation imaging: The emergence of a new microscopy. *Metallurgic and. Materials Transactions A.* 1993;24: 819–831.
- 22. Tomaz RF, Santos DB, Camey K, Barbosa R, Andrade MS, Escobar DP. Complex phase quantification methodology using electron backscatter diffraction (EBSD) on low manganese

high temperature processed (HTP) microalloyed steel. *Journal of Materials Research and Technology*. 2022;8(2): 2423–2431.

- 23. Breumier S, Ostormujof TM, Frincu B, Gey N, Couturier A, Loukachenko N, Aba-perea PE, Germain L. Leveraging EBSD data by deep learning for bainite, ferrite and martensite segmentation. *Materials Characterization*. 2022;186: 111805.
- 24. Wright S, Nowell M, Field D. A review of strain analysis using electron backscatter diffraction. *Microscopy and Microanalysis*. 2011;17: 316–329.
- 25. Zisman AA, Zolotorevsky NY, Petrov SN, Ermakova NY. Effect of cooling rate on the bainite fraction in low carbon martensitic steel: combined analysis of transformation kinetics and crystal curvature. *Letters on Materials*. 2023;13: 67–72.
- 26. He SH, He BB, Zhu KY, Huang MX. On the correlation among dislocation density, lath thickness and yield stress of bainite. *Acta Materialia*. 2017;135: 382–389.
- 27. Kennett SC, Krauss G, Findley KO. Prior austenite grain size and tempering effects on the dislocation density of low-C Nb–Ti microalloyed lath martensite. *Scripta Materialia*. 2015;107: 123–126.
- 28. Niessen F, Nyyssonen T, Gazder AA, Hielscher R. Parent grain reconstruction from partially or fully transformed microstructures in MTEX. *Journal of Applied Crystallograhy*. 2022;55: 180–194.
- 29. Knyazyuk TV, Novoskoltsev NS, Zisman AA, Khlusova EI. Influence of niobium microalloying on the kinetics of static and dynamic recrystallization during hot rolling of medium-carbon high-strength steels. *Inorganic Materials: Applied Research*. 2020;11: 1325–1332.
- 30. Taylor GI. The mechanism of plastic deformation of crystals. Part I. *Proceedings of the. Royal Society of London*. 1934;145: 362–387.
- 31. de Wit R. Theory of disclinations: IV. Straight dislocations. *Journal of Research of the National Bureau of Standards*. 1973;77A: 607–658.
- 32. Gallet J, Perez M, Guillou R, Ernoud C, Le Bourlot C, Langlois C, Beausir B, Bouzy E, Chaise T, Cazottes S. Experimental measurement of dislocation density in metallic materials: A quantitative comparison between measurements techniques (XRD, ECCI, HR-EBSD, TEM). *Materials Characterization*. 2023;199: 112842.

THE AUTHORS

Zisman A.A. (D)

e-mail: crism ru@yahoo.co.uk

Zolotorevsky N.Yu. 🗓

e-mail: zolotorevsky@phmf.spbstu.ru

Petrov S.N. (D)

e-mail: petrov.epma@mail.ru

Yakovleva E.A.

e-mail: mail@crism.ru

Electronic, magnetic properties and pressure-induced phase transition of new $D0_{19}$ Fe₂MnSn Heusler alloy

Submitted: January 5, 2023

Approved: May 2, 2023

Accepted: May 15, 2023

I. Bouhamou, H. Abbassa, C. Abbes, A. Boukortt, E.H. Abbes [™], A. Benbedra

Abdelhamid Ibn Badis University-Mostaganem, Mostaganem, Algeria

☐ habib.abbes.etu@univ-mosta.dz

Abstract. Using ab-initio calculations based on density functional theory (DFT) with the generalized gradient approximation (GGA), structural, electronic and magnetic properties of Fe₂MnSn full Heusler alloy are calculated within the framework to describe the effect of hydrostatic stress. The total system energy optimization indicates that the ground state corresponds to the hexagonal (D0₁₉) structure in ferromagnetic (FM) state. The compound undergoes a structural stress-induced phase transitions under pressure of 7 GPa. The total magnetic moment at the optimized lattice parameters is found 7.19 μ B, which does not follow the Slater-Pauling rule. The material tends to rapidly lose its spin polarization under 10 GPa hydrostatic stress.

Keywords: Full Heusler; electronic; magnetic; FP-LAPW calculations

Acknowledgements. This work is supported by the Algerian national research projects, PRFU/DGRSDT/MESRS-Algeria (project N° B00L02UN270120220001).

Citation: Bouhamou I, Abbassa H, Abbes C, Boukortt A, Abbes EH, Benbedra A. Electronic, Magnetic Properties and Pressure-induced Phase Transition of New D0₁₉ Fe₂MnSn Heusler Alloy. *Materials Physics and Mechanics*. 2023;51(6): 65-75. DOI: 10.18149/MPM.5162023_6.

Introduction

The search for new materials with specific physical properties is a major challenge for today's industry, depending on the field of application considered (spintronics, energy, materials, ...). In our era, simulation makes possible to explore various properties in the quantum domain such as the structural, electronic and even dynamic properties of matter, often far from any experimental knowledge of the system studied. Ab-initio methods currently have the ability to perform calculations with great precision for different quantities [1–16], such as elasticity, optical spectra, lattice vibration frequencies, etc. Today, spin electronics is looking for new materials and technological challenges that condition the realization of new devices. In many study subjects, Heusler alloys attract the interest of physicists of solid-state for their remarkable physical and magnetic properties, which are frequently encountered [17,18]. More than 3000 Heusler compounds have been discovered to be used in many fields [19] such as the domain of electronic and magnetic technologies (giant magnetoresistance (GMR) [20,21], tunnel magnetoresistance (TMR) [22], and others). It is a family of materials that affects several fields of application such as spintronic [23], superconductivity [24], shape memory alloys (SMA) [25,26] and other fields. The first prototype of Heusler alloy was discovered by Heusler Friedrich in 1903 [27], where it was possible to make magnetic alloys from non-magnetic components. Later, its crystal structure was determined by Bradley and Rodgers in 1934 [28].

Heusler alloys were classified as ternary ferromagnetic compounds with the chemical formula X_2YZ [29,30] where X and Y are transition metals and Z the main group element. Where X atoms occupy the Wyckoff positions (1/4,1/4,1/4) and (3/4,3/4,3/4) while the Y and Z atoms are in positions (1/2,1/2,1/2) and (0,0,0) respectively, in the cubic structure with the space group $Fm\overline{3}m$ (SG 225) according the prototype Cu₂MnAl, often noted (L2₁) [31,32].

This crystallographic structure can be sometimes distorted to a tetragonal structure (D0₂₂) [33] under the band Jahn-Teller effect. Another cubic structure is often observed in these alloys, known us the inverse structure (noted XA) where X atoms are located in different environments. Recently, a new hexagonal structure has been confirmed as the ground state structure for some Heusler alloys, this crystallographic structure (D0₁₉) has been derived from the Ni₃Sn prototype structure with the space group P6₃/mmc [34], where the chemical formula X_3Z is transformed to X_2YZ , by the substitution of one of X atoms with another transition metals Y. Non-cubic Heusler compounds used Fe₂MnSn may exhibit large magneto crystalline anisotropy [35], which gives them a special importance, it is a necessary condition for hard magnetic applications [36,37]. Motivating by this property, we have investigated the hexagonal D0₂₂ Heusler alloy Fe₂MnSn, which shows a high total magnetic moment (about 7 μ_B /f.u). The studied compound was synthesized experimentally [35], we note that our theoretical calculations showed that both cubic and hexagonal phases of Fe₂MnSn Heusler alloy are energetically very close.

In the present work, we focus our study on both electronic and magnetic properties of the Fe₂MnSn full-Heusler compound. In addition, we carry out a detailed study about the pressure induced phase transition of the new $D0_{19}$ structure (Fig. 1), and we discuss the anomalies of this specific Heusler material.

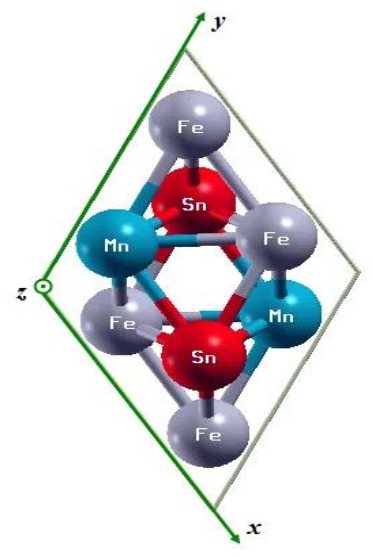


Fig. 1. D0₁₉ structure for Fe₂MnSn full-Heusler alloy

Computational method

In this study, electronic and magnetic structures calculations were performed using the FP-LAPW method (self-consistent full-potential linearized augmented plane wave) [38,39], this method was integrated into the WIEN2K code simulation [40,41] within the DFT (density functional theory) [42]. For the exchange-correlation correction, it used the GGA-PBE approximation (generalized gradient approximation) depending on the Perdewe-Burkee-Ernzerhof model [43,44] and the GGA-mBJ [45], where the space is divided into the non-overlapping muffin-tin spheres (MT), separated by an interstitial region. For these spheres, basis functions are expanded into spherical harmonic functions, while Fourier series are

expanded for the interstitial area. In our study, muffin-tin sphere radii are 2.10 a.u. for Mn and Fe, 2.25 a.u. for Sn. The convergence of the basis was controlled by $R_{MT}K_{max} = 9$ (cutoff parameter), where the R_{MT} is the smallest of the MT sphere radii, while K_{max} present the largest reciprocal lattice vector used in the plane wave expansion. The G_{max} parameter (magnitude of the most significant vector in charge density Fourier expansion) was 12. The cutoff energy (the separation of valence and core states) was chosen as -6 Ry. Energy test convergence was selected as 0.0001 Ry during self-consistency cycles. For the Brillouin zone integration (BZ), we used the tetrahedron method [40] with 104 particular k points (for cubic structure), and 180 k points (for hexagonal structure) in the irreducible wedge (3000 k-points in all Brillouin zone) in order to construct the charge density in each self-consistency step.

Results and Discussion

Structural Properties. From the first principle calculation based on the density function theory with the generalized gradient approximation, the structural properties of Fe₂MnSn Heusler alloy are calculated in order to well understand the ground state properties. Basing on the structural part, we can predict the other properties (electronic, magnetic, etc.). The structural parameters have always been determined by minimizing the total energy, in this procedure, we calculated and plotted the total energies versus volume for the cubic structure in both XA and L2₁ prototype and for the Hexagonal D0₁₉ structure in Fig. 2, where we took into consideration the ferromagnetic (FM) and non-magnetic (NM) orders. The structural analysis in Fig. 2 shows that the D0₁₉ (SG: 194) structure in the ferromagnetic state makes the ground state (i.e., the structure more stable) for the Fe₂MnSn compound. In order to determine the fundamental equilibrium parameters, we used the empirical Murnaghan equation of states (1) (E-O-S) [46]:

$$E(V) = \frac{B_0 V}{B'(B'-1)} \left[\left(\frac{V_0}{V} \right)^{B'} + B' \left(1 - \frac{V_0}{V} \right) - 1 \right] + E_0, \tag{1}$$

where V_0 is the unit cell volume of the ground state, B the bulk modulus and B' its first pressure derivative.

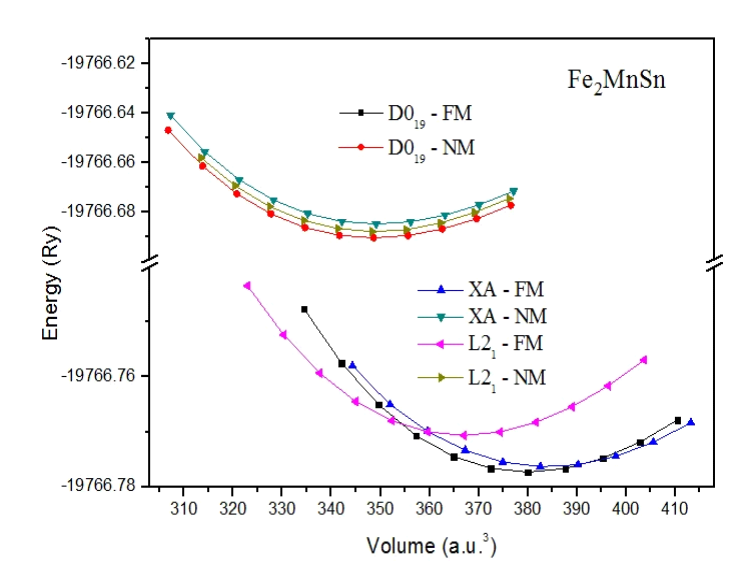


Fig. 2. Total energies vs. volume for Fe₂MnSn Heusler alloy: cubic structures (XA and L2₁) and D0₁₉ for non-magnetic (NM) and ferromagnetic (FM) states

Obtained results are listed in Table 1, where a and c are the equilibrium lattice parameters, and E_0 the energy of the ground state for each structure, in which the results of the other available calculations are also indicated. It is clear that our results are in good agreement with the others found in literature.

Table 1. Structural parameters, the lattice parameters a and c, Bulk modulus B and its first pressure derivative B' and system energy E_0 for Fe₂MnSn full-Heusler alloy in cubic and hexagonal structures

Structure		a, Å	c, Å	B ₀ , GPa	B'	E ₀ (Ry), eV
Cubic (XA)	This work	6.104		114.15	3.15	-19766.77636
	Ref.[47]	6.084		110.47	6.08	-19766.69924
Cubic (L2 ₁)	This work	6.014		125.92	3.30	-19766.77067
	Ref.[47]	5.958		178.15	5.23	-19766.69677
	Ref.[35]	6.027				
	Ref.[48]	6.010		123		-19766.6946
Hexagonal (D0 ₁₉)	This work	5.419	4.422	129.45	3.84	-19766.77734
	Ref.[35]	5.389	4.310			

Magnetic properties. To describe the magnetic moment, we take into consideration the spin magnetic moment, defined by the deference between the total occupancy of the majority spin and the total occupancy of the minority spin.

The calculated total and local magnetic moments for Fe₂MnSn Heusler alloy are listed in Table 2. We can see that the values μ_B obtained for the three structures studied (XA, L2₁ and D0₁₉) presents a remarkable anomaly between the theoretical and experimental work carried out on this material. For full Heusler X₂YZ alloys, the magnetization M and the number of valence electrons Z are related either by: M = Z - 18, M = Z - 24, or by M = Z - 28 [49–54]. All the results obtained, indicates that this specific compound does not follow any rule among these three rules, it is one of the few Heusler materials that has this particularity.

Table 2. Total and local magnetic moments per formula unit in (μ_B) for Fe₂MnSn full-Heusler alloy

Structure		Total	Fe (1)	Fe (2)	Mn	Sn	Interstitial
	This work (GGA)	7.65	2.25	2.54	2.93	-0.06	-0.01
Cubic (XA)	(mBJ)	7.66					
	Ref. [47]	8.33	2.47	2.67	3.30	-0.06	-0.05
	This work (GGA)	5.81	1.77	1.77	2.41	-0.06	-0.08
Cubic (L2 ₁)	(mBJ)	5.83					
	Ref. [47]	3.00	-0.20	- 0.17	3.37	-0.01	0.01
	Ref. [35]	6.04	1.83	1.83	2.57	-0.14	
	Ref. [48]	5.73	3.47	3.47	2.45	-0.07	
Hexagonal (D0 ₁₉)	This work (GGA)	7.19	2.23	2.23	2.79	-0.09	0.03
	(mBJ)	7.19					
	Ref. [35]	6.50	2.3	2.3	2.3	-0.15	

In our study, the calculated total magnetic moment M_{tot} for the ground state structure (D0₁₉) was found to be 7.19 μ_{B} . This non-integer value also indicates a metallic ferromagnetic behavior.

Electronic properties. The electronic properties (band structures, densities of states) depend essentially on the distribution of electrons in both valence and conduction bands, as well as on the value of the energy gap. In which, we can analyze and understand the nature of the bonds formed between the different elements of the material, in order to have a better understanding of its behavior.

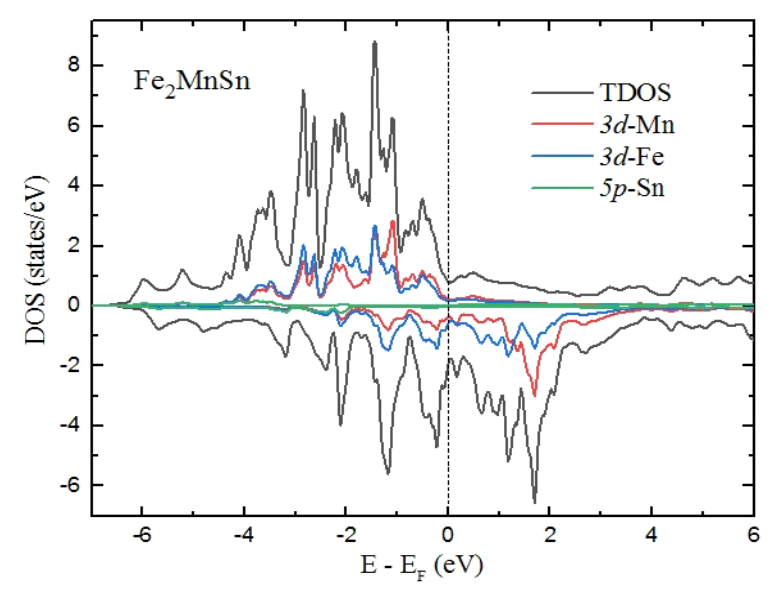


Fig. 3. The calculated total/atomic projected densities of states for Fe₂MnSn Heusler alloy in hexagonal D0₁₉ structure at the ground state

In this subsection, the calculation of the electronic properties such as total/partial densities of states and band structures are shown in Figs. 3 and 4, respectively. The calculations have been made for the equilibrium lattice parameter of the ground state (D0₁₉ structure).

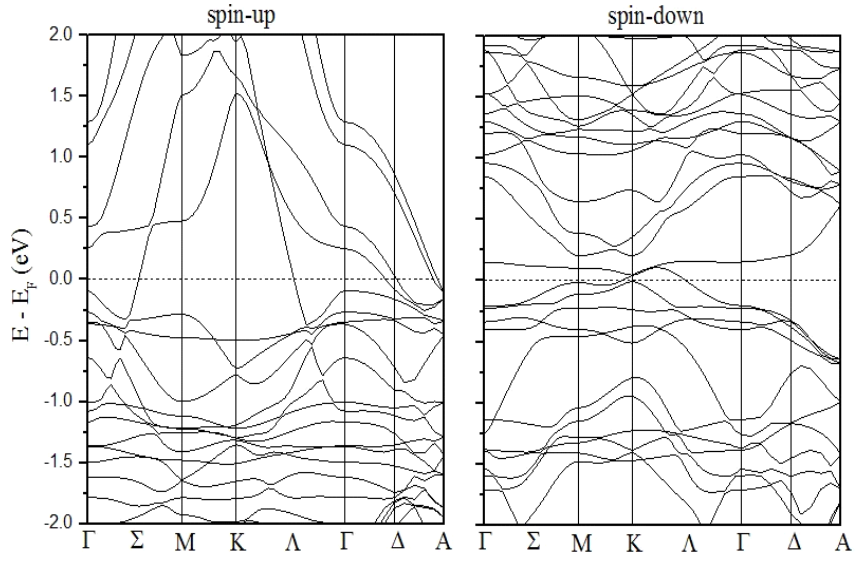


Fig. 4. The calculated band structures for Fe₂MnSn Heusler alloy in hexagonal D0₁₉ structure with both spin-up and spin-down electrons

From Fig. 3, we can see that the density of state of the majority spin-up and minority spin-down electrons show metallic intersections at the Fermi level (E_F), which indicates a metallic character for the studied compound. Below Fermi level, Mn atoms have a major contribution in the total density of states (DOS) for majority spin-up, due to the 3d-Mn electrons, while the DOS of the minority spin-down is dominated by 3d-Fe electrons. Above Fermi level, Mn atoms dominate both densities of states (spin-up and spin-down). Around Fermi level, the contributions of Mn and Fe atoms are almost identical. Unlike the D0₁₉ structure, the cubic structure has a gap energy. In Table 3, we give the obtained results for the gap energy, using both GGA and mBJ approximations.

Structure			Eg, eV
Suddure		GGA	mBJ
C-1: - (VA)	This work	0.14	0.16
Cubic (XA)	Ref.[47]	0.16	
	This work	0.30	0.35
Cubic (L2 ₁)	Ref.[47]	0.29	
Cubic (L2 ₁)	Ref.[35]	0.36	
	Ref.[48]	0.35	
Havaganal (D0)	This work	0	0
Hexagonal (D0 ₁₉)	Ref.[35]	0	

Table 3. Gap energy and spin polarisation for Fe₂MnSn full-Heusler alloy

According to Fig. 4, the spin-up and spin-down band structures along the points and directions of high symmetry in the first Brillouin zone have metallic intersections at the Fermi level, where no band gap appears around E_F . View of the overlap between the energy bands, this situation also confirms the metallic character of Fe₂MnSn Heusler alloy.

Pressure effect. The second objective in this paper is the study of the effect of hydrostatic pressure on the structural, magnetic and electronic properties, where we chose a range of low pressures (between 0 and 10 GPa). For the structural part, we predicted a phase transition from $D0_{19}$ hexagonal structure to $L2_1$ cubic structure, as is shown in Fig. 5. This prediction was made using two methods, the first is based on the structural optimization curves, and is calculating the slope of the common tangent between the two curves (Fig. 5(a)). The second one is based on the calculation of enthalpy variation versus pressure (Fig. 5(b)), where the intersection of the two lines determines the structural transition pressure P_t from hexagonal structure ($D0_{19}$) to cubic structure ($L2_1$). The intersection point in Fig. 5(b) indicates the equality of the system enthalpy for both cubic and hexagonal structures, and under the same pressure, 7 GPa. Beyond this critical value, the enthalpy of the cubic structure represents the minimum energy (the line of $L2_1$ phase passes below that of the $D0_{19}$ phase), which leads to a structural transition from hexagonal structure to cubic structure. The enthalpy H is given by the following equation:

$$H = E + P.V \tag{2}$$

The two methods present a good coherence and indicate the same value, P_t = 7 GPa.

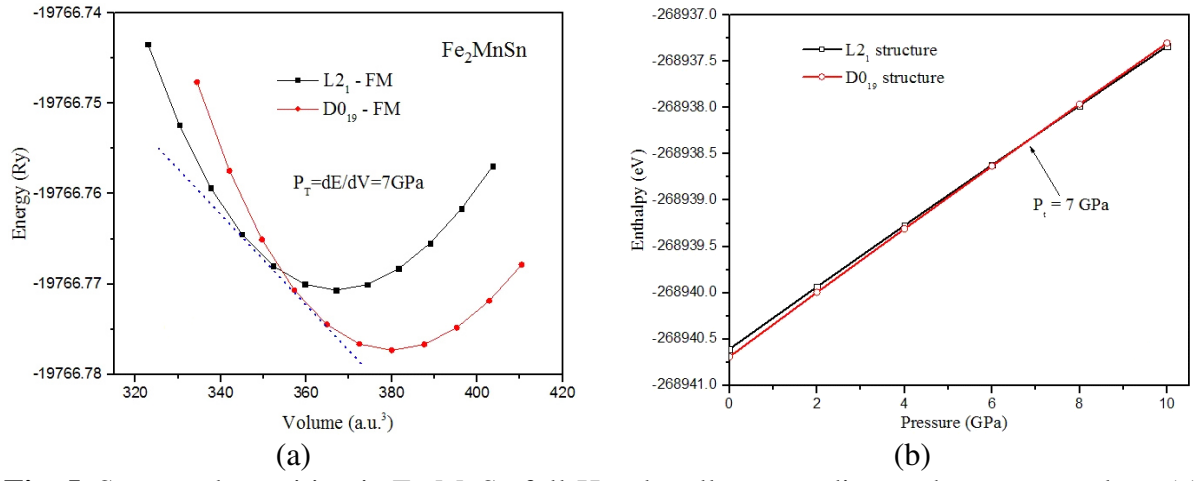


Fig. 5. Structural transition in Fe₂MnSn full-Heusler alloy according to the common slope (a) and the enthalpy variation (b)

We have further studied the effect of pressure on the magnetic and electronic properties for both hexagonal and cubic structures. Figure 6 shows that increasing the pressure reduces the total magnetic moment for the two structures studied, an integer total magnetic moment is found under the effect of the pressures, we found 5.00 μ_B under 6.20 GPa and 7.00 μ_B under 4.78 GPa for the two structures (D0₁₉) and (L2₁) respectively. Generally, an integer total magnetic moment indicates obedience to Slater-Pauling rule and half-metallic character. It is for this purpose that we have calculated and plotted the densities of states of the two structures under the effect of the two pressures indicated in Fig. 7. Contrary to what is expected, the material has another peculiarity, the densities of states present metallic intersections for the two orientations of the spin and for the two structures, then the material keeps its ferromagnetic metallic behavior, and always deviates from Slater-Pauling rule.

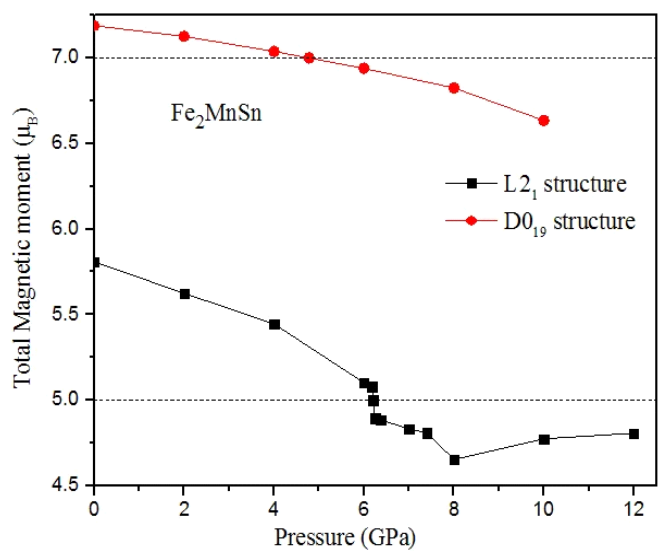


Fig. 6. Total magnetic moment variation as a function of pressure for Fe₂MnSn full-Heusler alloy

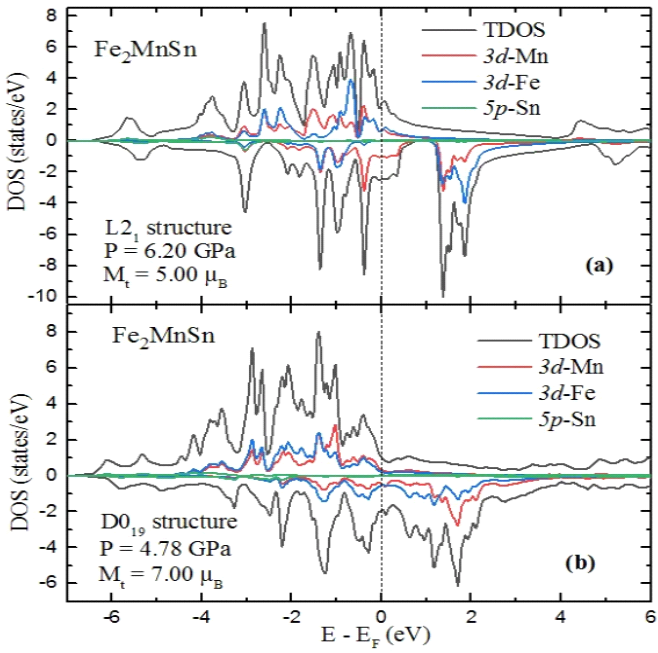


Fig. 7. The calculated total/atomic projected densities of states for Fe₂MnSn Heusler alloy for integer value of total magnetic moment: (a) cubic L2₁ structure(5.00 μ B); (b) hexagonal D0₁₉ structure $(7.00 \mu_B)$

To examine the effect of pressure on the metallic character of the material, we calculated and plotted in Fig. 8, the variation of spin polarization versus pressure for the same range and for both hexagonal and cubic structures. We notice that increasing the pressure rapidly decreases the spin polarization for the hexagonal structure $(D0_{19})$, while for the cubic structure $(L2_1)$ the variation is slight and alternating.

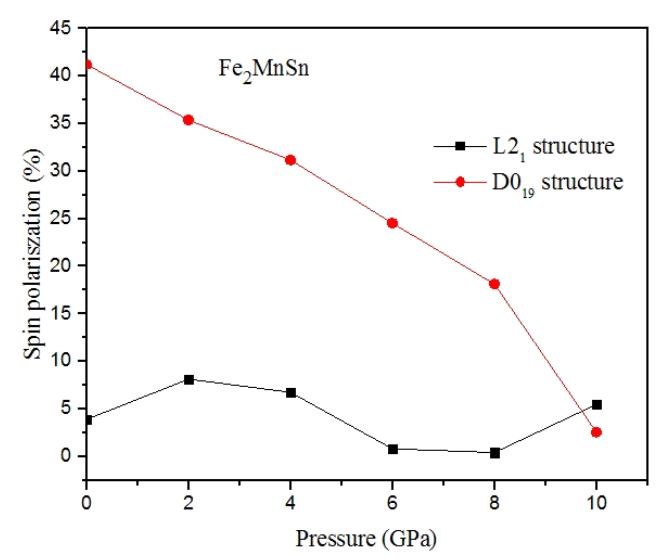


Fig. 8. Spin polarisation variation versus pressure for Fe₂MnSn full-Heusler alloy

Conclusion

In this paper, we have performed a first-principles study of the structural, electronic and magnetic properties, for the ternary full Heusler alloy Fe_2MnSn in the ground state. We also examined the effect of pressure on the evolution of these properties. Our results reveal that the ferromagnetic hexagonal $D0_{19}$ structure makes the ground state for Fe_2MnSn Heusler alloy, and a pressure-induced phase transition (from hexagonal to cubic structure) was predicted under 7 GPa. The study of the electronic band structure and the density of states show that the Fe_2MnSn compound has a metallic character. It retains this character even under the effect of hydrostatic pressure, with a range of 0 to 10 GPa. The total magnetic moment is found 7.19 μ_B , it never follows Slater-Pauling rule, even for an integer total magnetic moment (under pressure). The material tends to rapidly lose its spin polarization under the effect of hydrostatic pressure.

References

- 1. Ramdane O, Labidi M, Masrour R, Labidi S, Ellouze M, Rehamnia R. Study of Structural, Electronic, and Magnetic Properties of Cubic and Tetragonal Ba2FeMoO6. *Journal of Superconductivity and Novel Magnetism.* 2023;36(1): 373–387.
- 2. Chaabouni R, Ellouze M, Hlil EK, Masrour R, Jotania R. Role of nickel substitution in the structural, magnetic properties, and magnetocaloric effect in La0. 67Ba0. 22Sr0. 11Mn0. 95Ni0. 05O3 sample. *Journal of Materials Science: Materials in Electronics*. 2022;33(30): 23524–23541.
- 3. Kadim G, Masrour R. First-principles investigation of electronic and optical properties of Fe doped in CsBrO3 for enhanced photocatalytic hydrogen production. International *Journal of Hydrogen Energy*. 2022;47(61): 25522–25530.
- 4. Bessimou M, Masrour R. Magnetocaloric effect and magnetic properties of Dy2CoMnO6: Monte Carlo study. *Philosophical Magazine*. 2023;103(1): 56–66.

- 5. El Krimi Y, Masrour R. Cobalt-based full Heusler compounds Co2FeZ (Z= Al, Si, and Ga): A comprehensive study of competition between XA and L21 atomic ordering with ab initio calculation. Materials Science and Engineering: B. 2022;284: 115906.
- 6. Masrour R, Hlil EK, Hamedoun M, Benyoussef A, Mounkachi O, El Moussaoui H. Ab initio, mean field theory and series expansions calculations study of electronic and magnetic properties of antiferromagnetic MnSe alloys. Journal of Magnetism and Magnetic Materials. 2014;361: 197–200.
- 7. Masrour R, Hlil EK, Hamedoun M, Benyoussef A, Mounkachi O, El Moussaoui H. Ab initio, mean field theory and series expansions calculations study of electronic and magnetic properties of antiferromagnetic MnSe alloys. Journal of Magnetism and Magnetic Materials. 2014;361: 197–200.
- 8. Masrour R, Hlil EK, Hamedoun M, Benyoussef A, Mounkachi O. Electronic and magnetic structures of ferrimagnetic Mn2Sb compound. Journal of Magnetism and Magnetic Materials. 2015;374: 116-119.
- 9. Masrour R, Hlil EK, Hamedoun M, Benyoussef A, Boutahar A, Lassri H. Antiferromagnetic spintronics of Mn2Au: An experiment, first principle, mean field and series expansions calculations study. Journal of Magnetism and Magnetic Materials. 2015;393: 600–603.
- 10. Masrour R, Hlil EK, Hamedoun M, Benyoussef A, Mounkachi O. Electronic and magnetic properties of MnAu nanoparticles. Journal of Magnetism and Magnetic Materials. 2014;354: 159–162.
- 11. Baaalla N, Ammari Y, Hlil EK, Masrour R, El Kenz A, Benyoussef A. Study of optical, electrical and photovoltaic properties of CH3NH3PbI3 perovskite: ab initio calculations. Physica Scripta. 2020;95(9): 095104.
- 12. Baaalla N, Ammari Y, Hlil EK, Abid S, Masrour R, Benyoussef A, El Kenz A. The novel material based on strandberg-type hybrid complex (C6H10N2) 2 [Co (H2O) 4P2Mo5O23]. 6H2O: Experimental and simulations investigation on electronic, optical, and magnetocaloric properties. Ceramics International. 2021;47(2): 2338–2346.
- 13. Baaalla N, Hemissi H, Hlil EK, Masrour R, Benyoussef A, El Kenz A. Electronic and optical properties of organic-inorganic (CuII/ReVII)-heterobimetallic L-Arginine complex: Experimental and Computational studies. Journal of Molecular Structure. 2021;1246: 131153.
- 14. Baaalla N, Absike H, Ammari Y, Hlil EK, Masrour R, Benyoussef A, El Kenz A. An extensive investigation of structural, electronic, optical, magnetic, and thermoelectric properties of NaMnAsO4 cluster by first-principles calculations. International Journal of *Energy Research.* 2022;46(7): 9586–9601.
- 15. Belyaev FS, Evard ME, Volkov AE. Simulation of the plastic deformation of shape memory alloys considering shear anisotropy on the slip plane. Materials Physics and Mechanics. 2023;51(1): 61-67.
- 16. Breczko T, Barkaline VV, Grechishkin RM, Nelayev VV. Magnetic properties of Ni2MnGa alloy. *Materials Physics and Mechanics*. 2010;9(1): 53–67.
- 17. De Groot RA, Mueller FM. PG v. Engen, and KHJ Buschow. Phys. Rev. Lett. 1983;50(25): 2024–2027.
- 18. Julliere M. Tunneling between ferromagnetic films. *Physics letters A*. 1975;54(3): 225–226.
- 19. Pandey R, Jaffe JE, Kunz AB. Ab initio band-structure calculations for alkaline-earth oxides and sulfides. Physical Review B. 1991;43(11): 9228.
- 20. Yuasa S, Fukushima A, Kubota H, Suzuki Y, Ando K. Giant tunneling magnetoresistance up to 410% at room temperature in fully epitaxial Co/ MgO/ Co magnetic tunnel junctions with bcc Co (001) electrodes. Applied Physics Letters. 2006;89(4): 042505.

- 21. Parkin SS, Kaiser C, Panchula A, Rice PM, Hughes B, Samant M, Yang SH. Giant tunnelling magnetoresistance at room temperature with MgO (100) tunnel barriers. *Nature Materials*. 2004;3(12): 862–867.
- 22. Hülsen B, Scheffler M, Kratzer P. Thermodynamics of the Heusler alloy Co 2– x Mn 1+ x Si: A combined density functional theory and cluster expansion study. *Physical Review B*. 2009;79(9): 094407.
- 23. Viglin NA, Ustinov VV, Osipov VV. Spin injection maser. JETP Letters. 2007;86: 193–196.
- 24. Klimczuk T, Wang CH, Gofryk K, Ronning F, Winterlik J, Fecher GH, Griveau JC, Colineau E, Felser C, Thompson JD, Safarik DJ. Superconductivity in the Heusler family of intermetallics. *Physical Review B*. 2012;85(17): 174505.
- 25. Ağduk S, Gökoğlu G. First-principles study of elastic and vibrational properties of Ni 2 MnIn magnetic shape memory alloys. *The European Physical Journal B*. 2011;79: 509–514.
- 26. Uijttewaal MA, Hickel T, Neugebauer J, Gruner ME, Entel P. Understanding the phase transitions of the Ni 2 MnGa magnetic shape memory system from first principles. *Physical Review Letters*. 2009;102(3): 035702.
- 27. Heusler F. Über magnetische manganlegierungen. Verhandlungen der Deutschen Physikalischen Gesellschaft. 1903;5: 219.
- 28. Bradley AJ, Rodgers JW. The crystal structure of the Heusler alloys. *Proceedings of the royal society of london. Series A, Containing Papers of a Mathematical and Physical Character.* 1934;144(852): 340–359.
- 29. Gencer A, Surucu O, Usanmaz D, Khenata R, Candan A, Surucu G. Equiatomic quaternary Heusler compounds TiVFeZ (Z= Al, Si, Ge): half-metallic ferromagnetic materials. *Journal of Alloys and Compounds*. 2021;883: 160869.
- 30. Hocine H, Amara K, Khelfaoui F. Half-metallic stability of the Heusler alloys TiZrIrZ (Z= Al, Ga, and In) under volumetric strain and tetragonal deformation. *Applied Physics A*. 2020;126(3): 178.
- 31. Heusler F, Starck W, Haupt E. Magnetisch-chemische studien. Verh. Dtsch. Phys. Ges. 1903;5: 219–232.
- 32. Heusler O. Crystal structure and the iron magnetism of manganese-aluminium-copper alloys. *Ann. Phys.* 1934;19: 155–201.
- 33. Hellal T, Bensaid D, Doumi B, Mohammedi A, Benzoudji F, Azzaz Y, Ameri M. Mn2YGa (Y= Ir and Pt), a promising shape memory alloy by DFT methods. *Chinese Journal of Physics*. 2017;55(3): 806–812.
- 34. Kharel P, Huh Y, Shah VR, Li XZ, Al-Aqtash N, Tarawneh K et al. Structural and magnetic properties of Mn 2+δTiSn. *Journal of Applied Physics*. 2012;111(7): 07B101.
- 35. Dahal B, Al Maruf A, Prophet S, Huh Y, Lukashev PV, Kharel P. Electronic, magnetic, and structural properties of Fe2MnSn Heusler alloy. *AIP Advances*. 2020;10(1): 015118.
- 36. Keshavarz S, Naghibolashrafi N, Jamer ME, Vinson K, Mazumdar D, Dennis CL, Ratcliff II W, Borchers JA, Gupta A, LeClair P. Fe2MnGe: A hexagonal Heusler analogue. *Journal of Alloys and Compounds*. 2019;771: 793–802.
- 37. Sugihara A, Mizukami S, Yamada Y, Koike K, Miyazaki T. High perpendicular magnetic anisotropy in D22-Mn3+ xGe tetragonal Heusler alloy films. *Applied Physics Letters*. 2014;104(13): 132404.
- 38. Jansen HJ, Freeman AJ. Total-energy full-potential linearized augmented-plane-wave method for bulk solids: Electronic and structural properties of tungsten. *Physical Review B*. 1984;30(2): 561.
- 39. Kohn W, Sham LJ. Self-consistent equations including exchange and correlation effects. *Physical Review*. 1965;140(4A): A1133.

- 40. Blaha P, Schwarz K, Medsen GKH, Kvasnicka D, Luitz J. WIEN2k, An Augmented Plane Wave Plus Local Orbitals Program for Calculating Crystal Properties. Vienna, Austria: Vienna University Technology; 2001.
- 41. Schwarz K, Blaha P. Solid state calculations using WIEN2k. Comput. Mater. Sci. 2003;28: 259.
- 42. Kohn W, Sham LJ. Density functional theory. In: Conference proceedings Italian Physical Society 1996. p.561-572.
- 43. Perdew JP, Burke K, Ernzerhof M. Generalized gradient approximation made simple. Physical Review Letters. 1996;77(18): 3865.
- 44. Perdew JP, Chevary JA, Vosko SH, Jackson KA, Pederson MR, Singh DJ, Fiolhais C. Atoms, molecules, solids, and surfaces: Applications of the generalized gradient approximation for exchange and correlation. *Physical Review B*. 1992;46(11): 6671.
- 45. Tran F, Blaha P. Accurate band gaps of semiconductors and insulators with a semilocal exchange-correlation potential. Physical Review Letters. 2009;102(22): 226401.
- 46. Murnaghan FD. The compressibility of media under extreme pressures. *Proceedings of* the National Academy of Sciences. 1944;30(9): 244–247.
- 47. Sayah M, Zeffane S, Mokhtari M, Dahmane F, Zekri L, Khenata R, Zekri N. Firstprinciples investigation of half-metallic ferromagnetism of Fe \$ _2 \$ YSn (Y= Mn, Ti and V) Heusler alloys. Condens. Matter Phys. 2021;24(2): 23703.
- 48. Jain VK, Lakshmi N, Jain R, Chandra AR. Electronic Structure, Elastic, Magnetic, and Optical Properties of Fe 2 Mn Z (Z= Si, Ge, and Sn) Full Heusler Alloys: First-Principle Calculations. Journal of Superconductivity and Novel Magnetism. 2019;32: 739–749.
- 49. Slater JC. The ferromagnetism of nickel. Physical Review. 1936;49(7): 537.
- 50. Pauling L. The nature of the interatomic forces in metals. *Physical Review*. 1938;54(11): 899.
- 51. Galanakis I, Dederichs PH, Papanikolaou N. Slater-Pauling behavior and origin of the half-metallicity of the full-Heusler alloys. *Physical Review B*. 2002;66(17): 174429.
- 52. Skaftouros S, Özdoğan K, Şaşıoğlu E, Galanakis I. Search for spin gapless semiconductors: The case of inverse Heusler compounds. Appl. Phys. Lett. 2013;102: 022402.
- 53. Abbassa H, Meskine S, Labdelli A, Kacher S, Belaroussi T, Amrani B. Promising shape memory in NiCoMnZ (Z= Si, Ge and Sn) quaternary Heusler alloy from first principles. Materials Chemistry and Physics. 2020;256: 123735.
- 54. Abbes EH, Abbassa H, Meskine S, Bouhamou I, Boukortt A. First-principles investigation of magneto-electronic properties and band Jahn-Teller effects in NiCoMnSi1-xAlx quaternary Heusler. Journal of New Technology and Materials. 2022;12(2): 62–69.

THE AUTHORS

Bouhamou I.

e-mail: imen.bouhamou.etu@univ-mosta.dz

Abbes C.

e-mail: charef.abbes@univ-mosta.dz

Abbes E.H.

e-mail: habib.abbes.etu@univ-mosta.dz

Abbassa H.

e-mail: abshmz@gmail.com

Boukortt A.

e-mail: boukortt@yahoo.fr

Benbedra A.

e-mail: abdesamed.benbedra@gmail.com

Disclination models in the analysis of stored energy in icosahedral small particles

Submitted: October 5, 2023

Approved: November 3, 2023

Accepted: November 14, 2023

¹ Institute for Problems of Mechanical Engineering RAS, St. Petersburg, Russian Federation

² ITMO University, St. Petersburg, Russian Federation

⊠ anna.kolesnikova.physics@gmail.com

Abstract. A discrete disclination model that describes the stored energy in icosahedral small particles (ISPs) is proposed. The particle energy is defined as a superposition of the energies of six interacting wedge disclinations, each of which connects the opposite vertices of the icosahedron. Isotropic elasticity analytical solution is given for a spheroid with the volume being equal to that of the icosahedron. Distributed disclination model, also known as Marks-Ioffe model, is used for calculation of the stored in ISP energy. The influence of the Poisson's ratio on the stored in ISP energy is studied within both considered disclination models.

Keywords: disclination; icosahedral small particle; discrete disclination model; distributed disclination model

Acknowledgements. The work was supported by the Russian Science Foundation (grant No 19-19-00617).

Citation: Kolesnikova AL, Dorogov MV, Krasnitckii SA, Smirnov AM, Romanov AE. Disclination models in the analysis of stored energy in icosahedral small particles. *Materials Physics and Mechanics*. 2023;51(6): 76-83. DOI: 10.18149/MPM.5162023_7.

Introduction

The interest to pentagonal crystals did increase after Dan Shechtman discovery of quasicrystals in the mid-1980s [1,2], for which he was awarded by Nobel Prize in chemistry in 2011. Being different from quasicrystals in the type of atomic ordering, icosahedral small particles (ISPs) share with the first ones a remarkable feature of having habitus with five-fold symmetry [3]. It was first proposed [4,5] and then supported by experimental data [6,7] that a ISP consists of twenty crystalline domains with FCC crystal structure interconnected by coherent twin boundaries. Such multiple cyclic twinning induces inhomogeneous elastic deformation in particle interior, which can be described in terms of wedge disclinations [8]. These structural features largely determine the unique functional properties of ISPs. In particular, it is precisely with the presence of twin boundaries and residual deformations that the higher chemical activity of ISPs is associated having the same size as for cubic or octahedral shape monocrystalline ones [9–11]. In addition, specific pentagonal shape of particles contributes to an increase in the intensity of plasmon resonance peaks, and can also leads to their splitting [12,13].

It should be noted that despite the active research of many unique nanomaterials over the past 20 years, only a small part has reached the large-scale applied use in various household and specialized devices of electronics and optoelectronics. The reason for this is not so much the

high cost and complexity of producing nanomaterials, but the significant uncontrolled effect of crystal structure defects on the functional properties of nanomaterials [14–16]. This highlights the great impact of theoretical studies of the defect structure of ISPs, too.

The distributed disclination model [17], also known as Marks-Ioffe model, for the analysis of intrinsic elastic strain in ISPs has been usually employed to provide a theoretical description of the relaxation phenomena in such microparticles. According to this model, the ISP is treated as an elastic sphere with the residual strain caused by removing the solid angle 0.0613 with subsequent recovering of the continuity. Theoretical studies [18] have shown that the distributed disclination model makes it possible to find the elastic fields and energy of ISPs, expressed in simple for analysis analytical equations. On the other hand, the behavioral features of the ISPs, such as the growth of a pentagonal crystalline whisker from the apex of the ISP [19–21], can only be explained by discrete disclination model. The residual elastic strain in the discrete model is induced by six wedge disclinations with strength ~7.333° crossing the particle through the opposite icosahedron vertices [7,22]. This representation is able to describe the inhomogeneous residual strains in ISPs to precise the results of existing theoretical models of stress relaxation as well as to create new models taking into consideration the defect formation in vicinity of disclination lines.

Even though the discrete model of ISPs was proposed more than twenty years ago, some of its aspects require clarification, in particular, ISP nonuniform elastic filed and stored energy associated with this field, which are the purpose of this work.

Discrete disclination model

A pentagonal microcrystal with a habitus of regular icosahedron contains six positive wedge disclinations penetrating the crystal and passing through its center (Fig. 1(a)) [7,22]. The outcrops of the disclination lines on the surface coincide with the vertices of the icosahedron. The plane angles between the disclination lines α are all the same and equal to 63.435°:

$$\alpha = \arccos\left(\frac{2R_{\rm cs}^2 - g_{\rm ih}^2}{2R_{\rm cs}^2}\right) = \arccos\left(\frac{1}{\sqrt{5}}\right) \approx 63.435^{\circ},\tag{1}$$

where $R_{\rm cs}$ is circumscribed sphere radius, $R_{\rm cs} = \sqrt{2(5+\sqrt{5})}g_{\rm ih}/4$; $g_{\rm ih}$ is icosahedron edge.

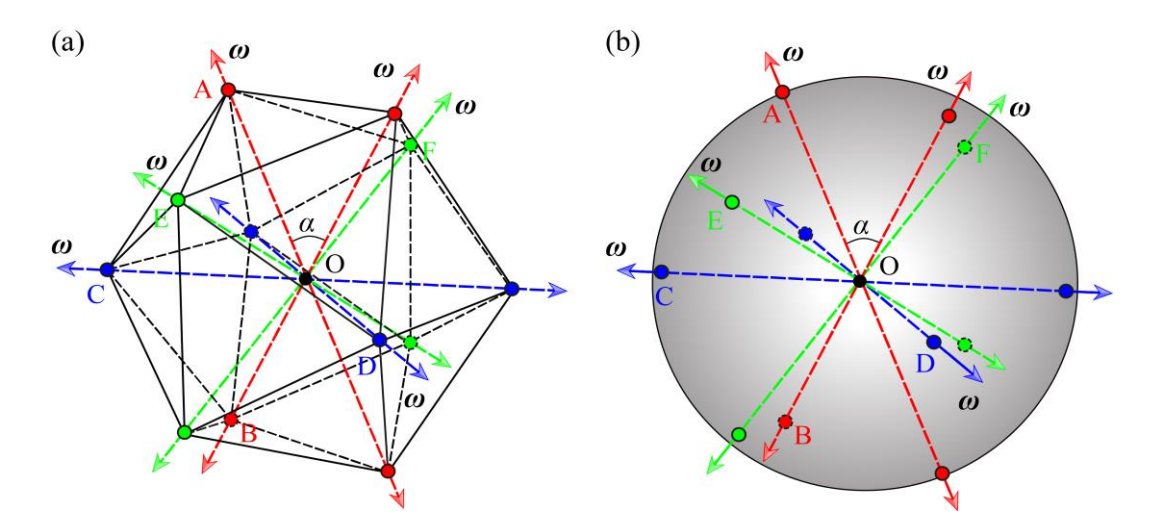


Fig. 1. Schematics of icosahedral small particle (a) and its discrete disclination model (b). A, B, C, D, E, and F are wedge disclinations in the particle interior; O is the center of the icosahedron and the point of the intersection of disclination lines; ω is Frank pseudovector; α is the flat angle between disclinations. The invisible edges of the icosahedron are indicated by black dashed lines. Disclination lines are shown by colored dashed lines

As a simplified discrete model of such an ISP, we adopted an elastic sphere with six positive disclinations with strength $\omega \approx 7.333^{\circ}$ passing through its center [23,24] (Fig. 1(b)). The disclinations are positioned in the sphere in the same way as they are positioned in the ISP shown in Fig. 1(a).

In the framework of the discrete disclination model, the stored in ISP energy $E_{\rm ISP}$ can be calculated based on the solution for elastic field of wedge disclination in an elastic sphere [25,26]; $E_{\rm ISP}$ can be expressed as the sum of six disclination self-energies $E_{\rm I}$ and 15 energies of interaction between intersecting disclinations I and II $E_{\rm I-II}$:

$$E_{\rm ISP} = 6E_{\rm I} + 15E_{\rm I-II}. \tag{2}$$

Figure 2 shows a geometric scheme for calculating elastic energies $E_{\rm I}$ and $E_{\rm I-II}$.

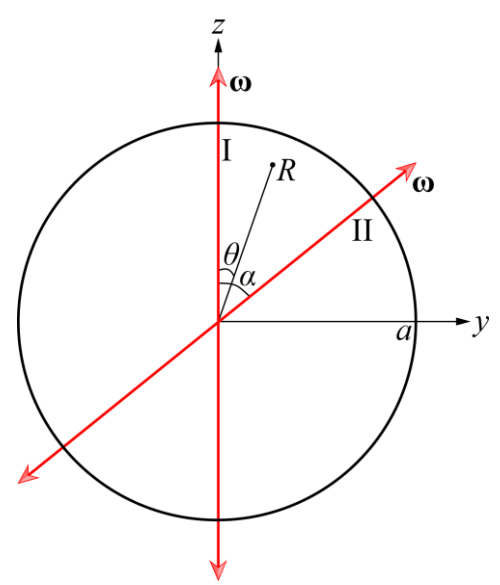


Fig. 2. Schematics for calculating the elastic energies of interacting wedge disclinations in a spheroid. a is a sphere radius; θ and R are angular and radial coordinates in the spherical coordinate system (R, θ, φ) , respectively

Elastic energy of a single disclination in a spheroid

The disclination self-energies $E_{\rm I}$ can be found using general formalism of the micromechanics of defects [27]:

$$E_{\rm I} = -\frac{1}{2} \int_{V}^{\rm I} \varepsilon_{ij}^{*} {}^{\rm I} \sigma_{ij} \, dV \,, \tag{3}$$

where ${}^{\rm I}\varepsilon_{ij}^*$ are eigenstrains of disclination I, and ${}^{\rm I}\sigma_{ij}$ are stresses of disclination I.

In the case of wedge disclination defined by the position of its line x = 0, $0 \le R \le a$ and $0 \le \theta \le \pi$ (see Fig. 2), the eigenstrain of positive disclination I, can be written as:

$${}^{\mathrm{I}}\varepsilon_{xx}^{*} = -\omega y H[(\pi - \theta), \theta] H(a - R) \delta(x) = -\omega R \sin \theta H[(\pi - \theta), \theta] H[a - R] \delta(x), \tag{4}$$

where $H[\xi]$ is Heaviside function, $\delta(x)$ is Dirac delta function. Using Eqs. (3) and (4) the energy of a single disclination in a sphere can be modified as follows:

$$E_{\rm I} = -\frac{1}{2} \int_{V}^{1} \varepsilon_{xx}^{*} {}^{1}\sigma_{xx} dV = \frac{\omega}{2} \int_{0}^{a} \int_{0}^{\pi} R^{2} \sin \theta {}^{1}\sigma_{xx} |_{x=0} dR d\theta , \qquad (5)$$

with the known disclination stress component ${}^{\rm I}\sigma_{xx}|_{x=0} = {}^{\rm I}\sigma_{\varphi\varphi}$ [25]:

$$\frac{1}{\sigma_{xx}}\Big|_{x=0} = \frac{1}{\sigma_{\varphi\varphi}} = -\frac{G\omega}{60\pi(1-\nu)(7+5\nu)} \times \left[75\nu(1+3\nu)\left(\frac{R}{a}\right)^{2} - 4(91+53\nu) - 15(1+3\nu)(7+11\nu)\cos^{2}\theta\left(\frac{R}{a}\right)^{2} - 30(7+5\nu)\ln\frac{R\sin\theta}{2a}\right] + \frac{G\omega}{2\pi(1-\nu)}\sum_{m=2}^{\infty} \left[\bar{A}_{m}(2m+1)(2m-2-2\nu-8m\nu)\left(\frac{R}{a}\right)^{2m} + 2\bar{B}_{m}m\left(\frac{R}{a}\right)^{2m-2}\right] P_{2m}(\cos\theta) + \frac{G\omega}{2\pi(1-\nu)}\sum_{m=2}^{\infty} \left[\bar{A}_{m}(2m+5-4\nu)\left(\frac{R}{a}\right)^{2m} + \bar{B}_{m}\left(\frac{R}{a}\right)^{2m-2}\right] P_{2m}^{1}(\cos\theta)\cot\theta, \tag{6}$$

for
$$m \ge 2$$
 $\overline{A}_m = \frac{(\overline{\sigma}_m - 2m\overline{\tau}_m)}{2[1 + \nu + 2m(1 + 2m + 2\nu)]};$
 $\overline{B}_m = -\frac{(2\nu - 1 + 4m(1 + m))\overline{\sigma}_m + 2(1 + \nu - 4m^3 + m(3 + 2\nu))\overline{\tau}_m}{2(2m - 1)[1 + \nu + 2m(1 + 2m + 2\nu)]};$
 $\overline{\sigma}_m = \frac{(-2m^2\nu - m\nu + \nu + 1)(4m + 1)}{(m - 1)m(2m + 1)(2m + 3)};$
 $\overline{\tau}_m = \frac{(1 - 2\nu)(4m + 1)}{2(m - 1)m(2m + 1)(2m + 3)},$

where $P_{2m}(\cos\theta)$ are Legendre polynomials, $P_{2m}^{1}(\cos\theta)$ are associated Legendre polynomials; G is shear modulus; v is Poisson's ratio.

After integrating Eq. (5), the expression for the stored (elastic energy) of a single wedge disclination in a spheroid $E_{\rm I}$ acquires the final form:

$$E_{\rm I} = \frac{G\omega^2 a^3}{\pi (1-\nu)} \left[\frac{1}{12} - \frac{\nu (1+3\nu)}{15(7+5\nu)} - \sum_{m=2}^{\infty} \frac{(1+4m)(32m^4\nu^2 - 8m^3(\nu^2 - 7\nu + 1) - 4m^2(1-\nu) + 2m(11\nu^2 - 7\nu - 9) - (1+\nu)(5-4\nu))}{4(m-1)m(2m-1)(3+8m+4m^2)^2(1+\nu+2m+4m^2+2m\nu)} \right], \tag{7}$$

that leads to the specific energy per unit volume of the sphere w_1 :

$$w_{\rm I} = \frac{3}{4} \frac{E_{\rm I}}{\pi a^3} = \frac{G\omega^2}{\pi^2 (1 - \nu)} \left[\frac{1}{16} - \frac{\nu (1 + 3\nu)}{20(7 + 5\nu)} - \frac{3}{4} \sum_{m=2}^{\infty} \frac{(1 + 4m)(32m^4\nu^2 - 8m^3(\nu^2 - 7\nu + 1) - 4m^2(1 - \nu) + 2m(11\nu^2 - 7\nu - 9) - (1 + \nu)(5 - 4\nu))}{4(m - 1)m(2m - 1)(3 + 8m + 4m^2)^2 (1 + \nu + 2m + 4m^2 + 2m\nu)} \right].$$
(8)

Figure 3 presents the specific energy w_1 as a function of Poisson's ratio v. For comparison, the same Fig. 3 shows the disclination energy per unit volume of a long cylinder of radius a [28]:

$$w_{\text{Icyl}} = \frac{E_{\text{Icyl}}}{(\pi a^2)} = \frac{G\omega^2}{16\pi^2(1-\nu)}.$$
 (9)

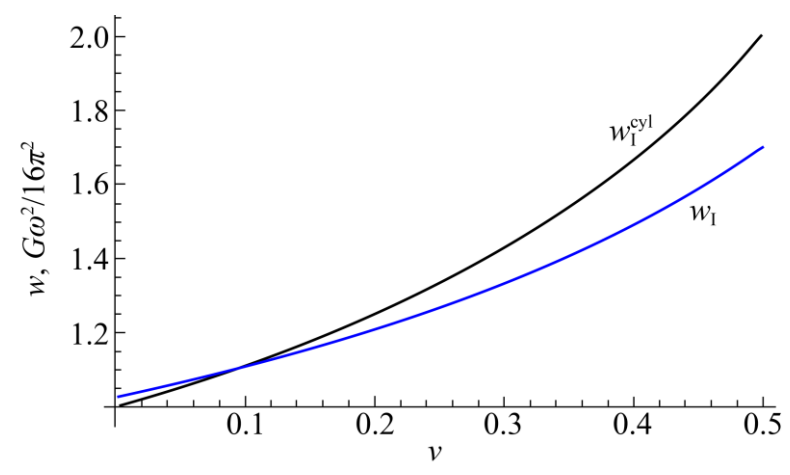


Fig. 3. Dependences of the elastic energy of a single wedge disclination per unit volume w on the Poisson's ratio v in a sphere and a cylinder

It is worth to note that the graphs in Fig. 3 are identical to those first given in Ref. [26], where the formula for disclination energy in a spheroid had a different from Eq. (8) form (apparently, the terms of the series were grouped in another way than in the present work).

Interaction energy of intersecting wedge disclinations in a spheroid

The interaction energy of intersecting disclinations in a sphere $E_{\text{I-II}}$ can also be found using general formulas of micromechanics of defects [27]:

$$E_{\text{I-II}} = -\int_{V}^{I} \varepsilon_{xx}^{*} \,^{\text{II}} \sigma_{xx} dV = \omega \int_{0}^{a} \int_{0}^{\pi} R^{2} \sin \theta \,^{\text{II}} \sigma_{xx} \big|_{x=0} dR d\theta , \qquad (10)$$

where ${}^{\mathrm{I}}\varepsilon_{ij}^*$ are eigenstrains of disclination I, and ${}^{\mathrm{II}}\sigma_{ij}$ are stresses of disclination II.

Independence of the disclination elastic fields on the angle φ in the coordinate system associated with the disclination axis, see Eq. (6), allows one to make the transition from ${}^{\text{II}}\sigma_{xx}|_{x=0}$ to ${}^{\text{II}}\sigma_{\varphi\varphi}$ in Eq. (10), and also write down the following relation:

$${}^{\mathrm{II}}\sigma_{xx}\mid_{x=0} = {}^{\mathrm{I}}\sigma_{xx}\mid_{\substack{x=0,\\\theta\to\theta-\alpha}}$$

$$\tag{11}$$

Considering Eq. (11), Eq. (10) is reduced to the following form:

$$E_{\text{I-II}} = \omega \int_{0}^{a} \int_{0}^{\pi} R^{2} \sin \theta \, {}^{\text{I}}\sigma_{\varphi\varphi}(\theta - \alpha) dR d\theta = \omega \int_{0}^{a} \int_{-\alpha}^{\pi - \alpha} R^{2} \sin(\theta' + \alpha) \, {}^{\text{I}}\sigma_{\varphi\varphi}(\theta') dR d\theta' \,. \tag{12}$$

In Eq. (12), it is necessary to account for the following: dependence ${}^{1}\sigma_{\varphi\varphi}$ on the angle θ or θ' assumes that $0 \le \theta \le \pi$. Therefore, the integration over the variable φ in Eq. (12) should be performed by dividing the integration interval $(-\alpha, \pi - \alpha)$ into $(-\alpha, 0)$ and $(0, \pi - \alpha)$. Note that the integration over a variable R gives an analytical result, and then the integration over the angle can be done numerically. In addition, it is necessary to consider the fact that for the interval $(-\alpha, 0)$, the eigenstrain of the disclination (and the elastic field) changes sign to the opposite.

Figure 4 shows the dependence of the energy of intersecting disclinations in a spheroid $E_{\text{I-II}}$ on the flat angle between disclinations α . The five-pointed stars show calculated values, and the solid curve is the envelope.

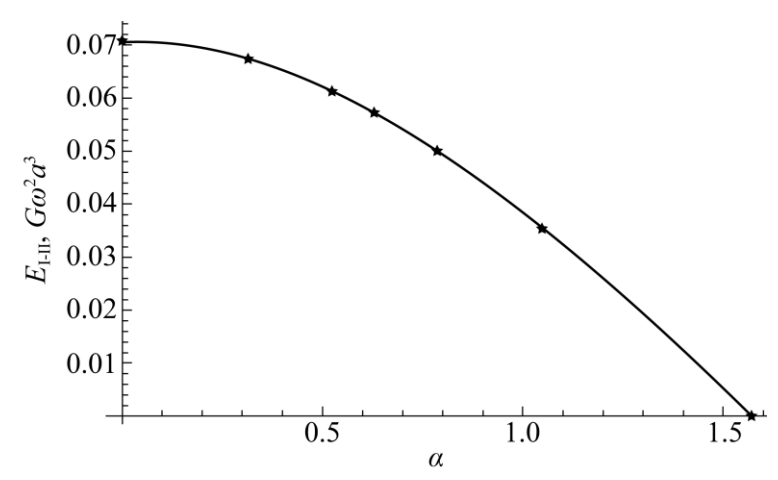


Fig. 4. Dependence of the energy of intersecting wedge disclinations in a spheroid $E_{\text{I-II}}$ on the flat angle α between them

Results and Discussion

It is obvious that in the case of coincidence of two interacting disclinations ($\alpha = 0$ or $\alpha = \pi$), the interaction energy between two dislocations is equal to twice the elastic energy of a single disclination: $E_{\text{I-II}} = 2E_{\text{I}}$, and the total energy of such a system is $4E_{\text{I}}$. This corresponds to the single disclination energy E_{I} with strength 2ω ($\omega \rightarrow 2\omega$ in Eq. (7)). At mutually perpendicular position of disclinations ($\alpha = \pi/2$), the integral interaction energy between two dislocations $E_{\text{I-II}}$ is zero.

Consider all the results of the analytical and numerical calculations, the stored in the ISP elastic energy $E_{\rm ISP}$ defined within the framework of discrete disclination model can be calculated by exploring Eq. (2) ($\alpha = 63.435^{\circ}$, $\omega \approx 7.333^{\circ}$, $\nu = 0.3$):

$$E_{\text{IPP}} \approx 0.687 G\omega^2 a^3 \approx 0.0113 Ga^3$$
. (13)

For comparison, let us find the value of ISP energy in the distributed disclination model (Marx-Ioffe model), in which six intersecting disclinations are replaced by continuously distributed conical stereo disclinations with total strength $\chi = 3\omega/2\pi \approx 0.06$ [17]:

$$E_{\text{IPP}}^{\chi} = \frac{8\pi (1+\nu)G\chi^2 a^3}{27(1-\nu)} = \frac{2(1+\nu)G\omega^2 a^3}{3\pi (1-\nu)} \bigg|_{\nu=0.3} \approx 0.394G\omega^2 a^3 \bigg|_{\omega\approx7.333^\circ} \approx 0.00646Ga^3.$$
 (14)

For the same radius of spheroid, the distributed disclination model gives a lower value of ISP energy compared to those found with the discrete disclination model, at least for the Poisson's ratio v = 0.3, the energy values differ by 1.7 times: $E_{\rm IPP} / E_{\rm IPP}^{\chi} \approx 1.7$. Table 1 shows the ratio of the stored in ISP energies calculated within the framework of two models (discrete and distributed ones) for several values of Poisson's ratio v.

Table 1. Icosahedral small particle energy values found within discrete (E_{ISP}) and distributed (E_{IPP}^{χ}) disclination models for several values of Poisson's ratio

Poison's ratio v	$E_{\rm ISP},G\omega^2a^3$	$E^{\chi}_{ m ISP},G\omega^2a^3$	$E_{ ext{ISP}}$ / $E_{ ext{ISP}}^{\chi}$
0	0.528	0.212	2.5
0.1	0.576	0.259	2.2
0.2	0.626	0.318	2.0
0.3	0.687	0.394	1.7
0.4	0.785	0.495	1.6
0.5	0.882	0.637	1.4

As can be seen from Tab. 1, for any positive values of Poison's ratio v, ISP energy in discrete disclination model is larger than in distributed disclination model: $E_{\rm IPP} > E_{\rm IPP}^{\chi}$, and

with a decrease in the Poisson's ratio v of the ISP material, the discrepancy in ISP energy within discrete and distributed models becomes larger.

Conclusions

In this work, we have presented the discrete disclination model of icosahedral small particles (ISPs). The discrete disclination model considers ISP as an elastic spheroid with six positive wedge disclinations passing through its center in opposite to the distributed disclination model based on conical stereo disclinations continuously distributed over spheroid volume. In order to calculate the stored (elastic) in ISP energy, the pair interaction energy of disclinations in a spheroid has been calculated for the first time as a function of the plane angle between wedge disclinations. It has been shown that for disclinations located strictly opposite each other, the energy of their interaction is equal to twice the elastic energy of the single disclination in the sphere. On the other hand, for disclinations located at right angles to each other, the interaction energy has zero value.

We have also analyzed the influence of Poison's ratio on the energy of ISP found within both discrete and distributed disclination models. It has been established that for any positive values of Poisson's ratio of ISP material, the stored energy calculated within the discrete disclination model demonstrates larger values than those calculated within the distributed disclination model. The differences are stronger, the smaller the value of Poisson's ratio.

Summarizing the findings, the discrete disclination model proposed opens the possibility to the strict analysis of icosahedral small particles.

References

- 1. Shechtman D, Blech I, Gratias D, Cahn JW. Metallic phase with long-range orientational order and no translational symmetry. *Physical Review Letters*. 1984;53(20): 1951–1953.
- 2. Cahn JW, Shechtman D, Gratias D. Indexing of icosahedral quasiperiodic crystals. *Journal of Materials Research*. 1986;1(1): 13–26.
- 3. Steurer W. Twenty years of structure research on quasicrystals. Part I. Pentagonal, octagonal, decagonal and dodecagonal quasicrystals. *Zeitschrift für Kristallographie Crystalline Materials*. 2004;219(7): 391–446.
- 4. Ino S. Epitaxial growth of metals on rocksalt faces cleaved in vacuum. II. Orientation and structure of gold particles formed in ultrahigh vacuum. *Journal of the Physical Society of Japan.* 1966;21(2): 346–362.
- 5. Galligan JM. Fivefold symmetry and disclinations. Scripta Metallurgica. 1972;6(2): 161–163.
- 6. Marks LD, Smith DJ. High resolution studies of small particles of gold and silver. *Journal of Crystal Growth*. 1981;54(3): 425–32.
- 7. Gryaznov VG, Heydenreich J, Kaprelov AM, Nepijko SA, Romanov AE, Urban J. Pentagonal Symmetry and Disclinations in Small Particles. *Crystal Research and Technology*. 1999;34(9): 1091–119.
- 8. Romanov AE, Kolesnikova AL. Elasticity boundary-value problems for straight wedge disclinations. A review on methods and results. *Reviews on Advanced Materials and Technologies*. 2021;3(1): 55–95.
- 9. Wu J, Qi L, You H, Gross A, Li J, Yang H. Icosahedral platinum alloy nanocrystals with enhanced electrocatalytic activities. *Journal of the American Chemical Society*. 2012;134(29): 11880–11883.
- 10. Ji G, Ji A, Lu N, Cao Z. Formation and morphology evolution of icosahedral and decahedral silver crystallites from vapor deposition in view of symmetry misfit. *Journal of Crystal Growth*. 2019;518: 89–94.
- 11. Liu M, Lyu Z, Zhang Y, Chen R, Xie M, Xia Y. Twin-directed deposition of Pt on Pd icosahedral nanocrystals for catalysts with Enhanced activity and durability toward oxygen reduction. *Nano Letters*. 2021;21(5): 2248–2254.
- 12. Sharma M, Pudasaini PR, Ruiz-Zepeda F, Vinogradova E, Ayon AA. Plasmonic effects of

Au/Ag bimetallic multispiked nanoparticles for photovoltaic applications. *ACS Applied Materials & Interfaces*. 2014;6(17): 15472–15479.

- 13. Fontana J, Dressick WJ, Phelps J, Johnson JE, Rendell RW, Sampson T et al. Virus-templated plasmonic nanoclusters with icosahedral symmetry via directed self-assembly. *Small*. 2014;10(15): 3058–3063.
- 14. Gutkin MY. Elastic behavior of defects in nanomaterials I. Models for infinite and semi-infinite media. *Reviews on Advanced Materials Science*. 2006;13(2): 125–161.
- 15. Ovid'ko IA, Sheinerman AG. Plastic deformation and fracture processes in metallic and ceramic nanomaterials with bimodal structures. *Reviews on Advanced Materials Science*. 2007;16: 1–9.
- 16. Romanov AE, Kolesnikova AL. Micromechanics of defects in functional materials. *Acta Mechanica*. 2021;232(5): 1901–1915.
- 17. Howie A, Marks LD. Elastic strains and the energy balance for multiply twinned particles. *Philosophical Magazine A*. 1984;49(1): 95–109.
- 18. Dorogin LM, Vlassov S, Kolesnikova AL, Kink I, Lõhmus R, Romanov AE. Crystal mismatched layers in pentagonal nanorods and nanoparticles. *Physica Status Solidi* (*B*). 2010;247(2): 288–298.
- 19. Lu L, Wang J, Zheng H, Zhao D, Wang R, Gui J. Spontaneous formation of filamentary Cd whiskers and degradation of CdMgYb icosahedral quasicrystal under ambient conditions. *Journal of Materials Research*. 2012;27(14): 1895–1904.
- 20. Vikarchuk AA, Dorogov M V. Features of the evolution of the structure and morphology of the surface of icosahedral copper particles in the annealing process. *JETP Letters*. 2013;97(10): 594–598.
- 21. Abramova AN, Dorogov MV, Vlassov S, Kink I, Dorogin LM, Lohmus R et al. Nanowhisker of copper oxide: fabrication technique, structural features and mechanical properties. *Materials Physics and Mechanics*. 2014;19: 88–95.
- 22. Romanov AE, Vikarchuk AA, Kolesnikova AL, Dorogin LM, Kink I, Aifantis EC. Structural transformations in nano- and microobjects triggered by disclinations. *Journal of Materials Research*. 2012;27(3): 545–551.
- 23. Grünbaum B. Regular polyhedra–old and new. Aequationes Mathematicae. 1977;16(1–2): 1–20.
- 24. Hargittai I. Fivefold symmetry. Budapest: World Scientific Publishing; 1992.
- 25. Kolesnikova AL, Gutkin MY, Proskura AV, Morozov NF, Romanov AE. Elastic fields of straight wedge disclinations axially piercing bodies with spherical free surfaces. *International Journal of Solids and Structures*. 2016;99: 82–96.
- 26. Polonsky IA, Romanov AE, Gryaznov VG, Kaprelov AM. Disclination in an elastic sphere. *Philosophical Magazine A*. 1991;64(2): 281–287.
- 27. Mura T, Barnett DM. Micromechanics of Defects in Solids. *Journal of Applied Mechanics*. 1983;50(2): 477–477.
- 28. Romanov AE, Vladimirov VI. Disclinations in crystalline solids. In: *Dislocations in solids*. Amsterdam: North-Holland; 1992.

THE AUTHORS

A.L. Kolesnikova 🗓

e-mail: anna.kolesnikova.physics@gmail.com

S.A. Krasnitckii 🗓

e-mail: Krasnitsky@inbox.ru

A.E. Romanov 🗓

alexey.romanov@niuitmo.ru

M.V. Dorogov 🗓

e-mail: mvdorogov@itmo.ru

A.M. Smirnov 🗓

e-mail: andrei.smirnov@niuitmo.ru

Determination of the formation energy of edge, screw and twinning dislocations in fcc metals using the molecular dynamics

Submitted: June 27, 2023

Approved: July 25, 2023

Accepted: August 14, 2023

G.M. Poletaev ^{1 ™}, R.Y. Rakitin ^{1 ™}

¹ Polzunov Altai State Technical University, Barnaul, Russia

²Altai State University, Barnaul, Russia

□ gmpoletaev@mail.ru

Abstract. A method is proposed for determining the energy of moving edge, screw, and twinning dislocations in fcc metals using molecular dynamics, which consists in constructing and analyzing the graph of the time dependence of the potential energy of the calculation area of the crystal through which the dislocation passes. Nickel, copper, silver, and austenite are considered as examples of fcc metals. The initiation of the formation and movement of a dislocation was carried out by simulating a shear at a constant rate from the end of the computational cell. It was found that the shear rate above about 40 m/s affects the energy of dislocation: with increasing rate, the energy of the dislocation increases. According to the data obtained, the energy of an edge dislocation is approximately one and a half times higher than the energy of a screw dislocation. The energy of a twinning dislocation in the model was obtained as a result of the splitting of a screw dislocation on the twin into two partial dislocations that slide along the twin after splitting.

Keywords: molecular dynamics; metal; dislocation; dislocation energy; twinning dislocation

Citation: Poletaev GM, Rakitin RY. Determination of the formation energy of edge, screw and twinning dislocations in fcc metals using the molecular dynamics. *Materials Physics and Mechanics*. 2023;51(6): 84-91. DOI: 10.18149/MPM.5162023 8.

Introduction

The formation, motion, and interaction of dislocations with each other and with other defects are important questions, the search for answers to which is necessary for the development of theory of the mechanisms of plastic deformation of crystalline materials. The variety of crystalline systems, slip systems and types of dislocations, as well as options for the interaction of dislocations with other defects, gives rise to the complexity of this phenomenon.

Dislocations in metals are the subject of many works, including those performed using computer simulation [1–5]. In addition to complex issues of the interaction of dislocations with each other and with various defects, attention in modern works is also paid to relatively simple questions: for example, the dependence of the dislocation glide rate on temperature and strain rate [3,6]. As the strain rate increases, as is known, the dislocation velocity first increases and then reaches a certain limit, which, as a rule, is less than the speed of sound in a given material. Moreover, different authors give different values of this limit in relation to the speed of sound [3,6–8]. With increasing temperature, as noted by most researchers, the dislocation slip rate decreases [3,6,7].

Earlier in [9], using the method of molecular dynamics, the sliding of edge and screw dislocations in a fcc metal was studied using nickel and silver as an example, depending on the

temperature and shear rate, as well as the effect of impurity atoms of carbon, nitrogen, and oxygen on the sliding speed of dislocations.

This work is devoted to the determination of the energy of formation of edge, screw, and twinning dislocations in fcc metals (nickel, copper, silver, and austenite) using the molecular dynamics method.

Theoretically, the dislocation energy W per unit of its length l is determined by the formula [7,10]:

$$\frac{W}{l} = \frac{\mu b^2}{4\pi K} \ln \frac{R}{r_0},\tag{1}$$

where μ is the shear modulus, b is the modulus of the Burgers vector, R is the radius of the computational area, and r_0 is the conditional radius. The parameter K depends on the type of dislocation: K=1 for a screw dislocation and $K=1-\nu$ for an edge one, where ν is Poisson's ratio.

The energy of a perfect edge dislocation is relatively high and can take values of 1-3 eV/Å for different metals [7,10,11]. Even in aluminum, with a relatively low binding energy of atoms, according to [11], the dislocation energy, depending on the orientation and the Burgers vector, can take values even up to several eV/Å.

Determination of the energy of edge and screw dislocations

To describe interatomic interactions in the metals under consideration, EAM potentials were used: Clery-Rosato [12] for modeling interactions in nickel, copper, and silver, and the Lau potential [13] for modeling interactions in γ -Fe. Both potentials have been repeatedly used in molecular dynamics models and have been successfully tested for a large number of structural, energy, and mechanical characteristics of the considered metals [12–16].

In fcc crystals, the {111}<110> slip system is predominant [7, 8]. The Burgers vector of a complete dislocation is 1/2<110>. A complete dislocation, as a rule, splits into two partial dislocations with Burgers vectors 1/6<112>, between which a stacking fault is formed.

To simulate a moving dislocation, in this work, we created a computational cell containing about 30,000 atoms (Fig. 1) with axes oriented: $X = [\overline{1}10]$, $Y = [\overline{1}\overline{1}2]$, Z = [111]. The XY plane in this case corresponds to the dislocation glide plane (111). To initiate the movement of a dislocation, a shift was created from the end face of the computational cell [17,18]. Figure 1 shows the scheme for creating a moving perfect edge dislocation $\frac{1}{3}[\overline{1}01](111)$. The shaded regions from the left end moved as a whole along the directions shown in the figure: in the case of modeling an edge dislocation, the upper part of the end moved along the closepacked direction $[\bar{1}01]$, the lower part – along the opposite direction $[10\bar{1}]$. In the case of modeling a screw dislocation, the upper part was displaced along the $[\bar{1}10]$ direction (X axis), while the lower part was displaced along the $[1\bar{1}0]$ direction. Atoms inside the shaded region were displaced during computer simulation only along the indicated directions with a constant shear rate V_{τ} . The boundary conditions on this side were thus rigid. Along the X axis, along the dislocation core, the boundary conditions were set to be periodic, i.e. an infinite repetition of the structure of the computational cell along the X axis was simulated. For other boundaries, we used a special type of boundary conditions – conditionally rigid: all boundary atoms from above, below, and on the right had the ability to move only along the XY plane, movement along the Z axis was excluded. This was enough to keep, on the one hand, the given rectangular shape of the computational block and, on the other hand, the free exit of dislocations outside the computational cell.

The time integration step in the molecular dynamics method was 2 fs. The temperature in the model was set in terms of the initial velocities of the atoms according to the Maxwell distribution. A Nose-Hoover thermostat was used to keep the temperature constant during the simulation.

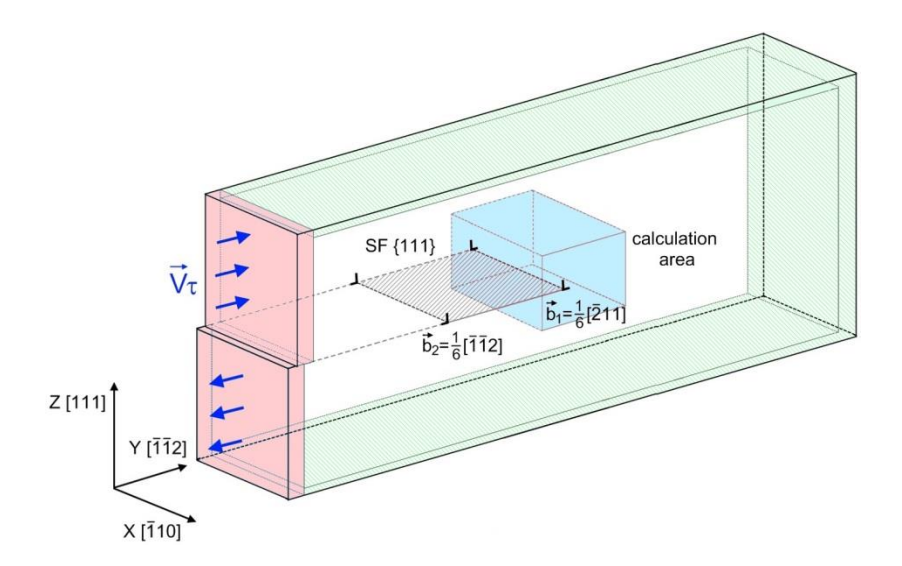


Fig. 1. To the description of the method for determining the energy of edge and screw dislocations

At some point in time, the shear in the left part of the computational cell provoked the appearance of a dislocation – edge or screw, depending on the shear direction. A dislocation appeared immediately in the form of a split into a pair of partial Shockley dislocations separated by a stacking fault in the (111) plane. For an edge dislocation, the splitting reaction had the form $\frac{1}{2}[\overline{1}01] \rightarrow \frac{1}{6}[\overline{2}11] + \frac{1}{6}[\overline{1}12]$, for screw dislocation – $\frac{1}{2}[\overline{1}10] \rightarrow \frac{1}{6}[\overline{1}2\overline{1}] + \frac{1}{6}[\overline{2}11]$. The distance between partial dislocations is known to be determined by the stacking fault energy [7,8]. In the present work, it was several nanometers (depending on the shear rate), which agrees with the results of modeling by other authors, for example [3–5].

During the movement of a dislocation through the calculation area (highlighted in color in the middle of the computational cell in Fig. 1), a graph of the change in the potential energy of the calculation area depending on time was plotted. The width of the calculation area was chosen such that, on the one hand, it was wider than the distance between partial dislocations (so that the entire complex of two partial dislocations could simultaneously fit in the calculation area) and, on the other hand, not so large that it could include part of the next dislocations. The temperature was set close to 0 K (more precisely, the starting temperature was 0 K, but in the process of creation and movement of the dislocation, the computational cell was heated to a low temperature of about 10 K).

First of all, in this work, we studied the effect on the obtained values of the energy of full dislocations (that is, the entire complex of two partial dislocations plus the stacking fault energy between them) of the width of the computational cell (the size along the X axis in Fig. 1) and the shear rate V_{τ} .

Figure 2 shows overlays of plots of changes in the specific energy of the calculation area (eV/Å) during the passage of a full edge dislocation in pure FCC iron at different widths of the computational cell (Fig. 2(a)) and different shear rates (Fig. 2(b)).

As can be seen, starting from 8 interatomic distances (approximately 20 Å), the width does not affect at all – the superimposed dependences repeat each other very well, the curves for different widths differ by no more than the value of ordinary fluctuations (it can be seen from the enlarged fragment in Fig. 2(a)). Up to 8 interatomic distances, as was shown in [16], the dislocation velocity can depend on the cell width.

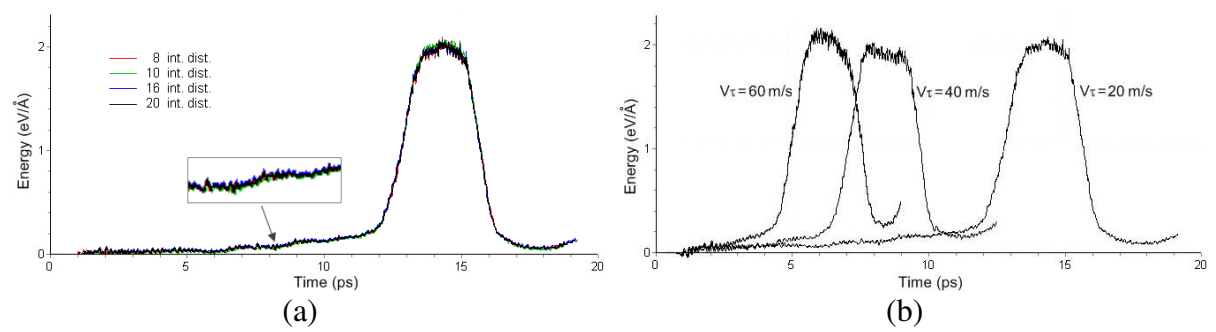


Fig. 2. Overlays of the change in the energy of the calculation area during the passage of an edge dislocation in γ -Fe: (a) at different widths of the computational cell (here, four graphs are superimposed at a width of 8, 10, 16, 20 interatomic distances); (b) at different shear rates (20, 40 and 60 m/s)

The shear rate V_{τ} , as it turned out, also has almost no effect on the height of the energy peak of the calculation area, but up to values of about 40–50 m/s. At a shear rate V_{τ} greater than 40–50 m/s, the energy slightly increases due to additional stresses and a smaller distance between neighboring dislocations. The velocity of the dislocations themselves also increases as they pass through the calculation area, which can be seen, for example, from the narrower peak for 60 m/s in Fig. 2(b). By the way, the dislocation velocity can also be determined from the width of this peak – this is another possible method for determining it. For the examples considered in the figure for austenite, its value was: 1500 m/s for a shear rate of 20 m/s, 1850 m/s for 40 m/s, and 2090 m/s for 60 m/s. In [19], we showed that with an increase in the shear rate, the dislocation slip velocity increases to a certain limit, which depends on the propagation velocity of the corresponding elastic waves: longitudinal in the case of an edge dislocation and transverse in the case of a screw one. For austenite, these are 5450 and 2865 m/s, respectively; for Ni, 5630 and 2960 m/s; for Cu, 4700 and 2260 m/s; for Ag, 3600 and 1590 m/s [8,10]. In further studies, the width of the computational cell was usually taken to be 10 or 12 interatomic distances.

Figure 3 shows a graph of the change in the energy of the calculation area for a screw dislocation in γ -Fe. It can be seen that the energy of a screw dislocation is noticeably lower than that of an edge one. The found energies of edge and screw dislocations in the metals under consideration are given below in the general table.

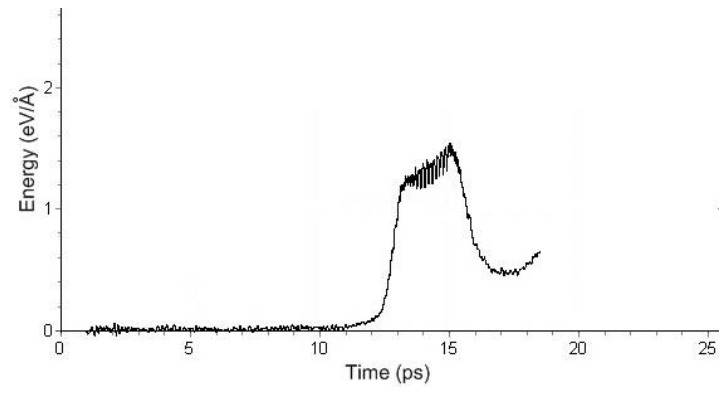


Fig. 3. Change in the energy of the calculation area during the passage of a screw dislocation in γ -Fe at a shear rate of 20 m/s

Determination of the energy of a twinning dislocation

Twinning dislocations are formed during the formation and migration of twins. As shown by molecular dynamics modeling in [16,20,21], when an edge dislocation overcomes a twin boundary and the slip plane changes, a twinning dislocation is formed at the boundary itself, which rapidly moves along the twin boundary, and if there is no obstacle to its movement, it "heals" the border [16]. The screw dislocation does not pass through the twin, but is absorbed by it, thus changing the glide plane [16,20,21]. This occurs at much lower stresses compared to edge dislocation. After changing the slip plane, both partial dislocations diverge in different directions along the twin boundary, "healing" the boundary, as in the case of the passage of an edge dislocation [16].

To calculate the energy of a twinning dislocation, it was assumed that the energy of twinning dislocations, which are formed during the passage of an edge dislocation and the splitting of a screw one, are the same. The method for determining the energy of a twinning dislocation resulting from the splitting of a screw dislocation at a twin boundary was as follows (Fig. 4). As in the case of an edge or screw dislocation, a similar graph was plotted for the change in the potential energy of the calculation area per unit of its width along the X axis in the process of splitting a screw dislocation on a twin. At the same time, to fix the moment of splitting of the screw dislocation on the twin, a graph of the displacement of the reference point located on the twin was displayed. The displacement of the reference point in this case was determined from the displacement relative to each other of two atoms located on opposite sides of the dislocation glide plane near the twin boundary. When splitting, which could be fixed by the peak of the displacement of the reference point, there was a slight decrease in the energy of the computational domain ΔE , caused by the disappearance of the stacking fault between partial dislocations. Partial dislocations changed the slip plane to the twin plane, which itself is, in fact, a stacking fault. The attraction between partial dislocations, which existed before the interaction with the twin and was due to the presence of a stacking fault, disappeared, which led to the repulsion of partial dislocations on the twin and their divergence in opposite directions (Fig. 4). The energy of a twinning dislocation was determined by the formula:

$$E_T = \frac{1}{2}(E_S - \Delta E),$$
 where E_S is the energy of a perfect screw dislocation. (2)

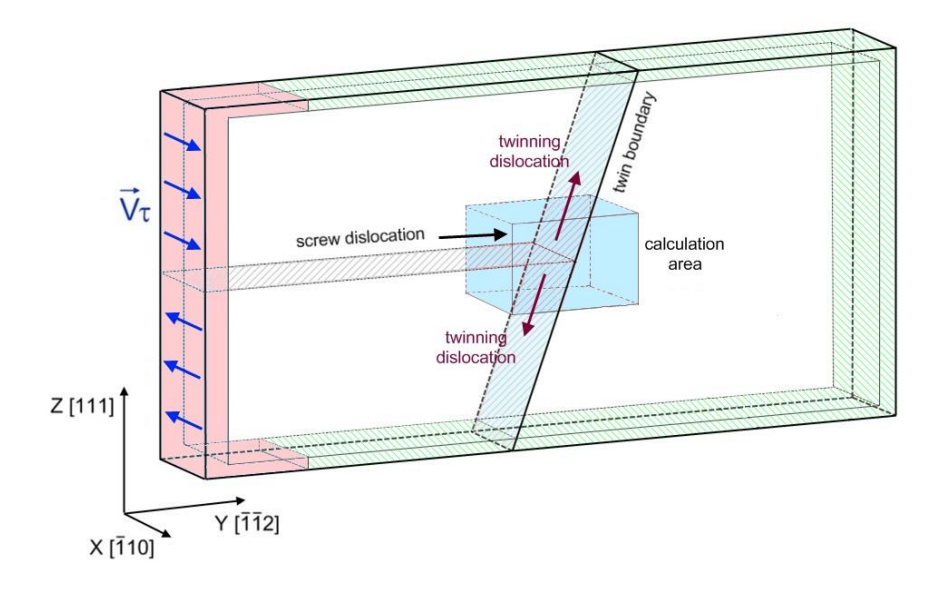


Fig. 4. To the description of the method for determining the energy of a twinning dislocation

Figure 5 shows an example of the change in the energy of the calculation area when a screw dislocation enters it and its subsequent splitting into two twinning dislocations. Comparing these graphs with the graphs of the passage of a screw dislocation through the calculation area in a pure crystal in Fig. 3, it should be noted that the width of the peaks is noticeably smaller, which means that the twinning dislocations leave the calculation area faster than the screw dislocation, i.e. they are more mobile, which was also noted in [16]. The Table 1 shows the obtained energies of edge, screw, and twinning dislocations.

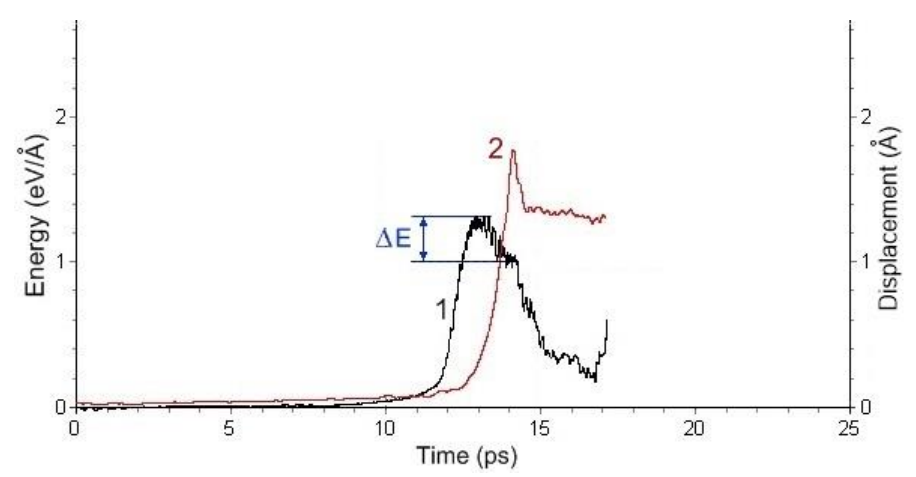


Fig. 5. Changes in the energy of the calculation area upon splitting of a screw dislocation into two twinning ones in γ -Fe at a shear rate of 20 m/s: 1 is the energy of the calculation area, 2 is the displacement of the reference atom on the twin boundary to determine the moment of splitting of the screw dislocation

Table 1. Edge, screw, and twinning dislocation energies in Ni, Cu, Ag, and γ-Fe (eV/Å)

	Edge	Screw	Twinning
Ni	1.7	1.1	0.4
Cu	1.0	0.6	0.2
Ag	0.7	0.5	0.2
γ-Fe	2.0	1.3	0.5

According to the data obtained, the energy of an edge dislocation is approximately one and a half times higher than the energy of a screw dislocation, which is consistent with theoretical formula (1). For the metals under consideration, the dislocation energies correlate with the elastic characteristics, which also agrees with formula (1). The energy of a twinning dislocation is substantially less than the energy of edge or screw dislocations. In fact, according to the method of obtaining it in the model, this is one of the partial dislocations that was formed during the splitting of a screw dislocation on a twin, so it should obviously be approximately two times lower than the energy of a full screw dislocation minus half the stacking fault energy between partial dislocations in the original screw dislocation.

Conclusion

A method is proposed for determining the energy of moving edge, screw, and twinning dislocations in fcc metals using molecular dynamics, which consists in constructing and analyzing the graph of the time dependence of the potential energy of the calculation area of the crystal through which the dislocation passes. Nickel, copper, silver, and austenite are considered as examples of fcc metals.

An edge or screw dislocation appeared in the simulation as a split into a pair of partial Shockley dislocations separated by a stacking fault. The distance between partial dislocations was several nanometers. At high shear rates, it decreased.

It was found that the shear rate affects the dislocation energy only up to values equal to approximately 40 m/s. At high velocities, the dislocation energy increases. In addition, it was found that, starting from 8 interatomic distances (approximately 20 Å), the width of the simulated computational cell with periodic conditions does not affect the obtained values of the dislocation energy.

According to the data obtained, the energy of an edge dislocation is approximately one and a half times higher than the energy of a screw dislocation. For the metals under consideration, the dislocation energies correlate with the elastic characteristics. The energy of a twinning dislocation is substantially less than the energy of edge or screw dislocations. The moving twinning dislocation in the model was obtained as a result of the splitting of a screw dislocation on the twin into two partial dislocations that slide along the twin after splitting.

References

- 1. Chen C, Meng F, Ou P, Lan G, Li B, Chen H, Qiu Q, Song J. Effect of indium doping on motions of <a>-prismatic edge dislocations in wurtzite gallium nitride. *Journal of Physics: Condensed Matter.* 2019;31(31): 315701.
- 2. Olmsted DL, Hector Jr LG, Curtin WA, Clifton RJ. Atomistic simulations of dislocation mobility in Al, Ni and Al/Mg alloys. *Modelling and Simulation in Materials Science and Engineering*. 2005;13(3): 371–388.
- 3. Zhao Sh, Osetsky YuN, Zhang Y. Atomic-scale dynamics of edge dislocations in Ni and concentrated solid solution NiFe alloys. *Journal of Alloys and Compounds*. 2017;701: 1003–1008.
- 4. Rodney D, Ventelon L, Clouet E, Pizzagalli L, Willaime F. Ab initio modeling of dislocation core properties in metals and semiconductors. *Acta Materialia*. 2017;124: 633–659.
- 5. Hunter A, Beyerlein IJ, Germann TC, Koslowski M. Influence of the stacking fault energy surface on partial dislocations in fcc metals with a three-dimensional phase field dislocations dynamics model. *Physical Review B*. 2011;84(14): 144108.
- 6. Po G, Cui Y, Rivera D, Cereceda D, Swinburne TD, Marian J, Ghoniem N. A phenomenological dislocation mobility law for bcc metals. *Acta Materialia*. 2016;119: 123–135.
- 7. Friedel J. Dislocations. Oxford: Pergamon press; 1964.
- 8. Hirth JP, Lothe J. Theory of Dislocations. 2nd ed. NY: Wiley; 1982.
- 9. Poletaev GM, Zorya IV. Effect of light element impurities on the edge dislocation glide in nickel and silver: molecular dynamics simulation. *Journal of Experimental and Theoretical Physics*. 2020;131(3): 432–436.
- 10. Cahn RW, Haasen P. *Physical Metallurgy*. 3th ed. Amsterdam: North-Holland Physics Publishing; 1983.
- 11. Zhou XW, Sills RB, Ward DK, Karnesky RA. Atomistic calculations of dislocation core energy in aluminium. *Physical Review B*. 2017;95(5): 054112.
- 12. Cleri F, Rosato V. Tight-binding potentials for transition metals and alloys. *Physical Review B*. 1993;48(1): 22–33.
- 13. Lau TT, Forst CJ, Lin X, Gale JD, Yip S, Van Vliet KJ. Many-body potential for point defect clusters in Fe-C alloys. *Physical Review Letters*. 2007;98(21): 215501.
- 14. Lv B, Chen C, Zhang F, Poletaev GM, Rakitin RY. Potentials for describing interatomic interactions in γFe-Mn-C-N system. Metals. 2022;12(6): 982.
- 15. Poletaev GM. Self-diffusion in liquid and solid alloys of the Ti–Al system: molecular-dynamics simulation. *Journal of Experimental and Theoretical Physics*. 2021;133(4): 455–460.

- 16. Chen C, Zhang F, Xu H, Yang Z, Poletaev GM. Molecular dynamics simulations of dislocation—coherent twin boundary interaction in face-centered cubic metals. *Journal of Materials Science*. 2022;57: 1833–1849.
- 17. Poletaev GM, Rakitin RY. Molecular dynamics study of stress-strain curves for γ -Fe and Hadfield steel ideal crystals at shear along the <111> direction. *Materials Physics and Mechanics*. 2021;47(2): 237–244.
- 18. Poletaev GM, Rakitin RY. Molecular dynamics simulation of severe plastic deformation of nanotwinned Hadfield steel. *Materials Physics and Mechanics*. 2022;50(1): 118–125.
- 19. Zorya IV, Poletaev GM, Rakitin RY. Energy and velocity of sliding of edge and screw dislocations in austenite and Hadfield steel: molecular dynamics simulation. *Steel in Translation*. 2022;52(12): 1121–1126.
- 20. Jin Z-H, Gumbsch P, Ma E, Albe K, Lu K, Hahn H, Gleiter H. The interaction mechanism of screw dislocations with coherent twin boundaries in different face-centred cubic metals. *Scripta Materialia*. 2006;54(6): 1163–1168.
- 21. Chassagne M, Legros M, Rodney D. Atomic-scale simulation of screw dislocation/coherent twin boundary interaction in Al, Au, Cu and Ni. *Acta Materialia*. 2011;59(4): 1456–1463.

THE AUTHORS

Poletaev G.M. © e-mail: gmpoletaev@mail.ru

Rakitin R.Y. 🗓

e-mail: movehell@gmail.com

Nanomaterials coating for bio-implant applications: a re-analysis

Submitted: January 7, 2023

Approved: February 1, 2023

Accepted: February 20, 2023

N. Kumar ^{10 1 ⊠}, A. Bharti ^{10 2}, A. Kumar ^{10 2}, R.K. Kushwaha ², K.K. Patel ^{10 2}

¹ Sanjivani College of Engineering, Kopargaon, India
 ² Motilal Nehru National Instutute of Technology Allahabad, Prayagraj, India
 *kumarnaveenmkcoe@sanjivani.org.in

Abstract. Bio-implants are inserted in the body to support the natural part of body either fractured or partially failed. Therefore, bio-implant should be compatible with the body; must not produce harmful effect to body tissues or organs. As body environment is corrosive in nature; the implant should have high corrosion resistance. Also, it should have high strength and low percentage elongation. Additionally, implant material must allow the growth of tissues so that high bonding between the implant and body tissue can be achieved. Based on all the above-mentioned requirements for being a good implant material, titanium, steel, cobaltchromium alloys, etc. are most widely used as implants. To further enhance the mechanical and biological properties of implants, different types of coating and surface modifications are done. Coating thickness, type of coating, and coating deposition techniques significantly affects the properties of an implant. In the present work, effects of the above-mentioned parameters are studied on the mechanical and biological properties of the implants. It was observed that the biocompatibility and wettability of polymer coatings were relatively less in comparison to ceramic and composite coatings. On the other hand, ceramic coatings were highly biocompatible and wettability was also high. For metallic coating, biocompatibility was less because of high reactivity. But, metals (like Bi) that form protective oxide layer on the surface of implants exhibits very good biocompatibility and mechanical strength.

Keywords: biological properties; coating; Implant; mechanical properties

Citation: Kumar N, Bharti A, Kumar A, Kushwaha RK, Patel KK. Nanomaterials coating for bio-implant applications: a re-analysis. *Materials Physics and Mechanics*. 2023;51(6): 92-106. DOI: 10.18149/MPM.5162023_9.

Introduction

Bio-implants are used to support or replace the partially functional or non-functional part of a living body. Use of implants started in the ancient times itself when glass eyes, gold filled teeth, wooden leg were used to replace the failed body parts [1]. Now, with the development of technology, use of implants have been increased tremendously. Now implants for almost all the body parts such as eye, teeth, breast, hip, knee, etc. are available. Fig.1 shows the use of implants for human body [2].

Primary function of implant material is to support the fractured body parts, so the strength of implant materials should be high enough to bear the body weight [3]. As an implant is inserted inside the living body. So, along with having sufficient mechanical properties, biological properties of an implant material should also be similar or better than the natural part. A schematic diagram of hip implant and various properties required in an implant material are shown in Fig. 2 [4].

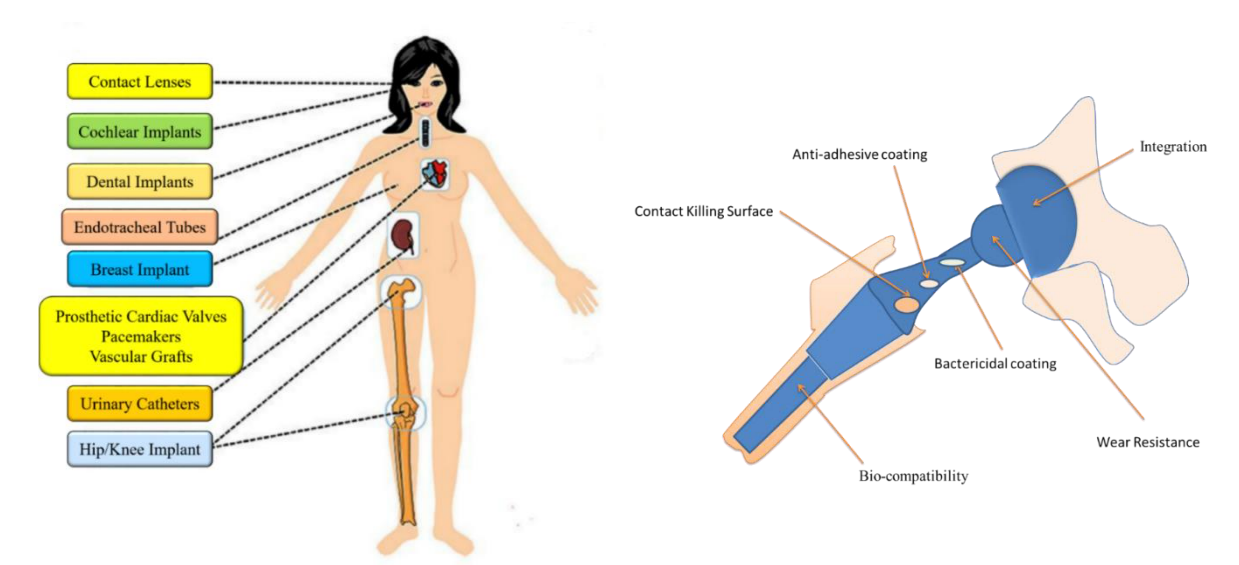


Fig.1. Use of implants

Fig. 2. Schematic diagram of hip implant and various properties required in an implant material

Considering the criticality of implant, the selection of appropriate material for implants become very important [5]. Some of the properties that are required in a good implant material are as follows:

- 1. It should have strength comparable to natural bone;
- 2. Percentage elongation should be very low;
- 3. It should be biocompatible;
- 4. It should not release toxic elements;
- 5. It must support the growth of tissue;
- 6. Ability to resist viral infections or contamination.

Most commonly used materials for implants like titanium (Ti), Ti alloys, stainless steel 316L (SS 316L), Co-Cr alloys, tantalum alloys, composites, ceramics, and polymers are given in Table 1 [6]. These materials are widely used in medical equipment because of their good corrosion resistance, and high strength [7,8].

Table 1. Implant materials and their applications

Tuble 1. Implant materials and then applications			
Biomaterials	Applications		
Stainless Steel	Hip and knee joint implant, dental implants, spinal, heart valve, hip nail, bone plate, shoulder prosthesis.		
Titanium Alloys	Cochlear implant, dental implants, orthodontic implant structure, artificial heart valves, bone and joint replacements, and pacemakers.		
Cobalt Chromium Alloys	Total joint replacements (hip and knee) mini plates, bone plates, screws, dental implants, orthopaedic implants.		
Alumina	Acetabula, femoral components, vertebral spacer and extensor, orthodontic anchors, dental implants, and artificial complete joint replacement.		
Zirconia	Replacement of hips, knees, tendons, ligaments, periodontal disease treatments, and bone fillers.		
Calcium Phosphate	Dental implants for throat repair, skin treatments, dental fillings, jawbone reconstructions, orthopaedic coatings on implants, and facial surgery.		

Problems with implant materials

Infection of the implant by microbial contamination on implant surfaces or adjacent tissue is one of the main problems of implant failure, as microorganisms can readily adhere to and then grow on implant surfaces [9,10]. This type of transplant infection often occurs in different parts of the human body. In addition, the open wound created during the implant placement process creates the right conditions for microbes to adhere, grow and multiply. Although the host's immune response is activated, this response is often insufficient to clear the infection around the implantation site [11,12].

Infections associated with biomedical devices and implants (e.g., catheters, heart valves, and hip and knee implants) remain a major risk for their long-term usage despite extensive research and development efforts [13]. Bacteria can apparently cling to and colonise a wide range of biomedical devices, resulting in a difficult-to-treat infection. Infections, lengthy hospitalisation, difficult revision operations, transplant failure, patient misery, financial load, and even death are some of these. As a result, the necessity to eliminate germs or limit bacterial colonisation is growing.

Infections, corrosion, wear, excessive inflammation, severe toxicity, poor osseointegration, and foreign body effects are all factors that shorten the life of orthopaedic implants [14]. Infection may cause the patient to suffer for a long time and eventually die. Corrosion and wear wreak havoc on a structure's structural integrity. However, the implants cause toxicity. Our immune system may mistake the implant material for a pathogen. System, causing chronic inflammation and foreign body reactions, which can lead to death. A local and most effective technique for resolving these issues and extending the life of implants is to coat them with biocompatible and bioactive material. Coatings transport biologicals directly to the injury site, allowing them to work more precisely than pharmaceuticals.

Requirement of coatings

The principle of bone on-growth or in-growth is linked to the optimal shape (design) of an implant, as well as its material, surface topography, and chemistry [15]. The materials typically utilised for orthopaedic implants, stainless steel and titanium (alloys), have differences or rather benefits in strength, ductility, stiffness, or cell responsiveness, and must be considered according to the medical necessity [16,17]. The implant's design can compensate for mechanical flaws, but host cells and bacteria have different reactions to the material [18]. The disadvantages of electropolished steel (smooth surface) implants are imaging artefacts, possible implant migration, release of toxic/allergic ions such as cobalt, chromium, nickel, and higher infection risk, according to preclinical research and clinical experience, whereas the disadvantages of rougher titanium implants are removal complications due to better osteointegration [19,20]. Polymers, such as PEEKs (polyetheretheretherketone), are primarily employed in the field of spine surgery as a radiolucent alternative to metallic implants, however due to biomechanical constraints when compared to titanium or stainless steel, a general application has yet to be established [21,22]. Because solid metal implants, particularly those made of cobalt-chrome or steel, have a lower degree of osteointegration than pure titanium, zirconium, and/or titanium-based coatings, they can be withdrawn more quickly (temporary implants) [23]. The surface chemistry (hydrophilic vs. hydrophobic) and the surface topography, specifically the roughness, are the primary determinants impacting osteointegration, in addition to the material's biological compatibility. If osteointegration is to be enhanced, specific material selection, surface modification, or extra coatings are required (permanent implants) [24]. Chemical, physical, and biological requirements are the most important for this purpose [25]. For an implant coating to promote osteointegration, biocompatibility is an obvious necessity. Despite the fact that various materials and surface modifications are utilised to maximise implants, comparative studies proving the evidence for

"the best" material, surface condition, or coating are still lacking. Another need is that the material's properties be preserved during use, and that the biological interaction in the body has no detrimental consequences. Coatings can address the tendency of wear and corrosion in an in vivo environment, which can result in particle loosening or the release of hazardous substances [26]. Implant-derived wear particles activate cells of the innate and adaptive immune systems, such as macrophages and lymphocytes, triggering an inflammatory response marked by the release of cytokines, chemokines, and growth factors, which can lead to osteolysis and bone loss due to increased osteoclast activity and necrosis [27]. In the creation of new coatings or the translation of authorised coatings into new applications, this in vivo interaction of the material must be taken into account. Another criterion is that the coating stay on the surface of the implant at least until it reaches its desired position and can perform its function.

Temperature resistance of the implant material to the temperature introduced during the coating or surface-structuring process is a production requirement. For example, the temperature during a plasma spray process for HA can exceed 500 °C, whereas it can exceed 1000 °C for calcium phosphates [28,29]. Laser structuring raises the surface temperature well over the boiling point of the substrate (e.g., 3260 °C for titanium). The influence of temperature, particularly for metallic implants, can cause metallurgical changes, necessitating further biomechanical considerations. Surface alteration (blasting, etching) and porous coatings can cause fracture initiation, which has been shown to affect biomechanical needs for fatigue and bending strength. Other obvious needs are the ability to sterilise the final implant without causing any unwanted effects, and the ability to meet the requisite shelf life without causing undesirable changes in the features over time.

Bioactive coatings

The demand to replace and restore damaged tissues has increased in tandem with the general population's longevity. This is especially true in dentistry and orthopaedics, where prosthetic implants have restored structure and function. These surgeries have been incredibly successful, and they have improved the lives of a lot of individuals. For the most part, this success can be credited to the body's ability to integrate with the implants. In exchange, implant materials and surface qualities that most effectively trigger bodily responses have been adopted. The implants' surface can be altered in a variety of ways, either directly or by applying a coating.

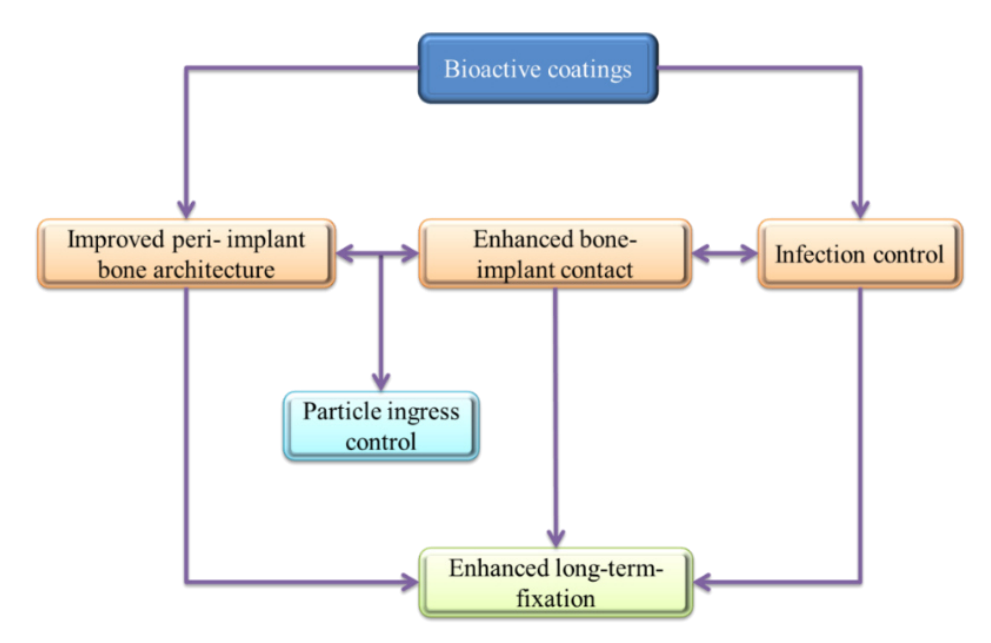


Fig. 3. Potential mechanisms of action of bioactive coatings

The goal of improving long-term mechanical fixation of the implant is based on the assumption that a stable bond between the implant and the host bone will contribute to long-term clinical success. Even if a bioactive coating does not allow an implant to perform its intended function for a longer amount of time (i.e., enhance survivorship), it would be useful to reduce the time required to achieve fixation. The implant surface can be affected by topography, chemistry, and surface energy in a broad sense. Potential mechanisms of action of bioactive coatings are shown in Fig. 3.

All implants are viewed as alien objects by the body, they stimulate a biological response in the form of a "non-self" material to counteract any negative consequences. This reaction is influenced by both implant-related and host-related factors. Implant-related aspects that are influenced by the physical, chemical, and biological features of the implant surface are discussed here. Tissue-related parameters such as the implant site, patient gender and age, tissue integrity, and systemic diseases are not discussed in any depth. The reader should be aware, however, that the biological response to a specific implant is not expected to be consistent across all patients. The features of the implant's manufacturing material, in general, impact the body's reaction to it. The word bio-inert refers to the absence of a reaction to the implant. In reality, when bio-inert materials are introduced in body, they interact very less with the surrounding tissue, resulting in a minimum response. As a result, a fibrous membrane forms around the implant has no effective bonding with body [30]. Bioactive materials, on the other hand, initiate a chain of events that leads to the production of new extracellular matrix, which, in the best-case scenario, forms in intimate contact with the implant and results in mechanical fixation.

Effect of different types of coatings

There are various types of coating materials such as polymer, metals, ceramics, composites, etc. Depending on the nature of coating materials and their interaction with the substrate, properties of a coated implant are very much different from the uncoated implant. As, polymers have high resistance to corrosion and are hydrophobic in nature. Polymer coating improve the corrosion resistant reduces the swelling. Metals are more reactive in comparison to polymers, so metallic coating reacts with oxygen to form metallic oxides. Metallic oxides are very less reactive and biocompatible in nature. Metallic coating also forms strong bond with metallic substrate. So, metallic coating improves the strength and biocompatibility of the implant. Ceramic and composite coatings also improves the biocompatibility and other properties of implants. Effect of different type of coatings on various properties of implants are studied below.

Bond strength. Bond strength is the measure of bonding between the coating material and substrate. High bond strength is desirable because high bond strength enhance the coating stability and life. The variation in bond strength of Ti alloy with different coating materials is shown in Fig. 4. It can be observed that the significant bond strength was obtained in all the coated Ti₆Al₄V implants. Ghaleh et al. investigated the effect of akermanite (tricalcium magnesium silicate) coating on the bond strength of coated Ti6Al4V titanium alloy [31]. Bond strength of 40.5 MPa was observed. Xue et al. investigated the effect of diopside (CaMgSi₂O₆) coating on the bond strength of coated Ti₆Al₄V titanium alloy [32]. Bond strength of 32.5 MPa was obtained. Yi et al. done the bredigite coating on the Ti₆Al₄V alloy and investigated the bond strength of the coated titanium alloy [33]. Highest bond strength of 49.8 MPa was observed in the Ti alloy coated with bredigite. Li et al. coated the titanium alloy Ti₆Al₄V with monticellite hardystonite (Ca₂ZnSi₂O₇) and investigated the bonding strength [34]. Bonding strength obtained was around 33.4 MPa. Liang et al. studied the effect of baghdadite ceramic coating on the bond strength of Ti₆Al₄V titanium alloy [35]. Lowest bonding strength of 28 MPa was obtained. Wu et al. investigated the effect of ceramic coating of Sr₂MgSi₂O₇ on the titanium alloy substrate on the bonding strength [36]. Bonding strength of 37 MPa was observed. So, it

can be concluded that the ceramic bredigite forms strong bond with the titanium alloy Ti_6Al_4V and hence the strength and life of coating will be more in comparison to other ceramic coatings. As, the implants are intended to work satisfactory for 5–15 years, so the bredigite coated titanium alloy will be preferred.

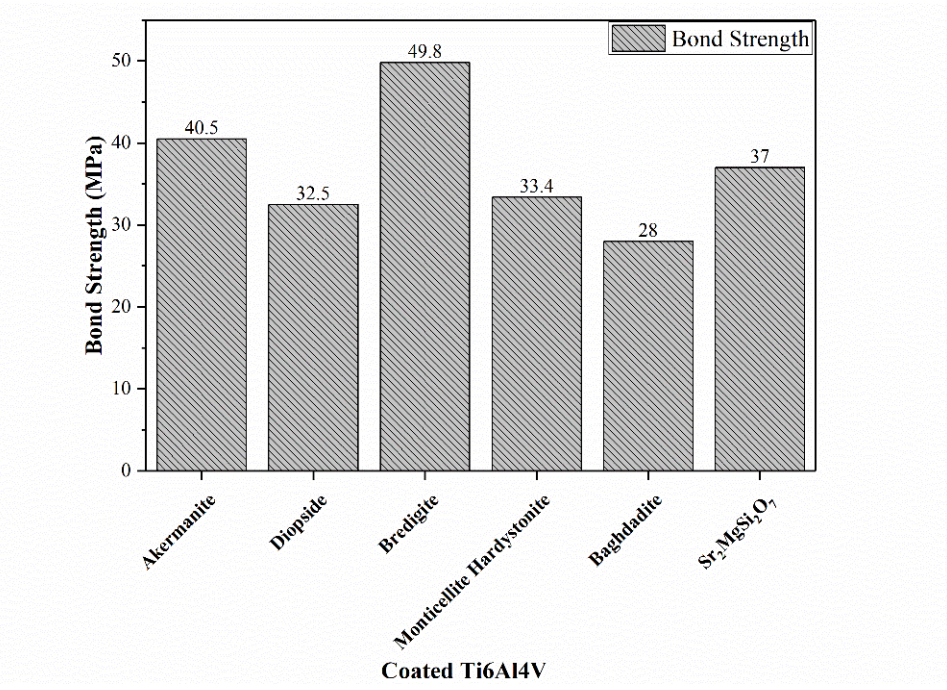


Fig. 4. Variation in bond strength of Ti alloy with different ceramic coating materials. Based on data [31–36]

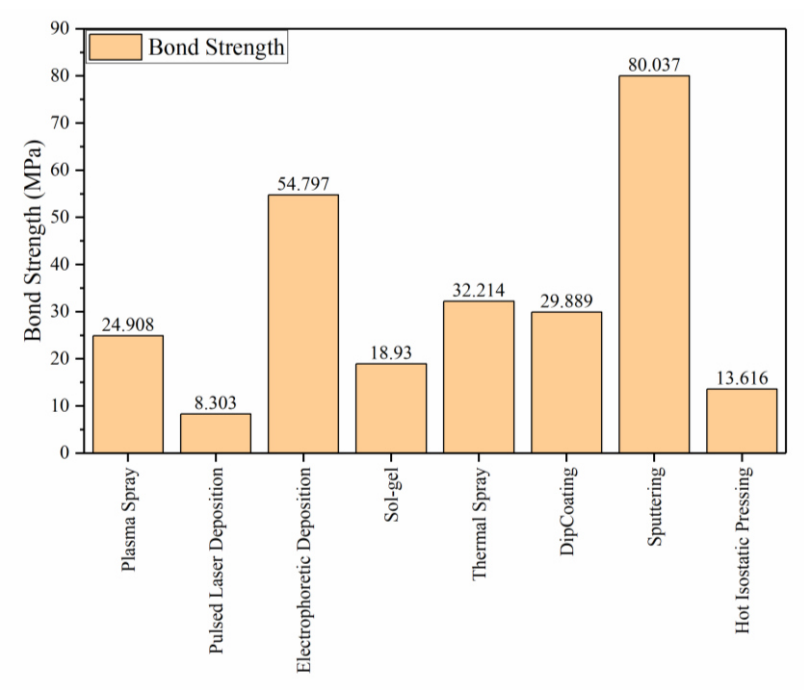


Fig. 5. Bond strength of hydroxyapatite coting over Ti₆Al₄V deposited by different coating technique. Based on data [37]

Coating technique also has a significant effect on the properties of coating. The effect of coating techniques on the bond strength of hydroxyapatite coated Ti₆Al₄V titanium alloy was studied by Mohseni et al. [37]. Bond strength of hydroxyapatite coting over Ti₆Al₄V deposited by different coating technique is shown in Fig. 5. It can be observed that the highest bond strength was obtained for hydroxyapatite coated by sputtering technique. On the other hand, the lowest bond strength was observed for pulsed laser deposited hydroxyapatite coating over Ti₆Al₄V substrate.

Contact angle. Contact angle is the measure of wettability of a coating material. Low contact angle (less than 90°) signifies the hydrophilic nature of coating, while high contact angle (more than 90°) signifies the hydrophobic nature of coating. High wettability (low contact angle) is desired for a coating material because wettability increase the proliferation, cell attachment, and mutual interaction of cells. Variation in contact angle of Ti alloy with different coating materials is shown in Fig. 6.

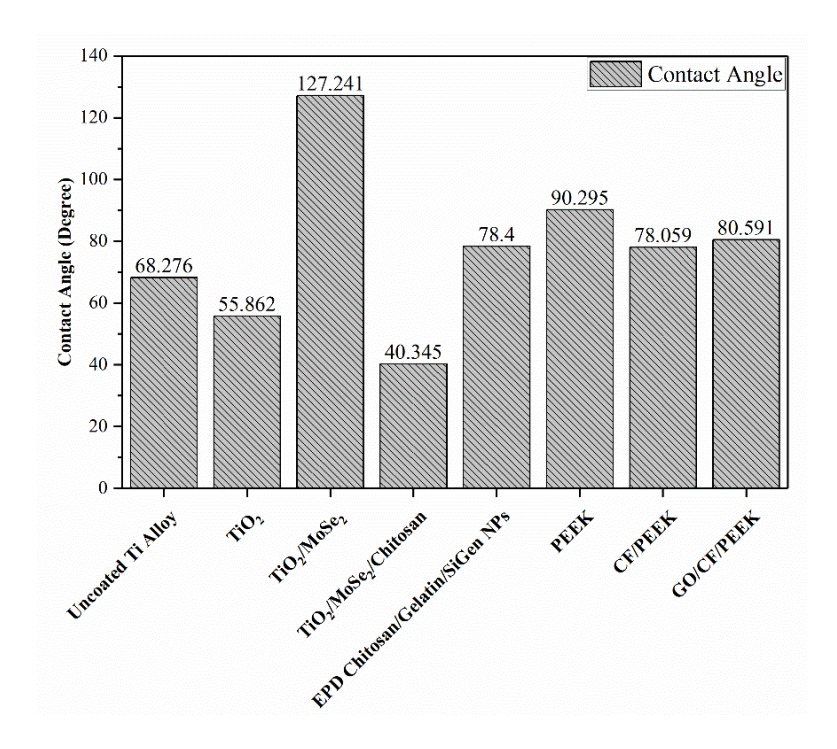


Fig. 6. Variation in contact angle of Ti alloy with different coating materials. Based on data [38–40]

Chai et al. [38] coated the titanium alloy with three different materials namely TiO₂, TiO₂/MoSe₂, and TiO₂/MoSe₂/Chitosan. It was observed that the lowest contact angle of 40.345° was obtained for TiO₂/MoSe₂/Chitosan coated sample. This indicates that TiO₂/MoSe₂/Chitosan enhance the wettability and will be helpful in combating infections. Aydemir et al. [39] investigated the effect of bioactive glass (Chitosan/Gelatin/SiGenNPs) composite coating on the contact angle of titanium alloy coated by electrophoretic deposition (EPD) technique. It was observed that the contact angle increased slightly. And hence the wettability reduced. Similar effect of polymer and composite coatings i.e., PEEK, carbon-fibre/PEEK (CF/PEEK), and graphene oxide/carbon-fibre/PEEK (GO/CF/PEEK) on the contact angle of coated titanium alloy was observed by Qin et al. [40].

Cell viability. Cell viability is the measure of biocompatibility of an implant material. If cell viability is high, then the fracture of living and healthy cells in the population is high. So, high value of cell viability is desirable. Hence, the coating materials that increase the cell viability will be preferred. Variation in cell viability of Ti and Mg alloys with different coating materials is shown in Fig. 7. Qin et al. [40] investigated the biocompatibility of titanium alloy

coated with polymer (PEEK) and composites (CF/PEEK and GO/CF/PEEK). It was observed that the highest cell viability was observed for PEEK coated titanium alloy. Hence, the PEEK coated titanium alloy was most biocompatible. But, the wettability was low for PEEK coated titanium alloy (Fig.6).

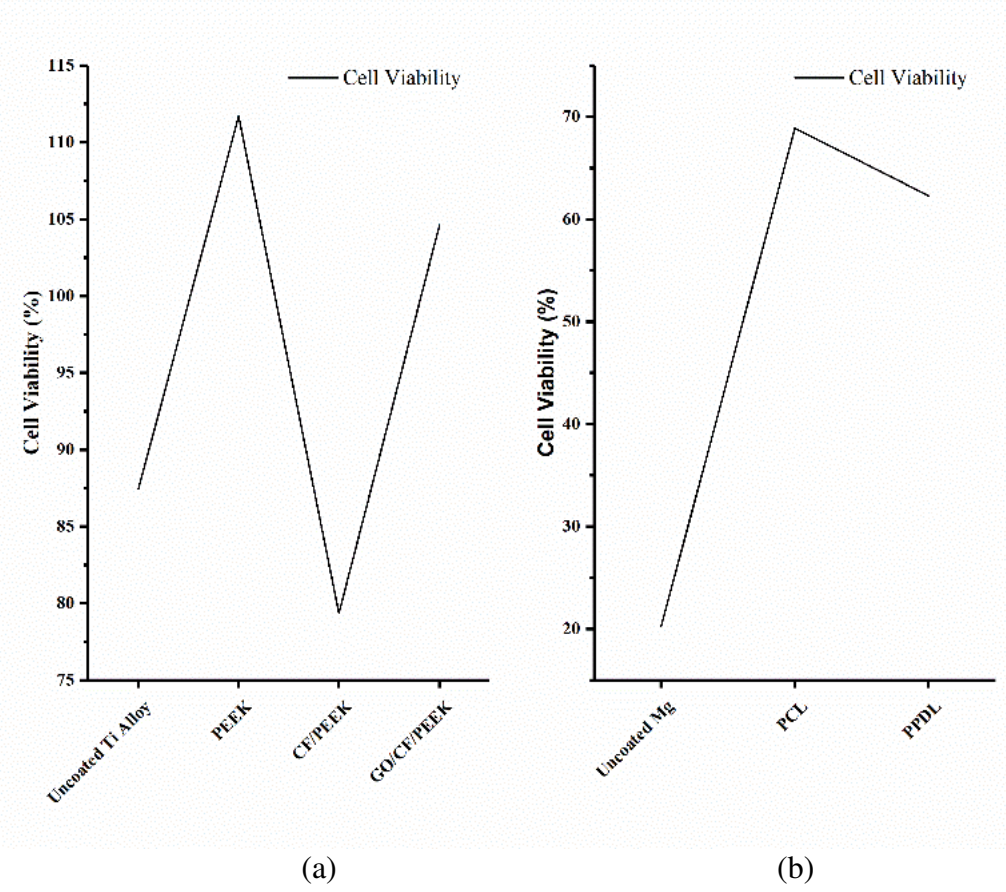


Fig. 7. Variation in cell viability of Ti alloy (a) and Mg (b) with different coating materials. Based on data [40-42]

For GO/CF/PEEK coated titanium alloy, both the wettability and the cell viability were high. Hence, the composite GO/CF/PEEK coating is preferable for titanium alloys. Ritwik et al. also investigated the biocompatibility of titanium alloy coated with chitosan [41]. It was observed that the cell viability enhanced after the chitosan coating over the titanium substrate.

Mahapatro et al. investigated the effect of polymer coatings on the biocompatibility of coated magnesium alloys [42]. It was observed that the cell viability was increased after the coatings of poly-caprolactone (PCL) and poly-pentadecalactone (PPDL) on the magnesium alloy. Highest cell viability was observed for the magnesium substrate coated with PCL. Hence, PCL is a better coating material for magnesium alloy if high biocompatibility is desired.

Surface roughness. Surface roughness is also one of the important property of an implant material. If surface roughness is high, tissues growth in the cavities will be high [43]. High tissue growth in cavities enhance the bonding between the implant and tissue. So, high surface roughness is desirable. Variation in surface roughness of steel and Ti alloy with different coating materials is shown in Fig. 8.

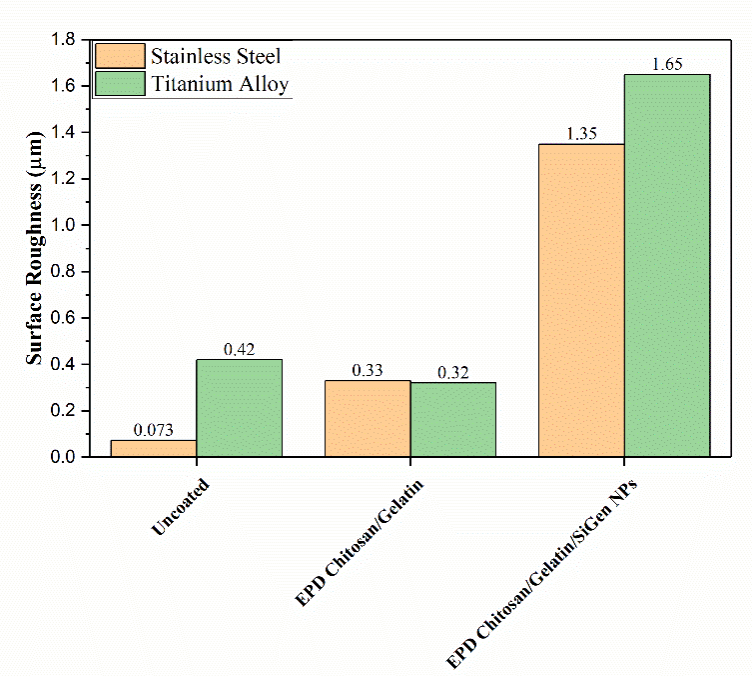


Fig. 8. Variation in surface roughness of steel and Ti alloy with different coating materials. Based on data [39,43]

It can be observed that the surface roughness increased after the composite coatings of chitosan/gelatin and chitosan/gelatin/SiGenNPs over the stainless steel substrate [39]. On the other hand, coating of chitosan/gelatin over titanium alloy slightly reduced the surface roughness. Surface roughness of chitosan/gelatin/SiGenNPs coated titanium sample was highest. Hence, chitosan/gelatin/SiGenNPs composite coating deposited by electrophoretic deposition technique is useful for both titanium alloys and stainless steel implants.

Oxide formation. Oxide formation is an important property for a metallic coating material. Metallic oxides are generally very less reactive and biocompatible in nature. Hence, the high oxide formation at the surface is desirable for an implant material.

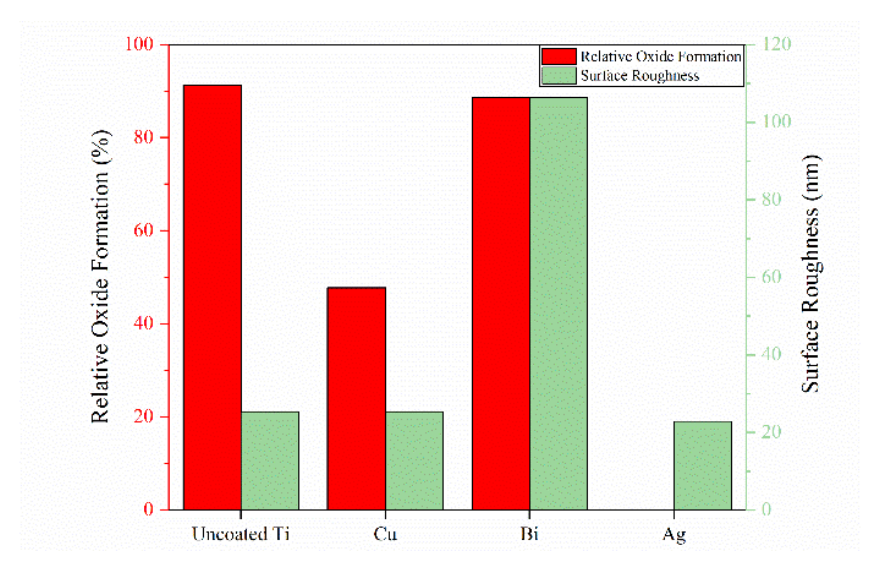


Fig. 9. Variation in oxide formation and surface roughness of Ti alloy with different coating materials. Based on data [44]

Gosau et al. investigated the oxide formation and surface roughness of coated and uncoated titanium implant materials [44]. Variation in oxide formation and surface roughness of Ti alloy with different coating materials is shown in Fig. 9. It can be observed that for the uncoated titanium sample, oxidation was high, but surface roughness was low. Bi coating enhanced the surface roughness and oxide formation was also very high (around 89 %). On the other hand, oxide formation was negligible in Ag coated sample because of very low reactivity of Ag. Oxide formation was around 50 % in Cu coated sample. Hence, the Bi is a very suitable coating material for titanium alloy implants.

Hardness. Surface hardness of an implant is dependent on the coating material. Higher the hardness, lower will be wear rate. So, the addition of hard coating over implant, reduces its wear and scratch and enhance its life. The effect of coating materials on the surface hardness of implants was studied by Vladescu et al. [45]. Surface hardness of implants with different coating materials is shown in Fig. 10. It can be observed that the highest hardness was obtained for an implant coated with diamond like carbon (DLC).

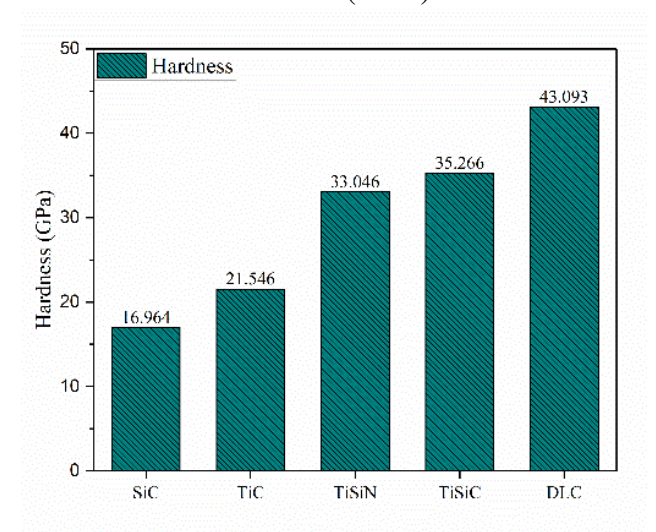


Fig. 10. Surface hardness of implants with different coating materials. Based on data [45]

Effect of coating thickness and processing parameters on bond strength

Coating thickness and processing parameters also have significant effect on the bond strength. Effect of these parameters on the bond strength is studied in detail in the following subsections.

Effect of coating thickness. Coating thickness is having a significant effect on the properties of a coated material. As an implant, it is used inside the body. So, it will work inside a corrosive environment. In a corrosive environment, materials dissolve at a higher rate. Hence, the thickness of a coating should be sufficient that it will last for the intended working life of the implant material. Coating thickness also affects other properties such as cell viability, corrosion resistance, surface roughness, and bond strength. Effects of coating thickness on the above-mentioned properties are studied in the following sections.

Kuo et al. investigated the effect of parylene coating thickness on the bond strength, cell viability, and surface roughness of the NiTi alloy [46]. Variation in bond strength, cell viability, and surface roughness with coating thickness is shown in Fig. 11,12. It can be observed that the cell viability decreased with an increase in the coating thickness. On the other hand, bond strength increased with an increase in the coating thickness. Surface roughness also increased initially with an increase in the coating thickness. On further increasing the coating thickness (beyond 5 μ m), surface roughness decreased [46].

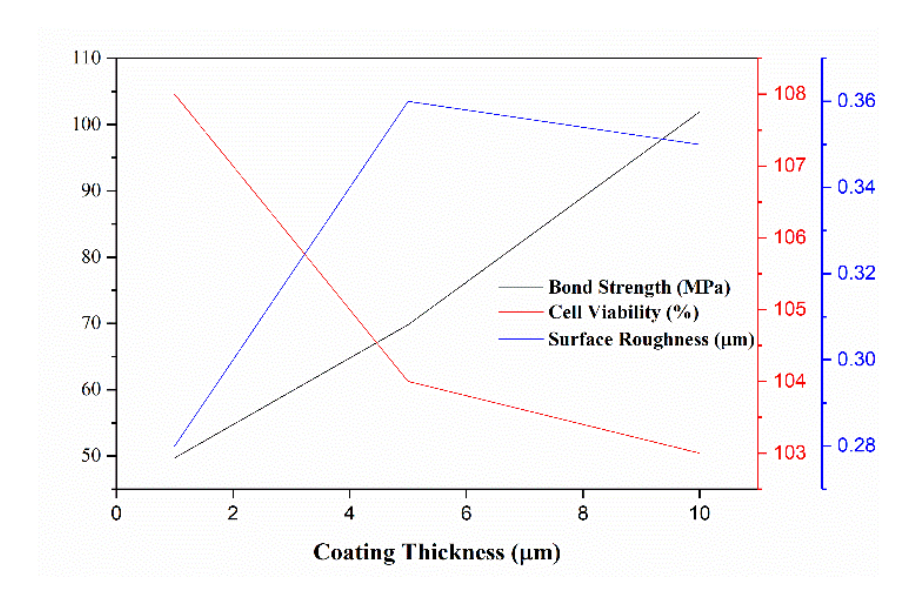


Fig. 11. Variation in bond strength, cell viability, and surface roughness with coating thickness. Based on data [42,46]

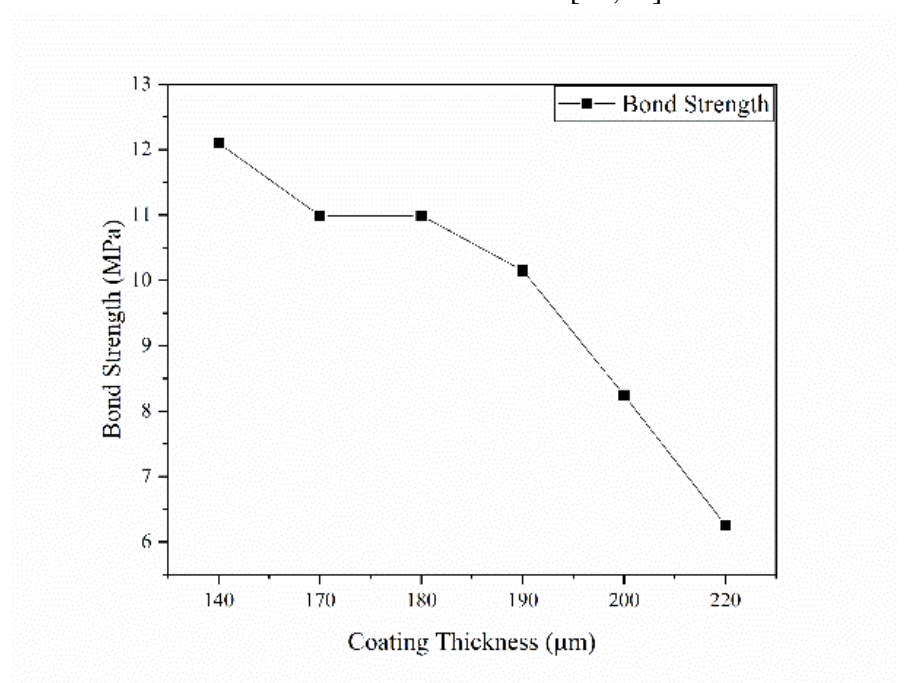


Fig. 12. Variation in bond strength with coating thickness. Based on data [37]

Mohapatro et al. [42] investigated the effect of coating thickness on the corrosion rate of coated magnesium substrate. It was observed that the corrosion rate reduced tremendously after the coating of PCL, as shown in Fig. 13. On increasing the coating thickness, corrosion rate decreased significantly.

Mohseni et al. [37] investigated the effect of hydroxyapatite coating thickness on the bond strength of Ti_6Al_4V titanium alloy. Variation in bond strength with coating thickness is shown in Fig. 12. It can be observed that the bond strength decreased with an increase in the coating thickness. So, the results are contrary to the results obtained by Kuo et al. [46]. This can be due to poor cohesion and adhesion of hydroxyapatite.

So, coating thickness has a mixed effect on the bond strength, cell viability, corrosion rate, and surface roughness. Corrosion resistance and bond strength increased with an increase

in the coating thickness. On the other hand, cell viability decreased. So, selection of coating should be based on the required application.

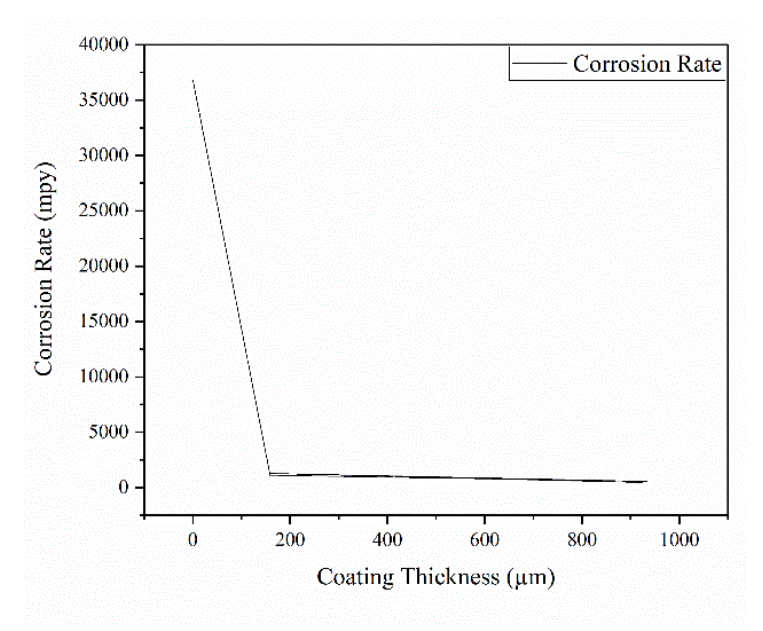


Fig. 13. Variation in corrosion rate with coating thickness. Based on data [37]

Effect of hot isostatic pressing temperature. Hot isostatic pressing is a technique used for the densification of the powders. This technique can be used for improving the bond strength of coating on the implant. Mohseni et al. investigated the effect of the temperature of hot isostatic pressing on the bond strength of hydroxyapatite coated Ti_6Al_4V titanium alloy [37]. Variation in bond strength with hot isostatic pressing temperature is shown in Fig. 14. It can be observed that the bond strength increased with an increase in the temperature of hot isostatic pressing for hydroxyapatite coating of $160 \, \mu m$. On the other hand, bond strength decreased with an increase in the temperature of hot isostatic pressing for hydroxyapatite coating of $200 \, \mu m$. So, the thicker coating has adverse effects on the bond strength.

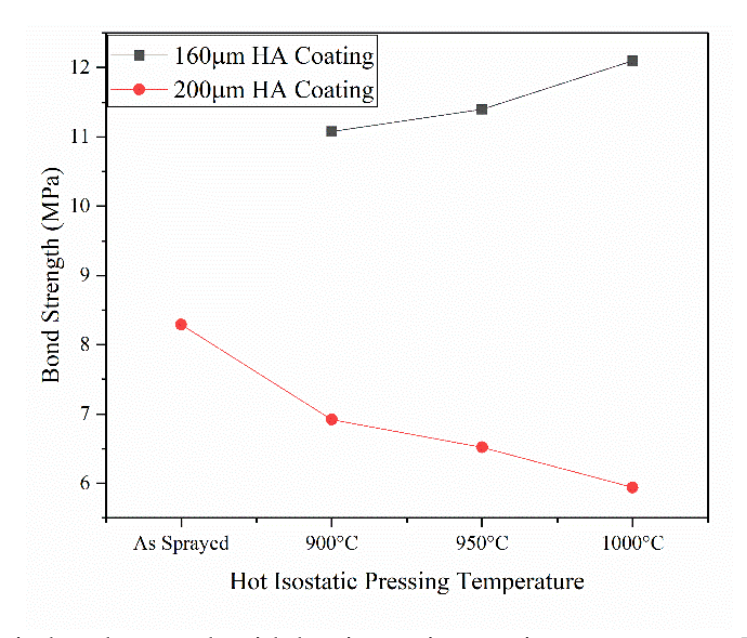


Fig. 14. Variation in bond strength with hot isostatic pressing temperature. Based on data [37]

Effect of surface cleaning and treatment. Surface of substrate play an important role in the coating efficiency. If the surface is not clean, coating adhesion will be poor. Also, various surface treatments and modification enhance the coating bond strength. Some of the surface treatment techniques are shown in Fig. 15. Hsiung et al. [47] investigated the effect of cleaning and cryogenic treatment on the bond strength of the hydroxyapatite coated Ti₆Al₄V implant material. Bond strength of untreated and cryogenically treated hydroxyapatite coated Ti₆Al₄V implant material cleaned by two different processes is shown in Table 2. It can be observed that the bond strength of ultrasonically cleaned sample was more than the bond strength of the sample cleaned by high pressure air. It shows that the ultrasonic cleaning is better than the high pressure air cleaning. Also, bond strength of cryogenically treated samples was higher than the bond strength of the untreated samples. So, the cryogenic treatment is a very useful technique to enhance the coating efficiency.

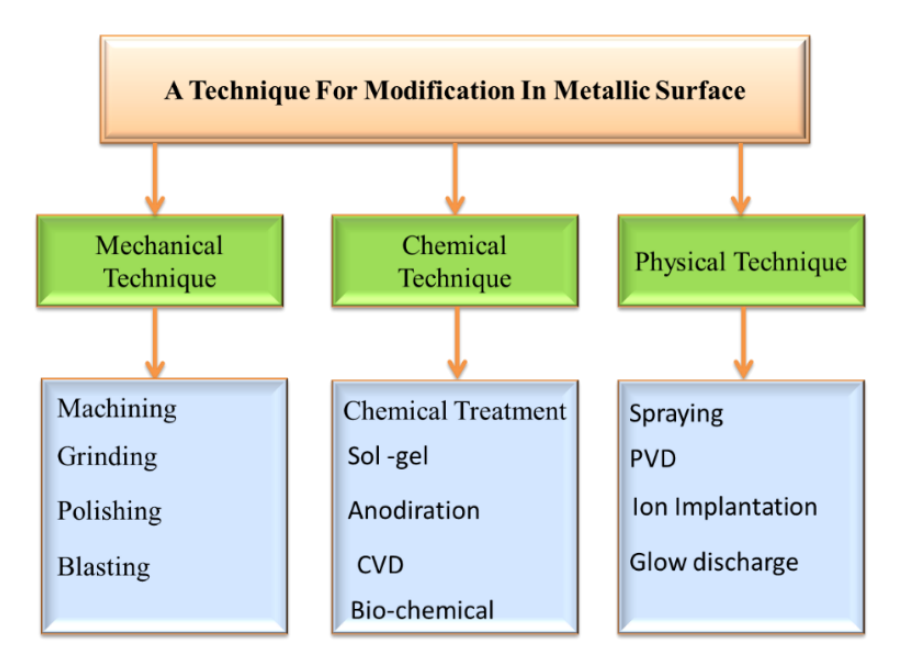


Fig. 15. Surface modification/treatment techniques

Table 2. Bond strength of untreated and cryogenically treated hydroxyapatite coated Ti6Al4V implant material

	Bond Strength, MPa		
	Ultrasonic Cleaning	Pressurised Air	
Untreated	26.56	18.91	
Cryogenic Treatment	36.65	29.30	

Conclusions

After detailed literature survey of coated and uncoated implant materials, following conclusions have been drawn:

- 1. It was observed that the ceramic, polymer, metallic, and composite are widely used for coating metallic implants;
- 2. Biocompatibility of polymer coatings were relatively less in comparison to ceramic and composite coatings. Also, wettability of polymer coatings was less;
- 3. On the other hand, ceramic coatings were highly biocompatible and wettability was also high;
- 4. For metallic coating, biocompatibility was less because of high reactivity. But, metals (like Bi) that form protective oxide layer on the surface of implants exhibits very good biocompatibility and mechanical strength;

- 5. Surface treatment is a very good technique to enhance the adhesion between the coating and the substrate;
- 6. Coating technique also significantly affect the properties of coating. Highest bond strength is obtained by sputtering coating.

Future Scope

Comparative study on the mechanical properties of nano-coated materials can be done in order to identify stress, elongation, and swelling behaviour. In this work, the effect of coatings on only cell viability, contact angle, surface roughness, and corrosion rate is studied. Other biological and mechanical properties can be investigated.

References

- 1. Alhamdi JR, Peng IM, Tao AN, Hawley KL, Spiller KL, Kuhn LT. Controlled M1-to-M2 transition of aged macrophages by calcium phosphate coatings. *Biomaterials*. 2019;196: 90-99.
- 2. Chinglenthoiba C, Ramkumar K, Shanmugaraja T, Sharma S. Study on Nanotechnology, Nanocoating and Nanomaterial. *International Journal of Computer Aided Manufacturing*. 2017;3(1): 17-25.
- 3. Cristea D, Ghiuja I, Munteanu D. Tantalum Based Materials for Implants and Prostheses Applications. *Materials Science*. 2015;8(57): 151-158.
- 4. Dong-Ping L, Yan-Hong L, Bao-Xiang C. Surface properties of diamond-like carbon films prepared by CVD and PVD methods. *Chinese Physics*. 2006;15: 575.
- 5. Kaushik A. Biomedical Nanotechnology Related Grand Challenges and Perspectives. *Frontiers in Nanotechnology*. 2019;1: 1.
- 6. León B, Jansen J. *Thin Calcium Phosphate Coatings for Medical Implants*. New York: Springer; 2009.
- 7. Nathanael AJ, Oh TH. Biopolymer Coatings for Biomedical Applications. *Polymers*. 2020;12: 3061.
- 8. Pahade VS, Chavan PS, Baisane VP. A review paper on Vapour deposition coating. *International Journal of Engineering and Applied Sciences*. 2016;3(6): 75-78.
- 9. Costerton JW, Geesey GG, Cheng KJ. How Bacteria Stick. *Scientific American*. 1978;238(1): 86-95. 10. Geesey GG, Richardson WT, Yeomans HG, Irvin RT, Costerton JW. Microscopic examination of natural sessile bacterial populations from an alpine stream. *Canadian Journal of Microbiology*. 1977;23(12): 1733-1736.
- 11. Qian Y, Deng S, Wu X, She Y, Liu R, Lin H. In vitro and in vivo evaluation of implantable bacterial-killing coatings based on host defense peptides and their synthetic mimics. *Journal of Materials Science & Technology*. 2021;91: 90-104.
- 12. Pesode PA, Barve SB. Recent advances on the antibacterial coating on titanium implant by micro-Arc oxidation process. *Mater Today: Proceedings*. 2021;47: 5652-5662.
- 13. Qiao Y, Liu X. Biocompatible Coating. In: *Comprehensive Materials Processing*. Elsevier; 2014. p. 425-447.
- 14. Kumar M, Kumar R, Kumar S. Coatings on orthopedic implants to overcome present problems and challenges: A focused review. *Mater Today: Proceedings*. 2021;45: 5269-5276.
- 15. Chavan AB, Gawade SKS, Bhosale AP. A review on surface coating techniques on Mg based bio-degradable implants. *Mater Today: Proceedings*. 2023;72: 1361-1366.
- 16. Borcherding K, Schmidmaier G, Hofmann GO, Wildemann B. The rationale behind implant coatings to promote osteointegration, bone healing or regeneration. *Injury*. 2021;52S2: 106-111.
- 17. Olmo JA, Pérez-Álvarez L, Martínez VS, Cid SB, Ruiz-Rubio L, González RP, Vilas-Vilela JL, Alonso JM. Multifunctional antibacterial chitosan-based hydrogel coatings on Ti6Al4V biomaterial for biomedical implant applications. *International Journal of Biological*

Macromolecules. 2023;231: 123328.

- 18. Singh N, Batra U, Kumar K, Ahuja N, Mahapatro A. Progress in bioactive surface coatings on biodegradable Mg alloys: A critical review towards clinical translation. *Bioactive Materials*. 2023;19: 717-757.
- 19. Hayes JS, Richards RG. The use of titanium and stainless steel in fracture fixation. *Expert Review of Medical Devices*. 2010;7(6): 843-853.
- 20. Lung CYK, Khan AS, Zeeshan R, Akhtar S, Chaudhry AA, Matinlinna JP. An antibacterial porous calcium phosphate bilayer functional coatings on titanium dental implants. *Ceramic International*. 2023;49(2): 2401-2409.
- 21. Kurtz SM, Devine JN. PEEK Biomaterials in Trauma, Orthopedic, and Spinal Implants. *Biomaterials*. 2007;28(32): 4845-4869.
- 22. Mugnai R, Tarallo L, Capra F, Catani F. Biomechanical comparison between stainless steel, titanium and carbon-fiber reinforced polyetheretherketone volar locking plates for distal radius fractures. *Orthopaedics & Traumatology: Surgery & Research*. 2018;104(6): 877-882.
- 23. Wang A, Venezuela J, Dargusch MS. Enhancing the corrodibility of biodegradable iron and zinc using poly(lactic) acid (PLA) coating for temporary medical implant applications. *Progress in Organic Coatings*. 2023; 174: 107301.
- 24. Wu G, Li L, Sun M, Wang Y, Luo F, Zhang Q, Liu R, Chen Z, Yao J. Microstructural evolution and biological properties of PEO coating on SLM-prepared NiTi alloy. *Surface and Coatings Technology*. 2023;452: 129065.
- 25. Maadani AM, Davoodian F, Salahinejad E. Effects of PLGA coating on biological and mechanical behaviors of tissue engineering scaffolds. *Progress in Organic Coatings*. 2023;176: 107406.
- 26. Hossain MH, Hossain N, Chowdhury MA, Kowser MA, Rana MM. Surface synthesization of magnesium alloys for improving corrosion resistance and implant applications. *Arabian Journal of Chemistry*. 2023;16(2): 104465.
- 27. Iqbal F, Ali A, Naveed M, Ikram F, Fatima H. Hydrothermal deposition of high strength biocompatible magnesium phosphate coating through in situ conversion of AZ91D-3Ca magnesium substrate. *Surface and Coatings Technology*. 2023; 129301.
- 28. Yang Y, Kim KH, Agrawal CM, Ong JL. Interaction of hydroxyapatite—titanium at elevated temperature in vacuum environment. *Biomaterials*. 2004;25(15): 2927-2932.
- 29. Radin SR, Ducheyne P. Plasma spraying induced changes of calcium phosphate ceramic characteristics and the effect onin vitro stability. *Journal of Materials Science: Materials in Medicine*. 1992;3: 33-42.
- 30. Tang J, Wu Z, Yao X, Zhou Y, Xiong Y, Li Y, Xu J, Dargusch MS, Yan M. From bio-inertness to osseointegration and antibacterial activity: A one-step micro-arc oxidation approach for multifunctional Ti implants fabricated by additive manufacturing. *Materials & Design*. 2022;221: 110962.
- 31. Ghaleh HM, Hafezi M, Hadipour M, Nadernezhad A, Aghaie E, Behnamian Y, Osman NAA. Effect of tricalcium magnesium silicate coating on the electrochemical and biological behavior of Ti-6Al-4V alloys. *Plos One*. 2015;10(9): e0138454.
- 32. Xue W, Liu X, Zheng X, Ding C. Plasma-sprayed diopside coatings for biomedical applications. *Surface and Coatings Technology*. 2004;185(2-3): 340-345.
- 33. Yi D, Wu C, Ma B, Ji H, Zheng X, Chang J. Bioactive bredigite coating with improved bonding strength, rapid apatite mineralization and excellent cytocompatibility. *Journal of Biomaterials Applications*. 2014;28(9): 1343-1353.
- 34. Li K, Yu J, Xie Y, Huang L, Ye X, Zheng X. Chemical stability and antimicrobial activity of plasma sprayed bioactive Ca2ZnSi2O7 coating. Journal of Materials Science: *Materials in Medicine*. 2011;22: 2781-2789.
- 35. Liang Y, Xie Y, Ji H, Huang L, Zheng X. Excellent stability of plasma-sprayed bioactive Ca3ZrSi2O9 ceramic coating on Ti–6Al–4V. *Applied Surface Science*. 2010;256(14): 4677-4681.

- 36. Wu C, Chen Z, Yi D, Chang J, Xiao Y. Multidirectional effects of Sr-, Mg-, and Sicontaining bioceramic coatings with high bonding strength on inflammation, osteoclastogenesis, and osteogenesis. *ACS Applied Material Interfaces*. 2014;6(6): 4264-4276. 37. Mohseni E, Zalnezhad E, Bushroa AR. Comparative investigation on the adhesion of hydroxyapatite coating on Ti–6Al–4V implant: A review paper. *International Journal of Adhesion and Adhesives*. 2014;48: 238-257.
- 38. Chai M, An M, Zhang X. Construction of a TiO2/MoSe2/CHI coating on dental implants for combating Streptococcus mutans infection. *Materials Science & Engineering C*. 2021;129: 112416. 39. Aydemir T, Pastore JI, Pique EJ, Roa JJ, Boccaccini AR, Ballarre J. Morphological and mechanical characterization of chitosan/gelatin/silica-gentamicin/bioactive glass coatings on orthopaedic metallic implant materials. *Thin Solid Films*. 2011;732: 138780.
- 40. Qin W, Ma J, Liang Q, Li J, Tang B. Tribological, cytotoxicity and antibacterial properties of graphene oxide/carbon fibers/polyetheretherketone composite coatings on Ti–6Al–4V alloy as orthopedic/dental implants. *Journal of the Mechanical Behavior of Biomedical Materials*. 2021;122: 104659.
- 41. Ritwik A, Saju KK, Binsi PK, Reghuraj AR. Development of biocompatible coating on Ti6Al4V implant materials using chitosan extracted from shellfish waste. *Materials Today: Proceedings*. 2021;47: 5209-5216.
- 42. Mahapatro A, Jensen K, Yang SY. Effect of polymer coating characteristics on the biodegradation and biocompatibility behavior of magnesium alloy. *Polymer-Plastics Technology and Materials*. 2020;59(3): 301-310.
- 43. Kamynina OK, Kravchuk KS, Lazov MA, Pestov SM. Effect of surface roughness on the properties of titanium materials for bone implants. *Russian Journal of Inorganic Chemistry*. 2021;66: 1073-1078.
- 44. Gosau M, Haupt M, Thude S, Strowitzki M, Schminke B, Buergers R. Antimicrobial effect and biocompatibility of novel metallic nanocrystalline implant coatings. *Journal of Biomedical Materials Research Part B: Applied Biomaterials*. 2015;104(8): 1571-1579.
- 45. Vladescu A, Surmeneva MA, Cotrut CM, Surmenev RA, Antoniac IV. Bioceramic coatings for metallic implants. In: Boccaccini AR. (ed.) *Handbook of Bioceramics and Biocomposites*. Cham: Springer; 2016. p.703-733.
- 46. Kuo WC, Wu TC, Wu CF, Wang WC. Bioperformance analysis of parylene C coating for implanted nickel titanium alloy. *Materials Today Communications*. 2021;27: 102306.
- 47. Hsiung JC, Tzeng J, Kung K, Chen H. A study of thermal spray coating on artificial knee joints. *Life Science Journal*. 2013;10(2): 236-241.

THE AUTHORS

Naveen Kumar 🗓

e-mail: kumarnaveenmkcoe@sanjivani.org.in

Abhishek Kumar 🗓

e-mail: abhishek@mnnit.ac.in

Kunvar Kant Patel (1)

e-mail: kunvarkantpatel@gmail.com

Ajaya Bharti 🗓

e-mail: abharti@mnnit.ac.in

Ritesh Kumar Kushwaha

e-mail: kushwahark169@yahoo.com

Effect of curing temperature on surface and subsurface properties of polyurethane elastomer

Submitted: February 10, 2023

Approved: February 17, 2022

Accepted: May 2, 2023

I.A. Morozov ¹ A.Yu. Beliaev ¹, M.G. Scherban ²

¹ Institute of Continuous Media Mechanics of the Ural Branch of Russian Academy of Science, Perm, Russia

² Perm State University, Perm, Russia

⊠ ilya.morozov@gmail.com

Abstract. Polyurethane elastomers are a class of polymers with two-phase segmented structure. The study of their features at the microstructure level will make it possible to control both macroscopic physical and mechanical properties of polymers and functional properties of surfaces. Polyurethanes of the same formulation were synthesized in this work, varying the curing temperature from 30 to 90 °C. Atomic force microscopy, dynamic mechanical analysis, and wettability were used in the study. Stiff fibrillar supramolecular structures (elastic modulus 14-22 MPa), distributed in a softer matrix, are formed in the polymers. Phase inhomogeneities are hidden under the surface by a soft nanolayer of variable thickness. An increase in the curing temperature leads to an increase in the thickness of this layer, and the stiff structure transforms from homogeneous to a network of agglomerates. Wettability, free surface energy and macroscopic viscoelastic properties nonlinearly depend on the curing temperature, which is explained by the physical and mechanical properties of the stiff and soft phases.

Keywords: polyurethane; microstructure; atomic force microscopy; physical and mechanical properties

Acknowledgements. The research was carried out at the expense of the grant of the Russian Science Foundation No. 23-22-00064.

Citation: Morozov IA, Beliaev AY, Scherban MG. Effect of curing temperature on surface and subsurface properties of polyurethane elastomer. *Materials Physics and Mechanics*. 2023;51(6): 107-118. DOI: 10.18149/MPM.5162023_10.

Introduction

Polyurethane elastomers are segmented polymers consisting of soft and hard segments [1]. Primary hard segments form secondary supramolecular structures (fibrils, cylinders, ribbons, meshes, globules) in a softer matrix. The properties of such structures depend on the chemical composition [2–5], the curing time or temperature [6,7], the presence of filler particles in the composition [8-10], the thickness of the material [11], additional heat treatment [12,13], the history of mechanical loading [14,15]. It has been established that the heterogeneous structure of polyurethane is covered with a low-molecular-weight nanolayer of the soft phase [16,17]. The images for the phase separation of polyurethane, presented in the majority of the studies, were obtained using the tapping mode of atomic force microscopy (AFM), and are in fact images of some transitional near-surface region [17,18].

In addition to obtaining materials with a given set of structural properties, a promising modern direction is modification of the polyurethane surface. In the latter case, this refers to improving specific functional characteristics: biocompatibility [19–22], antibacterial properties

© I.A. Morozov, A.Yu. Beliaev, M.G. Scherban, 2023.

Publisher: Peter the Great St. Petersburg Polytechnic University

[23], wettability [24], gas permeability [25]. The best results can be achieved by taking into account both the presence of a surface nanolayer and the particulars of phase separation in the internal supramolecular structure. In particular, it has been established that plasma ions interact differently with soft and hard subsurface regions; in some cases, this significantly increases the crack resistance and deformability of coatings with improved biocompatibility [21,22].

To date, numerous works have focused on the physical and mechanical characteristics of polyurethane elastomers. However, the results obtained on the structural characteristics of elastomers are often interpreted based on indirect data (typically, spectroscopic studies). This is insufficient given the complex structure of polyurethanes. Thus, study of the surface and subsurface properties of phase-separated polyurethanes is important both for predicting the physical and mechanical properties of materials and for their directed functionalization at the structural level of the material.

This paper considers polyurethanes with the same composition but synthesized with different curing temperatures. We focused on the microstructural surface and subsurface properties of polymers and on the characteristics of their phase separation. Supramolecular structures with different structural and physico-mechanical properties depending on the curing temperature were obtained in the materials, affecting the macroscopic characteristics of the materials.

Materials and Methods

Production of materials. Polyurethanes were prepared from commercially available prepolymer (urethane prepolymer based on polyester and toluene diisocyanate) and crosslinking agent (13.2 % MOCA hardener, 84.7 % polyfurite plasticizer, 2.1 % voranol catalyst) in a mass ratio of 100:47. The components were heated at 80 °C and evacuated. The mixture was vacuum-dried for 24 hours as plates with a free upper surface 2 mm thick. The curing temperature T was set to 30, 50, 70 or 90 °C. The resulting specimens are marked T30, T50, T70 and T90. The polyurethane does not fully cure in 24 hours at a low temperature. For this reason, the mixtures T30 and T50 were further cured after 24 hours at T = 70 °C for another 24 hours.

Wettability and free energy of the surface. The wetting contact angle was determined using a goniometer by the sessile drop method. Water and diethylene glycol were used as test liquids; droplet sizes ranged from 2 to 3 mm. The free surface energy was calculated by the Owens–Wendt–Rabel–Kaelble method as the sum of the dispersion (energy of Van der Waals interactions) and polar (dipole interactions and energy of hydrogen bonds) components.

Dynamic mechanical analysis. Rectangular specimens were tested for uniaxial tension on a DMA/SDTA861e Dynamic Mechanical Analyzer (METTLER TOLEDO, Switzerland). The base of the specimen is 10 mm long, about 6 mm wide, about 2 mm thick. The tests were carried out at a temperature of 25 °C and a deformation amplitude of 3 %, varying the frequency from 0.5 to 50.5 Hz in 5 Hz increments.

Atomic force microscopy. An AFM Ntegra Prima in nanomechanical mapping mode was used. ScanAsyst-Air probes with calibrated tip radii $R \sim 3-5$ nm and bending stiffness of the beam $k \sim 0.4-0.5$ nN/nm were used. In this mode, the probe indents the selected area at a high speed (10 nm/ms was set; the indentation frequency was ~ 20 Hz taking into account the vertical displacement of the piezoelectric scanner at 350 nm). The high indentation speed allows obtaining high-resolution data in the specimen plane: an array of interaction curves d(z) of the probe with the surface when the probe approaches the surface and withdraws from it, where d is the cantilever bending, z is the relative distance between the probe and the specimen; interaction force: F = kd.

The tip of the probe is strongly attracted to the surface under the action of van der Waals forces at some distance from the surface (point A in Fig. 1). The deviation d_c of the probe from the equilibrium position after the jump to contact has been completed is a measure of the Hamaker constant H_s of the surface [26]: $H_s = 9k^2d_c^6 / (R^2H_t)$, where H_t is the Hamaker constant of the probe material ($H_t = 18 \cdot 10^{-20}$ J for a probe made of silicon nitride). We assume that the indentation of the probe into the material begins at point B, then the indentation depth $u = (z-z_b) - (d-d_b)$. The polymer is indented in the segment BC until a given maximum load of ~3 nN is reached (the average indentation depth at such a load was 50 nm). The specimen is then unloaded as the probe is removed from the surface.

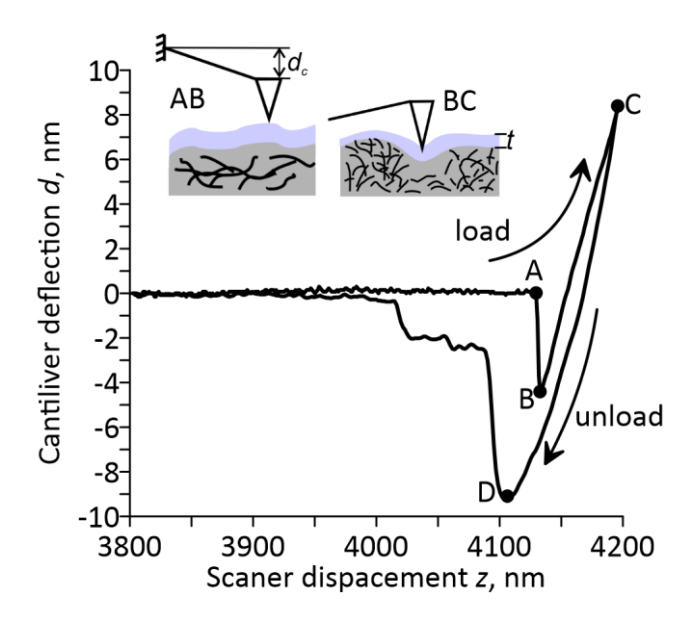


Fig. 1. Typical curve for interaction of AFM probe with polyurethane surface: loading and unloading curves, as well as characteristic stages of interaction are shown

The maximum magnitude of the force at the time when the probe separates from the surface (point D in Fig. 1) is related to the free energy of the surface and is widely used in the Derjaguin–Muller–Toporov or Johnson–Kendall–Roberts elastic indentation models to subsequently determine the elastic modulus of the surface. In general, the observed relief depends on the applied force: the probe pushes through the soft outer nanolayer with increasing loads, starting to detect the internal structures of the polymer hidden under the surface. The algorithms we developed [27] allow to monitor these changes in relief, as well as to estimate the thickness *t* of the upper homogeneous layer covering the subsurface structures.

The presence of a soft upper layer makes it difficult to use models for determining the elastic modulus taking into account the adhesion of the probe to the surface as a measure of the free energy of the surface. In this case, a comparative analysis of local stiffness is carried out using the Sneddon approach [28,29] for a parabolic indenter with non-uniform depth distribution of the elastic modulus: $E_i(u_i) = \frac{(1-v^2)}{4\sqrt{Ru_i}} \frac{d_i - d_{i-1}}{u_i - u_{i-1}} k$, where v = 0.5 is Poisson's ratio. The polymer has inelastic properties, i.e., the loading and unloading curves do not coincide. We use the viscosity coefficient as a measure of the viscoelastic properties of the surface. Similar to the elastic modulus, it depends on the indentation depth [30,31]: $\eta(u_i) = \frac{1}{du/dt} \frac{F_{dis}(1-v^2)}{6\sqrt{Ru_i}}$, where the dissipative component of the load F_{dis} is calculated as the difference between the forward and reverse scanning directions F_a and F_r : $F_{dis} = (F_a - F_r)/2$.

Results and Discussion

Let us start by considering some macroscopic properties of polymers. The material T30 has the best hydrophilic properties (Fig. 2); the wettability deteriorates with an increase in the curing temperature (the contact angle increases), and does not change significantly in the curing temperature range from 50 to 90 °C. The free energy of the surface behaves similarly (Fig. 2); its variation is due to a decrease in the polar component (the energy of hydrogen bonds and dipole interactions); the dispersion component increases slightly.

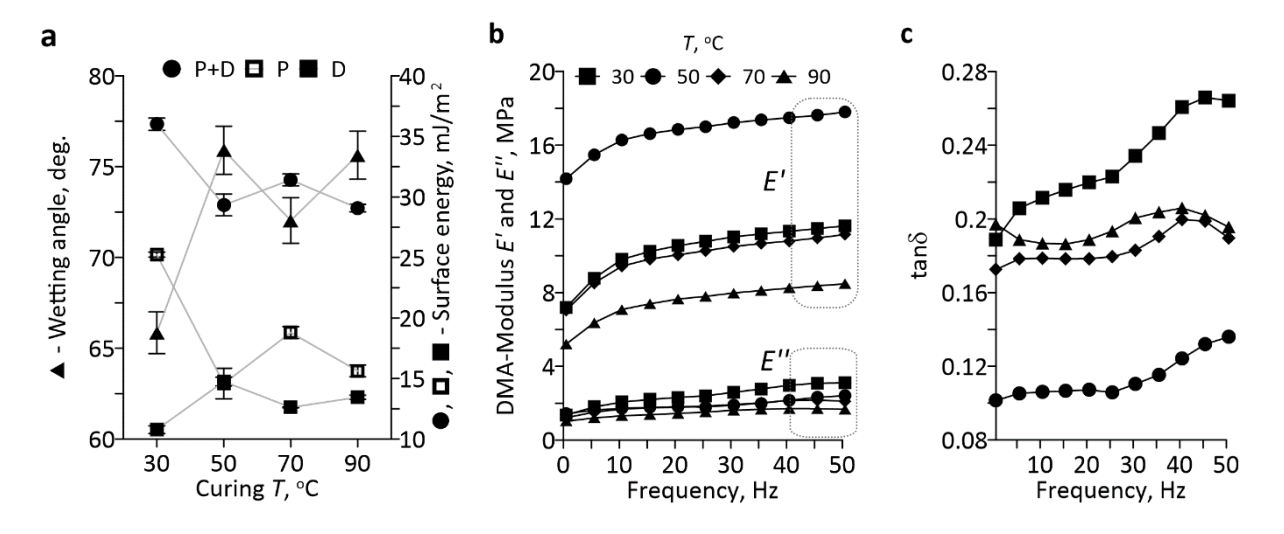


Fig. 2. Contact angle and free energy of the surface: dispersive (D) and polar components (P) (a), DMA-measurements: storage and loss moduli (b), tangent of mechanical losses (c)

DMA tests established (Fig. 2(b,c)) that the storage modulus E' of polyurethane T50 is approximately twice as high as those of other materials; the same polymer also has the least pronounced viscous characteristics. The material T90 turned out to be the softest from standpoint of DMA tests, T30 has the greatest mechanical losses.

The internal structure of synthesized polyurethanes (Fig. 3) represents rigid fibrillar structures (supramolecular formations with a high concentration of hard polyurethane segments), unevenly entangled in a softer matrix (regions of high concentration of soft segments and a small proportion of disordered hard segments). The most dense and homogeneous structure is produced at curing temperatures of 30–50 °C (Fig. 3(a,b)). In these cases, dense hard agglomerates are observed, the length of individual fibrils is no more than 20 nm. An increase in temperature leads to a more porous and more heterogeneous structure of hard segments in the form of a fibrillar mesh (Fig. 2(d)); the size of the fibrils can reach 1 μ m or more. The mean fibril width is 3–5 nm, which corresponds to the size of perpendicularly packed primary hard segments of polyurethane [2].

Polyurethane surfaces were smooth and uniform (see the insets in Fig. 3). The fibrillar heterogeneities in polymers (see enlarged view in Fig. 3) are hidden under the surface by a nanolayer with variable thickness t, homogeneous in its mechanical characteristics. The thickness of this outer layer was estimated by the transformations in the relief structure during indentation: given a small force, the AFM probe first interacts with the outer layer, pushing through this layer with increasing load, as the internal structure gradually evolves.

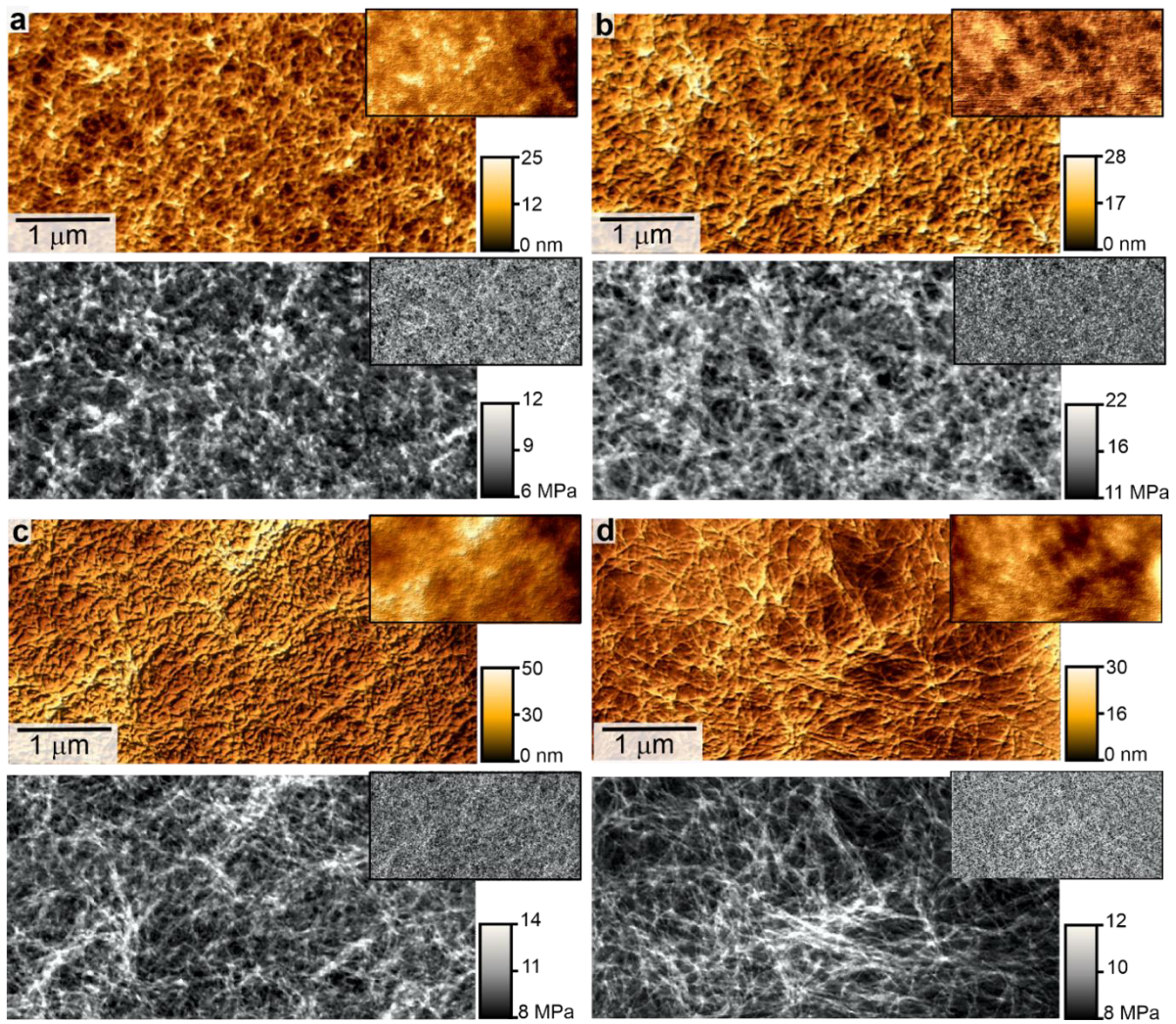


Fig. 3. AFM images for relief (top row) and stiffness maps (bottom row) of polyurethanes at curing temperatures of 30 (a), 50 (b), 70 (c) and 90 °C (d). Enlarged fragments of subsurface structures are shown; the corresponding surface maps are shown in the insets

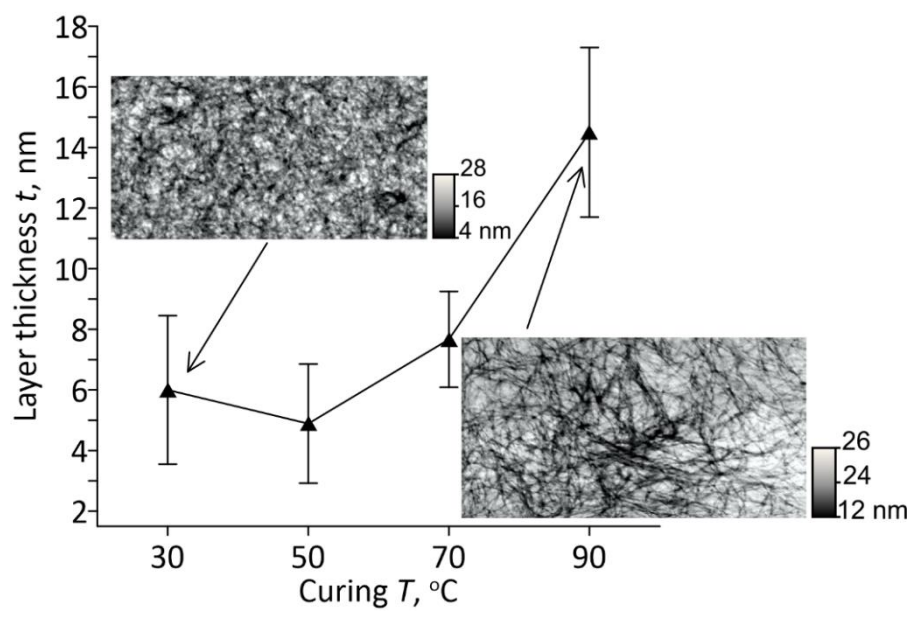


Fig. 4. Thickness of polyurethane surface nanolayer covering the elevations. The insets show the corresponding thickness distribution maps. AFM images of reliefs are shown in Fig. 3

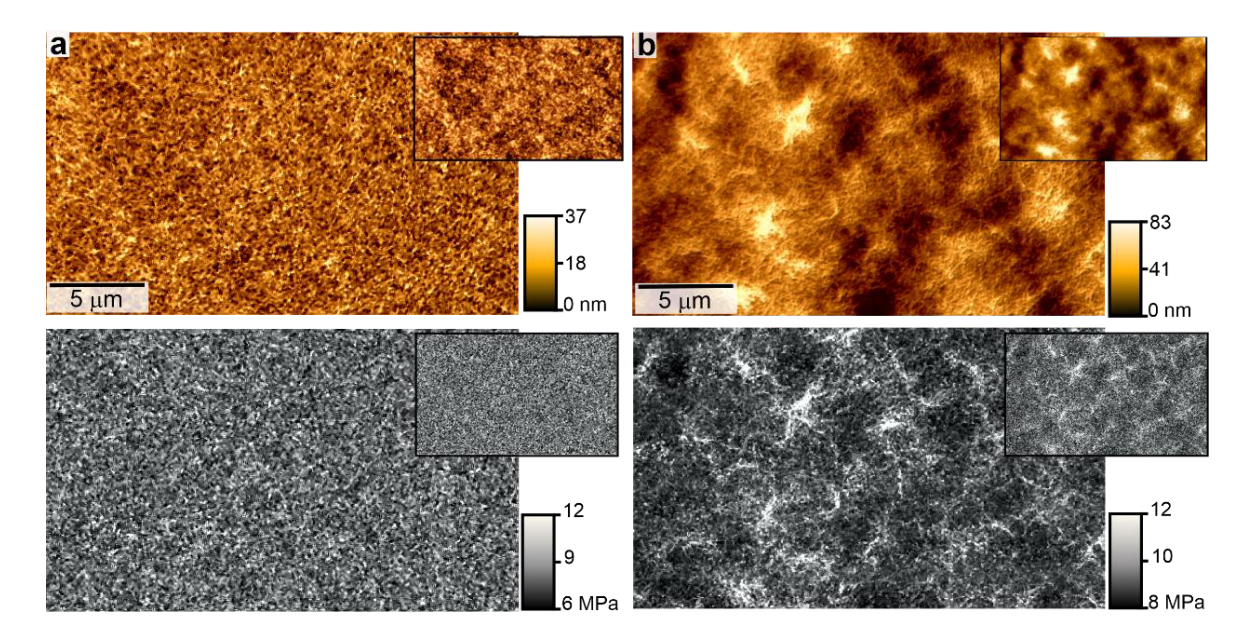


Fig. 5. Representative AFM images of relief and elastic modulus of subsurface (enlarged) and surfaces (insets) of materials T30 (a) and T90 (b)

The thickness of the outer layer (Fig. 4(a)) depends both on the features of the internal structure and on the curing temperature. The lowest thickness of the layer is achieved at elevations of subsurface relief, i.e., the peaks of hard supramolecular agglomerates (Fig. 4(b,c)); the thickness does not change at curing temperatures of 30–50 °C, then increasing from 5 to 14 nm. The thickness of the nanolayer in the regions free of hard subsurface structures (depressions of subsurface relief) does not change, fluctuating in the vicinity of 22-24 nm. In the latter case, the layer has no clear boundaries, merging into the matrix.

Representative AFM images are shown in Fig. 5: the reliefs for T30 and T50 (T50 is not shown here) are relatively flat. Agglomeration of hard structures occurs at curing temperatures of 70 and 90 $^{\circ}$ C (see the stiffness map in Fig. 5(b)); the size of the agglomerates is $\sim 5 \, \mu m$.

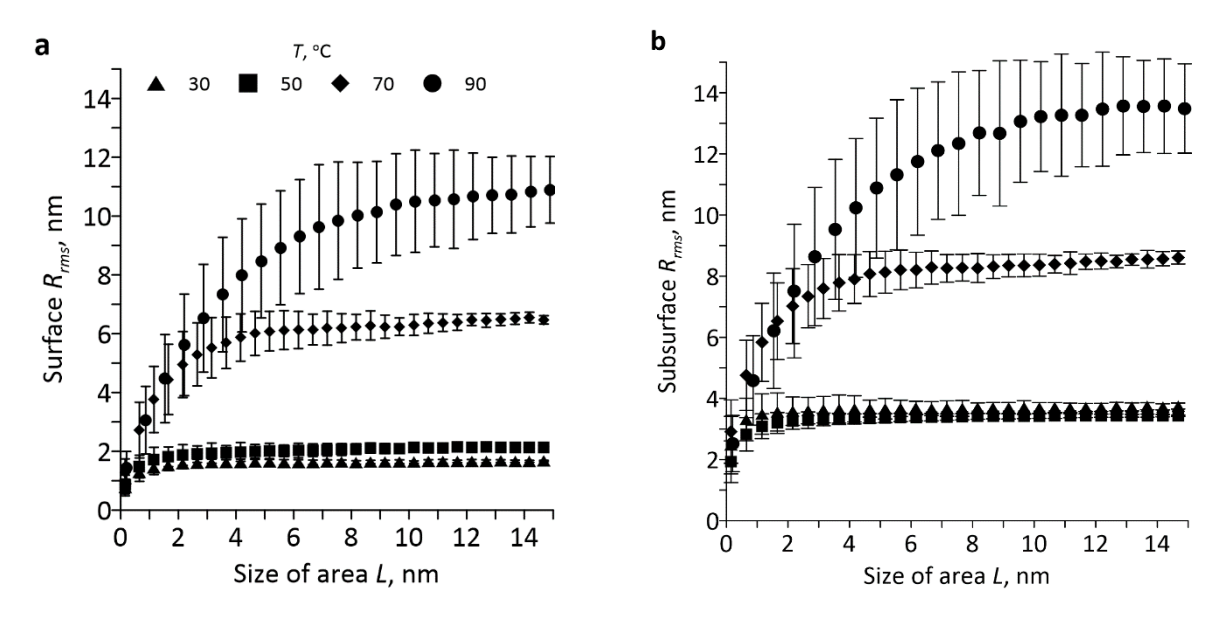


Fig. 6. RMS roughness of the surface (a) and subsurface reliefs (b) depending on the size of the region

Quantitative analysis of structural heterogeneities was performed by calculating the RMS roughness R_{rms} of the relief depending on the size L of a square region randomly selected in the image. The mean roughness increases, reaching the asymptote at a certain size L_{crit} of the region (Fig. 6). L_{crit} is the smallest size starting from which the distribution of hard structures in polyurethane can be considered homogeneous, in other words, the critical size of the heterogeneity: the size of the heterogeneity does not exceed 1.5–2 μ m T < 50 °C, then sharply increasing to 13 μ m at T = 90 °C.

Subsurface structures in AFM images are located at different heights relative to each other. What we actually observe is a fragment of a three-dimensional supramolecular structure of the material. We binarize representative AFM images of a three-dimensional subsurface relief, leaving only what lies within the mean height of the image \pm 3 nm (the mean fibril width). As a result, we obtain slices of the subsurface structure. The fractal dimension D of the obtained images is shown in Fig. 7 (to calculate D, we divide the image into squares with the side size L and calculate the number N of non-empty squares; we can prove that L and N are related by a fractal dependence: $N \sim L^{-D}$).

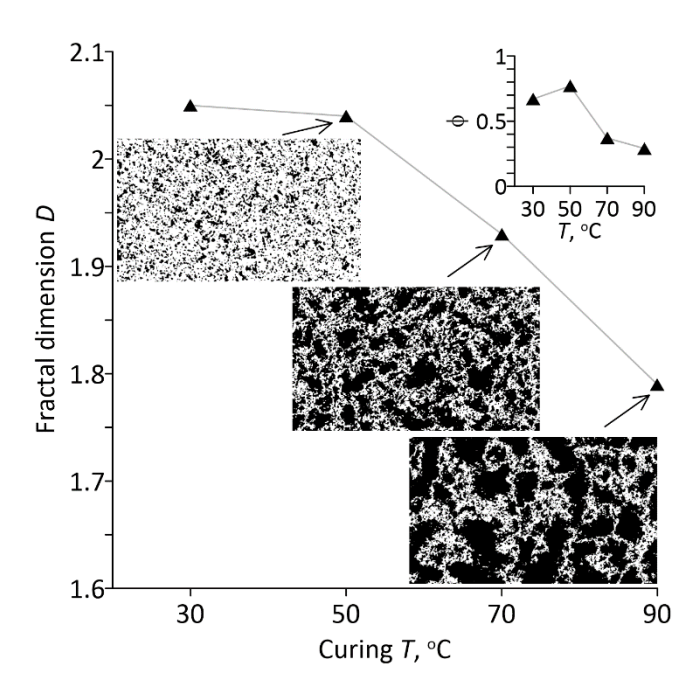


Fig. 7. Fractal dimension *D* and fraction of the mesh containing hard subsurface agglomerates. The insets show slices of the corresponding structures obtained by binarization of representative AFM images. The light regions correspond to hard subsurface structures. The structure of the material T30 is close to that of T50 and is not shown

The fractal dimension of the mesh of hard structures is close to 2 for materials T30 and T50, which corresponds to a homogeneous (cluster-free) distribution of hard structures in these materials. The picture radically changes with an increase in the curing temperature: the rigid supramolecular structure in polyurethanes T70 and T90 is a mesh of fractal agglomerates, whose tortuosity and heterogeneity increase with the curing temperature. The observed agglomerates are tangled dense clumps of fibrillar structures. The fraction of the material forming a dense hard mesh decreases from 70–80 % (T30, T50) to 40–30 % (T70, T90); the densest structure is observed in the T50 material. The space between the agglomerates is filled with a sparse mesh of individual fibrils (see Fig. 3(d)).

The jump d_c of the probe to the surface (see Fig. 1) is proportional to the Hamaker constant. The measurements showed that the mean values of d_c (Fig. 8(a)) do not change significantly with an increase in the curing temperature. The Hamaker constant, in turn, is directly proportional to the dispersion component of the free energy (interatomic interactions based on van der Waals forces) of the surface [32]. This result is confirmed by the experiments conducted to measure the wettability and free energy of the surface (Fig. 2(a)): the change in the dispersion component of the surface free energy correlates with the d_c measurements.

Maps of the jump to the surface made by the probe (see the insets in Fig. 8(a)) are inhomogeneous, i.e., there are regions with high and low values with \pm 10 % deviation from the mean (statistical distributions of d_c are close to normal). For example, regions with low values of d_c can be seen in the d_c map for T30 in the form of circular segments. The magnitude of the jump depends on the local irregularities in the relief [33]. In our case, the observed inhomogeneities in d_c are not related either to the outer surface of the polymer or to its internal fibrillar structure (see Fig. 3). This is to say that the outer nanolayer has region with inhomogeneous activity. No correlation was found between the curing temperature and the properties of these inhomogeneities.

The internal structure of the polymer does not affect the magnitude of the jump to the surface (the distance d_c+t between the probe and the subsurface is quite large). That is, the Hamaker constant calculated from d_c is a characteristic of only the outer layer. At the same time, as established below, the surface free energy measured by wetting depends on both the internal structure and the external nanolayer.

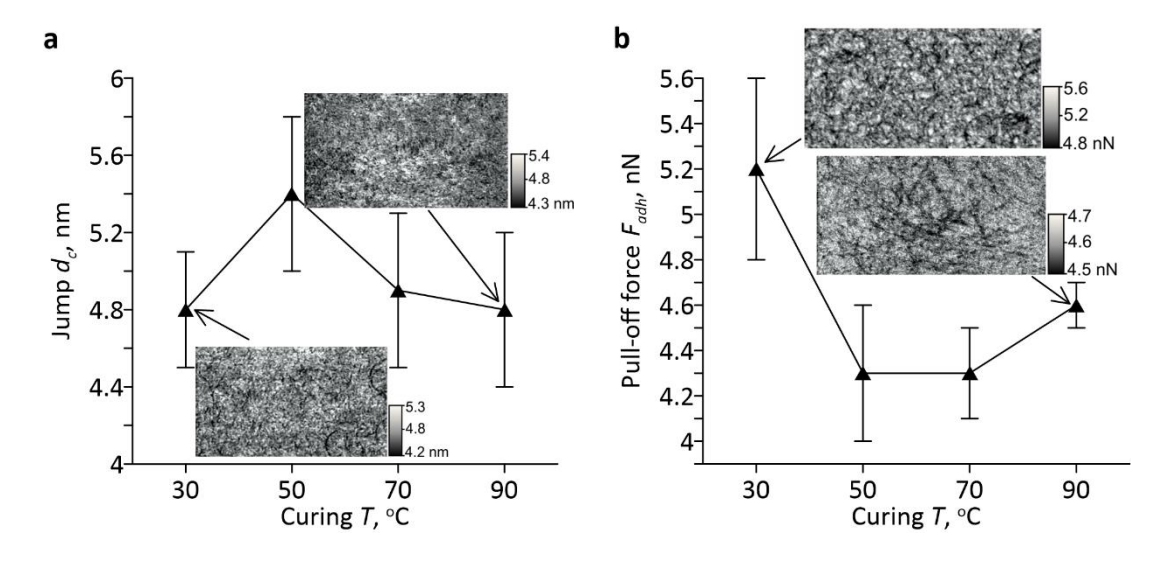


Fig. 8. Jump of the probe to the surface (a) and pull-off force (b). The insets show the corresponding maps. AFM images of reliefs are shown in Fig. 3

The force at the instant when the probe separates from the surface is traditionally associated with the surface free energy: it is maximum for the surface T30, reaches a minimum at T50–T70, and then begins to grow. These results (Fig. 8(b)) correlate with the changes in the surface free energy and the contact angle (Fig. 2(a)). Inhomogeneities in the maps characterizing the adhesion of the probe to the material (see the insets in Fig. 8(b)) are related to the internal structure of the polymer: regions with lower adhesion values correspond to hard structures in the elevations of subsurface relief; high adhesion values correspond to softer depressions. However, despite the pronounced inhomogeneities in the adhesion maps, the differences between the adhesion of hard and soft regions do not exceed \pm 5 %.

As the curing temperature increases, the thickness of the surface layer increases (see Fig. 4) and the adhesion inhomogeneities caused by subsurface structures become even less pronounced. On the other hand, the decrease in the surface free energy (Fig. 2(a)) occurs due to the polar component. Thus, the polar properties of hard subsurface structures influence the change in the polar component of the surface free energy.

The force experienced by the probe as it detaches from the material is used in common models for calculating Young's modulus of surfaces as a measure of the specific surface free energy. However, as shown above, the exact manner in which the measured adhesion is influenced by subsurface structures remains uncertain. This narrows the scope of application of the existing models, and the Sneddon approach was used in this paper to estimate the elastic modulus. The obtained maps of the elastic modulus are shown in Figs. 3 and 5. Figure 9(a) shows the mean values separately for hard (elevations in the subsurface relief) and soft (depressions) regions: with the exception of one of the polyurethanes, the modulus of hard subsurface structures does not change (14 MPa). The modulus of soft regions and the surface layer increases from 7 (T30) to 9 MPa (T90). That is, a part of the primary hard polyurethane segments does not have time to assemble into fibrillar structures at high curing temperatures, and remains distributed in the soft matrix. Polyurethane T50 does not follow this trend: the stiffness of its structures is 1.5 times higher than that of other materials.

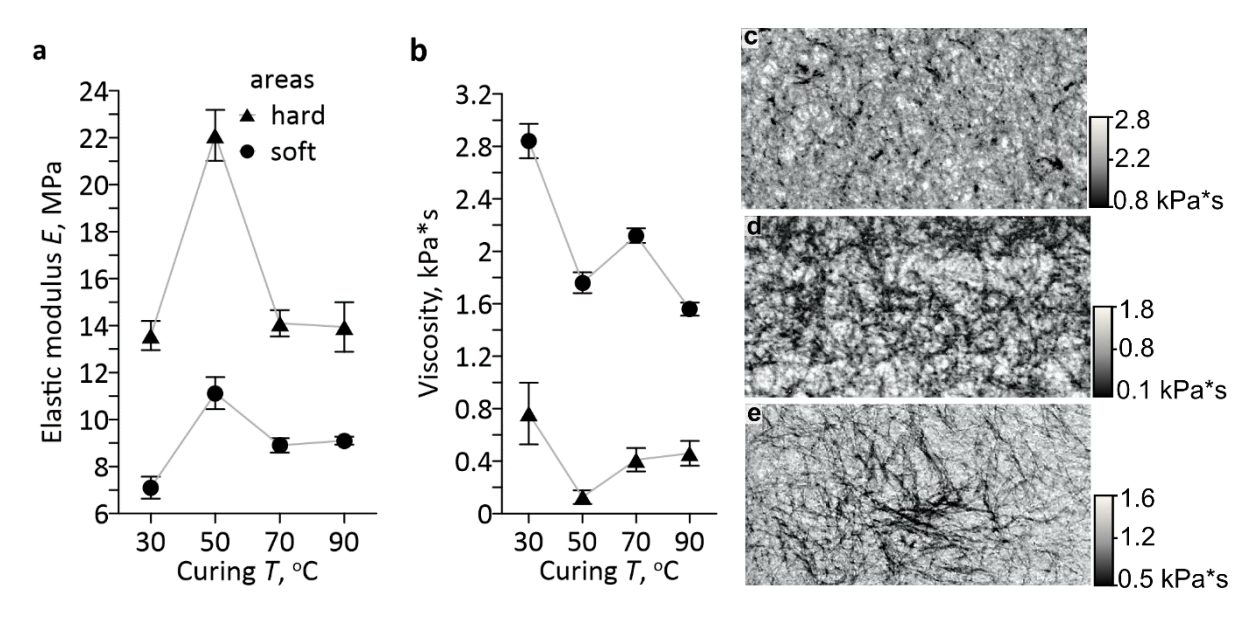


Fig. 9. Elastic modulus (a) and viscosity (b) of hard (elevations of subsurface relief) and soft segments of polyurethanes; viscosity distribution maps of materials T30 (c), T50 (d) and T90 (e). AFM images of reliefs are shown in Fig. 3

The viscosity (Fig. 9(b)) of hard subsurface structures is significantly lower than in the segments of the soft matrix. In general, the viscosity of the soft matrix decreases, which can be explained by an increase in the concentration of disordered primary hard polyurethane segments in it. Polyurethane T30 has the most pronounced viscous properties of both hard structures and the matrix. The low curing temperature of this material did not allow for it to produce a sufficient number of polymer crosslinks, giving elasticity to the polymer matrix.

Notably, both the elastic modulus and the viscosity measured using atomic force microscopy showed a good correlation with the moduli and tangent of mechanical losses obtained by DMA. The most elastic material is T50, and the strengthening of elastic properties occurs mainly due to a decrease in the viscosity of hard structures. The supramolecular hard

mesh in this material is the densest (see Fig. 7), therefore its viscoelastic properties have a significant impact on the macroscopic behavior of the material (see Fig. 2(b, c)).

Conclusion

We synthesized polyurethanes with a curing temperature from 30 to 90° C. It was established that the materials form hard (elastic modulus of 14–22 MPa) subsurface supramolecular structures (nanofibrils and agglomerates) located in a softer matrix (elastic modulus of 7–9 MPa). The most dense and homogeneous hard subsurface structure is formed in polyurethanes with a curing temperature of 30–50 °C; the structure becomes heterogeneous and loose with a further increase in temperature: agglomerates up to several microns appear; the soft phase space between the agglomerates is crossed by a mesh of extended fibrils. This entire internal heterogeneous structure of polyurethanes is hidden by a soft surface nanolayer. The mean thickness of this layer depends on the curing temperature, increasing from 6 (30 °C) to 14 nm (90 °C).

The observed fibrils and their agglomerates are secondary supramolecular structures with a high concentration of primary hard segments. Polymerization and formation of chemical crosslinking between macromolecules consisting of primary hard and soft segments occur during the curing of polyurethane. The polymer changes from a viscous state to an elastic one. At the same time, hard supramolecular structures are formed in polyurethanes [1,6]. A possible explanation for the differences in the structure is that the rate of chemical crosslinking and formation of a continuous mesh of macromolecules increases under curing at high temperatures, which makes it difficult to form a large number of supramolecular structures.

The curing temperature affects not only the structural features of the phase separation, but also the physico-mechanical properties of polymers: a correlation is shown between the features of the activity of inhomogeneous surfaces at the structural level and macroscopic measurements of the wettability and free energy of the surface (decreases with increasing curing temperature).

Curing at low temperature produces homogeneous and hard materials with high surface energies and pronounced dissipative properties (polyurethane obtained at 50 °C was the most stiff and elastic; the one obtained at 90 °C was the least stiff). The viscosity of materials obtained at high temperature is lower, they are more elastic, and their structure is more heterogeneous. All these results are explained by the mechanical properties of the supramolecular structures of these materials. Studies into these processes provide the key to obtaining polymers with the required properties.

References

- 1. Petrović ZS, Ferguson J. Polyurethane elastomers. *Progress in Polymer Science*. 1991;16(5): 695–836.
- 2. Sheth JP, Klinedinst DB, Wilkes GL, Yilgor I, Yilgor E. Role of chain symmetry and hydrogen bonding in segmented copolymers with monodisperse hard segments. *Polymer*. 2005;46(18): 7317–7322.
- 3. Klinedinst DB, Yilgör I, Yilgör E, Zhang M, Wilkes GL. The effect of varying soft and hard segment length on the structure—property relationships of segmented polyurethanes based on a linear symmetric diisocyanate, 1,4-butanediol and PTMO soft segments. *Polymer*. 2012;53(23): 5358–5366.
- 4. Tocha E, Janik H, Debowski M, Vancso GJ. Morphology of polyurethanes revisited by complementary AFM and TEM. *Journal of Macromolecular Science, Part B*. 2002;41(4-6): 1291–1304.
- 5. Yilgör I, Yilgör E, Wilkes GL. Critical parameters in designing segmented polyurethanes and their effect on morphology and properties: A comprehensive review. *Polymer*. 2015;58: A1–A36.
- 6. Kimball ME, Fielding-Russell GS. Effect of cure temperature on urethane networks. *Polymer.* 1977;18(8): 777–780.
- 7. Cheng BX, Gao WC, Ren XM, Ouyang XY, Zhao Y, Zhao H, Wu W, Huang CX, Liu Y, Liu XY, Li HN, Li RKY. A review of microphase separation of polyurethane: Characterization and applications. *Polymer Testing*. 2022;107: 107489.

- 8. Zheng J, Ozisik R, Siegel RW. Disruption of self-assembly and altered mechanical behavior in polyurethane/zinc oxide nanocomposites. *Polymer*. 2005;46(24): 10873–10882.
- 9. Zheng J, Ozisik R, Siegel RW. Phase separation and mechanical responses of polyurethane nanocomposites. *Polymer*. 2006;47(22): 7786–7794.
- 10. Larraza I, Alonso-Lerma B, Gonzalez K, Gabilondo N, Perez-Jimenez R, Corcuera MA, Arbelaiz A, Eceiza A. Waterborne polyurethane and graphene/graphene oxide-based nanocomposites: Reinforcement and electrical conductivity. *Express Polymer Letters*. 2020;14(11): 1018–1033.
- 11. Kojio K, Kugumiya S, Uchiba Y, Nishino Y, Furukawa M. The microphase-separated structure of polyurethane bulk and thin films. *Polymer Journal*. 2009;41(2): 118–124.
- 12. Takahashi A, Kita R, Kaibara M. Effects of thermal annealing of segmented-polyurethane on surface properties, structure and antithrombogenicity. *Journal of Materials Science: Materials in Medicine.* 2002;13: 259–262.
- 13. Li X, Lu Y, Wang H, Pöselt E, Eling B, Men Y. Crystallization of hard segments in MDI/BD-based polyurethanes deformed at elevated temperature and their dependence on the MDI/BD content. *European Polymer Journal*. 2017;97: 423–436.
- 14. Christenson EM, Anderson JM, Hiltner A, Baer E. Relationship between nanoscale deformation processes and elastic behavior of polyurethane elastomers. *Polymer*. 2005;46(25): 11744–11754.
- 15. Scetta G, Euchler E, Ju J, Selles N, Heuillet P, Ciccotti M, Creton C. Self-organization at the crack tip of fatigue-resistant thermoplastic polyurethane elastomers. *Macromolecules*. 2021;54(18): 8726–8737.
- 16. Shard AG, Davies MC, Tendler SJB, Jackson DE, Lan PN, Schacht E, Purbrick MD. Surface organization of polyurethanes observed by static secondary ion mass spectrometry. *Polymer*. 1995;36(4): 775–779.
- 17. McLean RS, Sauer BB. Tapping-mode AFM studies using phase detection for resolution of nanophases in segmented polyurethanes and other block copolymers. *Macromolecules*. 1997;30(26): 8314–8317.
- 18. Garrett JT, Siedlecki CA, Runt J. Microdomain Morphology of Poly(urethane urea) Multiblock Copolymers. *Macromolecules*. 2001;34(20): 7066–7070.
- 19. Alves P, Pinto S, de Sousa HC, Gil MH. Surface modification of a thermoplastic polyurethane by low-pressure plasma treatment to improve hydrophilicity. *Journal of Applied Polymer Science*. 2011;122(4): 2302–2308.
- 20. Chudinov V, Kondyurina I, Terpugov V, Kondyurin A. Weakened foreign body response to medical polyureaurethane treated by plasma immersion ion implantation. *Nuclear Instruments and Methods in Physics Research Section B: Beam Interactions with Materials and Atoms*. 2019;440: 163–174.
- 21. Morozov IA, Kamenetskikh AS, Beliaev AY, Izumov RI, Scherban MG, Lemkina LM, Kiselkov DM. Polyurethane treated in Ar/C2H2/Ar plasma: towards deformable coating with improved albumin adsorption. *Applied Sciences*. 2021;11: 9793.
- 22. Morozov IA, Kamenetskikh AS, Beliaev AY, Izumov RI, Bannikov MV, Scherban MG, Kiselkov DM. Carbon deposition and argon post-treatment of polyurethane surface: Structural-mechanical and fracture properties. *Surface and Coatings Technology*. 2022;437: 128372.
- 23. Santos TB, Vieira AA, Paula LO, Santos ED, Radi PA, Khouri S, Maciel HS, Pessoa RS, Vieira L. Flexible camphor diamond-like carbon coating on polyurethane to prevent Candida albicans biofilm growth. *Journal of the Mechanical Behavior of Biomedical Materials*. 2017;68: 239–246.
- 24. Barz J, Haupt M, Oehr C, Hirth T, Grimmer P. Stability and water wetting behavior of superhydrophobic polyurethane films created by hot embossing and plasma etching and coating. *Plasma Processes and Polymers*. 2019;16(6): 1800214.

- 25. Joshi M, Adak B, Butola BS. Polyurethane nanocomposite based gas barrier films, membranes and coatings: A review on synthesis, characterization and potential applications. Progress in Materials Science. 2018;97: 230–282.
- 26. Fronczak SG, Dong J, Browne CA, Krenek EC, Franses EI, Beaudoin SP, Corti DS. A new "quasi-dynamic" method for determining the Hamaker constant of solids using an atomic force microscope. Langmuir. 2017;33(3): 714-725.
- 27. Morozov IA. Atomic force microscopy nanoindentation kinetics and subsurface visualization of soft inhomogeneous polymer. *Microscopy Research and Technique*. 2021;84(21): 1959–1966.
- 28. Sneddon IN. The relation between load and penetration in the axisymmetric Boussinesq problem for a punch of arbitrary profile. *International Journal of Engineering Science*. 1965;3(1): 47–57.
- 29. Shulha H, Kovalev A, Myshkin N, Tsukruk VV. Some aspects of AFM nanomechanical probing of surface polymer films. European Polymer Journal. 2004;40(5): 949–956.
- 30. Garcia PD, Guerrero CR, Garcia R. Time-resolved nanomechanics of a single cell under the depolymerization of the cytoskeleton. Nanoscale. 2017;9(33): 12051–12059.
- 31. Guerrero CR, Garcia PD, Garcia R. Subsurface imaging of cell organelles by force microscopy. ACS Nano. 2019;13;(8): 9629–9637.
- 32. Aishwarya S, Shanthi J, Swathi R. Surface energy calculation using Hamaker's constant for polymer/silane hydrophobic thin films. Materials Letters. 2019;253: 409-411.
- 33. Stevenson MC, Beaudoin SP, Corti DS. Toward an improved method for determining the Hamaker constant of solid materials using atomic force microscopy. I. quasi-static analysis for arbitrary surface roughness. J. Phys. Chem. C. 2020;124(5): 3014–3027.

THE AUTHORS

Morozov I.A.

Beliaev A.Yu. e-mail: ilya.morozov@gmail.com e-mail: belyaev@icmm.ru

Scherban M.G.

e-mail: ma-sher74@mail.ru

Study of the influence of dispersed fillers on properties of rubber for gaskets of rail fastening

Submitted: March 4, 2023

Approved: May 2, 2023

Accepted: May 17, 2023

E.N. Egorov ^{1 □} S.I. Sandalov ^{1 □} N.I. Kol'tsov ^{1 □}

¹ I.N. Ulyanov Chuvash State University, Cheboksary, Russia
² V.I. Chapaev Cheboksary Production Association, Cheboksary, Russia

⊠ enegorov@mail.ru

Abstract. The effect of dispersed fillers (NDP-D-400 and NDP-230 diatomites, microquartz and magnesium hydrosilicate) on the rheometric, physical-mechanical, operational and dynamic (sound-absorbing) properties of rubber based on general and special purpose caoutchoucs used for the manufacture of rail fastening gaskets has been studied. The rubber mixture was prepared on laboratory rollers LB 320 160/160, and then vulcanized in a P-V-100-3RT-2-PCD press. For the rubber compound, the vulcanization characteristics were studied, and for the vulcanizates, the physical and mechanical properties, their changes after exposure to aggressive environments and dynamic performance. It has been established that dispersed fillers improve the technological properties of the rubber mixture, increase the physical and mechanical, dynamic performance and resistance of rubber to aggressive media. It is shown that vulcanizates containing diatomites NDP-230 and NDP-D-400 in an amount of 5.0 phr, are characterized by improved physical, mechanical, operational and dynamic properties.

Keywords: diatomites; caoutchoucs; rubber; rheometric; physical-mechanical; operational and dynamic properties

Citation: Egorov EN, Sandalov SI, Kol'tsov NI. Study of the influence of dispersed fillers on properties of rubber for gaskets of rail fastening. *Materials Physics and Mechanics*. 2023;51(6): 119-126. DOI: 10.18149/MPM.5162023_11.

Introduction

Railways during operation create increased levels of vibration and noise caused by the interaction of the rolling stock and the railway track [1–7]. The noise generated during the operation of railway transport has its negative impact on human health [8-14]. To solve this problem, rubber gaskets for rail fastenings are used [15–20]. These gaskets are made from noise-absorbing rubbers based on a combination of general and special purpose rubbers, as well as directional functional ingredients [21–26]. In [27,28], trans-polynorbornene and silica filler Silica 1165 were used as such ingredients. It is known [29–33] that dispersed fillers also improve the noise-absorbing properties of composite materials. In this regard, in this article, the effect of dispersed fillers (NDP-D-400 and NDP-230 diatomites, microquartz and magnesium hydrosilicate) on the properties of rubber used for the manufacture of rail fasteners was studied.

Materials and Method

The studied rubber mixture included the following caoutchoucs and ingredients: butadiene-methylstyrene SKMS-30ARK, butadiene-nitrile SKN-2655 and *cis*-isoprene SKI-3, vulcanization accelerator - N-cyclohexyl-2-benzothiazolesulfenamide; vulcanizing agents -

sulfur, tetramethylthiuram disulfide and N,N'-dithiodimorpholine; vulcanization activators stearic acid; stabilizers acetonanil N, protective N-phenyl-N'- isopropyl-p-phenylenediamine; dispersant - Hepsol HKP; softeners - rosin, industrial oil I-12A; scorch retarder - N-nitrosodiphenylamine; fillers - kaolin, carbons black N 220 and P 514, silicon dioxide Zeosil 1165 MP and trans-polynorbornene. As dispersed fillers, diatomites NDP-D-400 and NDP-230 were used (contain 84-87 % SiO₂, 5.5-6.0 % Al₂O₃, 2.5-3.0 % Fe₂O₃ and 0.6 % CaO), microquartz and magnesium hydrosilicate. Diatomite NDP-D-400 is a beige powder with a pink tint, particle size 25-30 μm, density 2.14 g/cm³, porosity 82.7 %, specific surface area 0.8-1.1 m²/g. Diatomite NDP-230 is a beige powder, particle size 5 μm, density 2.06 g/cm³, porosity 89.3 %, specific surface area 3.0-3.3 m²/g. Microquartz is a gray powder, mass fraction of silicon dioxide is not less than 98 %, specific surface area is 16.8 m²/g, density is 2.55 g/cm³. Magnesium hydrosilicate composition 3MgO·4SiO₂·H₂O is a dark gray powder with a scaly particle size of 5-20 µm, density 2.60-2.80 g/cm³. Kaolin was a beige powder with a particle size of 10–20 µm, a density of 2.5–2.63 g/cm³, and a specific surface area of 10–24 m²/g.

The rubber mixture was prepared on an LB 320 160/160 laboratory roller at 60–70 °C for 25 min. The vulcanization characteristics of the rubber compound were studied on a Mon Tech MDR 3000 Basic rheometer at 143 °C for 40 min in accordance with ASTM D2084-79. Standard samples for determining physical and mechanical properties were vulcanized at a temperature of 143 °C for 20 min in a P-V-100-3RT-2-PCD type vulcanizing press. The main characteristics of the vulcanizates were determined according to the standards in force in the rubber industry: elastic-strength properties were determined according to GOST 270-75; hardness - according to GOST 263-75; tear resistance - according to GOST 262-79; change in conditional tensile strength, relative elongation at break and hardness after aging in air according to GOST 9.024-74; change in conditional tensile strength, relative elongation at break and hardness after exposure to aggressive hydrocarbon media - according to GOST 9.030-74 (method B); change in mass after exposure to aggressive media - according to GOST 9.030-74 (method A). The dynamic parameters of the vulcanizates of the rubber compound were studied at 30 °C on a Metravib VHF 104 dynamic mechanical analyzer with a degree of deformation of 0.01 %, a frequency of 1000 Hz in the "tension-compression" deformation mode.

Results and Discussion

The possibility of partial and complete replacement of the fillers (kaolin, carbons black N 220 and P 514 and Zeosil 1165 MP silicon dioxide) included in the composition of the rubber mixture with dispersed fillers: NDP-D-400 and NDP-230 diatomites, microquartz and magnesium hydrosilicate was previously studied. As a result, the efficiency of the equal weight replacement of kaolin with the listed particulate fillers in the amount of 5.0 phr (parts per hundred parts of rubber), which was taken as the basis for further research. Table 1 shows the investigated options for the rubber mixture.

The first variant of the rubber mixture was made using kaolin. In the second-fifth variants of the rubber compound, an equal mass replacement of kaolin was carried out for diatomites NDP-D-400 and NDP-230, microquartz and magnesium hydrosilicate, respectively.

To establish the rheometric characteristics of the rubber mixture, the vulcanization kinetics of its various variants was studied. Figure 1 shows the resulting vulcanization curves.

Based on these curves, the rheometric properties were determined, which are given in Table 1. From the data in Table 1 it follows that the equal-mass replacement of kaolin with the above fillers leads to an increase in the maximum torque, the vulcanization start time and a decrease in the minimum torque, the optimal vulcanization time of the rubber mixture. The

rubber compound of the third variant has improved technological properties, which is characterized by the lowest value of the minimum torque and the longest vulcanization start time. The results of studies of the physical and mechanical characteristics of vulcanizates of various options for the rubber mixture are given in Table. 2.

Table 1. Variants of the studied rubber mixture

Fillers	Variants of the rubber mixture					
Fillers	1	2	3	4	5	
Kaolin, phr	5.0	ı	ı	ı	_	
Diatomite NDP-D-400, phr	ı	5.0	ı	ı	_	
Diatomite NDP-230, phr	ı	ı	5.0	ı	_	
Microquartz, phr	ı	ı	ı	5.0	_	
Magnesium hydrosilicate, phr	ı	ı	ı	ı	5.0	
Rheome	tric properties	of the rubber i	mixture			
S_{\max} , dN·m	18.30	18.43	18.53	18.48	19.03	
S_{\min} , $\mathrm{d}\mathbf{N}\cdot\mathbf{m}$	3.62	3.47	3.44	3.61	3.50	
$t_{\rm s}$, min	5.03	5.59	5.68	5.64	5.51	
<i>t</i> ₉₀ , min	16.26	15.89	15.69	15.47	15.52	

Note: S_{max} – maximum torque; S_{min} – minimum torque; t_{s} – start time of vulcanization; t_{90} – optimum vulcanization time.

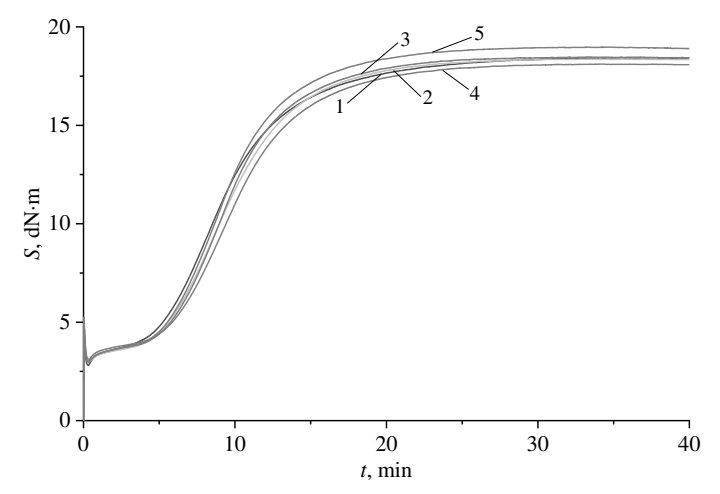


Fig. 1. Vulcanization curves of various variants of the rubber compound at 143 °C using various fillers: 1 – kaolin, 2 – diatomite NDP-D-400, 3 – diatomite NDP-230, 4 – microquartz, 5 – magnesium hydrosilicate

Table 2. Physical and mechanical properties of vulcanizates

Parameter	Variants of the rubber mixture				
	1	2	3	4	5
f_{100} , MPa	3.6	3.8	4.1	3.9	3.8
f _p , MPa	12.8	14.4	14.8	14.4	13.1
$\varepsilon_{ m p},\%$	350	400	380	370	400
H, Shore A units	70	70	70	68	70
B, kN/m	43	48	51	47	45
N. C. 1'.' 1 100	0.07 1 .	C 1'' 1	. '11	1	. 1 1

Note: f_{100} – conditional stress at 100 % stretching; f_p – conditional tensile strength; ε_p – elongation at break; H – hardness; B – tear resistance.

Based on these curves, the rheometric properties were determined, which are given in Table 1. From the data in Table 1 it follows that the equal-mass replacement of kaolin with the above fillers leads to an increase in the maximum torque, the vulcanization start time and a decrease in the minimum torque, the optimal vulcanization time of the rubber mixture. The

rubber compound of the third variant has improved technological properties, which is characterized by the lowest value of the minimum torque and the longest vulcanization start time. The results of studies of the physical and mechanical characteristics of vulcanizates of various options for the rubber mixture are given in Table. 2.

From the data in Table 2 it follows that the equal-mass replacement of kaolin with dispersed fillers contributes to an increase in the conditional stress at 100% stretching, conditional tensile strength, relative elongation at break, and tear resistance of vulcanizates. The vulcanizate of the third version of the rubber compound containing NDP-230 diatomite is characterized by the highest strength and tear resistance.

Further, the operational properties were studied - changes in the physical and mechanical parameters and hardness of vulcanizates after aging in air and exposure to SZhR-1 at a temperature of 100 °C for 24 hours (see Table 3).

Table 3. Changes in physical and mechanical properties and hardness of vulcanizates after

•			1		071 D 1
aging	1n	air	and	1n	SZhR-1

Damaratan		Variants of the rubber mixture					
Parameter	1	2	3	4	5		
	After a	ir aging					
$\Delta f_{ m p},\%$	-18.6	-18.4	-15.2	-17.5	-15.8		
$\Delta \mathcal{E}_{p},$ %	-34.3	-32.5	-30.2	-32.4	-33.5		
ΔH , Shore A units	+4	+3	+2	+1	+2		
After exposure to SZhR-1							
$\Delta f_{ m p},\%$	-48.4	-42.4	-39.6	-43.1	-43.5		
$\Delta \mathcal{E}_{ m p},\%$	-32.1	-29.5	-26.3	-30.1	-29.4		
ΔH , Shore A units	-23	-20	-17	-16	-19		
Note: $\Delta f_{\rm p}$, $\Delta \varepsilon_{\rm p}$, – relative change i	n tensile strength and	elongation at l	oreak, respectiv	velv:	•		

 ΔH – change in hardness.

From the data in Table 3 shows that after daily thermal-oxidative aging in air, a decrease in physical and mechanical parameters and an increase in the hardness of vulcanizates are observed. Moreover, the replacement of kaolin with dispersed fillers leads to smaller changes in the physical and mechanical properties and hardness of the vulcanizates. The vulcanizate containing NDP-230 diatomite has the least changes in physical and mechanical properties. Replacing kaolin with dispersed fillers also leads to smaller changes in the physical and mechanical parameters and hardness of vulcanizates after their daily holding in SZhR-1 heated to 100 °C. Moreover, in SZhR-1, the hardness of the vulcanizates is significantly reduced due to the loosening of the network structure of the vulcanizates with a standard mixture of hydrocarbons.

Figures 2-4 show the results of a study of the change in the mass of vulcanizates after their holding at a temperature of 23 °C for 24 hours in various media: industrial oil I-20A, distilled water and SZhR-1.

As can be seen from Figs. 2-4, the replacement of kaolin with dispersed fillers leads to a decrease in the change in the mass of vulcanizates after their daily exposure in all three media. In hydrocarbon media (SZhR-1 and industrial oil I-20A), changes in the mass of vulcanizates are higher than in distilled water. The smallest change in mass after exposure in all environments has a vulcanizate rubber mixture containing NDP-230 diatomite. In Table 4 shows the results of studies of the dynamic properties of vulcanizates.

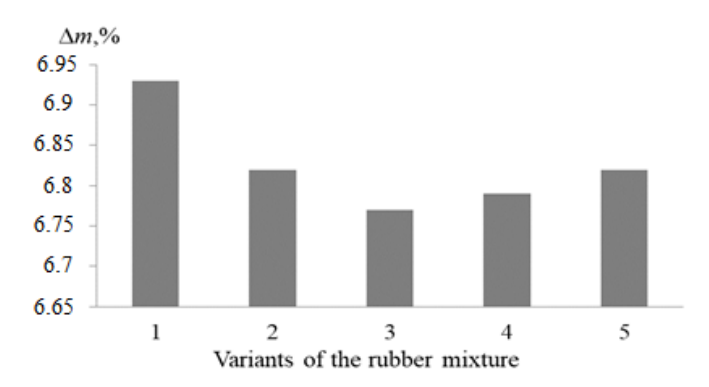


Fig. 2. Change in mass of vulcanizates after exposure in industrial oil I-20A

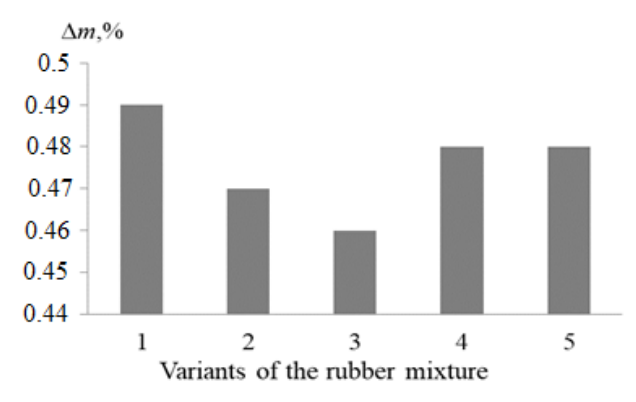


Fig. 3. Change in mass of vulcanizates after exposure in distilled water

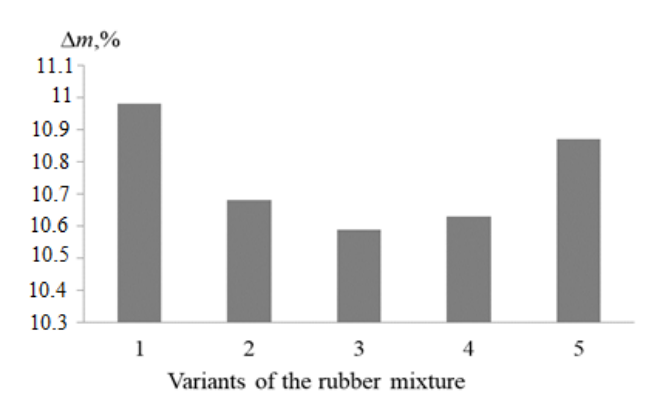


Fig.4. Change in mass of vulcanizates after exposure in SZhR-1

The data in Table 4 show that the equal-mass replacement of kaolin with dispersed fillers in the composition of the rubber mixture leads to an increase in the tan delta and the storage modulus of the vulcanizates. An increase in the storage modulus of vulcanizates indicates an increase in their physical and mechanical properties, which is consistent with the results given in Table 2 for vulcanizates containing particulate fillers. It is known [34,35] that polymer composite materials with increased values of the tan delta (loss factor) have improved dynamic properties. According to [36–38], such polymers should contain fillers with large particles and a low specific surface area. These conditions are met by the vulcanizate of the second variant of the rubber mixture containing NDP-D-400 diatomite, which, compared to other dispersed fillers used, consists of larger particles and has a smaller specific surface area. For the vulcanizate of the third variant of the rubber compound containing NDP-230 diatomite, the value of the tan delta is less than for the vulcanizate of the second variant of the rubber mixture, however, this value is sufficient for rail fasteners. The

second and third rubber options are similar in rheometric, physical, mechanical and operational properties. Therefore, diatomites NDP-D-400 and NDP-230 can equally be used in the rubber composition for rail fasteners.

Table 4. Dynamic properties of rubber compound vulcanizates

Parameter	Variants of the rubber mixture				
	1 2 3 4				5
$tg\delta$	0.230	0.246	0.241	0.235	0.238
$E' \cdot 10^{-7}$, Pa	5.19	5.20	5.23	5.21	5.22
Note: $tg\delta$ – tan delta (loss factor); E' – storage modulus.					

Conclusions

The effect of dispersed fillers (NDP-D-400 and NDP-230 diatomites, microquartz and magnesium hydrosilicate) on the rheometric properties of the rubber mixture, physical and mechanical, operational and dynamic performance of rubber based on general and special purpose caoutchoucs (isoprene, butadiene-methylstyrene and nitrile butadiene). It has been established that rubber containing diatomites NDP-230 and NDP-D-400 in the amount of 5.0 phr, can be recommended for the manufacture of rail fastening gaskets with improved physical, mechanical, operational and dynamic properties.

References

- 1. Ďungel J, Zvolenský P, Grenčík J, Leštinský L, Krivda J. Localization of Increased Noise at Operating Speed of a Passenger Wagon. *Sustainability*. 2021;13(2): 453.
- 2. Kaewunruen S, Ishida M, Marich S. Dynamic Wheel–Rail Interaction Over Rail Squat Defects. *Acoustics Australia*. 2015;43(1): 97–107.
- 3. Tavares de Freitas R, Kaewunruen S. Life Cycle Cost Evaluation of Noise and Vibration Control Methods at Urban Railway Turnouts. *Environments*. 2016;3(4): 34.
- 4. Barke DW, Chiu WK. A Review of the Effects of Out-Of-Round Wheels on Track and Vehicle Components. *Proceedings of the Institution of Mechanical Engineers, Part F: Journal of Rail and Rapid Transit.* 2005;219(3): 151–175.
- 5. Kouroussis G, Connolly DP, Vogiatzis K, Verlinden O. Modelling the Environmental Effects of Railway Vibrations from Different Types of Rolling Stock: A Numerical Study. *Shock and Vibration*. 2015;2015: 1–15.
- 6. Chiacchiari L, Loprencipe G. Measurement methods and analysis tools for rail irregularities: a case study for urban tram track. *Journal of Modern Transportation*. 2015;23(2): 137–147.
- 7. Colaço A, Costa PA, Connolly DP. The influence of train properties on railway ground vibrations. *Structure and Infrastructure Engineering*. 2015;12(5): 517–534.
- 8. Hao Y, Qi H, Liu S, Nian V, Zhang Z. Study of Noise and Vibration Impacts to Buildings Due to Urban Rail Transit and Mitigation Measures. *Sustainability*. 2022;14(5): 3119.
- 9. Mohamed AMO, Paleologos EK, Howar FM. Noise pollution and its impact on human health and the environment. *Pollution Assessment for Sustainable Practices in Applied Sciences and Engineering*. 2021: 975–1026.
- 10. Michali M, Emrouznejad A, Dehnokhalaji A, Clegg B. Noise-pollution efficiency analysis of European railways: A network DEA model. *Transportation Research Part D: Transport and Environment*. 2021;98: 102980.
- 11. Sahu P, Galhotra A, Raj U, Ranjan RV. A study of self-reported health problems of the people living near railway tracks in Raipur city. *Journal of Family Medicine and Primary Care*. 2020;9(2): 740–744.
- 12. Panulinova E, Harabinová S, Argalášová L. Tram squealing noise and its impact on human health. *Noise Health*. 2016;18(85): 329–337.

- 13. Demir E, Huang Y, Scholts S, Van Woensel T. A selected review on the negative externalities of the freight transportation: Modeling and pricing. *Transportation Research Part E: Logistics and Transportation Review.* 2015;77: 95–114.
- 14. Elmenhorst E-M, Pennig S, Rolny V, Quehl J, Mueller U, Maaß H, Basner M. Examining nocturnal railway noise and aircraft noise in the field: Sleep, psychomotor performance, and annoyance. *Science of The Total Environment*. 2012; 424: 48–56.
- 15. Wu B, Chen G, Lv J, Zhu Q, Kang X. Generation mechanism and remedy method of rail corrugation at a sharp curved metro track with Vanguard fasteners. *Journal of Low Frequency Noise, Vibration and Active Control.* 2019;39(2): 1–14.
- 16. Liu L, Zuo Z, Zhou Y, Qin J. Insights into the Effect of WJ-7 Fastener Rubber Pad to Vehicle-Rail-Viaduct Coupled Dynamics. *Applied Sciences*. 2020;10(5): 1889.
- 17. Huang Y, Wang J, Le W, Zhang L, Su J. Study on mechanical behaviours of rail fasteners and effects on seismic performance of urban rail viaduct. *Structures*. 2021;33: 3822–3834.
- 18. Liu W, Zhang H, Liu W, Thompson DJ. Experimental study of the treatment measures for rail corrugation on tracks with Egg fasteners in the Beijing metro. *Proceedings of the Institution of Mechanical Engineers, Part F: Journal of Rail and Rapid Transit.* 2017; 232(5): 1360–1374.
- 19. Xu J, Wang K, Liang X, Gao Y, Liu Z, Chen R, Wang P, Xu F, Wei K. Influence of viscoelastic mechanical properties of rail pads on wheel and corrugated rail rolling contact at high speeds. *Tribology International*. 2020;151: 106523.
- 20. Egorov EN., Ushmarin NF., Salomatina EV., Matyunin AN. The effect of polyisobutylene on physical-mechanical, operational, dielectric and dynamic properties of rubber for laying rail fasteners. *Izv. Vyssh. Uchebn. Zaved. Khim. Khim. Tekhnol.* 2022;65(5): 94–102 (in Russian).
- 21. Zhang J, Wang L, Zhao Y. Fabrication of novel hindered phenol/phenol resin/nitrile butadiene rubber hybrids and their long-period damping properties. *Polymer Composites*. 2012;33(12): 2125–2133.
- 22. Roche N, Ichchou MN, Salvia M, Chettah A. Dynamic Damping Properties of Thermoplastic Elastomers Based on EVA and Recycled Ground Tire Rubber. *Journal of Elastomers and Plastics*. 2011;43(4): 317–340.
- 23. Wang Y, Cao R, Wang M, Liu X, Zhao X, Lu Y, Feng A, Zhang L. Design and synthesis of phenyl silicone rubber with functional epoxy groups through anionic copolymerization and subsequent epoxidation. *Polymer*. 2020;186: 122077.
- 24. Ushmarin NF, Egorov EN, Grigor'ev VS, Sandalov SI, Kol'tsov NI. Influence of Chlorobutyl Caoutchouc on the Dynamic Properties of a Rubber Based on General-Purpose Caoutchoucs. *Russian Journal of General Chemistry*. 2022; 92(9): 1862–1865.
- 25. Sheng Z, Yang S, Wang J, Lu Y, Tang K, Song S. Preparation and Properties Analysis of Chlorinated Butyl Rubber (CIIR)/Organic Diatomite Damping Composites. *Materials*. 2018;11(11): 2172.
- 26. Zhou X.Q., Yu D.Y., Shao X.Y., Zhang S.Q., Wang S. Research and applications of viscoelastic vibration damping materials: A review. *Composite Structures*. 2016;136: 460–480.
- 27. Egorov EN, Ushmarin NF, Sandalov SI, Kol'tsov NI. Studying the Effect of trans-Polynorbornene on the Properties of a Rubber Mixture for Rail Fastener Pads. *Inorganic Materials: Applied Research.* 2022; 13(4): 1019–1023.
- 28. Egorov EN, Ushmarin NF, Sandalov SI, Grigor'ev VS, Kol'tsov NI, Voronchikhin VD. Study of the effect of silica filler Silica 1165 on the properties of rubber for rail fastening gaskets. *Journal of Siberian Federal University*. *Chemistry*. 2022;15(1): 110–117.
- 29. Kucuk, F, Sismanoglu S, Kanbur Y, Tayfun U. Effect of silane-modification of diatomite on its composites with thermoplastic polyurethane. *Materials Chemistry and Physics*. 2020;256: 123683.
- 30. Lapčík L, Maňas D, Lapčíková B, Vašina M, Staněk M, Čépe K, Vlček J, Waters KE, Greenwood RW, Rowson NA. Effect of filler particle shape on plastic-elastic mechanical

behavior of high density poly(ethylene)/mica and poly(ethylene)/wollastonite composites. *Composites Part B: Engineering*. 2018;141: 92–99.

- 31. Tekay E, Şen S. High strength, tough/damping and creep resistant EVA/HNT nanocomposites via help of EVA-g-MA compatibilizer. *Journal of Composite Materials*. 2022;56(19): 2951–2962.
- 32. Zeyuan S, Jincheng W, Siyuang Y, Shiqiang S. Novel polysiloxane microspheres: Preparation and application in chlorinated butyl rubber (CIIR) damping composites. *Advanced Powder Technology*. 2019;30(3): 632–643.
- 33. Pan Y, Wang J, Yang S. Preparation of novel damping layered silicates and its application in chlorinated butyl rubber (CIIR) composites. *Polymer-Plastics Technology and Materials*. 2019;59(4): 385–397.
- 34. Moradi G, Nassiri P, Ershad-Langroudi A, Monazzam MR. Acoustical, damping and thermal properties of polyurethane/poly(methyl methacrylate)-based semi-interpenetrating polymer network foams. *Plastics, Rubber and Composites*. 2018;47: 221–231.
- 35. Sharifi MJ, Ghalehkhondabi V, Fazlali A. Investigation of the underwater sound absorption and damping properties of polyurethane elastomer. *Journal of Thermal Analysis and Calorimetry*. 2022;147: 4113–4118.
- 36. Robertson CG, Lin CJ, Rackaitis M, Roland CM. Influence of Particle Size and Polymer–Filler Coupling on Viscoelastic Glass Transition of Particle-Reinforced Polymers. *Macromolecules*. 2008;41(7): 2727–2731.
- 37. Chuayjuljit S, Imvittaya A, Na-Ranong N, Potiyaraj P. Effects of Particle Size and Amount of Carbon Black and Calcium Carbonate on Curing Characteristics and Dynamic Mechanical Properties of Natural Rubber. *Journal of Metals, Materials and Minerals*. 2002; 12(1): 51–57.
- 38. Fang Q, Song B, Tee T-T, Sin LT, Hui D, Bee S-T. Investigation of dynamic characteristics of nano-size calcium carbonate added in natural rubber vulcanizate. *Composites Part B: Engineering*. 2014;60: 561–567.

THE AUTHORS

Egorov E.N.

E-mail: enegorov@mail.ru

Sandalov S.I. 匝

E-mail: sandalov-1963@yandex.ru

Kol'tsov N.I.

E-mail: koltsovni@mail.ru

Electromagnetic radiation reflection, transmission and absorption characteristics of microwave absorbers based on dilatant liquids and powdered activated wood charcoal

Submitted: September 6, 2023

Approved: November 8, 2023

Accepted: November 14, 2023

O.V. Boiprav [□] , V.A. Bogush [□] , L.M. Lynkou [□]

Belarusian State University of Informatics and Radioelectronics, Minsk, Belarus ⊠ smu@bsuir.by

Abstract. The paper presents new microwave absorbers based on dilatant liquids and powdered activated wood (birch) charcoal. The patterns of changes of electromagnetic radiation reflection, transmission and absorption coefficients values in the frequency range 2.0–17.0 GHz of the indicated absorbers are described. In accordance with these patterns, electromagnetic radiation reflection coefficient values in the frequency range of 2.0–17.0 GHz of the absorbers based on a dilatant liquid containing water vary from –2.0 to –15.0 dB, and absorbers based on dilatant liquid containing magnesium chloride water solution or sodium chloride water solution – from –2.0 to –17.0 dB and from –2.0 to –10.0 dB, respectively. Electromagnetic radiation transmission coefficient values of the above absorbers vary respectively from –15.0 to –27.0 dB, from –15.0 to –28.0 dB, from –15.0 to –30.0 dB. Electromagnetic radiation absorption coefficient values of these absorbers achieve a value of 0.95. These absorbers are recommended for use in lining the walls of containers intended for storage and transportation of electronic devices sensitive to microwave interference.

Keywords: absorption coefficient; activated wood charcoal; dilatant liquid; magnesium chloride; microwave absorber; reflection coefficient; sodium chloride; transmission coefficient

Citation: Boiprav OV, Bogush VA, Lynkou LM. Electromagnetic radiation reflection, transmission and absorption characteristics of microwave absorbers based on dilatant liquids and powdered activated wood charcoal. *Materials Physics and Mechanics*. 2023;51(6): 127-134. DOI: 10.18149/MPM.5162023_12.

Introduction

Water or water solutions are used for the fabrication of microwave absorbers at present [1–5]. This is due to high dielectric energy losses of microwave radiation provided by water, water solutions, and materials containing them [6]. In addition, based on water or water solutions, microwave absorbers can be obtained, which are characterized by the flexibility [5,7,8]. This property makes it possible to use such absorbers to cover the surfaces of objects that need to be protected from exposure to microwave radiation [9].

As a rule, currently proposed technologies for the fabrication of the considered absorbers (including flexible ones) consist in filling the cells of containers obtained by 3D printing with water or water solutions [9–11]. The main disadvantage of flexible microwave absorbers based on water or water solutions is low mechanical strength. Paper [12] presents the results of an experimental substantiation of the prospectivity of hydrogel use for mechanically strong microwave absorbers fabrication. However, hydrogel-based microwave absorbers [12] are high cost ones. This is due to the corresponding property of the hydrogel.

The authors of the paper proposed the following decisions for the obtaining of mechanically strong and low-cost flexible microwave absorbers on the base of water or water solutions:

- 1. to use of dilatant liquids;
- 2. to include the powdered electrically conductive materials particles in the content of dilatant liquids used for the microwave absorbers fabrication (to increase the electromagnetic radiation absorption coefficient and expand the operating frequency range of the absorbers) [13,14].

In this regard, the following was determined as the aim of the study, the results of which are presented in this paper:

- 1. to establish the dependence of electromagnetic radiation reflection, transmission and absorption coefficients values of microwave absorbers based on dilatant liquid and powdered electrically conductive material from this liquid composition;
- 2. based on the established patterns, to determinate the content of the dilatant liquid, which is most suitable for obtaining high effective microwave absorbers.

The process of aim achieving was targeted at improving the existing water-containing microwave absorbers.

Materials and Methods

In course of aim achieving, three kinds of experimental samples of microwave absorbers were fabricated. Samples of the 1^{st} kind were based on the dilatant liquid containing water. Samples of the 2^{nd} kind were based on the dilatant liquid containing 35.0 ± 1.0 wt. % magnesium chloride water solution. Samples of the 3^{rd} kind were based on the dilatant liquid containing 35.0 ± 1.0 wt. % sodium chloride water solution. The concentration of the indicated solutions corresponded to the solubility limit of sodium chloride in water.

The use of magnesium or sodium chloride water solution for the production of the dilatant liquids for microwave absorbers seems appropriate for the following reasons:

- 1. The specific electrical conductivity of magnesium or sodium chloride water solution exceeds the specific electrical conductivity of water. In this regard, electromagnetic radiation transmission coefficient values of microwave absorbers based on the dilatant liquid containing this solution are lower than electromagnetic radiation transmission coefficient values of microwave absorbers based on the dilatant liquid containing water.
- 2. The crystallization temperature of magnesium or sodium chloride water solution is lower than the crystallization temperature of water. In this regard microwave absorbers based on the dilatant liquid containing this solution, in contrast to microwave absorbers based on the dilatant liquid containing water, can be operated in conditions of negative temperatures.

Powdered activated wood (birch) charcoal was used as an electrically conductive material for these samples fabrication. The main advantages of this material compared to other electrically conductive powder materials are as follows:

- powdered activated wood (birch) charcoal is characterized by low cost [15];
- the particle size of powdered activated wood (birch) charcoal is close to the microwave length value; as a result, powdered activated wood (birch) charcoal ensures the loss of energy of microwaves interacting with it, not only due to the reflection and absorption phenomenon, but also due to the scattering phenomenon [16].

The thickness of the fabricated samples was 0.5 ± 0.1 cm. The top view of a fragment of the surface of one of the fabricated samples is shown in Fig. 1.

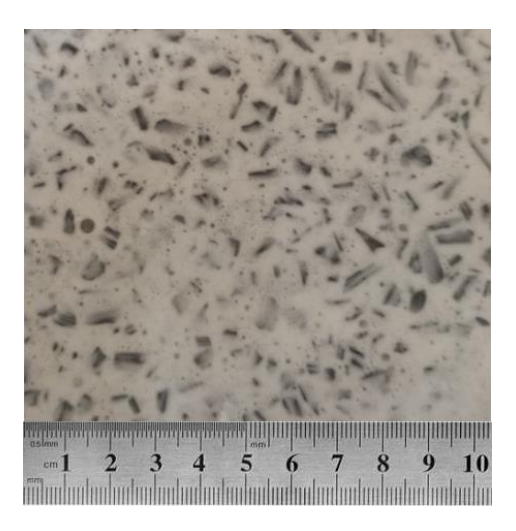


Fig. 1. Top view of the fabricated sample surface fragment

Electromagnetic radiation reflection and transmission coefficients (S_{11} and S_{21} respectively) values of the fabricated samples were measured in the frequency range of 2.0–17.0 GHz. The range was chosen because it belongs to the operating frequency bands of modern radio-electronic transceivers. The radiation generated by these devices can affect the performance of electronic devices that are sensitive to interference. Scalar network analyzer SNA 0.01–18 was used for measurements of S_{11} and S_{21} values of the fabricated samples. The measurements were carried out in accordance with the algorithm presented in [17].

Measurements of S_{11} values of the fabricated samples were carried out under the following conditions.

Condition 1: the sample was between the transmitting antenna and the matched load in course the measurements.

Condition 2: the sample was between the transmitting antenna and the short circuit (metal plate) in course the measurements.

Based on the results of measurements carried out under the first condition, it was estimated the fraction of the energy of electromagnetic radiation reflected by the surface of the experimental sample. Based on the results of measurements carried out under the second condition, it was estimated the fraction of the energy of electromagnetic radiation, which is a superposition of:

- 1. electromagnetic radiation reflected by the sample surface;
- 2. electromagnetic radiation reflected by the metal plate surface and after that absorbed by the sample.

Electromagnetic radiation absorption coefficient (A) values of the fabricated samples were calculated on the base of the measured S_{11} and S_{21} values. The algorithm presented in [17] was used for calculation.

To substantiate the patterns of change of electromagnetic radiation reflection, transmission and absorption coefficients values of experimental samples, the specific electrical conductivity values (σ) of dilatant liquids, on the base of which these samples were made, were measured. The method presented in the paper [18] was used for the measurements. This method is based on use of the two-electrodes measurement cell. The method includes the following four steps:

- 1. Filling with dilatant liquid of two-electrodes measurement cell.
- 2. Connection of the resistance meter to the electrodes of the measurement cell.
- 3. Measurement of the dilatant liquid resistance.

4. Calculation of the dilatant liquid specific electrical conductivity according to the formula $\sigma = \frac{l}{R \cdot S}$, S/m, where *l* is the distance between the electrodes of the measurement cell, m; *S* is the area of the measurement cell electrodes, m².

Results and Discussion

2.0–17.0 GHz frequency responses of S_{11} values of the fabricated samples are shown in Fig. 2.

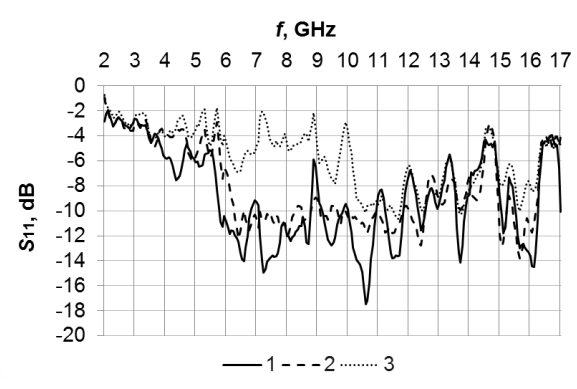


Fig. 2. 2.0–17.0 GHz frequency responses of S_{11} values of the samples of the 1st kind (graph 1), the samples of the 2nd kind (graph 2) and the samples of the 3rd kind (graph 3)

It follows from Fig. 2, that S_{11} values in the frequency range of 2.0–17.0 GHz of the samples of the 1st kind, the samples of the 2nd kind and the samples of the 3rd kind vary respectively from –2.0 to –17.0 dB, from –2.0 to –15.0 dB, from –2.0 to –10.0 dB. There are following average S_{11} values of the above samples: –8.9 dB, –8.0 dB and –5.7 dB respectively. S_{11} values of the samples of the 1st kind are lower compared with S_{11} values of the samples of the 2nd kind and the sample of the 3rd kind due to the set of the following facts:

- 1. σ value of the dilatant liquid containing water is lower than σ value of the dilatant liquid, containing magnesium chloride water solution or sodium chloride water solution (see Table 1); this is because σ value of water is lower than σ value of magnesium chloride water solution and lower in more degree than σ value of sodium chloride water solution [19];
- 2. electromagnetic radiation reflection losses in the material are connected with its σ value through the following formula [13]: $39.5 + 10 lg \frac{\sigma}{2\pi f \mu}$, dB (as it follows from the given formula, material S_{11} value increases if its σ value increases).

Table 1. The σ values of the dilatant liquids used for the samples fabrication

Dilatant liquid kind	σ, S/m
Liquid used for the samples of the 1st kind fabrication	4.4
Liquid used for the samples of the 2 nd kind fabrication	5.5
Liquid used for the samples of the 3 rd kind fabrication	6.8

2.0–17.0 GHz frequency responses of S_{21} values of the fabricated samples are shown are shown in Fig. 3. It follows from Fig. 3, that S_{21} values in the range of 2.0–17.0 GHz of the samples of the 1st kind, the samples of the 2nd kind and the samples of the 3rd kind vary respectively from–15.0 to –27.0 dB, from –15.0 to –28.0 dB and from –15.0 to –30.0 dB. There are following average S_{21} values of the above samples:: –21.7 dB, –22.7 dB and –24.8 dB respectively. As it also follows from Fig. 3, S_{21} values in frequency range 2.0–12.0 GHz of the considered microwave absorbers based on dilatant liquid containing sodium chloride water solution are higher than S_{21} values of the considered microwave absorbers based on dilatant liquid containing water or magnesium chloride water solution. This is because σ value of the

first specified dilatant liquid is higher than σ value of the second and the third dilatant liquids (see Table 1). Electromagnetic radiation transmission coefficient values of the considered microwave absorbers don't significantly depend on the content of dilatant liquid used for their fabrication, if this radiation frequency changes from 12.0 to 17.0 GHz. It may be because to the set of the following features:

- 1. the wavelength in the specified frequency range (~ 1.0 cm) is comparable with the size of the particles of activated wood (birch) charcoal (~ 0.5 cm);
- 2. the transmission losses of electromagnetic radiation interacting with the considered microwave absorbers due to its reflection and absorption is lower than transmission losses of such radiation due to its dissipation (scattering) on the particles of activated wood (birch) charcoal containing in these absorbers.

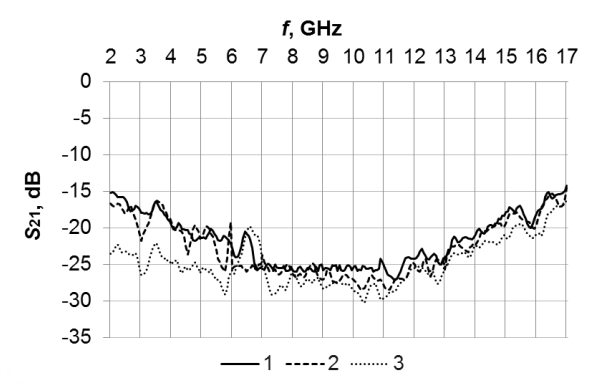


Fig. 3. 2.0–17.0 GHz frequency responses of S_{21} values of the samples of the 1st kind (graph 1), the samples of the 2nd kind (graph 2) and the samples of the 3rd kind (graph 3)

2.0-17.0 GHz frequency responses of A values of the fabricated samples are shown in Fig. 4. As it follows from Fig. 4, A values of the samples of the 1st kind and the samples of the 2nd kind achieve 0.95. A values of the samples of the 3rd kind achieve 0.9. Table 2 presents the parameters of electromagnetic radiation absorption characteristics of the samples. These parameters are based on the frequency responses presented on Fig. 4.

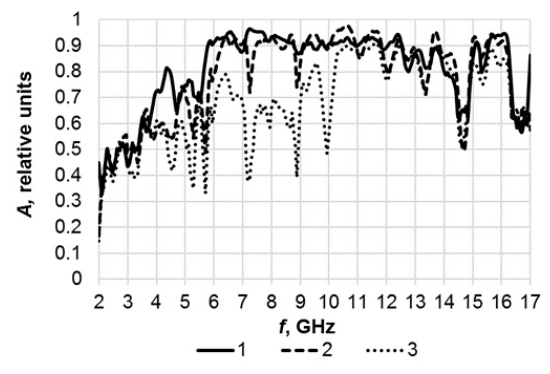


Fig. 4. 2.0–17.0 GHz frequency responses of *A* values of the samples of the 1st kind (graph 1), the samples of the 2nd kind (graph 2) and the samples of the 3rd kind (graph 3)

As it seen from Table 2, microwave absorbers fabricated on the base of dilatant liquid containing water or magnesium chloride water solution are wideband ones. This is because their effective absorption band width is more than central frequency value in this band. Microwave absorbers fabricated on the base of dilatant liquid containing sodium chloride water solution are multiple narrow band ones. There are three effective absorption bands of these absorbers in the frequency range 2.0–17.0 GHz. The width of these bands is lower than their central

frequency. Average A value of the samples of the 3^{rd} kind is lower than average A value of the samples of the 1st kind and the samples of the 2^{nd} kind. This is because the energy of electromagnetic radiation reflected by the samples of the 3^{rd} kind is more than the energy of electromagnetic radiation reflected by the samples of the 1^{st} kind and the samples of the 2^{nd} kind. It seen from the frequency responses presented in Fig. 2.

Table 2. The parameters of	electromagnetic rad	iation absorption c	characteristics of t	he samples

Commis Irind	Sample kind Average A value		Effective absorption band width
Sample Kind	Sample kind Average A value	absorption band	(absolute / relative to the central frequency)
1 st	1 st 0.85		13.5 GHz / 135.0 %
2 nd	2 nd 0.83		13.5 GHz / 135.0 %
3 rd		6.0-7.0 GHz;	1.0 GHz / 15.4 %;
	0.72	7.5–8.8 GHz;	1.3 GHz / 16.0 %;
		9.0-17.0 GHz	8.0 GHz / 61.5 %

2.0–17.0 GHz frequency responses of S_{II} values of the fabricated samples fixed on the metal plates are shown in Fig. 5. It follows from Fig. 4, that S_{11} values in the range of 2.0–17.0 GHz of the samples of the 1st kind, the samples of the 2nd kind and the samples of the 3rd kind fixed on the metal plates vary respectively from –2.0 to –15.0 dB, from –2.0 to –17.0 dB, from –2.0 to –10.0 dB. There are the following average S_{11} values of the above samples: –10.3 dB, –9.4 dB and –8.2 dB respectively. The average S_{11} values of the samples fixed on the metal plates are lower than average S_{11} values of the samples which are not fixed on the metal plates. This is may be due to the big phase difference between the electromagnetic waves reflected from the sample surface and the electromagnetic waves reflected from metal plate surface and after that absorbed by the sample [20,21].

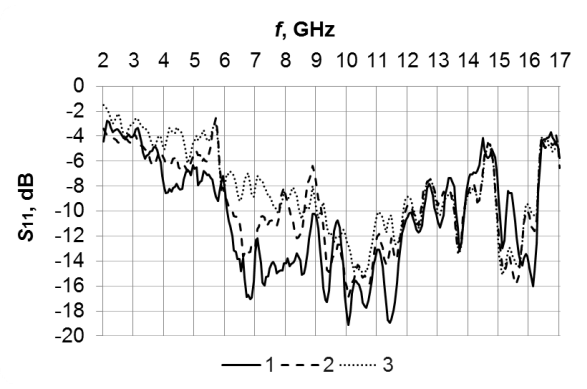


Fig. 5. 2.0–17.0 GHz frequency responses of S_{11} values of the samples of the 1st kind (graph 1), the samples of the 2nd kind (graph 2) and the samples of the 3rd kind (graph 3) fixed on the metal plates

2.0-17.0 GHz frequency responses of A values of the fabricated samples fixed on the metal plates are shown in Fig. 6. As it follows from Fig. 6, A values of all studied samples fixed on the metal plates achieve 0.98. Table 3 presents the parameters of electromagnetic radiation absorption characteristics of such samples. These parameters are based on the frequency responses presented on Fig. 6. As it seen from Table 3, all studied absorbers fixed on the metal plates are wideband ones. The average A values of the samples fixed on the metal plates is more than average A values of the samples which are not fixed on the metal plates. This is because S_{11} values of the first specified samples are lower than S_{11} values of the second specified samples, as it follows from Figs. 2 and 5.

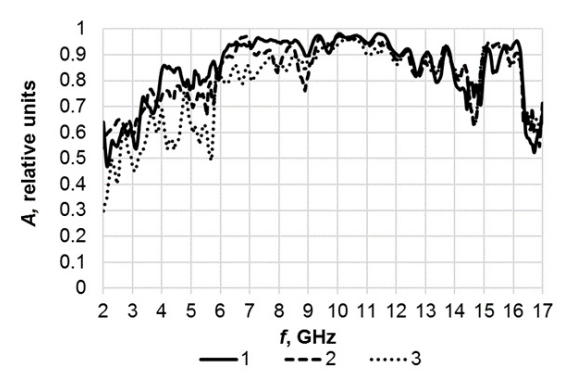


Fig. 6. 2.0–17.0 GHz frequency responses of *A* values of the samples of the 1st kind (graph 1), the samples of the 2nd kind (graph 2) and the samples of the 3rd kind (graph 3) fixed on the metal plates

Table 3. The parameters of electromagnetic radiation absorption characteristics of the samples fixed on the metal plates

Sample kind		Average	Effective	Effective absorption band width		
	Sample kind	A value	absorption band	(absolute / relative to the central frequency)		
	1 st	0.88	2.0-17.0 GHz	15.0 GHz / 158.0 %		
	2 nd	0.86	2.0-17.0 GHz	15.0 GHz / 158.0 %		
	3 rd	0.83	3.5-17.0 GHz	13.5 GHz / 135.0 %		

Conclusion

The absorbing properties of microwave absorbers based on the dilatant liquid containing water or magnesium chloride water solution and powdered activated wood (birch) charcoal are better than absorbing properties of microwave absorbers based on the dilatant liquid containing sodium chloride water solution and powdered activated wood (birch) charcoal. This is because the electromagnetic radiation reflection coefficient values of microwave absorbers based on the dilatant liquid containing sodium chloride water solution and powdered activated wood (birch) charcoal is higher than electromagnetic radiation reflection coefficient values of microwave absorbers based on the dilatant liquid containing water or magnesium chloride water solution and powdered activated wood (birch) charcoal. This is due to the fact that specific electrical conductivity value of the dilatant liquid containing sodium chloride water solution is higher than specific electrical conductivity value of the dilatant liquid containing water or magnesium chloride water solution.

It's possible to expend on 20.0 % the effective absorption band of the microwave absorbers based on the dilatant liquid containing water or magnesium chloride water solution and powdered activated wood (birch) charcoal. It's necessary to add the metal plate (or better a foiled polymer film) for this. The effective absorption band of the specified microwave absorbers is wider than effective absorption band of hydrogel-based microwave absorbers [12].

The absorbers are recommended for use in lining the walls of containers intended for storage and transportation of electronic devices sensitive to microwave interference.

References

- 1. Wei S, Zhao J, Sun Z, Chen K, Feng Y. Water Droplets: Toward Broadband Metamaterial Microwave Absorber. In: 2016 IEEE International Workshop on Electromagnetics: Applications and Student Innovation Competition. IEEE; 2016. p.16124944.
- 2. Meng ZF, Tao Z, Ruan JF, Zou RZ, Ji SW. Broadband-Absorption Mechanism in a Water-Based Metamaterial Absorber. *Physics Letters A*. 2022;445: 128269.
- 3. Kwon H, D'Aguanno G., Alú A. Optically Transparent Microwave Absorber Based on Water-Based Moth-Eye Structures. *Optics Express*. 2021;29(6): 9190-9198.

- 4. Zhao J, Wei S, Wang C, Chen K, Zhu B, Jiang T, Feng Y. Broadband Microwave Absorption Utilizing Water-Based Metamaterial Structures. Optics Express. 2018;26(6): 8522-8531.
- 5. Wu Z, Chen X, Zhang Z, Heng L, Wang S, Zou Y. Design and Optimization of a Flexible Water-Based Microwave Absorbing Metamaterial. Applied Physics Express. 2019;12(5): 057003.
- 6. Qin M, Zhang L, Wu H. Dielectric Loss Mechanism in Electromagnetic Wave Absorbing Materials. Advanced Science. 2022;9(10): 2105553.
- 7. Zhou Q, Xue B, Gu S, Ye F, Fan X, Duan W. Ultra Broadband Electromagnetic Wave Absorbing and Scattering Properties of Flexible Sandwich Cylindrical Water-Based Metamaterials. Results in Physics. 2022;38: 105587.
- 8. Zhou Y, Shen Z, Wu J, Zhang Y, Huang S, Yang H. Design of Ultra-Wideband and Nearunity Absorption Water-Based Metamaterial Absorber. *Applied Physics B.* 2020;126: 52.
- 9. Chen Y, Chen K, Zhang D, Li S, Xu Y, Wang X, Zhuang S. Ultrabroadband Microwave Absorber Based on 3D Water Microchannels. *Photonics Research*. 2021;9(7): 1391-1396.
- 10. Deng G, Chen W, Yu Z, Yang J, Yin Z. Broadband High-Power Microwave Absorber Based on Water-Based Metamaterial. Chinese Journal of Lasers. 2022;49(21): 2103001.
- 11. Deng G, Chen W, Yu Z, Cai F, Yang J, Yin Z. 3D-Printed Dielectric-Resonator-Based Ultra-Broadband Microwave Absorber Using Water Substrate. *Journal of Electronic Materials*. 2022;51: 2221-2227.
- 12. Chen X, Du L, Jiang G, Wu Z, Zou Y, Zou Y. Hydrogel-Based Optically and Mechanically Manipulable Broadband Microwave Absorber. Nano Research. 2023;16: 10175-10182.
- 13. Shukla V. Review of Electromagnetic Interference Shielding Materials Fabricated by Iron Ingredients. Nanoscale Advances. 2019;1: 1640-1671.
- 14. Winarno N, Firdaus RA, Afifah RMA. The effect of Conductivity and Permittivity on Propagation and Attenuation of Waves Using FDTD. Materials Physics and Mechanics. 2019;42(5): 617-624.
- 15. Boiprav OV, Belousova ES, Ahmetdinova ES, Bogush NV. Charcoal-Containing Building Materials for Electromagnetic Radiation Shielding. Magazine of Civil Engineering. 2023;117(1): 11709.
- 16. Krylova NG, Ovsiyuk EM, Ivashkevich AV, Red'kov VM. Maxwell Electrodynamics in Media, Geometry Effect on Constitutive Relations. Materials Physics and Mechanics. 2022;49(1): 1-16.
- 17. Boiprav O, Ayad H, Abdaljlil SA, Lynkou L, Abdulmawlay M. Charcoal- and Foil-Containing Materials for Radio Electronic Control Systems Protection from Electromagnetic Interferences. In: 2022 IEEE 21st international Conference on Sciences and Techniques of Automatic Control and Computer Engineering (STA). IEEE; 2022. p.299-304.
- 18. Dobrego KV, Chumachenko MA, Boiprav OV, Grinchik NN, Pukhir HA. Measurement of Electrical Resistance of Liquid Electrolytes and Materials Containing Them. Journal of Electromagnetic Analysis and Applications. 2020;12(2): 98175.
- 19. Matsushima T, Ito T, Prasanta Kumar Som P. Density and Electrical Conductivity of Fused Magnesium Electrolyte, (I) Typical Magnesium Electrolyte with Additives of NaCl, KCl, and CaCl₂. Transactions of the Japan Institute of Metals. 1969;10(3): 161-165.
- 20. Kolokolova L, Petrova E, Kimur H. Effects of Interaction of Electromagnetic Waves in Complex Particles. In: Zhurbenko V. (Ed.) Electromagnetic Waves. InTech; 2011.
- 21. Nefedov IS. Effects of Electromagnetic Interaction in Periodic Arrays of Single-Wall Metallic Carbon Nanotubes. Materials Physics and Mechanics. 2012;13(1): 1-8.

THE AUTHORS

Boiprav O.V. (1) e-mail: smu@bsuir.by Bogush V.A. (D) e-mail: bogush@bsuir.by

Lynkou L.M. ¹⁰

e-mail: leonid@bsuir.by

Tribological characteristics of bulk ($\overline{2}01$) β -Ga₂O₃ substrate crystals grown by EFG

Submitted: June 19, 2023

Approved: July 27, 2023

Accepted: September 27, 2023

P.N. Butenko 1, M.E. Boiko 1, A.V. Chikiryaka 1, L.I. Guzilova 1, A.O. Pozdnyakov 1, M.D. Sharkov 1, A.V. Almaev 1, V.I. Nikolaev 1,

¹ Ioffe Institute, St. Petersburg, Russia

² Tomsk State University, Tomsk, Russia

⊠ pavel.butenko@mail.ioffe.ru

Abstract. The tribological and mechanical tests of bulk substate crystals of gallium oxide β -polymorph grown by the EFG technique were carried out. The correlation of coefficient of friction and wear coefficient with hardness is discussed. It is shown that the smooth, epi-ready surface of ($\overline{2}01$) Ga₂O₃ samples has an extremely low resistance to abrasion by a sapphire ball. At the same time, the surface of the β -Ga₂O₃ wafer that has not undergone a complete postgrowth processing cycle has high mechanical properties. It is pointed out that this difference can be due to deformation defects, which are entered into the subsurface layers during the mechanical impact on the semiconductor material.

Keywords: gallium oxide; EFG; wear; coefficient of friction; tribology; bulk crystals

Acknowledgements. P.N. Butenko, and L.I. Guzilova gratefully appreciate the Russian Science Foundation for financial support (grant No. 23-29-10196).

Citation: Butenko PN, Boiko ME, Chikiryaka AV, Guzilova LI, Pozdnyakov AO, Sharkov MD, Almaev AV, Nikolaev VI. Tribological characteristics of bulk ($\overline{201}$) β -Ga₂O₃ substrate crystals grown by EFG. *Materials Physics and Mechanics*. 2023;51(6): 135-144. DOI: 10.18149/MPM.5162023_13.

Introduction

Gallium oxide is one of the most promising ultra-wide bandgap semiconductor material. The monoclinic β -modification is the only Gallic phase obtained so far in a bulk form [1]. It attracts general attention of researchers. Currently, it is already used in electronics, such as MOS structures [2], and as a material for substrates [3].

An important factor that may constrain the expansion of Ga₂O₃ applications is the insufficient study of its mechanical properties. In particular, the resistance of this material to such an important impact as a friction has not been investigated thoroughly. Moreover, there are a limited number of publications analyzing the structure of mechanically deformable gallium oxide samples [4–18]. There are even fewer works, in which the mechanical characteristics of gallium oxide, determined by experimental or computational methods, appear [4–8,11–16,18]. At the same time, commercial semiconductor substrates produced from bulk Ga₂O₃ crystals are available. They are mechanically post-growth processed to obtain *epi-ready* surfaces for epitaxial growth for microelectronic applications [19,20]. A number of laboratories grow epitaxial films of the most common gallium oxide polymorphs, which can be applied as protective and functional coatings [21–23]. There are numerous works devoted to the use of Ga₂O₃ as sensors [24–26], in these applications the material often operates at high temperatures and pressures. Such impacts are able to generate structure defects and cause internal stresses in crystals [9,10,17]. In all these cases, it is important to understand which changes occur in the

© P.N. Butenko, M.E. Boiko, A.V. Chikiryaka, L.I. Guzilova, A.O. Pozdnyakov, M.D. Sharkov, A.V. Almaev, V.I. Nikolaev, 2023. Publisher: Peter the Great St. Petersburg Polytechnic University

This is an open access article under the CC BY-NC 4.0 license (https://creativecommons.org/li-censes/by-nc/4.0/)

surface structure and subsurface layers upon the specified effects, whether it is post-growth processing or direct operation.

In this work, the tribological characteristics of the semiconductor substrates produced from bulk β -Ga₂O₃ crystals grown by edge-defined film-fed growth (EFG) were measured. The results were correlated with the hardness of the surfaces undergone post-growth processing.

Materials and Methods

The bulk β -Ga₂O₃ commercial wafer produced by *Tamura Corp* using EFG technology was investigated. The samples in a form of single-crystal ($\overline{2}01$) plates of 5 × 6 mm and 650 μ m thick were cut off from the wafer by a producer. For a chosen sample, one of it's ($\overline{2}01$) surfaces (referred to as "the bulk face" here and after) was chemically-mechanically polished (CMP) to make it applicable for epitaxial growth. The opposite surface (referred to as "the bulk back" here and after) was also subjected to post-growth treatment but having performed only a part of the processing cycle that terminates by polishing.

For the samples surface visualization, the Nikon Eclipse E200 was employed. The samples relief was studied with scanning electron microscopy (SEM) at *Phenom ProX* using secondary electron (SE) mode. The profiles of the sample surfaces and the roughness values were registered by *MarSurf PS-10* profilometer.

For a tribological experiment *AntonPaar TRB* tribometer was applied, employing reciprocating test, dry friction scheme and sphere-on-plane geometry. For all the samples ($\overline{201}$) oriented surfaces were studied. To reduce the influence of gallium oxide anisotropy, which a changes its properties depending on the direction [27], the probe-run direction was set at 45° to the [100] direction of both types of surfaces. The tests were processed at fixed probe load, the 4 mm diameter sapphire ball was applied as the counterbody. The coefficient of friction (COF) (μ) values were measured by the tribometer.

The wear coefficients (k) were calculated based on wear track geometry that was measured by the profilometer. The Archard model [28] was employed, which uses the following equation: $k = \frac{V}{F_n \cdot d}$, where V is the material volume that is removed during a tribotest, F_n is the probe load, d is the total probe run during a tribotest. For a more detailed description, see [16].

The phase composition of the samples was determined by X-ray diffraction (XRD) technique. The XRD data were registered at Bourevestnik DRON-6 laboratory device with the Cu K_{α} radiation (λ = 1.5406 Å) in a standard Bragg-Brentano configuration in the θ -2 θ mode within the range of angles from 10 to 130 °.

The hardness of the samples was studied by LOMO PMT-3 hardness tester equipped with Vickers type indenter, $Axio\ Vert.A1$ optical microscope and $Carl\ Zeiss\ Axiocam\ 208$ color digital optical system. With its help, the geometrical parameters of the indent imprints were measured and the hardness values H_V were calculated. All the experiments were performed in standard conditions (NTP) at air relative humidity of 40 % RH.

Results and Discussion

Relief of the initial surfaces. SEM images of the initial β -Ga₂O₃ sample surfaces are shown in Fig. 1. The surface (bulk face) morphology of the sample which was subjected to CMP (Fig. 1(a)) is homogeneous and has no visible relief features in the scale presented. The morphology of the polished surface (Fig. 1(b)) has a pronounced texture along a single direction due to the mechanical action (polishing without CMP).

To identify surface irregularities in depth, cross-sections were scanned in a plane perpendicular to the surface of the sample. The profiles and corresponding optical images are shown in Fig. 2. In both cases, the surface profiles are uniform and have no significant

heterogeneity. The roughness values of the surfaces were determined and amounted as: R_a (bulk face) = 6 nm, R_a (bulk back) = 164 nm.

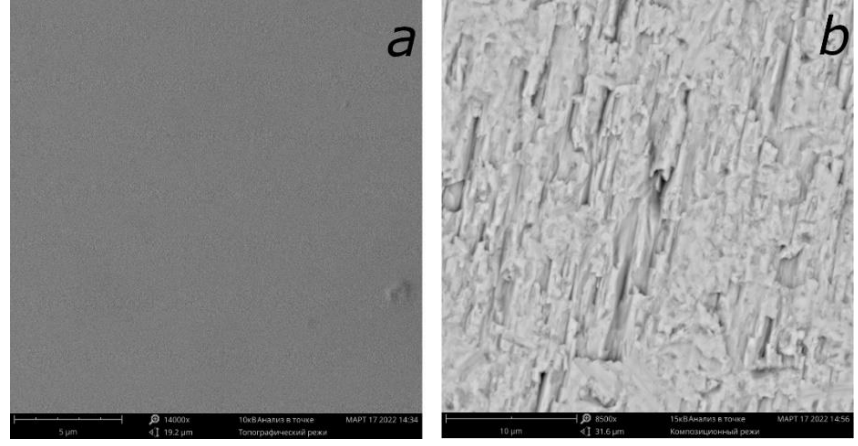


Fig. 1. SEM images of the initial surfaces of the β-Ga₂O₃ surface: bulk face (a), bulk back (b)

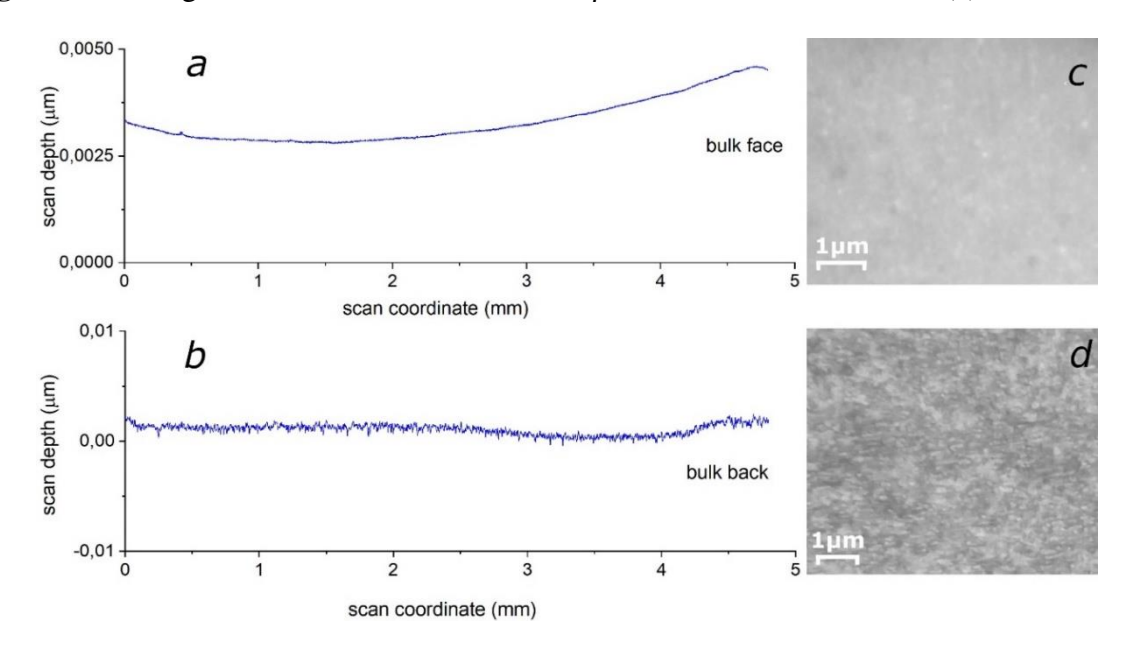


Fig. 2. The profiles and corresponding optical images the β-Ga₂O₃ surface: bulk face (a) and (c), bulk back (b) and (d), correspondingly

Hardness detection. The Vickers hardness values at the $(\overline{201})$ β-Ga₂O₃ samples surfaces were measured and calculated, they are: H_V (bulk face) = 8.80 ± 0.45 GPa; H_V (bulk back) = 9.25 ± 0.38 GPa. Considering the high anisotropy of the gallium oxide bulk crystal, the hardness values vary in a wide range. According to the majority of works [4,5,7,8,13] the hardness was measured at the (100), (010), (001) planes and is in the range of 8.3-12.8 GPa. We have found just one proceeding [18], where the hardness value was detected at the ($\overline{201}$) surface and amounted to H_V = 12.5 GPa. Overall, one can confirm that the H_V values calculated in the present paper falls within the range indicated above.

Tribological test, friction force (F_{fr}) and coefficient of friction (COF) (μ) determination. The amplitude of reciprocating motion in the experiments on friction of sapphire ball on crystal surfaces was 6 mm, the total length of the counterbody run was 50 m, the number of cycles was 4167, the maximum linear speed of the probe relative to the sample surface was 5.65 cm/s. The normal load (F_n) on the counterbody was 1 N. To increase the

reliability of the results, the test was performed three times for any considered surface of each specimen.

The results of the tribotests are shown in Fig. 3. In addition to the change of F_{fr} , it shows the depth of the probe immersion (depth) depending on the change of its position coordinate during the test. The sharp increase of F_{fr} on the surface of the bulk face sample (Fig. 3(a)) beginning from about 22 m of the probe run attracts attention. Hence, beginning from about 30 m of the probe run the F_{fr} value stabilizes at the 0.085 N. At the same time the amplitude of friction force modulation increases. For the rear sample side (bulk back) which is the rougher one, the increase in F_{fr} is observed at the beginning of the test (Fig. 3(b)) and persists until the end, but with a less intensity. At the same time, the overall level of the amplitude of friction force modulation is high throughout the entire tribotest.

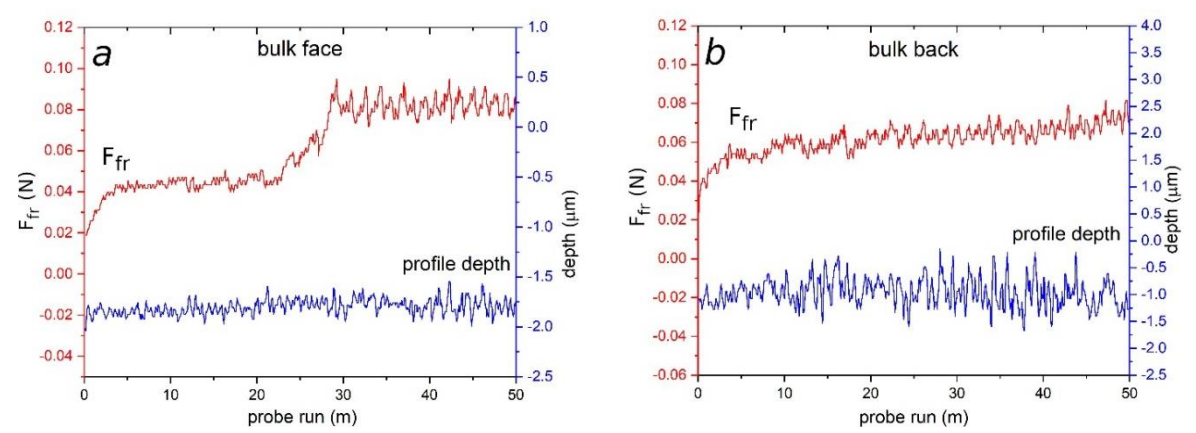


Fig. 3. The dependences of the friction force (F_{fr}) and probe immersion depth (depth) on the probe coordinate at the surfaces of the β-Ga₂O₃ sample: bulk face (a), bulk back (b)

The rise in the F_{fr} in the initial sections of the both tribotests may be related to the accumulation of wear particles in the friction zone [16,17]. The increased F_{fr} start-value for the bulk back sample experiment (0.04 vs. 0.02 N, see Fig. 3), as well as the higher overall level of the modulation amplitude can be explained by the higher initial surface roughness of this sample.

In our previous work [17] during a similar tribotest, but with a higher probe load value $(F_n = 2 \text{ N})$, we encountered a situation in which the correctness of the test was not ensured due to the catastrophic destruction of the surface in the wear track. This fact did not allow us to obtain a legitimate COF value. It was concluded that the subsurface layers of the substrate, which had been undergone the post-growth processing, altered from the sample volume by a more defective structure containing interdomain boundaries. In other words, in the friction process, the sample acquires a mosaic structure. At $F_n = 1$ N the correctness of the tribological test is complied, since according to the change in the coordinate of immersion of the probe no total destruction of the surface is occurred. Nevertheless, the F_{fr} value (also COF) for the bulk face sample is an average, because the experiment actually consists of two parts yielding two significantly different F_{fr} values (also COF). At the same time, this value coincides with the value measured for the bulk back sample with the accuracy of the experimental error. Obviously, in case of the bulk back sample (Fig. 3(b)) more stable course of friction force is registered and the given F_{fr} values (also with COF) should be considered reliable. Proceeding from the fact that the tribotest was carried out at $F_n = 1$ N, the values of COF and F_{fr} are equal in modulo.

The average COF values for the counterbodies involved in this tribotest are as follows: $\langle \mu \rangle$ (bulk face sample) = 0.063 ± 0.019, $\langle \mu \rangle$ (bulk back sample) = 0.062 ± 0.008. To the best of our knowledge, in 2020 an attempt to study the tribological characteristics of bulk gallium

oxide crystals using the *nano scratch test* was made for the first time [29,30]. However, these publications did not provide a reliable value for the COF of this material. Later, in 2021, our group realized a reciprocating test to determine the μ values for quasi-bulk β -Ga₂O₃ 5-15 μ m thick layers grown by the Halide Vapor Phase Epitaxy (HVPE) on sapphire substrates [16]. Those experiments performed under similar conditions show relatively similar results for a 5 μ m thick layer (μ = 0.07) and different ones for a 15 μ m thick layer (μ = 0.11). The discrepancy in COFs can be attributed to various degrees of crystalline perfection. The structure of the upper regions of the thicker heteroepitaxial layers is usually of higher crystallinity because of the greater distance from the interface. This is due to the reduced influence of the mismatch between the rhombohedral crystal system of the sapphire substrate and the monoclinic crystal system of the β -polymorph.

Finally, it should be noted that the COF values measured for the gallium oxide bulk crystals in this work, as well as for the gallium oxide layers in previous one are low, they are more than half the values obtained for sapphire [31].

XRD study. The first series of XRD measurements were performed for the initial samples. The θ -2 θ curves are similar to those obtained on the samples subjected to the tribological experiment. Therefore, to save space, initial samples XRD patterns are not given in this paper.

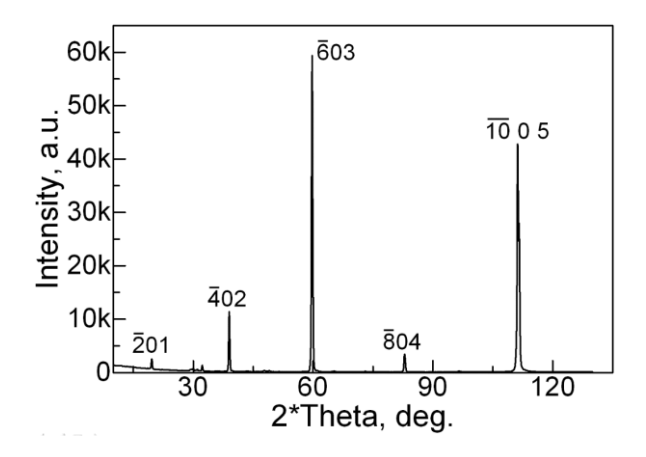


Fig. 4. The measured β -Ga₂O₃ diffraction pattern

The β-Ga₂O₃ diffraction pattern is shown in Fig. 4. It was measured in the θ-2θ mode for one of the samples after the tribotest. The most intense peaks at the pattern correspond to 5 orders of reflection in the [$\bar{2}01$] direction, from the $\bar{2}01$ itself up to the $\bar{1}005$. This XRD pattern confirms that the material of the sample corresponds to β-Ga₂O₃ (01-041-1103 in the ICDD file): a crystal of monoclinic system, C2/m (12) group with lattice constants a = 12.2270 Å, b = 3.0389 Å, c = 5.8079 Å and $\beta = 103.82^\circ$. Thus, the sample is a single-phase, it contains only the thermally stable β-modification, and the studied surface of the sample corresponds to the ($\bar{2}01$) plane.

The same diffraction curve (see Fig. 4) is depicted in semilogarithmic scale in the bottom part of the Fig. 5. The upper part of this figure shows a model X-ray powder diffraction pattern from β -Ga₂O₃ compiled from the data analysis of three ICDD files (00-041-1103, 01-074-1776, 01-087-1901). It can be seen that, in most cases, a possible correspondence among the model β -Ga₂O₃ reflection lines can be found for the low-intensity reflections that are presented on the measured diffraction curve. The exception are a few lines located in the region of relatively small 2 θ angles (up to 30°). This fact may be an evidence of the presence of a powder fraction or polycrystalline component in the sample. The low intensity of the powder diffraction reflections shows that the powder fraction in the sample is relatively small. The powder

particles were identified and analyzed in our previous study, in which a similar experiment was performed [17].

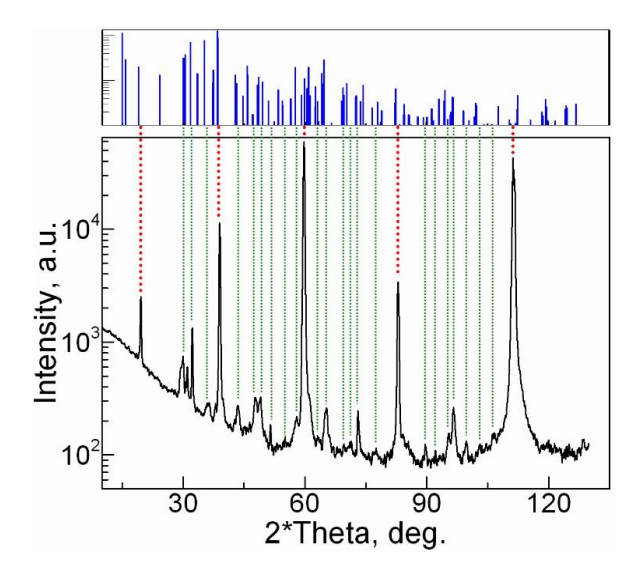


Fig. 5. The β-Ga₂O₃ XRD pattern recorded in θ-2θ mode at Cu $K_{\alpha 1}$ radiation (the bottom part) in semilogarithmic scale. The upper part: the same, but the model X-ray powder diffraction pattern. The green dashed lines show the correspondence between the experimental and model reflections. The red dotted lines correspond to reflections that are multiples of the $\overline{2}$ 01 plane

The reflections that correspond to 2θ angles scattering up to 30° are absent on the measured θ - 2θ curve. This may be due to the fact that in this part of the diffraction pattern there is a rapidly falling background, which can prevent direct observation of attenuated reflections from a relatively small in volume powder fraction.

Wear coefficient (k) calculation. Both surfaces were examined using SEM to visualize and measure wear tracks widths (see Fig. 6). It is noteworthy to see more than a sixfold (105 vs. 650 μ m, respectively) broadening of the wear track recorded at the bulk face sample surface. These data are consistent with the experimental results of the 3D wear tracks scanned by the profilometer. In Fig. 7 two such images of occasionally selected cross-sections perpendicular to the wear track are depicted. Based on calculation of these wear track areas and on assumption of averaging of the section geometry, the volumes of wear tracks were determined.

 $(k = [\text{mm}^3/\text{N}\cdot\text{m}])$ Then coefficients were the wear calculated according to the Archard model. The value of wear coefficient of the bulk face sample happened to be (2.2 ± 0.6) 10^{-2} mm³/N·m. It should be noted that this is an extremely high indicator, corresponding to the values of soft steels. The reason for this fact may be significant changes in the structure of the single crystal due to the influence of post-growth processing. In [17], our tribological test was actually a simulation of post-growth processing of the substrate single crystal, due to which the latter acquired a mosaic structure. In contrast, the wear coefficient measured on the opposite sample side (bulk back) has a rather low $((1.1 \pm 0.1) \ 10^{-7} \ \text{mm}^3/\text{N} \cdot \text{m})$. It is significantly lower than ones previously recorded for Ga₂O₃ β-polymorph 15 μm thick layers: $k = 5 \cdot 10^{-5}$ mm³/N·m (100Cr6 steel counterbody) [15] and $k = (3.7 \pm 1.0)10^{-4} \text{ mm}^3/\text{N} \cdot \text{m} \text{ (sapphire counterbody) [16]}.$

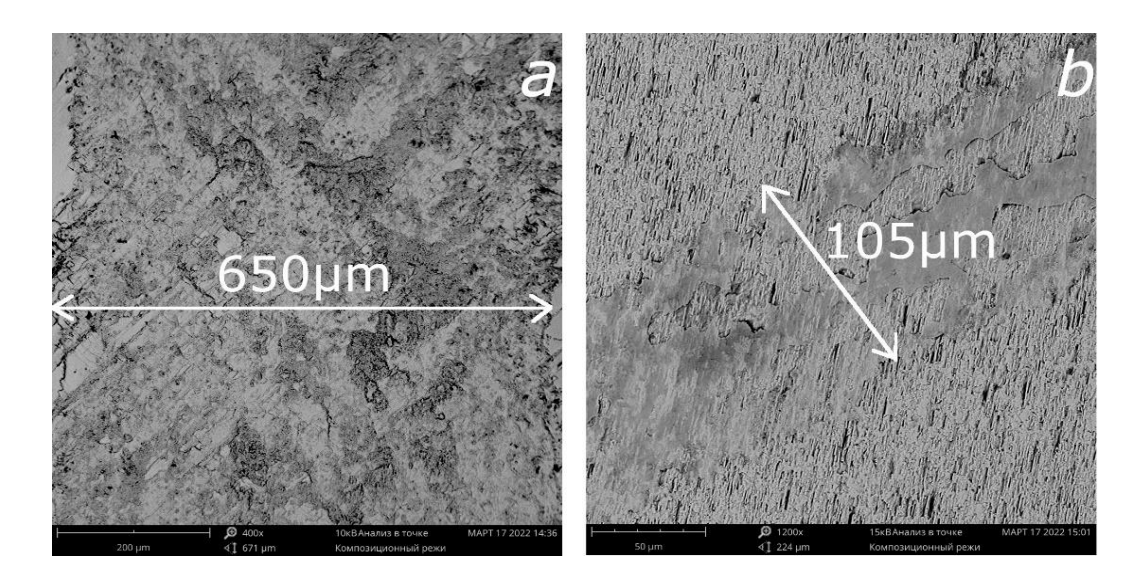


Fig. 6. SEM images of both the sample sides. The wear tracks upon the tribotest of the $(\overline{2}01)$ β -Ga₂O₃ surface: bulk face (a), bulk back (b)

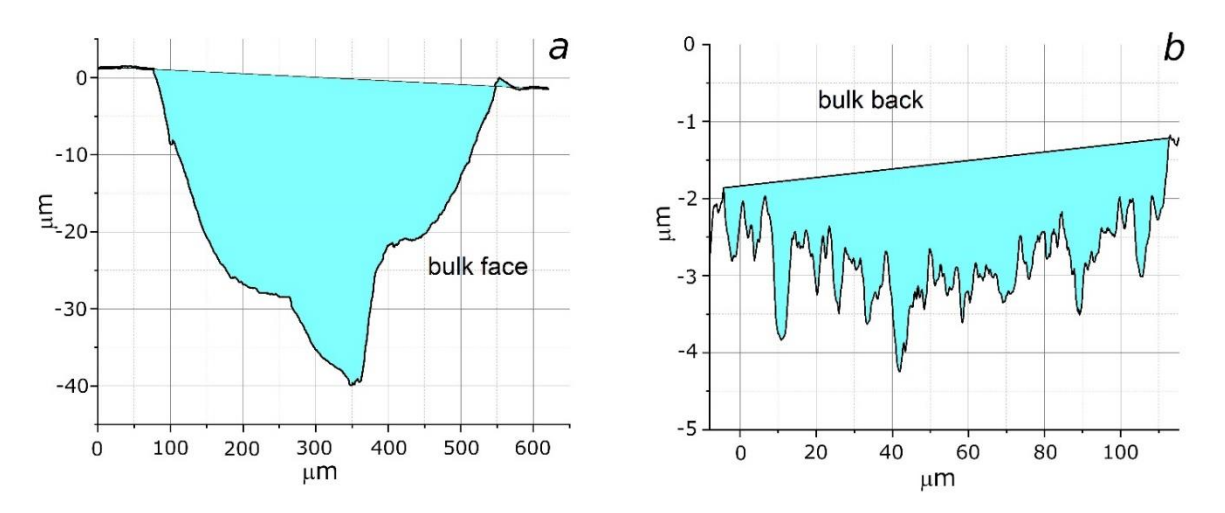


Fig. 7. Cross-sections of the wear tracks upon tribotest at β -Ga₂O₃ surface: bulk face (a), bulk back (b)

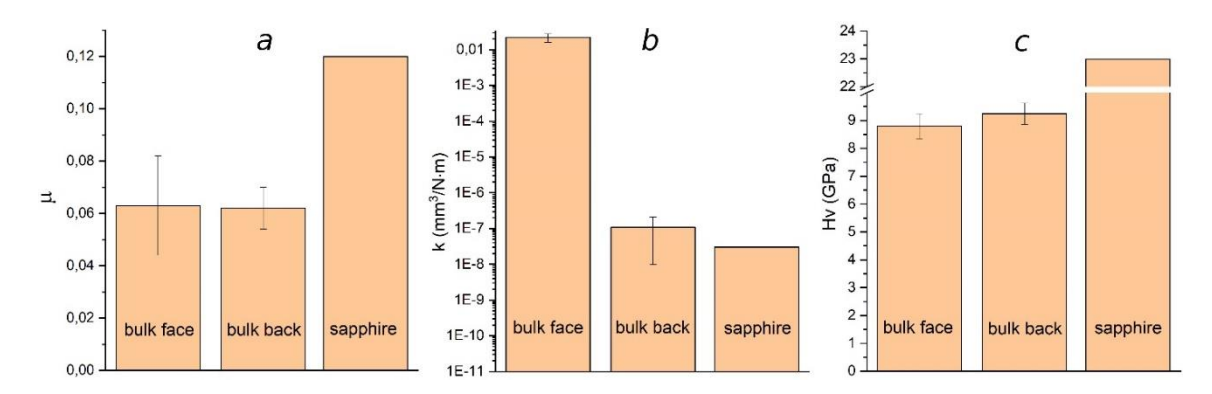


Fig. 8. Values of the COF (μ) (a), wear coefficient (k) (b) and hardness (H_V) (c) for the β-Ga₂O₃: bulk face, bulk back and sapphire. Based on [32]

Figure 8 compares the COF (μ) , wear coefficient (k) and hardness (H_V) values of the β -Ga₂O₃ samples: bulk face, bulk back and sapphire [32]. The bulk face sample has the lowest hardness and the highest wear coefficient. At the same time, the values of COFs of both sides of gallium oxide are low, almost 2 times lower than those of sapphire. Thus, the CMP-treated gallium oxide surface, i.e. the *epi-ready* surface, is the least perfect from the mechanical point of view.

Conclusions

The values of coefficient of dry friction (μ) and wear coefficient (k) of bulk ($\overline{2}01$) β -Ga₂O₃ single crystals used as *epi-ready* substrates were determined for the first time. The μ value is 0.063, which is significantly lower than the values for the currently used semiconductor materials. At the same time, the k values for the surface prepared (post-growth processing) by polishing and chemical-mechanical polishing (CMP) differ significantly: $1.1 \cdot 10^{-7}$ and $2.2 \cdot 10^{-2}$ mm³/N·m, correspondingly.

The hardness (H_V) of bulk gallium oxide crystals measured at the $(\bar{2}01)$ plane is relatively high (9 GPa), but it is more than half that of sapphire. Moreover, the hardness of the CMP polished substrates is slightly lower than that one measured on the polished surface. It is noteworthy that the lower H_V value of gallium oxide corresponds to its lower μ values.

An important result obtained in this study is the fact that the smoother *epi-ready* surface of gallium oxide semiconductor substrates happens to have lower mechanical parameters (tribological characteristics and hardness) compared to not completely post-growth-processed surface. The reason for this fact is that the structure of the *epi-ready* substrates might contain a large number of unrelaxed stresses in the subsurface layers due to the influence of deformation defects that were input during full-cycle post-growth processing. Thus, from the point of view of mechanical properties, the bulk β -Ga₂O₃ substrate crystals grown by the EFG are undoubtedly promising materials, however, it is obvious that their preparation for epitaxial growth processes should be studied more deeply.

References

- 1. Stepanov S, Nikolaev V, Bougrov V, Romanov A. Gallium Oxide: Properties and application: a review. *Rev. Adv. Mater. Sci.* 2016;44(1): 63–86.
- 2. Higashiwaki M. β -Ga₂O₃ material properties, growth technologies, and devices: A Review. *AAPPS Bulletin*. 2022;32: 3.
- 3. Goto K, Murakami H, Kuramata A, Yamakoshi S, Higashiwaki M, Kumagai Y. Effect of substrate orientation on homoepitaxial growth of β -Ga₂O₃ by halide vapor phase epitaxy. *Applied Physics Letters*. 2022;120(10): 102102.
- 4. Huang H, Li X, Mu D, Lawn BR. Science and art of ductile grinding of brittle solids. *International Journal of Machine Tools and Manufacture*. 2021;161: 103675.
- 5. Xu YM, Zhou H, Zhang JQ, Ren XP, Zhang CW. Experimental study on microscale mechanical behavior of easily cleavable gallium oxide crystals. *China Mech. Eng.* 2022;33(18): 27823-27835.
- 6. Wu YQ, Gao S, Huang H. The deformation pattern of single crystal β-Ga₂O₃ under nanoindentation. *Materials Science in Semiconductor Processing*. 2017;71: 321–325.
- 7. Zhang JQ, Zhou H, Jiang W, Hu SX, Ren XP, Zhang CW. Investigation of dynamic mechanical properties and constitutive model of (010) plane of gallium oxide crystals under shock loading. *Ceramics International*. 2022;48(19): 27823–27835.
- 8. Mu W, Jia Z, Yin Y, Hu Q, Li Y, Wu B. High quality crystal growth and anisotropic physical characterization of β-Ga₂O₃ single crystals grown by EFG Method. *Journal of Alloys and Compounds*. 2017;714: 453–458.
- 9. Gao S, Wu Y, Kang R, Huang H. Nanogrinding induced surface and deformation mechanism of single crystal β-Ga₂O₃. *Materials Science in Semiconductor Processing*. 2018;79: 165–170.

- 10. Gao P, Tan B, Yang F, Li H, Bian N, Sun X. Influence of diamond wire saw slicing parameters on (010) lattice plane beta-gallium oxide single crystal wafer. *Materials Science in Semiconductor Processing*. 2021;133: 105939.
- 11. Grashchenko AS, Kukushkin SA, Osipov AV, Red'kov AV. Investigation of the physicomechanical characteristics of nanoscale films by nanoindentation. *Mechanics of Solids*. 2018;53(5): 481–488.
- 12. Battu AK, Ramana CV. Mechanical properties of nanocrystalline and amorphous gallium oxide thin films. *Advanced Engineering Materials*. 2018;20(11): 1701033.
- 13. Zhou H, Wei J, Shen J, Xu Y, Zhang J. Study on the size effect of single crystal gallium oxide during the nanoindentation process. *Journal of Advanced Manufacturing Systems*. 2021;20(03): 575–587.
- 14. Wu YQ, Gao S, Kang RK, Huang H. Deformation patterns and fracture stress of beta-phase gallium oxide single crystal obtained using compression of micro-pillars. *Journal of Materials Science*. 2018;54(3): 1958–1966.
- 15. Butenko PN, Guzilova LI, Chikiryaka AV, Pechnikov AI, Grashchenko AS, Pozdnyakov AO, Nikolaev VI. Wear resistance of α -and β -gallium oxide coatings. *Materials Physics and Mechanics*. 2021;47(1): 52-58.
- 16. Butenko PN, Guzilova LI, Chikiryaka AV, Pechnikov AI, Nikolaev VI. Tribological Studies of α-β-Ga₂O₃ Layers Paired with a Sapphire Counterface. *Technical Physics*. 2021;66: 1186–1193.
- 17. Butenko PN, Guzilova LI, Chikiryaka AV, Boiko ME, Sharkov MD, Almaev AV. Impact on the subsurface layers of the single-crystal β -Ga₂O₃ wafers induced by a mechanical wear. *Materials Science in Semiconductor Processing*. 2022;143: 106520.
- 18. Víllora EG, Arjoca S, Shimamura K, Inomata D, Aoki K. β-Ga₂O₃ and single-crystal phosphors for high-brightness white LEDs and LDs, and β-Ga₂O₃ potential for next generation of power devices. *SPIE Proceedings*. 2014;8987: 371-338.
- 19. Blevins JD, Stevens K, Lindsey A, Foundos G, Sande L. Development of large diameter semi-insulating gallium oxide (Ga₂O₃) substrates. *IEEE Transactions on Semiconductor Manufacturing*. 2019;32(4): 466–472.
- 20. Galazka Z, Ganschow S, Seyidov P, Irmscher K, Pietsch M, Chou T-S. Two inch diameter, highly conducting bulk β -Ga₂O₃ single crystals grown by the Czochralski method. *Applied Physics Letters*. 2022;120(15): 152101.
- 21. Itoh T, Mauze A, Zhang Y, Speck JS. Epitaxial growth of β -Ga₂O₃ on (110) substrate by plasma-assisted molecular beam epitaxy. *Applied Physics Letters*. 2020;117(15): 152105.
- 22. Cheng Y, Xu Y, Li Z, Zhang J, Chen D, Feng Q. Heteroepitaxial growth of α -Ga₂O₃ thin films on a-, C- and R-plane sapphire substrates by low-cost mist-CVD method. *Journal of Alloys and Compounds*. 2020;831: 154776.
- 23. Biswas M, Nishinaka H. Thermodynamically metastable α -, ϵ (or κ -), and γ -ga2o3: From material growth to device applications. *APL Materials*. 2022;10(6): 060701.
- 24. Nikolic MV, Milovanovic V, Vasiljevic ZZ, Stamenkovic Z. Semiconductor gas sensors: Materials, technology, design, and application. *Sensors*. 2020;20(22): 6694.
- 25. Almaev A, Nikolaev V, Butenko P, Stepanov S, Pechnikov A, Yakovlev N. Gas sensors based on pseudohexagonal phase of gallium oxide. *Physica Status Solidi* (b). 2021;259(2): 2100306.
- 26. Yakovlev N, Almaev A, Butenko P, Tetelbaum D, Mikhaylov A, Nikolskaya A. Effect of Si+ ion implantation in α-Ga₂O₃ films on their gas sensitivity. *IEEE Sensors Journal*. 2023;23(3): 1885–1895.
- 27. Ma X, Xu R, Xu J, Ying L, Mei Y, Long H. In-plane crystalline anisotropy of bulk β-Ga₂O₃. *Journal of Applied Crystallography*. 2021;54(4): 1153–1157.
- 28. Archard J. Contact and rubbing of flat surfaces. *Journal of Applied Physics*. 1953;24(8): 981-988.
- 29. Zhou H, Xu Y, Zhang J, Shen J, Huang M. Effect of scratching speed on the brittle-plastic transition of single crystal gallium oxide. In: 2020 6th International Conference on Mechanical Engineering and Automation Science (ICMEAS). 2020. p.247–253.

- 30. Zhou H, Song F, Wei JH. Nanomechanical Properties of β-Ga₂O₃ with different Crystal Planes. *Journal of the Chinese Ceramic Society*. 2020;48(1): 135–139.
- 31. Zeng G, Tan C-K, Tansu N, Krick BA. Ultralow wear of gallium nitride. *Applied Physics Letters*. 2016;109(5): 051602.
- 32. Alisin V. Tribological properties of sapphire under dry friction against chromium and zirconium ceramics. *Materials Research Proceedings*. 2022;21: 18.

THE AUTHORS

Butenko P.N.

e-mail: pavel.butenko@mail.ioffe.ru

Chikiryaka A.V. 🗓

e-mail: chikiryaka@mail.ru

Pozdnyakov A.O.

e-mail: ao.pozd@mail.ioffe.ru

Almaev A.V.

e-mail: almaev_alex@mail.ru

Boiko M.E. 🗓

e-mail: M.E.Boiko@mail.ioffe.ru

Guzilova L.I. 🗓

e-mail: guzilova@mail.ioffe.ru

Sharkov M.D.

e-mail: mischar@mail.ru

Nikolaev V.I. D

e-mail: nikolaev.v@mail.ioffe.ru

Hydrogen diffusion in rotating cylindrical elastic bodies

Submitted: August 7, 2023

Accepted: October 27, 2023

Approved: September 20, 2023

A.K. Belyaev (1) 1,2, A.R. Galyautdinova (1) 1,2 ×, S.A. Smirnov (1) 1

¹ Institute for Problems in Mechanical Engineering of the Russian Academy of Sciences, St. Petersburg, Russia ² Peter the Great St. Petersburg Polytechnic University, St. Petersburg, Russia

⊠ aliyagalyautdinova@gmail.com

Abstract. In this paper, we study the distribution of the hydrogen concentration in a rotating cylindrical elastic body compressed by two concentrated forces. This problem is relevant for diagnostics of bearing failure due to the influence of hydrogen on the mechanical properties of structures. During the study, the plane stress state of a loaded cylindrical elastic body is determined by means of the theory of functions of a complex variable. We used the transition to a rotating coordinate system to obtain the static problem of hydrogen diffusion in a body loaded by the known stresses. The solution of the problem includes the methods of asymptotic analysis for the simplification of partial differential equation, the expansion in a Fourier series and the Galerkin approach for finding the expansion coefficients for several harmonics. The results can be useful for calculating the hydrogen concentration distribution in roller bearings. **Keywords:** hydrogen diffusion; hydrogen destruction; diffusion equation; stress state; rolling bearings

Acknowledgement. The research is carried out under the financial support by Russian Foundation for Basic Research, project № 20-08-01100 A.

Citation: Belyaev AK, Galyautdinova AR, Smirnov SA. Hydrogen diffusion in rotating cylindrical elastic bodies. *Materials Physics and Mechanics*. 2023;51(6): 145-151. DOI: 10.18149/MPM.5162023_14.

Introduction

Hydrogen is one of the factors that have a negative impact on the working capacity of structures. The phenomenon of hydrogen embrittlement can cause the destruction of constructions [1–5]. Therefore, tens of thousands of scientific works are devoted to the study of the nature of hydrogen embrittlement [6,7]. At the moment, there are several main approaches to describing the influence of hydrogen on the mechanical properties of materials: HELP model [8–10], HEDE model [11–13], model with taking into account the internal pressure of hydrogen [14] and multicontinual model [15,16], that takes into account the influence of hydrogen with different bond energies on the mechanical characteristics of the material. Even low hydrogen concentrations lead to degradation of mechanical properties of the material. When the limiting hydrogen concentrations are not exceeded, the diffusion laws formulated by Fick [17,18] are also fulfilled. Fick's second law describes the change in concentration in one dimension with respect to time. Generalizing Fick's equations to the three-dimensional case, we obtain the equation of diffusion of material in elastic body. And the equation of hydrogen diffusion in the field of elastic stresses [6] makes it possible to describe the distribution of hydrogen in a metal due to its diffusion under the action of external loads. The solution of this equation is investigated in our problem of hydrogen diffusion in loaded rotating elastic bodies.

Bearings are one of the important elements of many machines that use rotary motion in their work. Rolling bearings are used in electric motors, gear reducers, aircraft and vehicles, and in various industrial machine tools. Therefore, the study of the causes of bearing failure has a practical importance. In the literature, there are still no works devoted to the theoretical description of the distribution of hydrogen in rotating rolling elements of bearings. The diffusion of hydrogen in the cylindrical rolling elements of roller bearings will be the subject of our research.

The aim of this work is to investigate the distribution of hydrogen concentration in a rotating cylindrical elastic body under the action of mechanical stresses, as well as to demonstrate how to obtain an analytical solution to the diffusion equation in a rotating loaded body. Thus, it is necessary to solve the problem of the stress state of an elastic body under the action of two compressive concentrated forces, and then calculate the distribution of hydrogen concentrations in a rotating elastic body under the field of found elastic stresses.

Determination of the stress state of a cylindrical elastic body

We considered the cylindrical body under compression in the radial direction by two concentrated forces applied at diametrically opposite points of the outer circle. Cylindrical elastic bodies can be considered as models of rolling elements of roller bearings. The scheme of object of investigation is illustrated in Fig. 1.

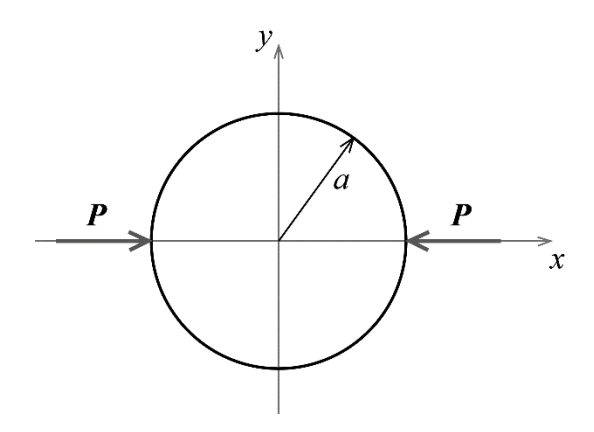


Fig. 1. The scheme of an object of research

It is known that in the plane problem the stress tensor has the form:

$$\tau = \sigma_r e_r e_r + \sigma_{\varphi} e_{\varphi} e_{\varphi} + \tau_{r\varphi} (e_r e_{\varphi} + e_{\varphi} e_r). \tag{1}$$

To find a stress state of an elastic body we used means of the theory of functions of a complex variable. According to the theory, the stress field throughout the body can be reconstructed from the known stress vector on the surface of the body. Using Kolosov's formulas [19], we can find the stress tensor components. The detailed description of the stress state solution by means of the theory of functions of a complex variable is written in [20]. Thus, the stress tensor components is determined:

$$\sigma_r = -\frac{P}{\pi a} \left(1 - \frac{r^2}{a^2} \right) \left[\frac{\left(1 + \frac{r^2}{a^2} \right) \left(1 + \frac{r^4}{a^4} \right) - 2\cos 2\varphi \left(\frac{r^2}{a^2} + 2\frac{r^4}{a^4} + 1 \right) + 4\frac{r^2}{a^2}}{\left[1 - 2\frac{r^2}{a^2}\cos 2\varphi + \frac{r^4}{a^4} \right]^2} \right], \tag{2}$$

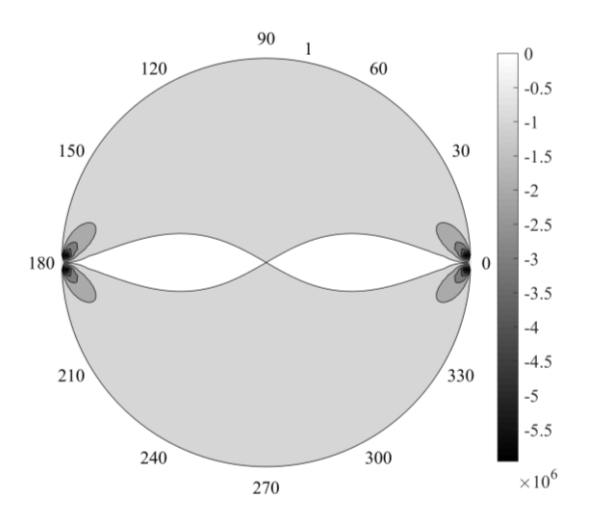
$$\sigma_{\varphi} = -\frac{P}{\pi a} \left(1 - \frac{r^2}{a^2} \right) \left[\frac{\left(1 + \frac{r^2}{a^2} \right) \left(1 + \frac{r^4}{a^4} \right) - 2\cos 2\varphi \left(3 + \frac{r^2}{a^2} + 4\frac{r^4}{a^4} \right) + 12\frac{r^2}{a^2}}{\left[1 - 2\frac{r^2}{a^2}\cos 2\varphi + \frac{r^4}{a^4} \right]^2} \right], \tag{3}$$

$$\tau_{r\varphi} = \frac{2P}{\pi a} \frac{\sin 2\varphi (1 - \frac{r^4}{a^4}) \left(1 - \frac{r^2}{a^2}\right)}{\left[(1 - \frac{r^2}{a^2}\cos 2\varphi)^2 + \frac{r^4}{a^4}\sin^2 2\varphi\right]^2}.$$
 (4)

Figures 2–4 show the contour plots of the distributions of the stress tensor components Eq. 2 – Eq. 4 in a cylindrical body under the action of two concentrated forces applied at two diametrically opposite points of the outer circle. Figure 5 shows a contour plot of the average normal stress distribution, which is determined through the normal components of the stress tensor as follows:

$$\sigma = \frac{1}{2} \left(\sigma_r + \sigma_{\varphi} \right) = -\frac{P}{\pi a} \frac{1 - \left(\frac{r}{a} \right)^4}{\left(1 - 2\frac{r^2}{a^2} \cos 2\varphi + \frac{r^4}{a^4} \right)}.$$
 (5)

As expected, from the figures we see that the highest values of stresses are achieved near the points of influence of the forces, and as they move away from the line of action of the load, the fields decrease rather quickly to a uniform distribution.



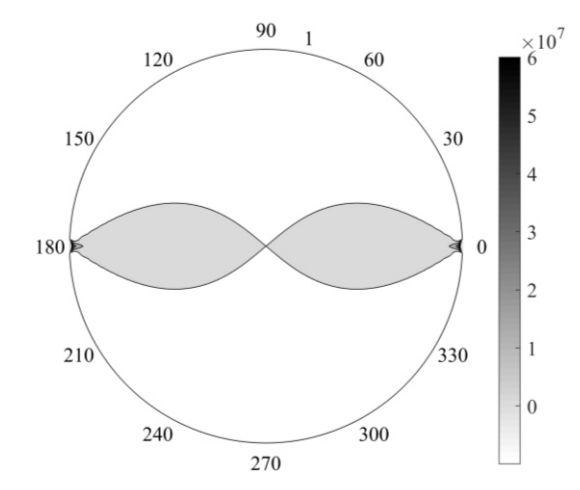
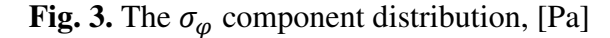
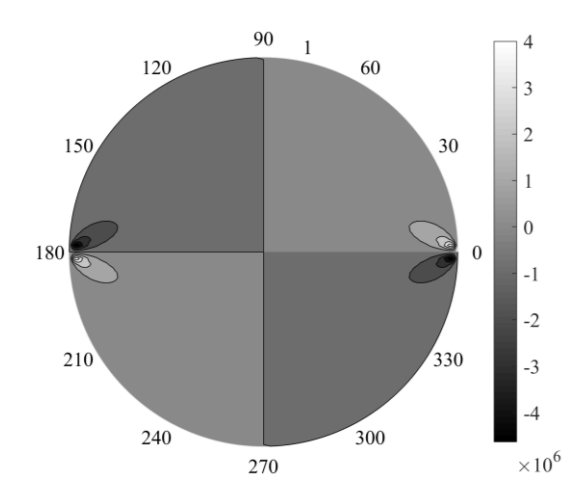
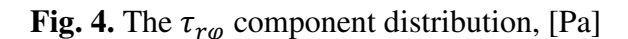


Fig. 2. The σ_r component distribution, [Pa]







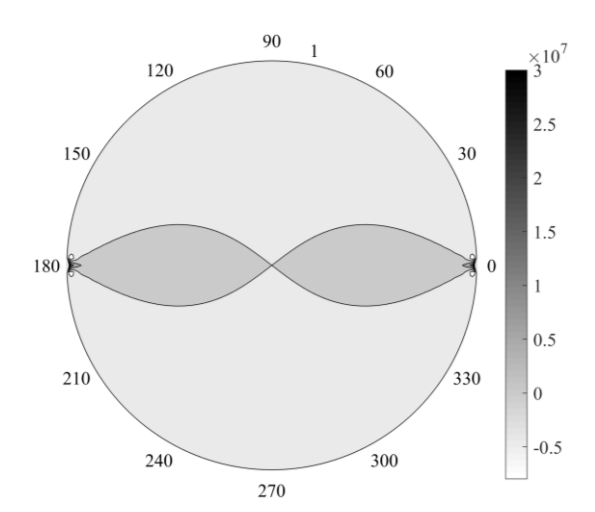


Fig. 5. The distribution of the average normal stress, [Pa]

Solution of the equation of hydrogen diffusion in a rotating cylindrical elastic body

The problem of hydrogen diffusion in rotating cylindrical elastic bodies is considered. According to [6], hydrogen diffusion in the field of elastic stresses is described by the following equation:

$$\dot{C} = D\Delta C - \frac{DV_H}{RT} \nabla C \cdot \nabla \sigma - \frac{DV_H}{RT} C\Delta \sigma, \tag{6}$$

where C – hydrogen concentration, D – hydrogen diffusion coefficient, V_H – partial molar volume of hydrogen, σ – average normal stress, R – gas constant, T – absolute temperature.

The differential equation is considered in a polar coordinate system, so the hydrogen concentration $C(r, \varphi, t)$ is a function of three independent variables: radius r, angle φ and time t. We assumed that the body rotates at a constant speed. In order to reduce the number of independent variables, the transition to rotating coordinate system is made and now the material derivative has the form:

$$\dot{C} = \frac{dC}{dt} = \frac{\partial C}{\partial t} + \frac{\partial C}{\partial r}\frac{\partial r}{\partial t} + \frac{\partial C}{\partial \varphi}\frac{\partial \varphi}{\partial t} = \omega \frac{\partial C}{\partial \varphi}.$$
 (7)

This expression is substituted in the Eq. 6 and the hydrogen diffusion equation in rotating coordinate system is obtained. In that equation as a stress field acting on a body the hydrostatic component of the found stress field Eq. 5 is operated and the following equation is obtained:

$$\Delta C + \frac{V_H}{RT} \frac{4P}{\pi a} \left[\frac{\frac{r}{a^2} (\cos 2\varphi - 2\frac{r^2}{a^2} + \frac{r^4}{a^4} \cos 2\varphi)}{\left(1 - 2\frac{r^2}{a^2} \cos 2\varphi + \frac{r^4}{a^4}\right)^2} \frac{\partial C}{\partial r} - \frac{1}{a^2} \frac{(1 - \frac{r^4}{a^4}) \sin 2\varphi}{\left(1 - 2\frac{r^2}{a^2} \cos 2\varphi + \frac{r^4}{a^4}\right)^2} \frac{\partial C}{\partial \varphi} \right] - \frac{\omega}{D} \frac{\partial C}{\partial \varphi} = 0.$$
 (8)

This two-dimensional partial differential equation appeared to be very complex. We had to simplify it by the methods of asymptotic analysis. We considered the concentration only near the line of action of the force, thus, the equation is simplified by assuming that the angles φ are small. So the following partial differential equation is obtained:

$$\Delta C + \frac{V_H}{RT} \frac{4P}{\pi a} \frac{1}{a^2} \frac{r}{\left(1 - \frac{r^2}{a^2}\right)^2} \frac{\partial C}{\partial r} - \left(\frac{V_H}{RT} \frac{4P}{\pi a} \frac{1}{a^2} \frac{\left(1 + \frac{r^2}{a^2}\right)}{\left(1 - \frac{r^2}{a^2}\right)^3} sin2\varphi + \frac{\omega}{D}\right) \frac{\partial C}{\partial \varphi} = 0. \tag{9}$$

Since the equation does not have coefficients that depend in a complex way on the variable φ , the required unknown function of hydrogen concentration can be represented in the form of a Fourier series:

$$C(r,\varphi) = \sum_{n=0}^{\infty} (A_n(r)sinn\varphi + B_n(r)cosn\varphi). \tag{10}$$

The expansion coefficients $A_n(r)$ and $B_n(r)$ need to be found. For this, we substituted Eq. 10 into the Eq. 9, multiplied the resulting expression by the basis functions $sinn\varphi$ and $cosn\varphi$ (where n=0,1,2...) and integrated it over the variable φ on the interval $[0; 2\pi]$. And we got an infinite system of ordinary differential equations for finding an infinite number of coefficients $A_n(r)$ and $B_n(r)$.

After completing this procedure, we see that A_0 can be taken equal to zero, and ordinary differential equations for finding $B_0(r)$, $A_1(r)$, $B_1(r)$ and other coefficients are determined. The equations for finding $B_0(r)$, $A_1(r)$, $B_1(r)$ have the following structure:

$$B_0''(r) + \left(\frac{1}{r} + \frac{V_H}{RT} \frac{4P}{\pi a} \frac{1}{a^2} \frac{r}{\left(1 - \frac{r^2}{a^2}\right)^2}\right) B_0'(r) + \frac{V_H}{RT} \frac{4P}{\pi a} \frac{1}{a^2} \frac{\left(1 + \frac{r^2}{a^2}\right)}{\left(1 - \frac{r^2}{a^2}\right)^3} B_2(r) = 0, \tag{11}$$

$$A_{1}^{\prime\prime} + \left(\frac{1}{r} + \frac{V_{H}}{RT} \frac{4P}{\pi a} \frac{1}{a^{2}} \frac{r}{\left(1 - \frac{r^{2}}{a^{2}}\right)^{2}}\right) A_{1}^{\prime} - \left(\frac{1}{r^{2}} + \frac{1}{2} \frac{V_{H}}{RT} \frac{4P}{\pi a} \frac{1}{a^{2}} \frac{\left(1 + \frac{r^{2}}{a^{2}}\right)}{\left(1 - \frac{r^{2}}{a^{2}}\right)^{3}}\right) A_{1} + \frac{1}{2} \left(\frac{1}{r^{2}} + \frac{1}{2} \frac{V_{H}}{RT} \frac{4P}{\pi a} \frac{1}{a^{2}} \frac{\left(1 + \frac{r^{2}}{a^{2}}\right)}{\left(1 - \frac{r^{2}}{a^{2}}\right)^{3}}\right) A_{1} + \frac{1}{2} \left(\frac{1}{r^{2}} + \frac{1}{2} \frac{V_{H}}{RT} \frac{4P}{\pi a} \frac{1}{a^{2}} \frac{1}{\left(1 - \frac{r^{2}}{a^{2}}\right)^{3}}\right) A_{1} + \frac{1}{2} \left(\frac{1}{r^{2}} + \frac{1}{2} \frac{V_{H}}{RT} \frac{4P}{\pi a} \frac{1}{a^{2}} \frac{1}{\left(1 - \frac{r^{2}}{a^{2}}\right)^{3}}\right) A_{1} + \frac{1}{2} \left(\frac{1}{r^{2}} + \frac{1}{2} \frac{V_{H}}{RT} \frac{4P}{\pi a} \frac{1}{a^{2}} \frac{1}{\left(1 - \frac{r^{2}}{a^{2}}\right)^{3}}\right) A_{1} + \frac{1}{2} \left(\frac{1}{r^{2}} + \frac{1}{2} \frac{V_{H}}{RT} \frac{4P}{\pi a} \frac{1}{a^{2}} \frac{1}{\left(1 - \frac{r^{2}}{a^{2}}\right)^{3}}\right) A_{1} + \frac{1}{2} \left(\frac{1}{r^{2}} + \frac{1}{2} \frac{V_{H}}{RT} \frac{4P}{\pi a} \frac{1}{a^{2}} \frac{1}{\left(1 - \frac{r^{2}}{a^{2}}\right)^{3}}\right) A_{1} + \frac{1}{2} \left(\frac{1}{r^{2}} + \frac{1}{2} \frac{V_{H}}{RT} \frac{4P}{\pi a} \frac{1}{a^{2}} \frac{1}{\left(1 - \frac{r^{2}}{a^{2}}\right)^{3}}\right) A_{1} + \frac{1}{2} \left(\frac{1}{r^{2}} + \frac{1}{2} \frac{V_{H}}{RT} \frac{4P}{\pi a} \frac{1}{a^{2}} \frac{1}{\left(1 - \frac{r^{2}}{a^{2}}\right)^{3}}\right) A_{1} + \frac{1}{2} \left(\frac{1}{r^{2}} + \frac{1}{2} \frac{V_{H}}{RT} \frac{4P}{\pi a} \frac{1}{a^{2}} \frac{1}{\left(1 - \frac{r^{2}}{a^{2}}\right)^{3}}\right) A_{1} + \frac{1}{2} \left(\frac{1}{r^{2}} + \frac{1}{2} \frac{V_{H}}{RT} \frac{4P}{\pi a} \frac{1}{a^{2}} \frac{1}{\left(1 - \frac{r^{2}}{a^{2}}\right)^{3}}\right) A_{1} + \frac{1}{2} \left(\frac{1}{r^{2}} + \frac{1}{2} \frac{V_{H}}{RT} \frac{4P}{\pi a} \frac{1}{a^{2}} \frac{1}{\left(1 - \frac{r^{2}}{a^{2}}\right)^{3}}\right) A_{1} + \frac{1}{2} \left(\frac{1}{r^{2}} + \frac{1}{2} \frac{V_{H}}{RT} \frac{4P}{\pi a} \frac{1}{a^{2}} \frac{1}{\left(1 - \frac{r^{2}}{a^{2}}\right)^{3}}\right) A_{1} + \frac{1}{2} \left(\frac{1}{r^{2}} + \frac{1}{2} \frac{V_{H}}{RT} \frac{4P}{\pi a} \frac{1}{a^{2}} \frac{1}{\left(1 - \frac{r^{2}}{a^{2}}\right)^{3}}\right) A_{1} + \frac{1}{2} \left(\frac{1}{r^{2}} + \frac{1}{2} \frac{V_{H}}{RT} \frac{4P}{\pi a} \frac{1}{a^{2}} \frac{1}{\left(1 - \frac{r^{2}}{a^{2}}\right)^{3}}\right) A_{1} + \frac{1}{2} \left(\frac{1}{r^{2}} + \frac{1}{2} \frac{V_{H}}{RT} \frac{4P}{\pi a} \frac{1}{a^{2}} \frac{1}{\left(1 - \frac{r^{2}}{a^{2}}\right)^{3}}\right) A_{1} + \frac{1}{2} \left(\frac{1}{r^{2}} + \frac{1}{2} \frac{V_{H}}{RT} \frac{4P}{\pi a} \frac{1}{a^{2}} \frac{1}{\left(1 - \frac{r^{2}}{a^{2}}\right)^{3}}\right) A_{$$

$$+\frac{3}{2}\frac{V_H}{RT}\frac{4P}{\pi a}\frac{1}{a^2}\frac{\left(1+\frac{r^2}{a^2}\right)}{\left(1-\frac{r^2}{a^2}\right)^3}A_3 + \frac{\omega}{D}B_1 = 0.$$
 (12)

$$B_{1}^{"} + \left(\frac{1}{r} + \frac{V_{H}}{RT} \frac{4P}{\pi a} \frac{1}{a^{2}} \frac{r}{\left(1 - \frac{r^{2}}{a^{2}}\right)^{2}}\right) B_{1}^{"} - \left(\frac{1}{r^{2}} - \frac{1}{2} \frac{V_{H}}{RT} \frac{4P}{\pi a} \frac{1}{a^{2}} \frac{\left(1 + \frac{r^{2}}{a^{2}}\right)}{\left(1 - \frac{r^{2}}{a^{2}}\right)^{3}}\right) B_{1} + \frac{3}{2} \frac{V_{H}}{RT} \frac{4P}{\pi a} \frac{1}{a^{2}} \frac{\left(1 + \frac{r^{2}}{a^{2}}\right)}{\left(1 - \frac{r^{2}}{a^{2}}\right)^{3}} B_{3} - \frac{\omega}{D} A_{1} = 0.$$

$$(13)$$

In order to find expressions for the unknown coefficients, it is necessary to restrict the infinite system to a finite number of equations and the required functions. Let B_2 be equal to zero, then the Eq. 11 can be calculated for finding B_0 . Using the Mathematica symbolic computation package, the solution is obtained:

$$B_0(r) = C_2 + \frac{1}{2}C_1 \left[-Ei \left(\frac{K}{2\left(-1 + \frac{r^2}{a^2}\right)} \right) + exp\left(-\frac{K}{2}\right) Ei \left(\frac{\frac{r^2}{a^2}K}{2\left(-1 + \frac{r^2}{a^2}\right)} \right) \right], \tag{14}$$

where $K = \frac{V_H}{RT} \frac{4P}{\pi a}$, Ei(x) – the exponential integral.

The coefficients of integration C_1 and C_2 are found from boundary conditions. Due to linearity of solution, we supposed that at the outer boundary the hydrogen concentration is set equal to one. Using this boundary condition and the condition of boundedness of the solution at zero, the expansion coefficient B_0 has been calculated:

$$B_0(r) = 1. (15)$$

Next, we considered the solution for $B_1(r)$. In order to simplify its calculation, we assumed that the hydrogen concentration at the outer boundary is set according to the following law:

$$C(a,\varphi) = B_0(a) + B_1(a)\cos\varphi, \tag{16}$$

where $B_0(a)$ $\bowtie B_1(a)$ are known. Due to symmetry, only an even function of the angle is considered. And the following simplified equation is obtained:

$$B_{1}^{"} + \left(\frac{1}{r} + \frac{V_{H}}{RT} \frac{4P}{\pi a} \frac{1}{a^{2}} \frac{r}{\left(1 - \frac{r^{2}}{a^{2}}\right)^{2}}\right) B_{1}^{"} - \left(\frac{1}{r^{2}} - \frac{1}{2} \frac{V_{H}}{RT} \frac{4P}{\pi a} \frac{1}{a^{2}} \frac{\left(1 + \frac{r^{2}}{a^{2}}\right)}{\left(1 - \frac{r^{2}}{a^{2}}\right)^{3}}\right) B_{1} = 0.$$
 (17)

This equation has a complex structure, since the coefficients depend on the variable r in a complex way. Thus, we found the approximate solution of this equation using the Galerkin approach. Since the method assumes the zero boundary condition, the solution is considered in the form:

$$B_1(r) = B_1(a) + C_1 f(r), \tag{18}$$

where the basis function vanishes at the boundary:

$$f(r) = 1 - \frac{r}{a}.\tag{19}$$

The constant C_1 should be calculated. To do this, the Eq. 18 is substituted into the Eq. 17, it is multiplied by the basis function and integrated over the variable r on the interval [0; a]. The constant C_1 has this view: $C_1 = -B_1(a) \left(1 + \frac{1}{2} \frac{V_H}{RT} \frac{4P}{\pi a}\right)$. Then the coefficient $B_1(r)$ is equal to:

$$B_1(r) = -B_1(a) \frac{1}{2} \frac{V_H}{RT} \frac{4P}{\pi a} + B_1(a) \left(1 + \frac{1}{2} \frac{V_H}{RT} \frac{4P}{\pi a} \right) \frac{r}{a}.$$
 (20)

As a result, the linear approximate solution of the hydrogen concentration distribution is obtained:

$$C(r,\varphi) = B_0(a) - B_1(a) \frac{1}{2} \frac{V_H}{RT} \frac{4P}{\pi a} cos\varphi + B_1(a) \left(1 + \frac{1}{2} \frac{V_H}{RT} \frac{4P}{\pi a}\right) \frac{r}{a} cos\varphi. \tag{21}$$

Therefore, the diffusion equation in a rotating body under the action of elastic stresses with taking into account the smallness of the angles and considering the region near the point of load application can be solved by representing the function of the hydrogen concentration in

the form of a Fourier series. The coefficients of this expansion can be found using numerical or approximate analytical methods. Using the Galerkin approach, in the first approximation, the coefficient standing in front of the cosine in the expansion of the function in the Fourier series is obtained, which we only considered due to the symmetry of this problem.

Discussion

We investigated the problem of the distribution of the hydrogen concentration in a rotating cylindrical elastic body compressed by two concentrated forces. The stress state of an elastic body was determined by means of the theory of functions of complex variable. As a result, we constructed the contour graphs of the stress distribution in the cylindrical body. The stress field has an areas of concentration of the maximum values of compressive stresses, located near the points of application of concentrated forces, however, the stress values rather quickly decrease with distance from these points. The stress field is distributed evenly in the remaining area of the cross-section of cylinder.

Then we wrote down the hydrogen diffusion equation in an elastic body under the action of concentrated forces. The obtained equation turned out to be very complex, it does admit a closed form solution. This equation was reduced to ordinary differential equations by expansion the sought-for function in a Fourier series. It was discovered to be possible to solve them only asymptotically for some harmonics. However, the asymptotic simplification is justified, since in this case the search of the hydrogen concentration is performed near the zone of action of external forces, where the stresses reach their maximum values.

In this research, we demonstrated the possibility of analytical determination of the hydrogen concentration distribution in a rotating cylindrical elastic body near the points of application of external forces. This problem has a practical importance, since the object of research can be interpreted as a model of many structural elements, for example, as rolling elements of roller bearings. Determination of the distribution of hydrogen concentration in bodies in a stressed state can help in studies of diffusion processes of hydrogen in metals, which affect their mechanical characteristics.

Conclusion

In this paper, the diffusion of hydrogen in a rotating cylindrical elastic body under the action of external concentrated forces was investigated. As a result, a stress field was found. The method of calculating a solution of hydrogen diffusion equation in a rotating body was demonstrated. Method includes a transition to a rotating coordinate system, expanding the function in a Fourier series and applying numerical and approximate methods for solving ordinary differential equations to find the expansion coefficients. The solution of ordinary differential equations was obtained asymptotically for several harmonics. The result confirms the possibility of applying the presented methods to solve the hydrogen diffusion equation in loaded rotating elastic bodies. This problem requires further research in order to obtain the hydrogen distribution throughout the cross-section of cylindrical body. The determination of hydrogen distribution in rolling elements is important in diagnostics of the residual life of roller bearings during their operation in environments with a high hydrogen content.

References

- 1. Fremy ME. On the composition of cast iron and steel. *Journal of the Franklin Institute*. 1861;72(5): 342–346.
- 2. Pfeil LB. The effect of occluded hydrogen on the tensile strength of iron. *Proceedings of the Royal Society of London. Series A, Containing Papers of a Mathematical and Physical Character.* 1926;112(760): 182–195.
- 3. Hirth JP. Effects of Hydrogen on the Properties of Iron and Steel. Metall. Trans. A. 1980;11: 861–890.

- 4. Askari M, Aliofkhazraei M, Afroukhteh S. A comprehensive review on internal corrosion and cracking of oil and gas pipelines. *Journal of Natural Gas Science and Engineering*. 2019;71: 102971.
- 5. Li X, Ma X, Zhang J, Akiyama E, Wang Y, Song X. Review of hydrogen embrittlement in metals: hydrogen diffusion, hydrogen characterization, hydrogen embrittlement mechanism and prevention. *Acta Metallurgica Sinica (English Letters)*. 2020;33: 759–773.
- 6. Kolachev BA. *Hydrogen embrittlement of metals*. Moscow: Metallurgiya; 1985. (In-Russian)
- 7. Vegter RH, Slycke JT. The Role of Hydrogen on Rolling Contact Fatigue Response of Rolling Element Bearings. *Journal of Astm International*. 2010;7(2): JAI102543.
- 8. Birnbaum HK, Sofronis P. Hydrogen-enhanced localized plasticity a mechanism for hydrogen-related fracture. *Material Science and Engineering: A.* 1994;176: 191–202.
- 9. Sedova YS, Polyanskiy VA, Bessonov NM. Accounting for the Skin Effect in Hydrogen-Charged Samples in the HEDE Model of Cracking. In: *International Summer School-Conference "Advanced Problems in Mechanics"*. Springer; 2021. p.133–147.
- 10. Lin M, Yu H, Ding Y, Wang G, Olden V, Alvaro A, Jianying H, Zhang Z. A predictive model unifying hydrogen enhanced plasticity and decohesion. *Scripta Materialia*. 2022;215: 114707.
- 11. Troiano AR. The role of hydrogen and other interstitials in the mechanical behavior of metals. *ASM-Trans*. 1960;52: 54–80.
- 12. Oriani RA. A mechanistic theory of hydrogen embrittlement of steels. *Berichte der Bunsengesellschaft für physikalische Chemie*. 1972;76: 848–857.
- 13. Djukic MB, Bakic GM, Zeravcic VS, Sedmak A, Rajicic B. The synergistic action and interplay of hydrogen embrittlement mechanisms in steels and iron: Localized plasticity and decohesion. *Engineering Fracture Mechanics*. 2019;216: 106528.
- 14. Carrasco JP, dos Santos NC, Silv AA. Numerical simulation of the hydrogen effect on the deformations of test body models loaded under tensile stress. *International Journal of Modeling and Simulation for the Petroleum Industry*. 2007;1: 55–62.
- 15. Belyaev AK, Polyanskiy AM, Polyanskiy VA, Yakovlev YA. An Approach to Modeling Structural Materials with Low Hydrogen Concentration. In: *Dynamical Processes in Generalized Continua and Structures*. 2019. p.63–87.
- 16. Belyaev AK, Polyanskiy VA, Porubov AV. Nonlinear dynamics of hydrogen concentration in high-strength and high-entropy alloys. *Contin. Mech. Thermodyn.* 2019;31: 1785–1794.
- 17. Fick A. Ueber diffusion. Annalen der Physik. 1855;170: 59–86.
- 18. Fick A. On liquid diffusion. *The London, Edinburgh, and Dublin Philosophical Magazine and Journal of Science*. 1855;10(63): 30–39.
- 19. Kolosov GV. *The use of a complex variable in the theory of elasticity*. Leningrad; 1935. (In-Russian)
- 20. Lurie AI. Theory of elasticity. Science; Moscow; 1970. (In-Russian)

THE AUTHORS

A.K. Belyaev 🗓

e-mail: vice.ipme@gmail.com

A.R. Galyautdinova 🗓

e-mail: aliyagalyautdinova@gmail.com

S.A. Smirnov 🗓

e-mail: serg.a.smir@gmail.com

Modeling the skin effect, associated with hydrogen charging of samples, within the framework of the HEDE mechanism of cracking

Submitted: August 7, 2023

Accepted: October 27, 2023

Approved: September 20, 2023

Yu.S. Sedova [□] , V.A. Polyanskiy [□], A.K. Belyaev [□], Yu.A. Yakovlev [□]

Abstract. The article is concerned with finite element solution of hydrogen-induced brittle fracture of a metal cylindrical specimen with a semicircular groove. The study is based on the HEDE model of hydrogen brittleness and considers the skin effect of charging the samples with hydrogen. The results showed that taking into account the skin effect leads to the changes in the mechanisms of destruction of samples, and it can be the true cause of the experimentally observed dual fracture pattern.

Keywords: cracking; decohesion; skin effect; hydrogen diffusion; dissolved hydrogen; destruction

Citation: Sedova YS, Polyanskiy VA, Belyaev AK, Yakovlev YA. Modeling the skin effect, associated with hydrogen charging of samples, within the framework of the HEDE mechanism of cracking. *Materials Physics and Mechanics*. 2023;51(6): 152-159. DOI: 10.18149/MPM.5162023_15.

Introduction

The influence of hydrogen on various properties of iron and its alloys has been studied since the 19th century. It was found that saturation with hydrogen leads to a strong decrease in strength properties, plasticity, impact strength and crack resistance characteristics, metal products and structures fail at loads less than the calculated ones.

As a rule, hydrogen dissolved in the material is the cause of the brittle fracture of steel. It is the only element that has a significant effect on the properties of steel, even at ultra-low concentrations (at a mass concentration of the order of one hundred thousandths of a percent) that are beyond the sensitivity range of most analytical methods for determining alloy components. The problem is complicated by the fact that hydrogen is everywhere, either in the form of chemical compounds, the most common of which is water, or in a gaseous state. Therefore, even if insignificantly low concentrations can be achieved during the production of alloys, the subsequent processing and operation of metal parts inevitably leads to the fact that the concentration of hydrogen increases, and it begins to noticeably affect the properties of metals and alloys. This makes it impossible to exclude the influence of hydrogen using special technologies. Therefore, it is necessary to take into account the effect of hydrogen on the structure and strength of materials at the stage of production of structures, as well as during their operation.

Nowadays, one of the generally accepted and most developed approaches to describing the mechanism of hydrogen embrittlement is hydrogen enhanced decohesion model (HEDE) [1]. Its concept states the following. Hydrogen moves under the action of internal stresses and accumulates near the regions of maximum normal tensile stress. An increase in its local concentration leads to a decrease in the free energy required for the formation of a fracture surface, as a result of which decohesion or "delamination" occurs.

To date, many works devoted to modeling the HEDE mechanism have been carried out. A detailed review of the latest results from this approach is given in [2]. Most of them are oriented and based on experimental data obtained for samples artificially charged with hydrogen in an electrolyte solution using a cathodic current. It should be noted here that in all the studies performed, the authors considered the distribution of hydrogen concentrations inside the metal, which occurs during the charging of the samples with it, as uniform. All redistributions and changes in hydrogen concentration were conditioned by external loading or crack growth.

Most often, the value of the initial hydrogen concentration is established only based on the fitting of the model parameters to the experimental data. Therefore, in different works it varies from 0.0001 to 2 ppm. As a result, the authors, summing up the research results, point out the emerging problems with determining a large number of model parameters and not only the qualitative agreement of the simulation results with experimental data.

Actually, charging with hydrogen leads to a highly non-uniform distribution of concentrations of this substance [3–5]. As a rule, the hydrogen content in the surface layer with a thickness of about one grain size of the metal (60-100 µm) exceeds its value inside the sample by tens of times. This phenomenon is called skin effect [6]. And despite such prolonged and thorough investigation of the problems of hydrogen brittleness, the modeling of this phenomenon has so far been carried out without taking into account the influence of the skin effect.

Obviously, skin effect will significantly affect the result of the simulation research, as well as it can discover new effects and improve understanding the mechanisms of hydrogen brittleness. And this article is concerned with a numerical investigation of the influence of the skin effect of hydrogen charging of samples on a crack growth within the framework of HEDE mechanism of cracking.

The HEDE model of brittle fracture

The process of hydrogen transport inside a solid is traditionally considered within the HEDE model as a diffusion process. To describe it, Fick's law [7] is applied with the additional term that takes into account the thermodynamic (or chemical) potential V[8]:

$$\frac{\partial C}{\partial t} = \nabla \cdot \left[D(T, \underline{r}) \left(\nabla C + \frac{C \nabla V}{RT} \right) \right]. \tag{1}$$

Here C is the hydrogen concentration, D is the diffusion coefficient, R is the gas constant, T is the absolute temperature, r is the radius vector, and t is the time. Taking into account the

effect of mechanical stresses, this equation can be rewritten as
$$\frac{\partial C}{\partial t} = D[T]\nabla^2 C - D[T]\frac{V_H \nabla C \cdot \nabla p}{RT} - D[T]\frac{CV_H \nabla^2 p}{RT}, \qquad (2)$$
 where p is the hydrostatic pressure determined by the spherical part of the stress tensor,

 $p = \frac{1}{3}I_1(\underline{\sigma})$, V_H is the partial molar volume of hydrogen.

Further, the fracture criterion associated with the magnitude of the crack opening comes into operation in the framework of the HEDE mechanism. According to Gorsky's law [9], the hydrogen is concentrated in the region of maximal spherical part of the stress tensor (i.e. hydrostatic tension) and reduces the adhesion of the crack faces which leads to the decohesion [10].

To describe these changes in the cohesion forces of grains one uses the parameter of the degree of filling the free surface of the crack with hydrogen atoms θ which can be represented as [11]:

$$\theta = \frac{C}{C + \exp\left(-\frac{\Delta g_H}{RT}\right)},\tag{3}$$

where Δg_H is the difference between the Gibbs free energy for hydrogen between the state of being adsorbed inside the crystal lattice and the free state (taken from experiment). The equation (3) was obtained by Serebrinsky [11] by comparing the value with the filling parameter of hydrogen traps in the metal based on the McLean ratio, cf. [12].

The value of the parameter θ determines the change in the specific energy of the free surface $\gamma(\theta)$ which depends on the surface sorption of hydrogen [11]:

$$\gamma(\theta) = (1 - 1.0467\theta + 0.1687\theta^2)\gamma(0). \tag{4}$$

From the energetical identity $2\gamma(\theta) = \sigma_{Zc}(\theta)\delta_c(\theta)$, where $\sigma_{Zc}(\theta)$ denotes the maximal cohesive stress normal to the crack edges and $\delta_c(\theta)$ is the maximal separation displacement between them without breaking of bonds (decohesion), the law of hydrogen degradation follows in the form [11]:

$$\sigma_Z(\theta) = (1 - 1.0467\theta + 0.1687\theta^2)\sigma_Z(0),\tag{5}$$

under the assumption of a weak dependence of the value of the $\delta_c(\theta)$ from the parameter θ .

In this paper, we investigate the applicability of the HEDE model to the description of hydrogen-induced destruction of a corset sample taking into account the skin effect.

The numerical experiment

We considered the problem of the hydrogen-induced fracture of steel cylindrical specimen with a semicircular groove under the action of uniaxial tension. In order to monitor and control all dependencies and parameters used in the model, we have abandoned the analysis using standard finite element packages and developed our own finite volume program code written in the C++ in the Microsoft Visual Studio.

The calculation procedure consists of two successive stages: (i) solving the mechanical problem of the stress-strain state of the sample and (ii) analyzing the diffusion problem with the simultaneous calculation of the cohesive stresses σ_z .

On the stage (i) to calculate the equations of the linear theory of elasticity, we solved the system of equations (6). It consists of the equilibrium equation, definition of linear strain tensor ε and generalized Hooke's law:

$$\begin{cases}
\nabla \cdot \underline{\sigma} + \underline{f} = 0, \\
\underline{\varepsilon} = \frac{1}{2} \left(\nabla \underline{u} + (\nabla \underline{u})^T \right), \\
\underline{\sigma} = \lambda \vartheta \underline{E} + 2\mu \underline{\varepsilon},
\end{cases} \tag{6}$$

where $\underline{\underline{\sigma}}$ - Cauchy stress tensor, \underline{f} - volumetric force density, \underline{u} - displacement vector, $\underline{\underline{E}}$ -Young modulus, $\vartheta = I_1(\underline{\varepsilon})$, λ and μ - Lame parameters.

To solve the differential equilibrium equation in (6) numerically we used the establishment method, proposed by Wilkins [13]. It lies in the fact that the stationary problem solution is obtained by solving it as the non-stationary problem and reaching the stationary mode.

The characteristics of the stress-strain state of the sample obtained at this step were transferred to the next stage (ii). It included solving the system of foregoing Eqs. (2), (3), (5):

$$\begin{cases} \frac{\partial C}{\partial t} = D[T] \nabla^2 C - D[T] \frac{V_H \nabla C \cdot \nabla p}{RT} - D[T] \frac{CV_H \nabla^2 p}{RT}, \\ \theta = \frac{55.85 \cdot C \cdot 10^{-6}}{55.85 \cdot C \cdot 10^{-6} + \exp(-\frac{\Delta g_H}{RT})}, \\ \sigma_Z(\theta) = (1 - 1.0467\theta + 0.1687\theta^2) \sigma_Z(0). \end{cases}$$
(7)

The numerical solution of Eq. (2) was also carried out based on the establishment method of Wilkins [13]. The value of stress $\sigma_z(0)$ was taken equal to $4.5\sigma_y$ following the recommendations of [14].

A schematic representation of the specimen that we studied is shown in Fig. 1 (right side). The diameter of a cylinder is d = 16 mm, the radius of a semicircular groove is r = 0.6 mm. We solved the problem in a two-dimensional axisymmetric formulation. Considering the symmetry, we modeled a quarter of the longitudinal section of the cylinder that is also shown in the Fig. 1. The tensile load $\sigma = 500$ MPa acting along the horizontal axis Ox was applied to

the right edge of the sample. Mesh nodes on the right edge of the simulated area were unable to move along the horizontal direction Ox, nodes on the lower edge - along the vertical direction Oy. The physical properties of the considered material are shown in Table 1.

Table 1. Physical properties of the PSB1080 steel

Tensile strength	Yield strength	Density	Bulk modulus	Shear modulus
$\sigma_{\rm B}$, MPa	$\sigma_{\rm Y}$, MPa	ρ , kg/m ³	K, GPa	μ , GPa
1498	1276	7800	160	79.3

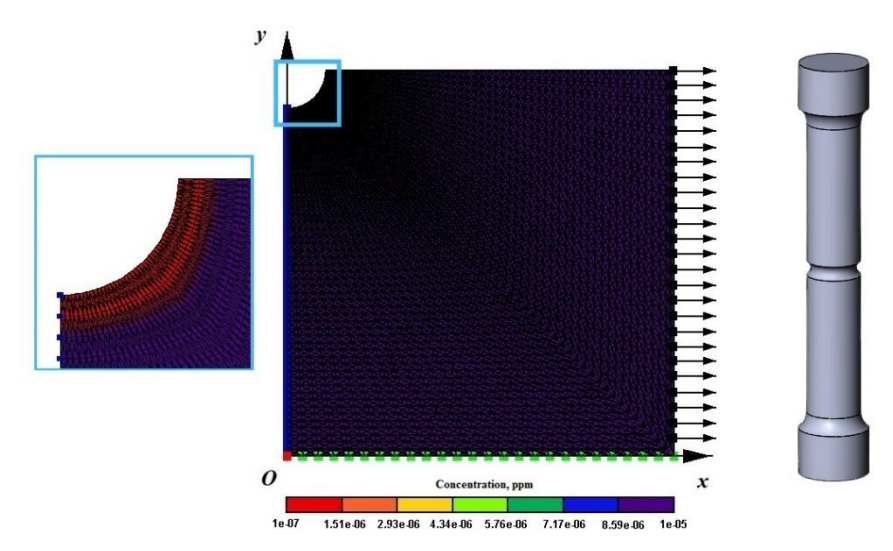


Fig. 1. Finite element model: initial and boundary conditions

The skin effect was represented by the established initial hydrogen concentration $c_0 = 10 \ ppm$ in a thin surface layer of the specimen with a thickness of one element (Fig. 1, zoom). At the same time in the entire volume of the cylinder the initial substance concentration was equal to the background value $c_{bq} = 0.1 \ ppm$, usually observed in experiments.

It was assumed that the crack would consistently propagate along the left edge of the simulated area, starting from the groove surface. The criterion for the destruction, that is, the breaking of the bond between the atomic planes of the material, was the elastic stress obtained from the solution of the static problem exceeding the magnitude of the cohesive stress. As soon as this relationship was fulfilled, the restriction on displacement along the vertical axis Oy was removed at the mesh node. This node was able to break away from the bottom face or, taking into account the symmetry, from the opposite nodal point and move upward under the action of the tensile load.

Simulation results

One of the values monitored during the simulation was the time elapsed between the fulfillment of the fracture criterion at two successive mesh nodes. It was found that the dependence of this value as the crack propagates deeper into the sample is strongly non-monotonic (Fig. 2).

The fracture criterion at the first mesh node was fulfilled instantly, at the very first integration time step. This is conditioned to the high hydrogen concentration in the surface layer of the sample. The same was observed for the second mesh node. The concentration of hydrogen in the sample remained almost unchanged.

Further, as can be seen in Fig. 2, starting from the third node, the value of calculation time increases and reaches its maximum at the sixth mesh node (at 0.85 mm from the sample surface). This is associated with the fact that now it takes some time in solving the diffusion problem, which is necessary for hydrogen to redistribute under the action of the internal stresses

and can accumulate near a new stress concentrator - the current crack tip. At the same time, it should be noted that undoubtedly the level of normal stresses acting in the horizontal direction near the concentrator is constantly increasing. The critical hydrogen concentration, at which the fracture criterion was fulfilled, at the third mesh node was 0.375 ppm, and at the sixth its value decreased to 0.226 ppm.

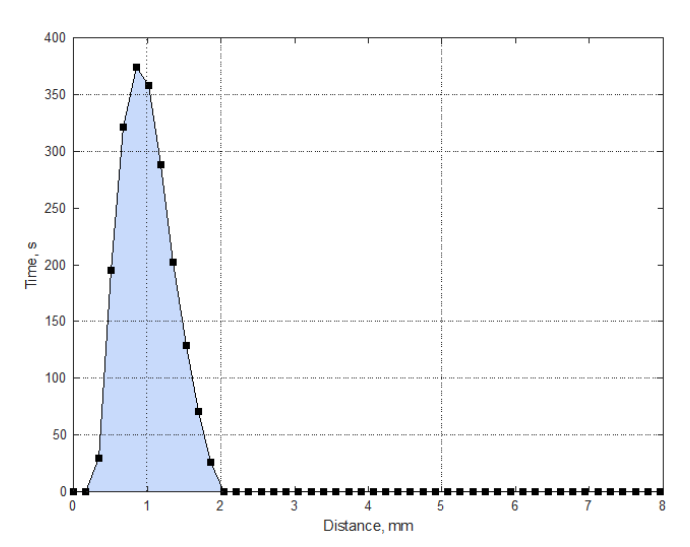


Fig. 2. Dependence of the time interval between the fulfilment of the fracture criterion in two successive nodes

After that, the value of the stresses acting near the concentrator begins to play a key role. Its value becomes more and more, that makes it possible to accumulate a lower content of hydrogen at the crack tip to fulfill the fracture criterion. Therefore, in Fig. 2, we observe a section of decreasing dependence up to the twelfth mesh node, that corresponds to 1.86 mm from the sample surface. The critical hydrogen concentration at this node was 0.112 ppm.

Hereafter, the level of the acting stresses becomes sufficient for the fracture criterion to be fulfilled even at the background hydrogen content. Therefore, the further propagation of the crack will occur instantly, at the very first integration time step.

The distribution of hydrogen concentration along the radius of a specimen is shown in Fig. 3. There are dependencies for different points in time - from the initial distribution, that we have established, to the propagation of a crack to a quarter of the cylinder thickness.

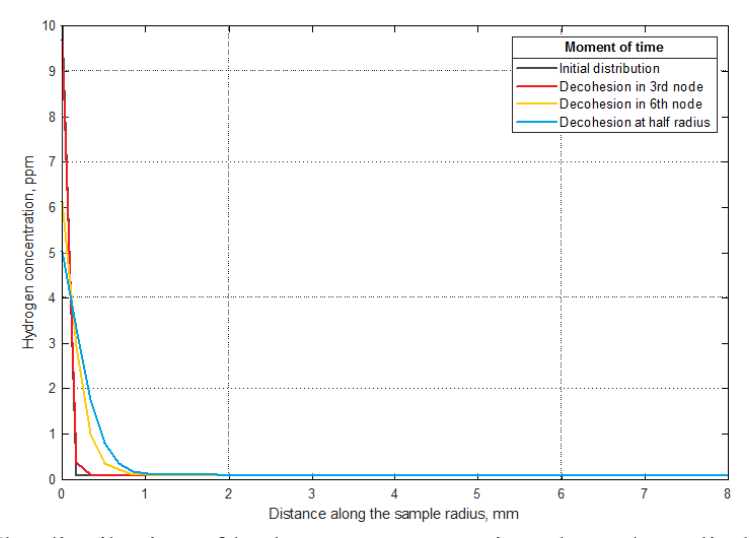


Fig. 3. The distribution of hydrogen concentration along the cylinder radius

It was found that, as the crack propagates, the increased hydrogen content, clearly limited by the surface layer and associated with the skin effect, gradually smooths out, it propagates deep into the material under the action of applied stresses. But at the same time, it does not penetrate deeper than a certain value, in this case 1.86 mm from the sample surface. Further crack propagation occurs at the background concentration without being accompanied by hydrogen diffusion. This is due to the high level of internal stresses acting near the crack tip.

Discussion

We carried out a numerical simulation of the hydrogen-induced brittle fracture of a cylindrical specimen with a semicircular groove based on the HEDE mechanism and considering the skin effect of charging the sample with hydrogen.

Of particular interest is the final distribution of hydrogen over the cylinder, obtained by solving the problem, taking into account such a non-uniform initial content of hydrogen. It is shown schematically in the Fig. 4.

While the crack is small and a relatively low stress acts near the tip, its growth will be provided by a high level of hydrogen concentration present in the surface layer and subsequently penetrates a little deeper into the bulk of the sample. This area corresponds to the zone of hydrogen-induced brittle fracture of the specimen. At the same time, when the crack propagates to the central part of the specimen, the level of internal stresses near the concentrator is high. Therefore, its growth will occur instantly, without the need for an increase in the background hydrogen concentration and without enough time for its further redistribution. This will correspond to the areas of the ordinary decohesion mechanism of crack growth. In this way, the fracture pattern becomes inhomogeneous.

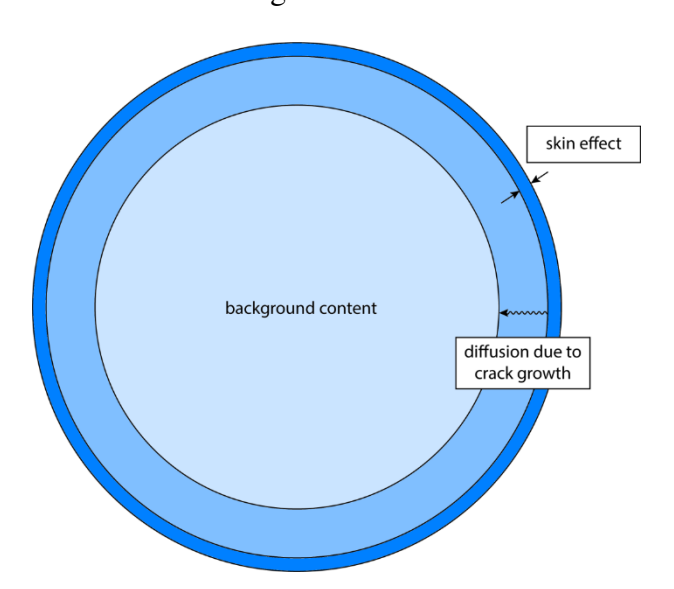


Fig. 4. The distribution of hydrogen content along the cylinder radius

Such a dual character of destruction is often observed in experiments [15,16]. This is usually explained by the successive action of two mechanisms of hydrogen-induced destruction – the HEDE model, that we used, and the HELP model (hydrogen enhanced localized plasticity) [17,18]. One or the other is chosen depending on the local concentration of hydrogen.

The main idea of the HELP is that hydrogen is concentrated at the crack tip under the action of internal stresses and reduces the energy required for the nucleation of dislocations, which are formed and accumulate near the stress concentrator. It produces the areas of localized plasticity, thereby the material "softens" at the crack tip.

Almost all studies on the HELP and HEDE models use the assumption of an initial uniform hydrogen concentration. As it follows from the calculations performed by the authors of the model [19] within the framework of HELP, a significant effect of hydrogen on the mechanical properties of the material begins at local relative mass concentrations of hydrogen of the order of 10⁻² ppm. This level of content is unattainable high and is not observed in most metals. At the same time, according to the theoretical calculation of the plasticity of cracks [20], local concentrations of this substance at the crack tip are about 100 times higher than average. From this, it follows that if the experimentally observed average values of mass hydrogen concentration are 10⁻⁶ ppm, local concentration cannot be greater than 10⁻⁴ ppm. In this way, it is impossible to achieve such an accumulation of substance caused by the application of an external load, that can start the physical mechanisms of HELP model.

The presence of such contradictions and inaccuracies in the approaches existing nowadays allows us to state that the highly uneven distribution of hydrogen over the specimen, associated with the charging of the samples with substance, is the true reason for the dual nature of the destruction observed in practice.

Conclusions

The finite element solution of the destruction of a hydrogen-charged steel cylindrical specimen with a semicircular groove was obtained. The modeling was performed based on the HEDE model of hydrogen brittleness, considering the experimentally observed skin effect of charging the samples with hydrogen.

The simulation results showed that at the sample surface, hydrogen-induced brittle fracture is observed, while crack propagation in the central part of the specimen occurs at background substance concentration.

Such a change in the destruction mechanism confirms that skin effect of charging samples with hydrogen has a significant effect on the fracture of metal samples despite its very shallow depth and can be the main reason of the experimentally observed dual nature of destruction.

References

- 1. Oriani RA. Hydrogen embrittlement of steels. Ber. Bunsen. Phys. Chem. A. 1972;76: 848–857.
- 2. Jemblie L, Olden V, Akselsen OM. A review of cohesive zone modelling as an approach for numerically assessing hydrogen embrittlement of steel structures. Philos. Trans. R. Soc. Lond. A. 2018;375: 20160411.
- 3. Wu TI, Wu JC. Effects of cathodic charging and subsequent solution treating parameters on the hydrogen redistribution and surface hardening of Ti-6Al- 4V alloy. J. Alloys Compnd. 2008;466(1-2): 153–159.
- 4. Martinsson Å, Sandström R. Hydrogen depth profile in phosphorus-doped, oxygen-free copper after cathodic charging. Journal of Materials Science. 2012;47: 6768–6776.
- 5. Alekseeva EL, Belyaev AK, Zegzhda AS, Polyanskiy AM, Polyanskiy VA, Frolova KP, Yakovlev YA. Boundary layer influence on the distribution of hydrogen concentrations during hydrogen-induced cracking test of steels. Diagnostics, Resource and Mechanics of materials and structures. 2018;3: 43–57.
- 6. Polyanskiy V, Belyaev A, Alekseeva E, Polyanskiy A, Tretyakov D, Yakovlev YA. Phenomenon of skin effect in metals due to hydrogen absorption. Cont. Mech. Thermodyn. 2019;31: 1961–1975.
- 7. Fick A. Ueber Diffusion. Ann. Phys. 1855;170: 59–86.
- 8. Shewmon P. Diffusion in solids. 2nd ed. New York: Springer; 2016.
- 9. Barenblatt GI. The formation of equilibrium cracks during brittle fracture. General ideas and hypotheses. Axially-symmetric cracks. J. Appl. Math. Mech. 1959;23: 622–636.
- 10. Scheider I, Pfuff M, Dietzel W. Simulation of hydrogen assisted stress corrosion cracking using the cohesive model. Eng. Fract. Mech. 2008;75: 4283–4291.

- 11. Moriconi C, Hénaff G, Halm D. Cohesive zone modeling of fatigue crack propagation assisted by gaseous hydrogen in metals. *Int. J. Fatigue*. 2014;68: 56–66.
- 12. Gorsky W. Theorie der elastischen Nachwirkung in ungeordneten Mischkristallen (elastische Nachwirkung zweiter Art). *Phys. Z. S.* 1935;8: 457–471.
- 13. Serebrinsky S, Carter E, Ortiz M. A quantum-mechanically informed continuum model of hydrogen embrittlement. *J. Mech. Phys. Solids*. 2004;52(10): 2403–2430.
- 14. Tvergaard V, Hutchinson JW. The relation between crack growth resistance and fracture process parameters in elastic-plastic solids. *J. Mech. Phys. Solids*. 1992;40(6): 1377–1397.
- 15. Peral L, Zafra A, Fernández-Pariente I, Rodríguez C, Belzunce J. Effect of internal hydrogen on the tensile properties of different CrMo (V) steel grades: Influence of vanadium addition on hydrogen trapping and diffusion. *Int. J. of Hydrogen Energy.* 2020;45(41): 22054–22079.
- 16. Venezuela J, Hill T, Zhou Q, Li H, Shi Z, Dong F, Knibbe R, Zhang M, Dargusch MS, Atrens A. Hydrogen-induced fast fracture in notched 1500 and 1700 MPa class automotive martensitic advanced high-strength steel. *Corros. Sci.* 2021;188: 109550.
- 17. Birnbaum H, Sofronis P. Hydrogen-enhanced localized plasticity a mechanism for hydrogen-related fracture. *Mat. Sci. Eng.* 1994;176(1-2): 191–202.
- 18. Sofronis P, Birnbaum H. Mechanics of the hydrogen-dislocation-impurity interactions I. Increasing shear modulus. *J. Mech. Phys. Solids*. 1995;43(1): 49–90.
- 19. Sofronis P, Liang Y, Aravas N. Hydrogen induced shear localization of the plastic flow in metals and alloys. *Eur. J. Mech.* 2001;20(6): 857–872.
- 20. Taha A, Sofronis P. A micromechanics approach to the study of hydrogen transport and embrittlement. *Eng. Fract. Mech.* 2001;68(6): 803–837.

THE AUTHORS

Yu.S. Sedova

e-mail: sedova.yus@mail.ru

A.K. Belyaev 🗓

e-mail: vice.ipme@gmail.com

V.A. Polyanskiy (1) e-mail: vapol@mail.ru

Yu.A. Yakovlev

e-mail: yura.yakovlev@gmail.com

МЕХАНИКА И ФИЗИКА МАТЕРИАЛОВ

51 (6) 2023

Учредители: Санкт-Петербургский политехнический университет Петра Великого, Институт проблем Машиноведения Российской академии наук Издание зарегистрировано федеральной службой по надзору в сфере связи, информационных технологий и массовых коммуникаций (РОСКОМНАДЗОР), свидетельство ПИ №ФС77-69287 от 06.04.2017 г.

Редакция журнала

Профессор, д.т.н., академик РАН, А.И. Рудской – главный редактор
Профессор, д.ф.-м.н., член-корр. РАН, А.К. Беляев – главный научный редактор
Профессор, д.ф.-м.н. И.А. Овидько (1961 - 2017) – основатель и почетный редактор
Профессор, д.ф.-м.н. А.Л. Колесникова – ответственный редактор
Профессор, д.ф.-м.н. А.С. Семенов – ответственный редактор
Л.И. Гузилова – выпускающий редактор, корректор

Телефон редакции +7(812)552 77 78, доб. 224

E-mail: mpmjournal@spbstu.ru Компьютерная верстка Л.И. Гузилова

Подписано в печать 27.11.2023 г. Формат 60x84/8. Печать цифровая Усл. печ. л. $\underline{10,0}$. Тираж 100. Заказ_____.

Отпечатано с готового оригинал-макета, предоставленного автором в Издательско-полиграфическом центре Политехнического университета Петра Великого. 195251, Санкт-Петербург, Политехническая ул., 29. Тел.: +7(812)552 77 78, доб. 224.

A review on the mechanical behaviour of aluminium matrix composites under high strain rate loading	1-13
S. Agarwal, S. Angra, S. Singh	
Qualitative and quantitative interdependence of physical and mechanical properties of stir-casted hybrid aluminum composites D. Kumar, S. Singh, S. Angra	14-23
Study on nanosized Al ₂ O ₃ and Al ₂ O ₃ -SiC on mechanical, wear and fracture surface of Al7075 composites for soil anchoring applications M. Ravikumar, R. Naik, B.R. Vinod, K.Y. Chethana, Y.S. Rammohan	24-41
On the precipitation behavior of Al-based automotive alloy with low Si content M.S. Kaiser, A.K. Hossain	42-53
Effect of industrial hot rolling mode on microstructure and properties of low carbon bainitic steel	54-64
A.A. Zisman, S.N. Petrov, N.Yu. Zolotorevsky, E.A. Yakovleva	
Electronic, magnetic properties and pressure-induced phase transition of new D019 Fe ₂ MnSn Heusler alloy	65-75
I. Bouhamou, H. Abbassa, C. Abbes, A. Boukortt, E.H. Abbes, A. Benbedra	
Disclination models in the analysis of stored energy in icosahedral small particles A.L. Kolesnikova, M.V. Dorogov, S.A. Krasnitckii, A.M. Smirnov, A.E. Romanov	76-83
Determination of the formation energy of edge, screw and twinning dislocations in fcc metals using the molecular dynamics G.M. Poletaev, R.Y. Rakitin	84-91
Nanomaterials coating for bio-implant applications: a re-analysis N. Kumar, A. Bharti, A. Kumar, R.K. Kushwaha, K.K. Patel	92-106
Effect of curing temperature on surface and subsurface properties of polyurethane elastomer I.A. Morozov, A.Yu. Beliaev, M.G. Scherban	107-118
Study of the influence of dispersed fillers on properties of rubber for gaskets of rail fastening E.N. Egorov, S.I. Sandalov, N.I. Kol'tsov	119-126
Electromagnetic radiation reflection, transmission and absorption characteristics of microwave absorbers based on dilatant liquids and powdered activated wood charcoal	127-134
O.V. Boiprav, V.A. Bogush, L.M. Lynkou	
Tribological characteristics of bulk (201) β-Ga ₂ O ₃ substrate crystals grown by EFG P.N. Butenko, M.E. Boiko, A.V. Chikiryaka, L.I. Guzilova, A.O. Pozdnyakov, M.D. Sharkov, A.V. Almaev, V.I. Nikolaev	135-144
Hydrogen diffusion in rotating cylindrical elastic bodies	145-151
A.K. Belyaev, A.R. Galyautdinova, S.A. Smirnov	
Modeling the skin effect, associated with hydrogen charging of samples, within the framework of the HEDE mechanism of cracking	152-159



Yu.S. Sedova, V.A. Polyanskiy, A.K. Belyaev, Yu.A. Yakovlev